



UNIVERSITÀ DEGLI STUDI DI NAPOLI
FEDERICO II

Scuola Politecnica e
delle Scienze di Base



University of Naples Federico II

Ph.D. Program in

Ingegneria Strutturale, Geotecnica e Rischio Sismico

THESIS FOR THE DEGREE OF DOCTOR OF PHILOSOPHY

Satellite SAR data for the monitoring and structural assessment of the built environment

by

ANNALISA MELE

Advisor: Prof. Andrea Prota

Co-Advisor: Dr. Andrea Miano

2023



SCUOLA POLITECNICA E DELLE SCIENZE DI BASE

DIPARTIMENTO DI STRUTTURE PER L'INGEGNERIA E L'ARCHITETTURA

Satellite SAR data for the monitoring and structural assessment of the built environment

Ph.D. Thesis presented
for the fulfilment of the Degree of Doctor of Philosophy
in Ingegneria Strutturale, Geotecnica e Rischio Sismico

by

ANNALISA MELE

2023



Approved as to style and content by

Prof. Andrea Prota, Advisor

Dr. Andrea Miano, Co-advisor

University of Naples Federico II
Ph.D. Program in Structural and Geotechnical Engineering and Seismic Risk
XXXV cycle - Chairman: Prof. Iunio Iervolino



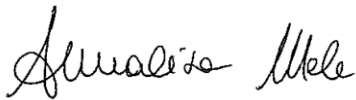
www.dist.unina.it/dottorati-di-ricerca/dottorati

Candidate's declaration

I hereby declare that this thesis submitted to obtain the academic degree of Philosophiæ Doctor (Ph.D.) in Ingegneria Strutturale, Geotecnica e Rischio Sismico is my own unaided work, that I have not used other than the sources indicated, and that all direct and indirect sources are acknowledged as references.

Parts of this dissertation have been published in international journals and/or conference articles (see list of the author's publications at the end of the thesis).

Naples, March 09, 2023

A handwritten signature in black ink, reading "Annalisa Mele". The signature is written in a cursive style with a large initial 'A' and a distinct 'M'.

Annalisa Mele

Abstract

The development of increasingly advanced methodologies for Structural Health Monitoring (SHM) of the built environment is a very current research topic. In recent years, the possibility of using satellite remote sensing data for the monitoring of Earth's surface deformation is receiving great attention. In particular, many literature results highlighted the potential of multi-temporal Differential Synthetic Aperture Radar Interferometry (DInSAR) techniques, not only for ground deformation monitoring but also in the field of SHM. These non-invasive technologies can significantly help to improve the maintenance and assessment of existing constructions, not interfering with their functionality. The potential of DInSAR techniques blends with the increasing improvement of the resolution quality and revisiting time of the modern generation of SAR satellites. In this thesis, new methodological approaches based on DInSAR-derived data for the SHM and assessment of existing buildings are proposed. After an overview of the remote sensing satellite acquisition techniques and satellites, and of the main processing techniques, attention is devoted to illustrating different strategies for the elaboration of the DInSAR measurements to provide useful information for structural applications. At the territorial scale, the proposed methodologies aim to identify "critical" buildings, affected by potentially dangerous displacements, that should be investigated more in detail. Moreover, in view of using DInSAR-derived data to predict future displacements, when possible, these approaches could represent valid support for civil protection prevention plans. At a single construction scale, approaches to exploit the DInSAR-derived data finalized to an estimation of the damage, are proposed, at two different accuracy levels: for a preliminary structural assessment and monitoring and an effective structural assessment and monitoring. Not only the potentials but also the limitations of the use of DInSAR-derived data for SHM and assessment are highlighted. All the proposed methodologies are applied to real case studies.

Keywords: satellite SAR data, structural monitoring, structural assessment, DInSAR, existing constructions

Sintesi in lingua italiana

Lo sviluppo di metodologie avanzate per il monitoraggio (Structural Health Monitoring, SHM) del patrimonio costruito è un tema di ricerca molto attuale. Negli ultimi anni ci si sta focalizzando molto sulla possibilità di utilizzare dati di telerilevamento satellitare per il monitoraggio delle deformazioni superficiali della Terra. In particolare, le tecniche multi-temporali di interferometria RADAR ad apertura sintetica differenziale (DInSAR) si sono rivelate molto promettenti, non solo per il monitoraggio della deformazione del suolo, ma anche nel campo dello SHM. Queste tecnologie non invasive possono aiutare a migliorare notevolmente la manutenzione e la diagnosi delle costruzioni esistenti, senza interferire con il loro esercizio. Le potenzialità delle tecniche DInSAR si accompagnano al crescente miglioramento della qualità della moderna generazione di satelliti, in termini di risoluzione e tempo di rivisitazione. In questa tesi si propongono nuove metodologie basate su dati DInSAR per lo SHM e la diagnosi di edifici esistenti. A seguito di una panoramica riguardo le tecniche di acquisizione, i satelliti e le principali tecniche di processamento, si pone l'attenzione su varie strategie per l'elaborazione dei dati DInSAR che forniscono prodotti utili per applicazioni strutturali. Le metodologie proposte per applicazioni a scala territoriale mirano all'individuazione di edifici "critici", ossia interessati da spostamenti alla base potenzialmente pericolosi, che dovrebbero essere studiati in dettaglio. Inoltre, quando è possibile l'estrapolazione di spostamenti futuri a partire da dati DInSAR, questi approcci possono rappresentare un valido supporto per i piani di prevenzione della protezione civile. A scala di singola costruzione vengono proposti alcuni approcci per sfruttare i dati DInSAR al fine di stimare il danno atteso correlato, a due diversi livelli di accuratezza: per una diagnosi strutturale preliminare e una più accurata. In questa tesi non sono messe in luce solo le potenzialità dell'utilizzo di dati DInSAR ai fini di applicazioni strutturali, bensì anche i limiti. Tutte le metodologie proposte sono applicate a casi studio reali.

Parole chiave: dati satellitari SAR, monitoraggio strutturale, diagnosi strutturale, costruzioni esistenti

Acknowledgements

I express my thanks and gratitude to my Advisor, Prof. Andrea Prota, for trusting me and allowing me to complete my Ph.D. program serenely. The discussions with Prof. Prota about my research have been fundamental to better address my efforts, thanks to his suggestions and observations, always appropriate and illuminating for me.

I thank my Co-advisor, Dr. Andrea Miano, for having been a present and patient guide for me, as well as a friend, and for sharing with me his research experience, from the beginning of my Ph.D. program. The goodness of the results presented in this thesis depended especially on daily discussions with Dr. Andrea Miano.

Many thanks to all the Professors, Researchers, and Ph.D. students with which I have collaborated during these years because from each of them I learned something. In particular, I express my gratitude to Riccardo Lanari and Manuela Bonano from the Institute for Electromagnetic Sensing of the Environment of the National Research Council (CNR-IREA) for their kindness and great willingness to clarify any of my doubts.

I also thank Dr. Michele Crosetto, who hosted me for three months at the Centre Tecnològic de Telecomunicacions de Catalunya (CTTC) in Castelldefels (Spain), where I experimented an important part of the research presented in this dissertation. Working with him has allowed me to see some aspects of my research topic from a different perspective and has been very inspiring.

I would like to express my gratitude to the Reviewers of this thesis, Prof. Anna Saetta (University Iuav of Venice) and Prof. Felice Carlo Ponzo (University of Basilicata), for their valuable comments that helped me to improve the quality of my thesis.

Finally, I warmly thank my family for always supporting me in my choices, and my Luigi for his constant and indispensable support. All my achievements are yours too.

Contents

Abstract	i
Sintesi in lingua italiana	iii
Aknowledgements	v
List of acronyms	xi
List of symbols	xv
List of figures	xix
List of tables	xxix
1. Introduction	1
1.1 General overview	1
1.2 Objectives.....	6
1.3 Organization of the thesis	6
2. Remote sensing RADAR satellite data	11
2.1 Remote sensing RADAR technique	11
2.1.1 Satellites and sensors	19
2.1.1.1 <i>COSMO-SkyMed constellation</i>	21
2.1.1.2 <i>Sentinel-1 constellation</i>	22
2.2 DInSAR technique	23
2.2.1 PSInSAR™	29
2.2.2 SBAS-DInSAR	30
2.3 DInSAR products used for SHM applications	31
2.3.1 CSK data processed through SBAS-DInSAR technique (dataset of Rome, Italy)	32
2.3.2 CSK data processed through CPT technique (dataset of Moio della Civitella, Italy).....	36
2.3.3 EGMS data (dataset of Barcelona, Spain).....	39
3. Elaboration of the DInSAR satellite data for structural applications	45
3.1 Use of a single dataset.....	46
3.2 Use of both ASC and DES datasets	49

3.3	Spatial resampling.....	55
3.4	Applications in Rome.....	57
3.4.1	Application - Torri Stellari.....	59
3.4.2	Application - Collector sewer's point of disposal n. 7.....	68
3.4.3	Application - Corviale.....	70
4.	Potential use for SHM purposes at territorial scale	75
4.1	Preliminary identification and ranking of critical constructions based on DBSCAN technique	76
4.1.1	Proposed methodology.....	78
4.1.2	Applications in Rome.....	83
4.1.3	Discussion.....	95
4.2	ADAFinder tool for SHM of urban settlements	97
4.2.1	Proposed methodology.....	98
4.2.2	Applications in Barcelona.....	101
4.2.2.1	<i>Application - Eixample</i>	101
4.2.2.2	<i>Application - Zona Franca</i>	109
4.2.3	Discussion.....	117
5.	Potential use for SHM purposes at single construction scale	121
5.1	Preliminary structural assessment and monitoring.....	122
5.1.1	Applications in Rome.....	126
5.1.1.1	<i>Application - Torri Stellari</i>	126
5.1.1.2	<i>Application - Collector sewer's point of disposal n. 7</i>	129
5.1.1.3	<i>Application - Vittorino da Feltre</i>	135
5.1.2	Discussion.....	152
5.2	Structural assessment and monitoring	154
5.2.1	Application in Moio della Civitella.....	159
5.2.2.1	<i>Infill damage under landslide settlements</i>	162
5.2.2.2	<i>Seismic safety assessment under landslide-induced damage</i>	177
5.2.2	Discussion.....	188

6. Conclusions	191
Bibliography.....	197
Author's publications	213

List of acronyms

The following acronyms are used throughout the thesis.

3D	Three-dimensional
ADA	Active Deformation Areas
A-DInSAR	Advanced SAR Interferometry
AI	Artificial Intelligence
ASC	Ascending orbit
ASI	Italian Spatial Agency
CLSM	Copernicus Land Monitoring Service
COSMO-SkyMed	CONstellation of small Satellites for Mediterranean basin Observation
CPT	Coherent Pixels Techinque
CSA	Canadian Space Agency
CSG	COSMO-skymed Second Generation
CSK	CONstellation of small Satellites for the Mediterranean basin Observation
CTR	Regional Technical Numerical Map
DBSCAN	Density-based Spatial Clustering of Applications with Noise
DCP	Civil Protecion Department (ITALIAN)
DEM	Digital Elevation Model
DESC	Descending orbit
DInSAR	Differential Synthetic Aperture RADAR Interferometry
DL	Damage Limitation
DLR	German Aerospace Center
DS	Damage State
DTM	Digital Terrain Model

EBK	Empirical Bayesian Kriging
EGMS	European Ground Motion Service
ENVISAT	Environmental Satellite
EO	Earth Observation
EQ	Earthquake
ERS	European Remote-Sensing satellite
ESA	European Space Agency
EW	East-West
GIS	Geographical Information System
GNSS	Global Navigation Satellite Systems
GPS	Global Positioning System
IDR	Interstory Drift Ratio
IDW	Inverse Distance Weighted
IWS	Interferometric Wide Swath
JAXA	Japan Aerospace Exploration Agency
LAN	Landslide
LOS	line of sight
ls	limit state
LS	Life Safety
MDOF	Multi-Degree Of Freedom System
ML	Machine Learning
NS	North-South
PGA	Peach Ground Acceleration
PS	Persistent Scatterer approach
PSs	Persistent Scatterers
RADAR	RADio Detection and Ranging
RADARSAT	RADAR Satellite
RAR	Real Aperture RADAR

RC	Reinforced Concrete
RSLab	Remote Sensing Laboratory
S-1	Sentinel-1
SAOCOM	Satellite Argentino di Osservazione COn Microonde
SAR	Synthetic Aperture RADAR
SB	Small Baseline
SBAS	Small BAseline Subset
SHM	Structural Health Monitoring
SLC	Single Look Complex
SRTM	Shuttle RADAR Topography Mission
SVD	Singular Value Decomposition
TomoSAR	Tomographic Synthetic Aperture RADAR
TOPS	Terrain Observation by Progressive Scans

List of symbols

The following symbols are used throughout the thesis.

a	Width of the diagonal strut equivalent to the infill panel
b	Spatial baseline
c	Speed of light
D	Length of the diagonal strut equivalent to the infill panel
dim	Dimension of the dataset in DBSCAN application
D_{inel}	Inelastic demand point
d_{LOS}	Projection of a surface displacement along the sensor LOS
D_{max}	Maximum displacement component
E	Modulus (or amplitude) of a SAR image
eps	Clustering distance for DBSCAN application
L	Length of the satellite antenna
M_{cr}	Cracking moment
M_y	Yielding moment
M_u	Conventional ultimate capacity moment
$minPoints$	Minimum number of points for DBSCAN application
n_{EW}	Direction cosine with respect to East-West direction
n_{NS}	Direction cosine with respect to North-South direction
n_V	Direction cosine with respect to vertical direction
R	Slant range (or range direction) of a RADAR system
r	Distance between the sensor and the target
t_w	Net thickness of the diagonal strut equivalent to the infill
V_b	Base shear
V_{EW}	East-West component of the mean displacement velocity
V_{LOS}	Component of the mean deformation velocity along a line of sight

V_m	Average value of the mean deformation velocity
V_V	Vertical component of the mean deformation velocity
x	Flight direction (or azimuth) of a RADAR system
X_{LOS}	Generic measurement along the line of sight
X_V	Vertical component of the generic measurement
X_{EW}	East-West component of the generic measurement
a	Slope of the terrain measured with respect to the horizontal plane
β	Angular distortion
δ	Topography value of a
$\delta\rho$	Relative settlement
Δf	Electromagnetic signal band
Δ/L	Deflection ratio
Δr	Resolution in range
Δtop	Roof displacement
$\Delta\varphi$	Phase difference or interferometric phase
Δx	Resolution in azimuth
ε_h	Horizontal strain
ζ_E	Safety Index
θ_{cr}	Cracking chord-rotation
θ_y	Yielding chord-rotation
θ_u	Chord-rotation of conventional ultimate capacity moment
θ	Off-nadir or look angle
λ	Wavelength of the transmitted signal
ρ	Settlement
σ	Standard deviation
τ	Pulse duration
φ	Phase of a SAR image
Φ	Heading angle of a RADAR system

List of figures

Figure 1.1. Organization of the thesis.....	8
Figure 2.1. Scheme of the SAR images acquisition from ASC and DESC orbits (TRE Altamira [62])......	12
Figure 2.2. Scheme of the acquisition system of a RADAR satellite system (Bouaraba et al. (2018) [63])......	13
Figure 2.3. Scheme of the SAR [64]......	16
Figure 2.4. Examples of reflectivity of the scene [64]......	17
Figure 2.5. Geometric deformations related to the soil morphology: (a) foreshortening, (b) layover, (c) shadowing [64]......	18
Figure 2.6. Timeline of the main satellite SAR sensors operating since 1992 to the present.....	20
Figure 2.7. San Paolo stadium (Naples, Italy), as seen through the amplitude SAR images taken by (a) the ENVISAT sensor, (b) the RADARSAT-1 sensor, and (c) the COSMO-SkyMed sensor (Bonano et al. (2013) [65])......	20
Figure 2.8. Revisiting time of the COSMO-SkyMed sensors [64]......	21
Figure 2.9. Revisiting time of the Sentinel-1 sensors [64]......	22
Figure 2.10. Example of DInSAR scenario in the plane orthogonal to the azimuth direction. A displacement component dLOS is detected [64]......	24
Figure 2.11. Full resolution SBAS-DInSAR results obtained from the CSK images collected along the 2011-2019 time in the urban area of Rome, relevant to ASC dataset (modified from [31])......	34
Figure 2.12. Full resolution SBAS-DInSAR results obtained from the CSK images collected along the 2011-2019 time in the urban area of Rome, relevant to DES dataset (modified from [31])......	35
Figure 2.13. Zoom views of the full resolution SBAS-DInSAR results highlighted by the white boxes in Figure 2.12 and displacement time series of selected pixels: (a) mean velocity map of a portion of the A90-A91 Roma-Fiumicino highway (zone A); (b) mean velocity map of the Fiumicino airport runway (zone B) (modified from [31])......	36

Figure 2.14. LOS mean velocity maps of targets identified within Moio della Civitella urban area by CSK data along (a) ASC and (b) DES tracks, for the period 2012-2016 [56].	38
Figure 2.15. LOS mean velocity maps of targets identified within Moio della Civitella urban area by CSK data along (a) ASC and (b) DES tracks, for the period 2017-2019 [56].	39
Figure 2.16. Example of calibrated product by EGMS: (a) ASC and (b) DES (Campi Flegrei, Naples, Italy). Velocities expressed in mm/year.	41
Figure 2.17. Example of ortho product by EGMS: (a) Vertical and (b) horizontal EW (Campi Flegrei, Naples, Italy). Velocities expressed in mm/year.	41
Figure 2.18. ASC calibrated products by EGMS, Barcelona (Spain). Velocities expressed in mm/year.	42
Figure 2.19. DESC calibrated products by EGMS, Barcelona (Spain). Velocities expressed in mm/year.	43
Figure 3.1. Satellite acquisition geometry for (a) ASC and (b) DES orbits [64].	47
Figure 3.2. Variability of the measured LOS mean velocity component as a function of the real deformation direction: (a)-(b) real mean velocity vector with a component parallel to the LOS; (c) real mean velocity vector orthogonal to the LOS.	48
Figure 3.3. Example of PSs spatial distribution of ASC (red markers) and DES (green markers) orbits.	50
Figure 3.4. Decomposition of (a)-(b) vertical real mean velocity vector and (c)-(d) horizontal EW real mean velocity vector along the ASC and DES LOS directions.	52
Figure 3.5. LOS directions and mean LOS velocities for ASC and DES orbit acquisitions represented in a three-dimensional Cartesian reference system.	53
Figure 3.6. From the discrete mean velocity map to the interpolated map.	56
Figure 3.7. LOS mean velocity maps of the investigated area: (a) ASC and (b) DESC. White, violet, and black benchmarks indicate Torri Stellari, Collector sewer point of disposal n. 7, and Corviale, respectively (modified from [38]).	59
Figure 3.8. Original design drawings of Tower n. 1 (M. De Renzi): plan of the first	

floor and section AA, 27 June 1950 (courtesy of <i>Accademia Nazionale di San Luca</i>).	60
Figure 3.9. PSs localization on Torri Stellari (a) accurate volumes and (b) CTR volumes, in ASC (red triangles) and DESC (green circles) orbits [38]......	62
Figure 3.10. Selection of a pair of ASC (triangles) and DES (circles) PSs of Tower n. 1 [38]......	63
Figure 3.11. Mean velocity maps of the Torri Stellari area: (a) ASC and (b) DES data, through EBK interpolation; (c) Vertical and (d) EW components of the mean velocity (period 2011-2019) [38]......	65
Figure 3.12. Adopted grid in the Torri Stellari area, with superimposed ASC (red) and DES (green) PSs [38].	66
Figure 3.13. Comparison of the Vertical and EW displacement components for the three approaches: (a) and (b) DES data resampled on ASC ones; (c) and (d) ASC data resampled on DES ones [38]......	67
Figure 3.14. Collector sewer's point of disposal n. 7: original design drawings (1882) (Courtesy of <i>Rome State Archive, Ufficio Speciale per il Tevere e l'Agro Romano collection</i>).	68
Figure 3.15. Collector sewer's point of disposal n. 7. Considering PSs at the ground level: (a) ASC and DES PSs; mean velocity maps along (b) Vertical and (c) EW direction. Considering all PSs: (d) ASC and DES PSs; global mean velocity maps along (e) Vertical and (f) EW direction [46]......	69
Figure 3.16. Original design drawings of Corviale complex, sector F (ATER Archive).	70
Figure 3.17. PSs localization in ASC (red triangles) and DESC (green circles) orbits, on the Corviale block B accurate volume: from (a) East and (b) West sides; on the Corviale block B CTR volume: from (c) East and (d) West sides [38]......	71
Figure 3.18. LOS mean velocity of all the PSs identified in the area of the Corviale complex: (a) ASC and (b) DESC [38].	72
Figure 3.19. ASC (red) and DESC (green) PSs distribution for the Corviale complex in Rome [38].	72
Figure 4.1. Example representing how DBSCAN works. In this figure, the	

minPoints hyper-parameter is 4, and the eps radius is indicated by the circles. N is a noise point, A is a core point, and points B and C are density reachable from A [94].	77
Figure 4.2. Flowchart of the proposed methodology [36].	79
Figure 4.3. Flowchart of the identification of the buildings through the DBSCAN algorithm [36].	80
Figure 4.4. Flowchart of the operations for the preliminary identification and ranking of critical constructions [36].	82
Figure 4.5. Areas chosen for the algorithm performance: (a) top view, (b) Area 1, (c) Area 2, (d) Area 3 (source: Google Earth Pro) [36].	84
Figure 4.6. Frequency of PSs topography distribution, Area 1 [36].	85
Figure 4.7. Frequency of PSs topography distribution, Area 2 [36].	85
Figure 4.8. Frequency of PSs topography distribution, Area 3 [36].	85
Figure 4.9. Points sorted by distance to the kth nearest neighbor, Area 1 [36].	87
Figure 4.10. Points sorted by distance to the kth nearest neighbor, Area 2 [36].	87
Figure 4.11. Points sorted by distance to the kth nearest neighbor, Area 3 [36].	88
Figure 4.12. Area 1: (a) top view of ASC and DESC PSs, (b) clustering obtained through DBSCAN [36].	89
Figure 4.13. Area 2: (a) top view of ASC and DESC PSs, (b) clustering obtained through DBSCAN [36].	89
Figure 4.14. Area 3: (a) top view of ASC and DESC PSs, (b) clustering obtained through DBSCAN [36].	90
Figure 4.15. Area 1: (a) mean velocity Vertical component and (b) mean velocity East-West component for the combinable pairs of PSs [36].	91
Figure 4.16. Area 2: (a) mean velocity Vertical component and (b) mean velocity East-West component for the combinable pairs of PSs [36].	91
Figure 4.17. Area 3: (a) mean velocity Vertical component and (b) mean velocity East-West component for the combinable pairs of PSs [36].	92
Figure 4.18. Summary maps for Area 1: graphical representation of the meaningful values of (a) mean velocity Vertical components and (b) mean	

velocity East-West components, for each cluster [36].	93
Figure 4.19. Summary maps for Area 2: graphical representation of the meaningful values of (a) mean velocity Vertical components and (b) mean velocity East-West components, for each cluster [36].	94
Figure 4.20. Summary maps for Area 3: graphical representation of the meaningful values of (a) mean velocity Vertical components and (b) mean velocity East-West components, for each cluster [36].	95
Figure 4.21. Flowchart of the proposed methodology (modified from [28]).	98
Figure 4.22. Distribution of the selected PSs on the buildings of the selected area of Eixample: (a) ASC and (b) DESC [28].	103
Figure 4.23. ADA extraction from the active PSs of the selected area of Eixample from (a) ASC and (b) DESC datasets [28].	105
Figure 4.24. Maps of buildings in Eixample area having an average value of mean velocity along (a) ASC and (b) DESC orbit [28].	107
Figure 4.25. Maps of (a) VEW and (b) VV components for the “unstable” buildings in Eixample area [28].	108
Figure 4.26. Maps of average values of mean velocity along (a) ASC and (b) DESC orbit for one of the quadrangular blocks of the Eixample and (c) map of VEW/VV components for one of the quadrangular blocks of the Eixample. The labels indicate the number of PSs used to compute the average mean deformation velocities for each building [28].	109
Figure 4.27. Distribution of the selected PSs on the buildings of the selected area of Zona Franca: (a) ASC and (b) DESC [28].	111
Figure 4.28. ADA extraction from the active PSs of the selected area of Zona Franca from (a) ASC and (b) DESC datasets [28].	114
Figure 4.29. Maps of buildings in Zona Franca area having an average value of mean velocity along (a) ASC and (b) DESC orbit [28].	115
Figure 4.30. Maps of (a) VEW and (b) VV components for the “unstable” buildings in Zona Franca area [28].	116
Figure 5.1. (a) Definitions of settlement ρ , relative settlement $\delta\rho_{max}$, rotation θ and angular strain α ; (b) definitions of relative deflection Δ and deflection ratio	

Δ/L ; (c) definitions of tilt ω and relative rotation (angular distortion) β	124
Figure 5.2. 3D model of the structure of Tower n. 1: (a) section and (b) lateral view [46].....	127
Figure 5.3. 3D integrated model of Torri Stellari (modified from [46]).	127
Figure 5.4. (a) Scheme of Tower n. 2 with the position of the three considered columns; (b) example of settlement profiles of the southern side of Tower n. 2 along Vertical and horizontal East-West direction (modified from [38]).	129
Figure 5.5. Lateral views of the 3D model of the building of the Collector sewer's point of disposal n. 7 with the Collector sewer underground tunnel [46].	130
Figure 5.6. A 3D integrated model of the Collector sewer's point of disposal n. 7 (red circles: ASC PSs, green circles: DES PSs) (modified from [46]).	130
Figure 5.7. Collector sewer's point of disposal n. 7: (a) plan view; (b) settlement profiles along the four building sides (modified from [46]).	131
Figure 5.8. Collector sewer's point of disposal n. 7: picture of the Southern side (survey in November 2021).	132
Figure 5.9. Damage assessment for the considered wall, based on Boscardin and Cording scheme, in function of the angular distortion β and horizontal strain ϵ_h [46].	133
Figure 5.10. Damage assessment for the considered wall, based on Boscardin and Cording's (1989) [54] scheme, in function of the angular distortion β and horizontal strain ϵ_h , by conceptually supposed to know the damage state at the beginning of the monitoring period [46].	134
Figure 5.11. (a) Top view and (b) external lateral view of the Vittorino da Feltre school building (source: <i>Google Earth</i>) [111].	135
Figure 5.12. Plan of the first floor.	136
Figure 5.13. North façade. Cracking pattern detected in (a) 2021 (blue lines) and (b) 2010 (red lines) [111].	139
Figure 5.14. South façade. Cracking pattern detected in (a) 2021 (blue lines) and (b) 2010 (red lines) [111].	140
Figure 5.15. East façade. Cracking pattern detected in (a) 2021 (blue lines) and (b)	

1989 (black lines) [111].	141
Figure 5.16. Damage at the 1 st floor: (a) vertical crack, North-West corner; (b) crack orthogonal to the vault director line in the barrel vault of the hallway parallel to the North façade; (c) double cracks parallel to the vault director line in the barrel vault of the hallway parallel to the North façade; (d) passing diagonal crack in the wall orthogonal to the vault director line in the hallway parallel to the East façade.	142
Figure 5.17. Distribution of ASC (red) and DESC (green) PSs relative to the school building and the adjacent building, considered to be referred to the ground [111].	143
Figure 5.18. Location of the selected PSs: (a) top view with ASC and DESC PSs; (b) 3D view of the building with the selected ASC and DESC PSs on the structure [111].	144
Figure 5.19. LOS displacement time series of the selected (a) ascending and (b) descending PSs [111].	145
Figure 5.20. Maps of the mean velocity components related to the school buildings considering only the PSs located at the ground level along (a)-(b) Vertical and (c)-(d) East-West directions, for the two considered time sub-intervals (modified from [111]).	147
Figure 5.21. Displacement profiles of North façade along (a) Vertical and (b) horizontal East-West component [111].	148
Figure 5.22. Relationship of damage to angular distortion and horizontal extension strain (modified from Boscardin and Cording [54]) [111].	149
Figure 5.23. Displacement profiles of South façade along (a) Vertical and (b) horizontal East-West component [111].	151
Figure 5.24. Displacement profiles of East façade along (a) Vertical and (b) horizontal East-West component [111].	152
Figure 5.25. Structural assessment and monitoring procedure [31].	156
Figure 5.26. Flowchart of the proposed methodology (modified from [56]).	158
Figure 5.27. (a) Geometrical plan; (b) front view of the SW façade; (c) external picture; (d) smooth bars at the base of the column; (e) RC with hollow tiles mixed	

floor, focus on the RC joists and hollow bricks (on-site survey, December 2020) [56].	160
Figure 5.28. Infills details: (a) tuff, (b) solid clay bricks, and (c) hollow clay bricks [56].	160
Figure 5.29. Building prospects with identification of the different infills types, differentiated: I) for color, in hollow clay bricks (blue lines), solid clay bricks (orange lines), and tuff bricks (green lines); II) for typology of line, in: without openings (continuous lines, (a-b)) and with openings (dashed line, (c-d)) (modified from [56]).	161
Figure 5.30. Example of plastic hinges backbones of RC (a) beam T1 and (b) column P1 on the 1 st floor (with reference to Figure 5.27) [57].	163
Figure 5.31. (a) Strut geometry (Al-Chaar, 2002 [119]); (b) Force-displacement envelope for infills by Panagiotakos and Fardis (1996) [118] [57].	164
Figure 5.32. 3D structural model of the building [57].	164
Figure 5.33. LOS mean velocity map of targets identified on the analyzed building using COSMO-SkyMed data: along (a) ascending and (b) descending tracks (modified from [57])	165
Figure 5.34. Displacement profiles affecting building foundations at the end of each year in the period 2012–2016 (modified from [57]).	166
Figure 5.35. Identification of crack pattern on infills in 2015 of (a) NW side and (b) SE side (modified from [57]).	167
Figure 5.36. Damage states (DSs) of masonry infills without openings [57]. ...	168
Figure 5.37. Identification of DSs on infills' backbone according to: (a)-(d) Cardone and Perrone (2015) [123] and (e)-(h) De Risi et al. (2018) [102], [57].	171
Figure 5.38. Infills that have reached the <i>i</i> -th DS, divided by floor and year of evaluation: (a) and (b) 2012; (c) and (d) 2013; (e) and (f) 2014; (g) and (h) 2015; (i) and (j) 2016 (modified from [57]).	174
Figure 5.39. (a) Identification in plane of RC examined columns; linear regression of displacements along X, Y and Z direction at the base of (b) column 1 and (c) column 12 (modified from [57]).	176
Figure 5.40. Prevision of the number of infills that will reach the <i>i</i> th DS in 2025,	

on (a) first floor and (b) second floor [57].	177
Figure 5.41. Characteristic points and assumed parameters of the base moment (M) - chord rotation (θ) response envelope [56].	178
Figure 5.42. 3D structural model of the building [56].	179
Figure 5.43. Time series of displacements of an ascending (A1) and a descending (D1) PS, located on the investigated building [56].	179
Figure 5.44. Displacement profiles extracted for the building foundations at the end of each year in the period 2012–2020: (a) horizontal, (b) Vertical (modified from [56])	180
Figure 5.45. Comparison of the pushover curves and relative failure mechanism progress of structural elements, until the demand point, in the EQ and LAN+EQ for scenarios (a) Mass X and (b) Mode X (modified from [56]).	183
Figure 5.46. Comparison of the pushover curves and relative failure mechanism progress of structural elements, until the demand point, in the EQ and LAN+EQ for scenarios (a) Mass Y and (b) Mode Y (modified from [56]).	184
Figure 5.47. Number of elements in crisis at LS-ls and at DL-ls, versus number of total elements, in EQ and LAN+EQ scenarios, with a focus on the most damaged infill in the 2020 survey	186
Figure 5.48. Comparison of the structural safety index in the EQ and LAN+EQ scenarios, at LS-ls and at DL-ls, for the eight performed analyses	187

List of tables

Table 2.1. Main parameters of ASC and DES CSK datasets (modified from [64]).	32
Table 2.2. CSK SAR data stacks processed through CPT technique for Moio della Civitella urban area.	37
Table 3.1. Sensibility evaluation of the instruments in the different directions.	48
Table 4.1. Topography ground level δ , and δ limit values.	86
Table 4.2. Statistics of the mean velocity of the selected area of Eixample [28].	102
Table 4.3. Summary of the number of buildings in Eixample area [28].	102
Table 4.4. Statistics of the mean velocity of the active PSs in the selected area of Eixample [28].	104
Table 4.5. Statistics of the mean velocity of the selected area of Zona Franca [28].	112
Table 4.6. Summary of the number of buildings in Zona Franca area [28].	112
Table 4.7. Statistics of the mean velocity of the active PSs in the selected area of Zona Franca [28].	113
Table 5.1. Summary of criteria for settlement and differential settlement of structures by literature source (L=length between panels, H=height).	125
Table 5.2. Maximum angular distortion β_{max} and horizontal strain ε_h of the East-West directed walls.	135
Table 5.3. North façade, maximum angular distortion β_{max} and horizontal strain ε_h [111].	149
Table 5.4. Comparison between the DSs classification based on empirical observation and the classification obtained by analytical previsions (DS0=no damage, DS1=light cracking, DS2=extensive cracking, DS3=corner crushing, DS4=collapse, T=both tense struts, compatible with extensive damage) (modified from [57]).	172

Chapter

1

1. Introduction

1.1 General overview

In recent years, the development of increasingly advanced techniques for structural monitoring of the built environment (which means constructions – buildings, structures, and infrastructures – and surroundings) is a highly explored research topic. The worldwide built heritage needs to be monitored for its maintenance, preservation, and supervision. In general, the constructions that need to be monitored and controlled are, mainly, the strategic ones, but also all those exposed to problematic conditions require particular attention. The natural and anthropic phenomena that can induce dangerous actions on constructions are, for example, earthquakes, landslides, subsidence, excavations, thermal variations, shrinkage, viscous phenomena, and degradation processes.

The traditional monitoring techniques allow to take under control single constructions, but the challenge for the future is the creation of methodologies allowing to control simultaneously a high number of constructions. Moreover, the development of non-invasive structural monitoring technologies can significantly improve the maintenance and safety assessments of the existing constructions, reducing the impact of disturbances on their functionality.

In this regard, in recent years, the possibility of using satellite remote sensing data for the monitoring of the deformation of Earth's surface, also in the long

period, is receiving great attention [1]. In particular, the Satellite remote sensing techniques referred to as multi-temporal Differential Synthetic Aperture RADAR (SAR) Interferometry (DInSAR), have been widely used to analyze typically slow Earth surface displacement processes, such as volcanic unrests, seismic phenomena, landslides, subsidence [2]–[5]. In Confuorto et al. (2019) [6] the integration of ground-based subsurface monitoring (inclinometers and piezometers) and DInSAR superficial data has provided consistent results for landslide characterization and helped define the state of activity and the areal distribution of the sliding surface.

The advancements achieved through the DInSAR techniques went hand in hand with the development of the modern generation of SAR satellites and constellation (e.g., COSMO-SkyMed, TerraSAR-X/TanDEM-X, Sentinel-1) with improved capabilities in terms of revisit time, spatial resolution and ground coverage, which have strongly encouraged the monitoring over time of surface deformations in urban and/or built-up environments. Today, SAR images can be acquired with a spatial resolution of a few meters and with a revisit time of some days, so allowing increasingly more reliable detection of differential displacements in urbanized sites compared to that of the first-generation systems (such as ERS-1/2, ENVISAT, RADARSAT-1), aiming at monitoring and assessing the potential critical behavior of single constructions.

The potentialities of these techniques are of great interest. The modalities of elaboration and interpretation of the data are different when making analysis at territorial scale or at single construction scale.

RADAR-based techniques are very useful for the monitoring of the ground deformation of wide areas, as demonstrated by many literature works (e.g., [2]–[4], [7]–[12]), as well as national and regional services born in different countries in the last five years. Regarding the latter topic, at a national scale, the first Ground Motion Service (GMS) started in Italy in 2007 [13], followed by Norway in 2018 [14] and Germany in 2019 [15]. Denmark and the Netherlands are working on their own GMSs, too. In Italy, this kind of monitoring service has been developed also at territorial scale, from 2016 in Tuscany [5], [16], from 2018 in Valle d’Aosta [17] and from 2019 in Veneto. A review of the evolution of wide-

area deformation monitoring initiative based on the DInSAR techniques applied to SAR and Copernicus Sentinel-1 images can be found in Crosetto et al. (2020) [18]. At international level, the introduction of the European Ground Motion Service (EGMS) was approved in 2017 [18]–[20].

Many applications based on using DInSAR techniques and satellite data for performing analyses of ground deformations on extended urbanized areas caused by landslides (e.g., [21], [22]) or subsidence (e.g., [8], [9], [23]–[26]) can be found in the literature. In Barra et al. (2017) [27] a new tool aimed at the semi-automatic extraction of active deformation areas starting from the deformation maps obtained through the Persistent Scatterer Interferometry (PSI) technique, is presented. The same tool has been integrated into a new methodology for the detection of critical buildings, presented in Mele et al. (2023) [28]. Zhu et al. (2018) [29] proposed a new method for automatically detecting potential instability risks affecting buildings and infrastructures, by searching for anomalies in the measuring points deformations, utilizing a hierarchical clustering method. Del Soldato et al. (2019) [30] presented a fragility analysis based on the combination of landslide-induced damage on constructions and ground displacement detected through satellite data.

A comprehensive approach for the processing, interpretation, and proper use of satellite SAR data for structural analyses at urban and single-construction scales is proposed in Talledo et al. (2021) [31].

For large, urbanized areas, the management and elaboration of satellite data require the use of advanced methodologies based on appropriate algorithms, e.g., from machine learning (ML), because of their great volume and dynamism (since they are continuously increasing in time). However, the worldwide literature regarding this aspect, aimed at structural monitoring, is very scarce. For this reason, this topic has been deepened in this thesis. The intuition of applying ML techniques is supported by successful applications in the research field of the automatic extraction of buildings footprints in urban areas, from point clouds. Indeed, Zhang et al. (2006) [32] presented algorithms for the extraction of building footprints from LIDAR measurements, focusing more on two-dimensional (2-D) footprint extraction than 3D building models. Then, the majority of the

existing approaches derive from large scale airborne laser scanning point clouds. Aljumaily et al. (2017) [33] extracted the urban objects from a digital surface model created from aerial laser scanning data, with a fully automatic approach that takes raw 3D points and converts them into sets of clusters through Density-based Spatial Clustering of Applications with Noise (DBSCAN), where each cluster represents an object, such as building or a portion of a ground surface. Zhang and Zhang (2018) [34] proposed a deep learning-based classification algorithm that integrates different neural networks to classify the point clouds into categories of interest, including trees, buildings, and ground. More recent works proposed automatic feature extraction methods using remote-sensing-derived products. Guo et al. (2021) [35] proposed a point cloud extraction method based on the DBSCAN algorithm, using Tomographic Synthetic Aperture RADAR (TomoSAR) point clouds. Also, in Mele et al. (2021) [36], the DBSCAN has been integrated into a new procedure for the detection of critical buildings. Finally, Rahimzad et al. (2021) [37] proposed an application for multi-sensor remote-sensing images with a new unsupervised feature learning method for efficient urban image clustering.

In recent times, many applications in the field of structural monitoring and assessment of single constructions have also been performed (e.g., [38]). In Arangio et al. (2014) [39], an integration of the results of a DInSAR analysis with a semi-empirical model for the assessment of the structural damage induced by subsidence is presented, for three Reinforced Concrete (RC) buildings located in Rome. Chen et al. (2019) [40] illustrate the potential of high-resolution tools in the preventive monitoring and health diagnosis of three typical targets, building, bridge, and heritage remains. The interest is also towards historical heritage. In Cavalagli et al. (2019) [41] an overview of the results of diagnostic and monitoring activities carried out through satellite RADAR interferometry and on-site measurements of two historical buildings is reported. Berto et al. (2021) [42] examine two cultural heritage buildings to evaluate the major issues occurring in the use of DInSAR data and their reliability for monitoring their health status. Drougkas et al. (2021) [43] proposed a methodology for assessing the development of damage in building structures subjected to differential settlement and

uplift. Bridges have been studied, too. Cusson et al. (2021) [44] proposed the use of RADAR satellite data as an early warning system for the detection of unexpected bridge displacements and a decision-support tool. Ponzo et al. (2021) [45] present an example about how the integration of on-site sensors with remotely sensed data and the exploitation of detailed knowledge regarding the on-site conditions represent a key factor for sustainable structural and infrastructural monitoring.

The combination of ground displacement time-series based on the analysis of DInSAR data, with information about the geology of the area and the geometry of the structure under monitoring, can be of great help for the structural assessments [46]. Scifoni et al. (2016) [47] combined the DInSAR measurements with the geological setting and the structural characteristics of the buildings, in order to investigate the deformation causes and evaluate the variation in magnitude of the settlements at the scale of single constructions.

The deformations monitored through DInSAR techniques can be used as input for a preliminary structural assessment and monitoring of the existing constructions. The correlation of the expected damage with the deformation parameters of the constructions refers mainly to a classical literature ([48]–[54]).

Moreover, an in-depth structural assessment can also be pursued starting from DInSAR data, if specific information about the construction are available, to predict the structural response and damage level under a settlement distribution. Many applications can be found in literature about this topic (e.g., [43], [55]–[57]). The amount and quality of available information impose how detailed the structural model to create could be. It ranges from empirical models (e.g., [58]), based on simplifying assumptions that must be met, to semi-empirical approaches (e.g., [59]), up to more sophisticated finite element assessment methods. The latter require a detailed description of the structural characteristics, as well as information about the soil, and is definitely more computationally burdensome than the first two methods. The more accurate the model is, the more reliable the results of the assessment will be.

The aforementioned literature review highlights that the use of DInSAR measurements in the field of structural monitoring is becoming increasingly

important and, at the same time, quite popular.

The advantages of the availability of displacement values are clear in large areas without the presence of ground instrumentation. The possibility to carry out retrospective analyses to investigate the deformative evolution of an area of interest through the generation of time series, by accessing in many cases to satellite images acquired down to 1992, enriches the potential of this instrumentation, allowing to detect eventual information on seasonal or other cyclical trends of displacements.

1.2 Objectives

In this research scenario, this thesis proposes to show some new methodological approaches based on the application of satellite data for the structural monitoring and assessment of existing buildings, included in a framework that furnishes all information necessary for understanding the principles of the satellite-data-based techniques that can be used for structural monitoring purposes. The new tools and strategies identify critical buildings, affected by potentially dangerous displacements, so their aim is the improvement of practices for the conservation and protection of the existing built heritage, providing support for the management of the urban areas. Another goal is to highlight the importance of introducing ML algorithms in the methodologies, for the management and elaboration of the huge amount of data. Not only the potentials but also the limitations of the use of DInSAR data analysis for structural monitoring are highlighted because it is important to realize what really can be done through this technique. The examination of the various elaboration approaches is important to realize which one could be the best for one application, or another. For instance, applications at a territorial scale or a single construction scale have many distinctions, since the scale of the problem is very different.

1.3 Organization of the thesis

The structure of the rest of the thesis is schematized in the flowchart in Figure

1.1. It is organized as follows. Chapter 2, “Remote sensing RADAR satellite data” (blue boxes of the flowchart) introduces the remote sensing RADAR satellite techniques, starting from the basic principles. The description of all satellites and sensors used for image acquisition is reported, other than a summary of the most spread processing techniques, with a focus on the DInSAR technique. Three different datasets of SAR satellite datasets exploited for the following SHM applications are illustrated. Chapter 3, “Elaboration of the DInSAR satellite data for structural applications” (green box of the flowchart) presents different strategies that can be employed to analyze the DInSAR measurements to provide useful information for the SHM and assessment of structures. The potential approaches for the use of the datasets are explained and three applications are shown. In Chapter 4, “Potential use for SHM purposes at territorial scale” (yellow boxes of the flowchart), two methodologies for the management and elaboration of satellite data at the territorial scale are presented. The first one is based on ML algorithms. The second one is based on the use of a tool specifically developed at the Research Unit of Geomatics of the Centre Tecnològic de Telecomunicacions de Catalunya (CTTC). Three applications that highlight the potential use of the two methodologies for SHM purposes at a territorial scale are shown. In Chapter 5, “Potential use for SHM purposes at single construction scale” (red boxes of the flowchart), procedures for the SHM and assessment at single construction scale are described, separating the preliminary structural assessment and monitoring and the “accurate” preliminary structural assessment and monitoring, focusing on the combined use of DInSAR results and additional information, retrieved from on-site surveys and traditional monitoring techniques. In particular, in this thesis, attention is focused on the monitoring of ground settlements, and the assessment of their effects on both structural and non-structural elements. Finally, Chapter 6, “Conclusions”, summarizes the main points of all the previous Chapters of the thesis and contains some future development proposals.

The applications included in this thesis constitute a selection of the numerous applications experimented by the group formed by me and my tutors, in collaboration with other National and International units. All the applications included

in this thesis have been published on International Scientific Journals or are contained in the Proceedings of prestigious National or International Conferences.

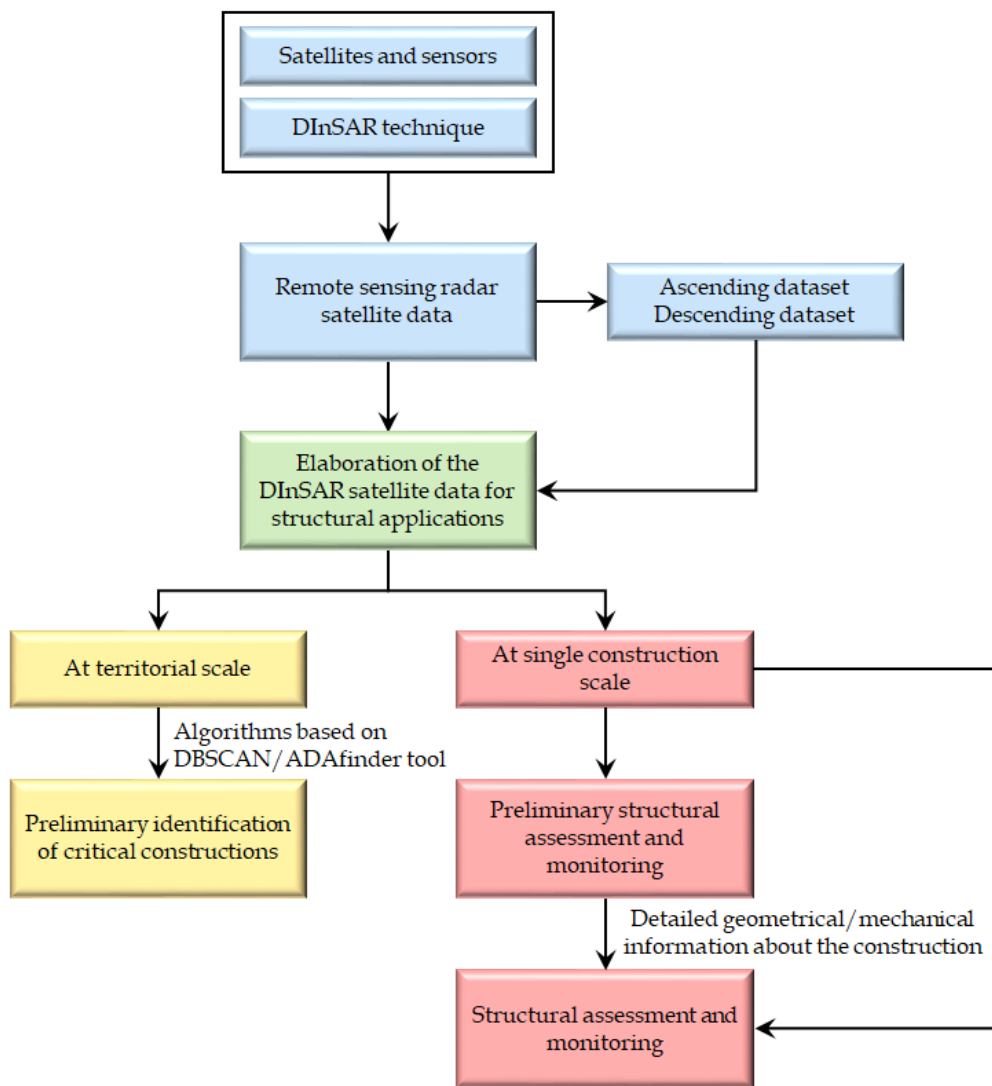


Figure 1.1. Organization of the thesis.



Chapter 2

2. Remote sensing RADAR satellite data

In this Chapter, the Remote Sensing RADAR Satellite techniques are introduced. These techniques are very advantageous for Earth Observation (EO) applications, thanks to the ability to perform remote observations with high coverage in both spatial and temporal terms (coverages up to tens thousands of km² and satellites revisiting times from a few hours to tens of days).

The principles of the RADAR Remote Sensing Satellite Techniques are described in §2.1. A summary of the existing elaboration techniques most used worldwide is reported in §2.2. Finally, in §2.3 the features of the different datasets of SAR satellite datasets exploited for SHM are illustrated.

2.1 Remote sensing RADAR technique

Remote sensing is defined as the set of techniques that allow to observe and study portions of the Earth's surface through the interaction among electromagnetic waves and objects (*targets*) placed at a considerable distance from the observer. The existing Remote Sensing techniques can use "passive" or "active" sensors, based on their working principle. The passive ones work without a signal transmitter and exploit the natural electromagnetic radiations emitted by the bodies or radiated by the sun. The active ones, on the other hand, are equipped

with a system transmitting an appropriate signal on the area of interest, and a receiver (*antenna*) through which to record the reflected information [60], [61].

The active Remote Sensing sensors most used for monitoring the bio-geophysical parameters of the Earth's surface are the satellite RADAR (acronym of *RA*dio *D*etection and *R*anging) systems [2].

The RADAR is an active remote sensing system operating at the microwave wavelength. The wavelength varies typically in the range 1 m-1 mm, corresponding to a frequency range of about 300 MHz-300 GHz. One of the main features of these sensors is the possibility to work in any light condition (indifferently during day and night) since they transmit their own emission and capture the returning echoes, in any climatic condition, thus allowing continuous monitoring. The RADAR satellite systems most commonly used for EO rotate around the Earth at an altitude between 500 and 800 km above the Earth's surface. They travel a half of the orbit from the North pole to the South pole (*descending* orbit) and a half from the South pole to the North pole (*ascending* orbit). In Figure 2.1a and Figure 2.1b, a scheme of the SAR image acquisition from ascending (ASC) and descending (DESC) orbits, respectively, is shown.

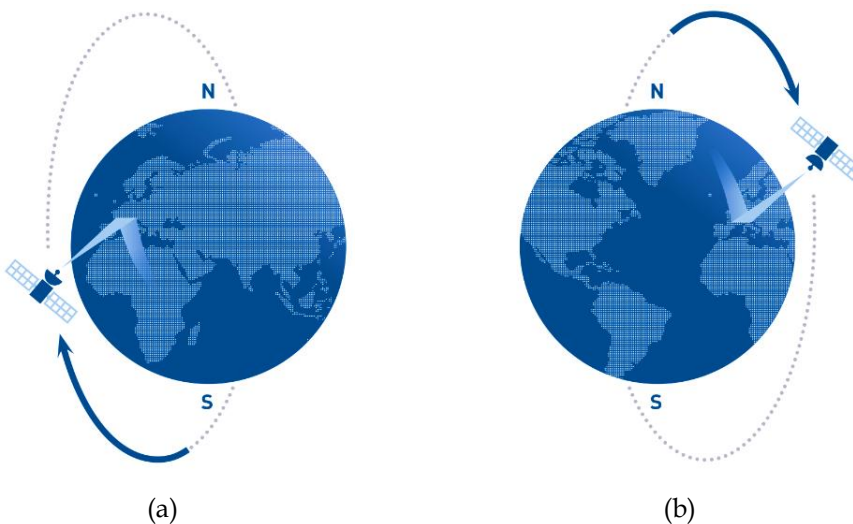


Figure 2.1. Scheme of the SAR images acquisition from ASC and DESC orbits (TRE Al-tamira [62]).

In Figure 2.2, a scheme of the acquisition geometry of a RADAR satellite, with refers to a cylindrical coordinate system (x, R, θ) , is shown. RADAR systems travel along x direction, called *flight direction* (also *azimuth*), generally slightly inclined to the meridians of a *heading angle* Φ . The direction connecting the sensor and the target on the ground surface, R , is called *slant range* (or *range*), and coincides with the satellite *line of sight* (LOS). The projection of the range direction on the Earth surface is called *ground range*. The angle θ , formed between the vertical and the LOS, is the *off-nadir* or *look angle*. It varies depending on the type of satellite and the operation mode.

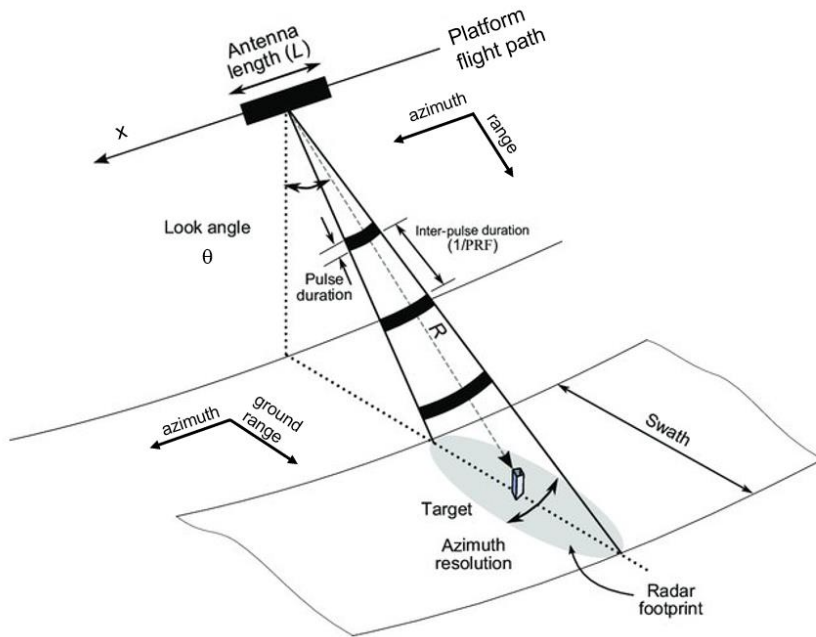


Figure 2.2. Scheme of the acquisition system of a RADAR satellite system (Bouaraba et al. (2018) [63]).

The functioning of a RADAR system is explained in the following. A transmitter sends electromagnetic signals within a certain frequency band, that illuminates the Earth's surface in an area, called *footprint*, having a certain extension in the two directions parallel and orthogonal to the flight line of the satellite

(*azimuth* and *ground range*, respectively). The waves, affecting the Earth's surface, undergo a phenomenon of disordered reflection (*scattering*), and a part of the reflected waves returns to the transmitter station, also equipped for the reception. The station is able to detect the electromagnetic target (*detecting*) and to evaluate its distance (*ranging*) along the direction of pointing of the antenna (*direction of range*), by measuring the time delay between the moment of transmission and that of reception. By processing a set of recorded digital echoes relative to a certain area (an operation generally called *focusing* of the raw data), a RADAR image of the observed area is generated. The motion of the satellites along their orbit, combined with the rotational motion of the Earth around its axis, allows obtaining RADAR images of the same area in different times. The time taken by the satellite to review the same area is called *revisiting time*.

A RADAR image consists of pixels defined in the two RADAR coordinates, represented by the azimuth and slant range directions. The RADAR image has a certain resolution in the two RADAR coordinates. The resolution in range Δr is the minimum distance, along the slant range, that two targets should have to be distinguished by the RADAR. It is defined as:

$$\Delta r = c \cdot \frac{\tau}{2} \cong \frac{c}{2\Delta f} \quad (1)$$

where c is the speed of light and τ is the pulse duration, while factor 2 takes into account the path of the round-trip route of the electromagnetic wave. The pulse duration can also be expressed as the inverse of the electromagnetic signal band Δf . Then, a high resolution in range is obtained for a wide band signal, which results in a short pulse. Analogously, two targets can be distinguished in azimuth if they are in different antenna beams. Then, the resolution in azimuth Δx depends on the width of the antenna's beams, through the following expression:

$$\Delta x = r \cdot \lambda/L \quad (2)$$

where r is the distance between the sensor and the target, λ is the wavelength of the transmitted signal, L is the length of the antenna, and λ/L represents the angular extension of the antenna's beam in azimuth.

The most used frequency bands in civilian space-borne SAR missions are L-

band, C-band and X-band. The L-band is characterized by wavelengths λ of about 23 cm. It is the only one capable of crossing vegetation and wet soil. The C-band is characterized by wavelengths λ of about 5 cm. The satellite is able to slightly detect some reflective elements in vegetated areas, but this band is useful in slightly urbanized areas. The X-band is characterized by wavelengths λ of about 3 cm. The satellite is not able to detect any target in vegetated areas, that appear completely dark in a SAR image. The X-band is very performant in urbanized zones.

For a *Real Aperture RADAR* (RAR), the resolution in azimuth is generally of the order of tens of kilometers, greatly worse than the resolution in range, that is of the order of the meters.

This aspect can be improved by enlarging the antenna, since the larger it is, the narrower the antenna's footprint is and the better the target is located. For this reason, the SAR systems have been introduced. In the SAR, a small antenna of length L is moved by the sensor along the flight direction in a series of successive positions, from each of which the antenna transmits a pulse and receives its return echo. The antenna thus synthesizes an array of antennas (*synthetic array*) along the flight direction. This means that through the movement and processing of the signal a fictitious antenna opening, extremely large, is "synthesized" by coherently combining the data acquired by the sensor in successive positions (Figure 2.3). The antenna motion along the satellite's flight line is used to improve the spatial resolution in the azimuth direction, leaving the resolution unchanged in the range, compared to the RAR, without increasing the size of the physical antenna.

The increase of resolution obtainable with the SAR implies an indispensable phase of focusing that leads from the raw data registered by the sensor to the generation of a complex image called *Single Look Complex* (SLC). Then, SAR gives coherent images in digital format, expressed as matrixes of $n*m$ pixels in RADAR coordinates, with a *modulus* (or *amplitude*) E and a *phase* φ . The modulus contains information about the intensity of the backscattered signal, due to the scene reflectivity properties. The phase depends on the geometrical and electromagnetic features of the observed scene and by the distance between the sensor and the

targets on the Earth's surface. The phase component is the information used to generate the so-called *interferograms*.

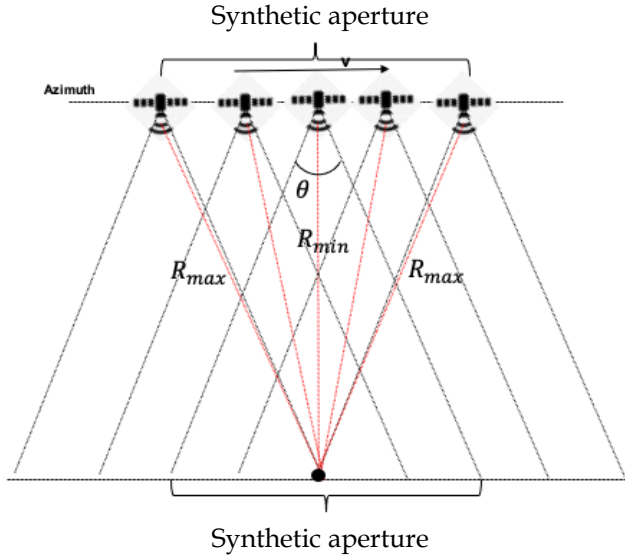


Figure 2.3. Scheme of the SAR [64].

The SAR image of a scene can be very different from an optical image of the same scene. SAR images don't have color, but gray levels, with lighter areas in correspondence of the targets with a great ability to reflect the impulse coming from the RADAR. The reflectivity depends not only on the characteristics of the observation geometry and those of the transmitted signals but also on the physical and geometric features of the illuminated scene. Generally, the rougher the surface, the more the image appears with a greater level of light. Flat surfaces, such as roads and highways, have a very low retro-diffusion then they appear very dark in a RADAR image. The vegetation typically appears uniformly grey. Surfaces inclined towards the sensor, such as mounting walls, appear very clear, contrary to surfaces with slopes in opposite direction to the RADAR, that have a bad back-spread. In urbanized areas, the presence of construction, buildings, and streets means that the signal emitted by the RADAR is often reflected several times. This strong back spread makes the image very clear (Figure 2.4).

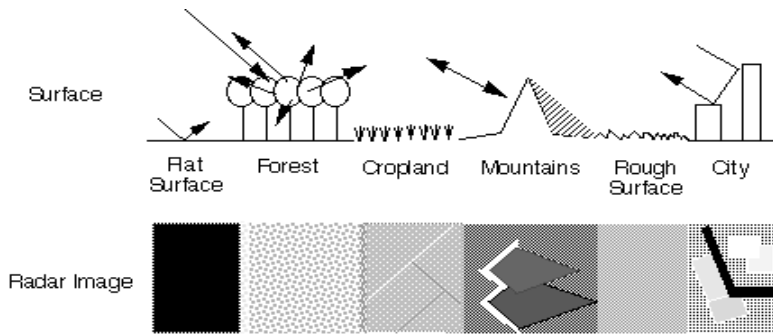


Figure 2.4. Examples of reflectivity of the scene [64].

When interpreting a RADAR image, it must be taken into account that SAR images are characterized by some geometric distortions, due to the fact that the antenna does not "look" at the scene vertically, but laterally with respect to the nadir. The most common distortions are due to the morphology of the scene, which can generate three typologies of perspective deformations: foreshortening, layover e shadowing, shown in Figure 2.5. The *foreshortening* (Figure 2.5a) depends on the sign of the slope α of the terrain, measured with respect to the horizontal plane. A α greater than 0° led to an effect of expansion of the resolution cell (or pixel). On the contrary, a α less than 0 led to a compression of the pixel, which will have a higher brightness. As the slope α approaches the angle θ , (in other words, the ground becomes perpendicular to the LOS), the compressed distance is reduced more and more, and the brightness increases more and more. This effect is particularly noticeable in the SAR images of mountainous areas where you see exposed slopes very bright. The foreshortening can become *layover* in areas where the slope of the ground is greater than the angle θ . The upper part of the mountain, in this case (Figure 2.5b) is closer to the satellite and then is represented in RADAR coordinates in a wrong position, i.e., reversed in slant range with respect to the lower part (point "a"). Therefore, the order of appearance of the elements in the RADAR image is opposite to the real order on the ground. Finally, the *shadowing* regards those areas screened from other areas, that are not lightened by the pulse emitted by the RADAR (Figure 2.5c). The effects of the geometric distortions in SAR images, however, vary considerably depending on the angle of view θ at which the satellite sensor operates.

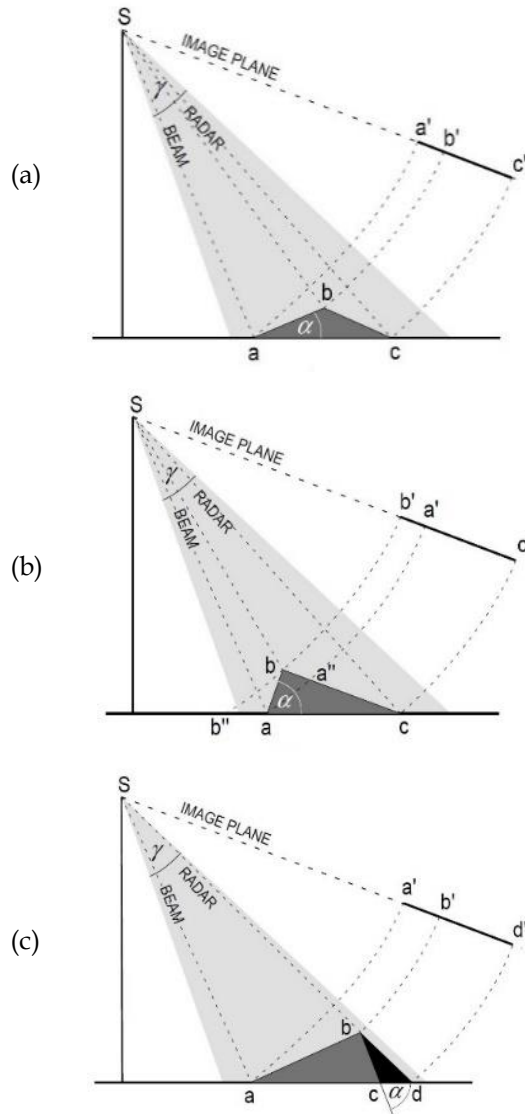


Figure 2.5. Geometric deformations related to the soil morphology: (a) foreshortening, (b) layover, (c) shadowing [64].

2.1.1 Satellites and sensors

The monitoring of the deformation of Earth's surface is possible today, also in the long period, exploiting the available huge archives of SAR images acquired from different sensors. Over the past thirty years, numerous sensors with different characteristics in terms of spatial resolutions, wavelengths, revisiting time, and space coverage, have been launched. The SAR image archives start from 1991, by the sensors onboard the satellites ERS-1/2 (European Space Agency, ESA), Radarsat (Canadian Space Agency, CSA), and Envisat (ESA), working in C-band. From 2006, ALOS-1, followed in 2014 by ALOS-2 (Japan Aerospace Exploration Agency, JAXA), provided L-band data. From 2007, TerraSAR-X (German Aerospace Center, DLR) and COSMO-SkyMed (Italian Spatial Agency, ASI) gave a great improvement, providing X-band data with a very high resolution. Moreover, the launch of the two satellites of the Sentinel 1 (S-1) constellation (ESA), S-1A and S-1B, respectively in 2014 and 2016, has even more improved the area coverage and the revisiting time (six days) of the available data acquired in band C. Finally, the SAOCOM satellite series by Argentina's Space Agency work in L-band since 2018. A timeline of the main satellite SAR sensors operating in Europe is shown in Figure 2.6, with a macro-classification according to the frequency bands.

The impact of the spatial resolution improvement from C-band to X-band is evident looking at Figure 2.7, where the amplitude images of the zone nearby the San Paolo stadium, located in the Fuorigrotta quarter (Naples, Italy), are reported as images by the ENVISAT (Figure 2.7a), RADARSAT-1 (Figure 2.7b), and COSMO-SkyMed (Figure 2.7c) RADAR systems, respectively.

According to the satellite resolution, the accuracy of the final products changes. Then, the PS maps obtained by processing images acquired by the different sensors, are suitable for different monitoring applications.

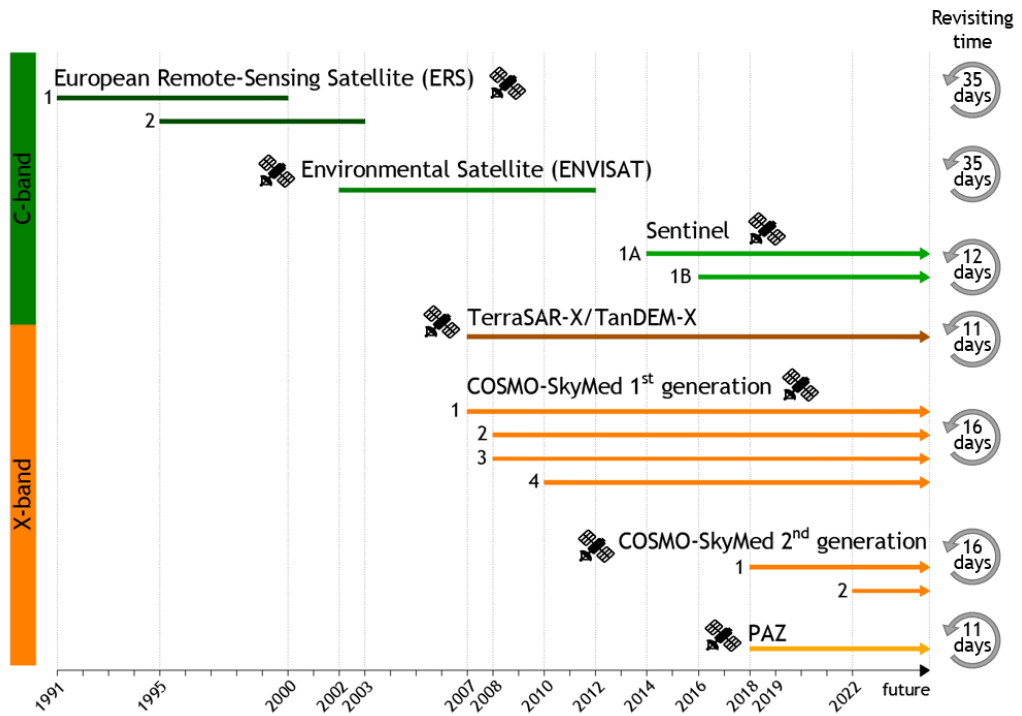


Figure 2.6. Timeline of the main satellite SAR sensors operating since 1992 to the present.

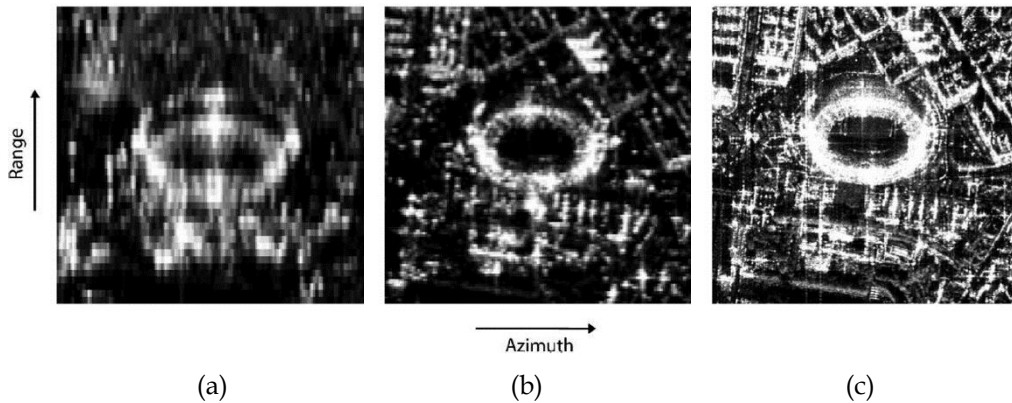


Figure 2.7. San Paolo stadium (Naples, Italy), as seen through the amplitude SAR images taken by (a) the ENVISAT sensor, (b) the RADARSAT-1 sensor, and (c) the COSMO-SkyMed sensor (Bonano et al. (2013) [65]).

A brief description of the main characteristics of the SAR sensors, from which the data used for the structural applications of this thesis, is reported in the following. The two constellations are the abovementioned COSMO-SkyMed, developed by the ASI in cooperation with the Ministry of Defense, and S-1, developed by the ESA under the European Copernicus Program.

2.1.1.1 COSMO-SkyMed constellation

The COSMO-SkyMed constellation (Constellation of small Satellites for the Mediterranean basin Observation, often called CSK) is an EO mission developed by the ASI in cooperation with the Ministry of Defense. The first generation of CSK consists of 4 identical satellites, equipped with a SAR sensor operating in the X-band, with a wavelength equal to 3.1 cm. The satellites were launched at different times, from June 2007 to November 2010. The revisiting time for each satellite of the constellation is equal to 16 days, so the presence of four satellites, in conditions of full operation, theoretically allows for the observation of the same scene on the ground on average every four days (see Figure 2.8).

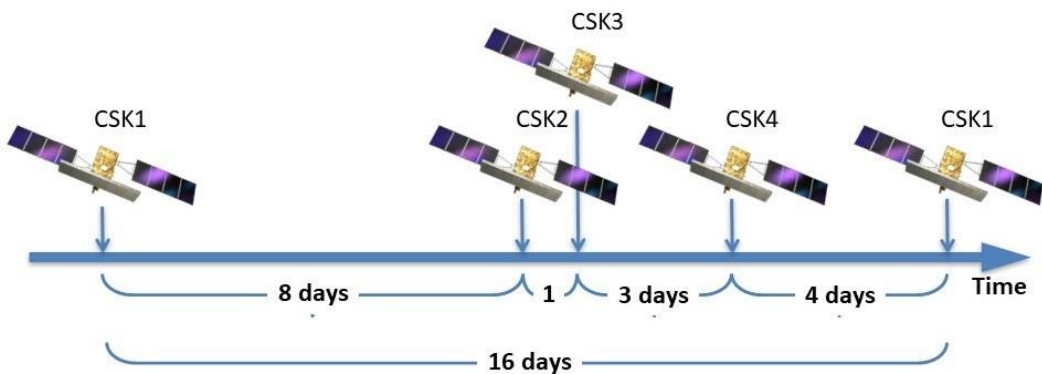


Figure 2.8. Revisiting time of the COSMO-SkyMed sensors [64].

The four CSK satellites are designed to acquire in different modes; the most used are: Stripmap HIMAGE, characterized by a spatial resolution of about 3 m x 3 m (along the azimuth direction and range) and a swath of about 40 km along

the range; Spotlight, with a spatial resolution of less than 1 m and with a swath of about 10 km x 10 km (along the range and azimuth).

On December 2019 and January 2022, respectively the first and the second one of the four planned satellites of COSMO-SkyMed Second Generation (CSG) constellation were launched and went alongside the four first-generation ones.

The use of such high-resolution input data guarantees a high density of targets for every single structure, all located in the three-dimensional (3D) space with metric precision. This is an important characteristic for building and infrastructure monitoring because it makes it possible to associate the deformation measurement with the corresponding point over the structure.

2.1.1.2 Sentinel-1 constellation

The S-1 constellation currently consists of 2 satellites with installed on board each a SAR sensor operating in the C-band (wavelength equal to 5.56 cm). The first satellite, Sentinel-1A (S-1A) was put into orbit on 3 April 2014; the second satellite, Sentinel-1B (S-1B), a twin of the first, on 25 April 2016. The revisiting time is equal to 12 days for a single satellite of the constellation. This interval has dropped to 6 days with the full operation of the second satellite (see Figure 2.9).

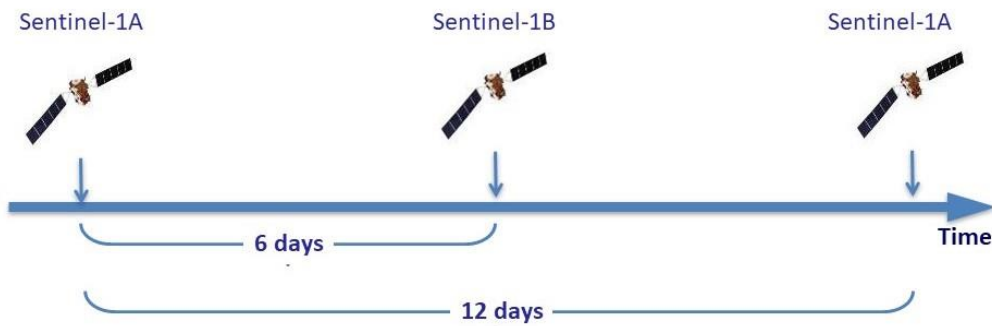


Figure 2.9. Revisiting time of the Sentinel-1 sensors [64].

The satellites of the constellation S-1 have been designed to acquire on the emerged lands in Terrain Observation by Progressive Scans (TOPS) mode, which

allows collecting of images in the acquisition mode Interferometric Wide Swath (IWS), with a spatial resolution of about 15 m along the azimuth and about 4 m along the direction range. The illuminated area on the ground (slice) has an extension of about 200 km (along the azimuth) \times 250 km (along the range).

The S-1 constellation acquires in programmed mode intending to generate robust image archives on large portions of Earth's surface for long-term monitoring programs. Moreover, it operates with a fully free and open data access policy.

2.2 DInSAR technique

Starting from two SAR images acquired by the satellite on the same area at different times, it is possible to extract information on the displacement of elements on the Earth's surface, thanks to the Differential Synthetic Aperture RADAR Interferometry (DInSAR) technique [7]. The time between the two acquisitions is called *temporal baseline*, and the distance between the two positions along the orbit of the satellite during the two acquisitions is called *spatial baseline* (which is null if the satellite can describe exactly the same orbit in the two passages). The measured displacements are calculated with respect to the date of the master image (*reference date*) and with respect to a pixel (*reference point*), chosen in a stable zone or a zone with a known deformation. It means that the displacement value associated with each single PS is computed as the difference of its recorded measurement with respect to the corresponding value of the reference point. For these reasons, the displacement measurements obtained from the interferometric analysis are differential both in time and in spatial terms.

An example of DInSAR scenario is schematized in Figure 2.10. Two sensor passages are represented in the plane orthogonal to the flight direction, i.e., the azimuth direction. The passages occurred at moments t_1 and t_2 with a spatial baseline b between SAR_1 and SAR_2 . The sensor-target distances, respectively at moments t_1 and t_2 , are r_1 and r_2 , while θ is the angle of view of the sensor. A surface displacement, whose projection along the sensor LOS is equal to d_{LOS} has been detected, due to a deformation of the ground occurs, indicated with a dashed line.

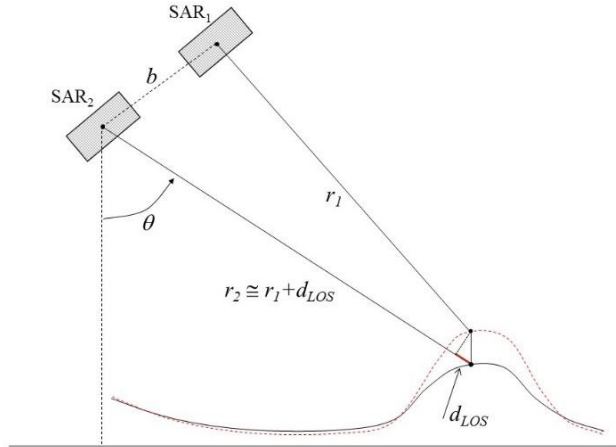


Figure 2.10. Example of DInSAR scenario in the plane orthogonal to the azimuth direction. A displacement component d_{LOS} is detected [64].

DInSAR technique exploits the phase difference between two SAR images, after the removal of the mean topography of the ground scene from a Digital Terrain Model (DTM) or a Digital Elevation Model (DEM), to derive the measurement of the displacement component along the sensor LOS. One of the two images, generally those acquired before in time, is chosen as a reference and takes the name of *master*, while the other one is called *slave*. The measured phase difference (or interferometric phase) $\Delta\varphi$ is defined as the phase variation of the slave image relative to the master reference image. It gives the so-called *interferogram* or *interferometric fringe*:

$$\Delta\varphi(x', r') = \frac{4\pi}{\lambda} \Delta r(x', r') + \Delta\varphi^{noise}(x', r') \quad (3)$$

Where (x', r') are the generic coordinates of the pixel, λ is the wavelength of the transmitted/received signal, Δr represents the difference between the sensor-target distance of the first and the second image for each pixel, and $\Delta\varphi^{noise}$ is the noise signal. The interferogram is a two-dimensional image in the range-azimuth plane, characterized by a series of fringes with values included in the interval $[-\pi; +\pi]$.

The interferogram summarizes the different aspects responsible for the phase variations. In fact, $\Delta\varphi$ is the sum of several phase contributions and can be

expressed as follows (to simplify the notations used, the generic coordinates (x', r') of the pixel will be omitted):

$$\Delta\varphi = \Delta\varphi^{flat} + \Delta\varphi^{topo} + \Delta\varphi^{atm} + \Delta\varphi^{mov} + \Delta\varphi^{noise} \quad (4)$$

where:

- $\Delta\varphi^{flat}$ represents the phase residues due to the inaccurate knowledge of the orbits described by the satellite during the acquisitions, in particular, due to the slight variation of the angle of incidence θ between the two acquisitions;
- $\Delta\varphi^{topo}$ is the residual topography signal of the observed scene with respect to a global reference system, and depends on the baseline of the interferogram and the point topography;
- $\Delta\varphi^{atm}$ is the signal due to possible atmospheric inhomogeneities between the two SAR acquisitions (e.g., different humidity conditions) that introduce spurious delays in the signal;
- $\Delta\varphi^{mov}$ is the deformation signal corresponding to the displacement between the two SAR acquisitions;
- $\Delta\varphi^{noise}$ is the signal related to the spatial decorrelation caused by an excessive distance - spatial baseline - between the orbits covered by the satellite during the two acquisitions, and the temporal decorrelation, caused by the change of the electromagnetic properties of the scene on the ground (e.g., due to weather events, the effect of a fire, that changed the characteristics of the scene between the two steps).

It is possible to separate the phase contribution related to ground scene deformation from those related to DEM errors used for the compensation of the topographic phase, errors due to inaccuracy of orbital information, and changes in atmospheric conditions between acquisitions, in presence of reliable atmospheric models, with a certain accuracy.

Starting from the differential interferogram, assuming no topographic phase residuals and that the phase contributions due to the atmosphere, orbital errors and noise can be neglected under appropriate considerations, the only contribution of $\Delta\varphi$ is $\Delta\varphi^{mov}$, and can be expressed as:

$$\Delta\varphi = \Delta\varphi^{mov} \approx \frac{4\pi}{\lambda} \cdot d_{los} \quad (5)$$

From which the measure of the displacement along the LOS can be obtained as follows:

$$d_{LOS} \approx \frac{\Delta\varphi}{2\pi} \cdot \frac{\lambda}{2} \quad (6)$$

From Eq. (6) it's evident that the surface displacements can be measured with an accuracy equal to a fraction of the wavelength at which the SAR sensor operates. Then, working in the field of microwaves (typically of a few cm) it is possible to achieve an accuracy of even a few millimeters.

The analysis of individual or few interferograms has great limitations, due to the accuracy with which it is possible to effectively separate the phase contributions. Moreover, the quality of the results is intrinsically limited, sometimes completely compromised, in relation to the noisy sources intrinsic to the interferograms themselves, linked to the spatial decorrelation and to the changes in the electromagnetic characteristics of the ground targets over the time interval of the observation of the phenomenon (temporal decorrelation), that affect their reflectivity. The temporal decorrelation phenomena can be caused, for example, by the presence of snow and vegetation or climatic and meteorological changes. These effects are reduced in the presence of exposed urban centers and rocks, characterized by a constant RADAR signal response over time, and decrease using larger wavelengths (e.g., L band instead of X band).

The limitations of the conventional DInSAR technique have been overcome with the advanced multi-temporal DInSAR techniques developed over the last 20 years, characterized by algorithmic complexity and longer calculation times. These techniques use a large number of images (tens or hundreds) related to the same area and a large number of differential interferograms, which are suitably combined to obtain information on the temporal evolution of surface displacements.

The information obtained in the multi-temporal DInSAR techniques lead to a significant improvement in the accuracy of displacement measurements, thanks

to the estimation of possible atmospheric contributions of images and topographic errors and thanks to the use of techniques for the so-called *phase unwrapping*, based on algorithms that simultaneously exploit interferometric phase information in space and time.

The multi-temporal DInSAR techniques can be grouped into two broad categories based on the approach: *Persistent Scatterer* (PS) and *Small Baseline* (SB).

PS techniques work with full spatial resolution interferograms (*single look*), in which, within the resolution cell, only one dominant scatterer is assumed to be consistent throughout the observation time interval. The dominant scatterers, called *Persistent Scatterers* (PSs), have an electromagnetic response that “persists” over time. In other words, their phase information is preserved in all differential interferograms, regardless of the effects of spatial and temporal decorrelation. This allows it to work even with very large spatial and temporal baselines and to make use of interferograms compared to a single master image common to the dataset, then to use a minimum number of interferograms. However, such approaches are characterized by limited spatial densities of the detected points, especially in the case of interferometric analysis carried out on vegetated and rural areas characterized by a reduced number of dominant scatterers. Moreover, PS techniques are not suitable for the analysis of strongly non-linear deformation phenomena.

In the SB techniques, it is assumed that the scattering is spatially distributed within the resolution cell, where also *distributed scatterers* can be found. The distributed targets are much more sensitive to the effects of spatial and temporal decorrelation than the dominant ones. Then, the density of points that can be detected in SB interferometric analysis increases significantly compared to PS methods. Nevertheless, a careful selection of differential interferograms to be used is required, based on the minimization of spatial and temporal baselines. The selection of small baseline interferometric pairs leads to the need to consider more than a single master image for the dataset, with the disadvantage of having to manage subsets of SB interferograms separated by large baselines. In this case, the subsets are independent, and the displacement information obtained for each subset individually must be suitably combined to derive the time series of

displacement related to the entire dataset. SB techniques typically operate at reduced spatial resolution through a complex media operation (called *multi-look*) on interferograms, to increase the signal-to-noise ratio of interferometric phases. This leads to a loss in terms of spatial resolution, but also increases the density of the points detected even in rural or poorly urbanized areas, allowing the potential of satellite SAR systems to carry out large-scale interferometric analysis with limited monitoring costs to be preserved. More recently, SB techniques have been extended to multi-scale interferometric analysis, using full and medium resolution spatial interferograms, to identify both dominant and distributed scatterers.

The products obtained from multi-temporal DInSAR analysis consist in a large set of PSs relevant to the investigated area, for which measures of the displacements along the LOS direction are given, within the analyzed time frame. Each PS can be associated with an area on the surface whose dimensions depend on the resolution cell size of the processed SAR data. For instance, in the case of ERS/ENVISAT data, the resolution cell size is about 5 m x 20 m in the RADAR azimuth and range directions, respectively; in the Sentinel-1 TOPS mode case, the resolution size is about 20 m x 4 m, whereas for CSK Stripmap-mode data it is about 3 m x 3 m. It is worth noting that the PSs distribution is usually very heterogeneous in an urban zone: the buildings generally have good reflective properties, so it is very common to detect a density of PSs falling on them.

For each single PS, generally the LOS displacement time series, the LOS mean deformation velocity ($V_{LOS,ASC}$ and $V_{LOS,DES}$, respectively for ASC and DES dataset, called “mean velocity” for brevity in the following) the geographical coordinates (latitude and longitude) and the altitude (with respect to a global reference system) are provided. Directional cosines of the LOS for each PS are given to univocally identify the direction vector to which the displacement value refers, as well as the temporal coherence parameter.

Furthermore, a parameter called *temporal coherence* [66], [67] is provided, containing information on the quality and/or reliability of the displacement measurement for that point. It is not possible to provide a unique definition for this parameter, which depends by the multi-temporal DInSAR technique and by the

type of interferometric processing mode. However, coherence can be assigned only to pixels that have experienced little or very slow displacements. Pixels that have moved very quickly or in a very short time interval are not monitorable through the DInSAR technique. For this reason, points that experience quick movements may disappear in the context of processing because they lost their coherence. A proper selection of the final PSs of the interferometric analysis is achieved by setting a threshold on the temporal coherence, which is given within the $[0,1]$ interval, to exclude not reliable pixels. The coherence threshold is empirically set up by considering the characteristics of the processed dataset, such as the number of SAR acquisitions, the overall time interval, and the regularity in time of the available acquisitions. This value is generally set at 0.50 but, in specific cases (e.g., very good temporal sampling and distribution of the acquisitions, analysis on urban areas) the threshold may be lowered, for example, to 0.35.

Some of the most spread advanced multi-temporal techniques of SAR satellite interferometry are PSInSARTM, Small BAseLine Subset (DInSAR-SBAS), SqueeSARTM, Stanford Method for PS (StaMPS) and Tomographic SAR (TomoSAR). A description of the two techniques exploited to derive the data used for the applications that will be illustrated in this dissertation, which are PSInSARTM and DInSAR-SBAS, is reported in the following.

2.2.1 PSInSARTM

PSInSARTM [62], [68] is a PSI technique that works with a small subset of RADAR targets, called *permanent scatterers*, essentially immune to the effects of geometric and temporal decorrelation. The permanent scatterers are identified by the satellite on the Earth's surface through a complex algorithm of numerical processing of signals. They are represented by elements that have high stability of the electromagnetic response over time, typically portions of buildings, monuments, roads, railway lines, antennae, pylons, metal elements – or natural elements – rocky outcrops, and accumulations of debris. Permanent scatterers cannot be found in vegetated or periodically covered snow areas.

The analysis is conducted on the entire dataset of images available in the area of interest. All the slave images are compared with the master image generating overall $(N - 1)$ interferograms, where N is the number of available SAR images.

One of the potentials of the PSInSARTM technique is the estimation of the atmospheric component, based on the analysis of a subset of points. Since the atmospheric contribution is slowly variable in space, it is extended to all the points of the area with an appropriate interpolation process and eliminated from the interferometric phase.

Regarding the accuracy of the measurements provided, considering a data set of at least 40 images covering a period of 2 years, a measuring point located less than 1 km away from the reference point has an error of 1 mm/year on measurements of the mean velocity and 5 mm on measurements of displacement.

For PSI approaches like the PSInSARTM, the temporal coherence is defined as an index that measures the correspondence between the movement of the measuring point and a certain analytical model chosen a priori.

2.2.2 SBAS-DInSAR

The SBAS approach [66], [69] is one of the most well-established in the framework of the existing multi-temporal DInSAR techniques. It requires the collection of many SAR images of the investigated area, with both a small temporal and spatial separation between the acquisition orbits, to minimize noise effects and maximize the spatial pixel density in the multi-temporal sequence of differential interferograms. The generated interferograms, unwrapped to solve for the 2π ambiguities [69], are thus the starting point for the computation of the deformation time series. They are obtained through the solving of a linear system of equations in the least squares sense, by applying a minimum norm energy constraint (in some cases, the Singular Value Decomposition - SVD - method). The computational process ends with a filtering operation, for detecting and removing possible atmospheric artifacts from the displacement time series.

One key point of the SBAS-DInSAR approach is the possibility to generate displacement time series and corresponding mean velocity maps at different

spatial scales, referred to as territorial and local scale analysis. The first one is aimed to investigate natural or anthropic deformation phenomena associated with large areas, whereas the latter allows detecting spatially localized displacements related to full resolution pixels, particularly suitable to investigate and monitor over time deformation phenomena associated with single buildings and/or infrastructures [70], [71]. When operating at a local scale, such as for investigating the structural assessment of a single building [71], [72] or detecting critical infrastructure behavior [14], full resolution differential interferograms, generated from the single-look data with the full spatial resolution of the sensor ranging from 3 to 10 m, are used [8], [12].

The SBAS approach allows the generation of advanced DInSAR products with an accuracy of about 1-2 mm/year and 5-10 mm, respectively for the mean velocity and the single displacement measurements [65], [73], [74].

With reference to the SBAS-DInSAR full spatial resolution approach, temporal coherence is a factor that provides an estimate, for each measuring point, of the quality of the time series of displacement, by evaluating the similarity between the initial wrapped deformation signal and the adopted phase model.

2.3 DInSAR products used for SHM applications

During my Ph.D. program, I collaborated in performing many Structural Health Monitoring (SHM) applications using three different DInSAR datasets. The exploited datasets derive from separate sensors, located on different constellations (CSK, S-1) and have been obtained by using distinct processing techniques (SB and PS). It is worth specifying that the processing of the SAR satellite images is not part of my Ph.D. program, since it's an operation to be performed by experts in the field of interferometry. The products of the processing operations are generally given to structural engineers as input for SHM applications.

The DInSAR products datasets are described in the following §2.3.1, §2.3.2, and §2.3.3, while the SHM applications will be reported in the sub-sections of the following Chapters.

2.3.1 CSK data processed through SBAS-DInSAR technique (dataset of Rome, Italy)

The first dataset of DInSAR products has been processed by the Institute for Electromagnetic Sensing of the Environment of the National Research Council (CNR-IREA) in the context of the Italian Civil Protection Department (DCP) - ReLUIS project 2019-2021. The DInSAR data are obtained by applying the full resolution SBAS-DInSAR approach (§2.2.2) to SAR images collected from ASC and DES orbits by the sensors of the Italian CSK constellation, in the period March 2011-March 2019. The investigated area is the whole metropolitan area of Rome (Italy). The images are acquired through the standard Stripmap mode with HH polarization and a ground spatial resolution of about 3 m in both azimuth and range directions. The identified datasets comprise 129 ascending and 107 descending SLC acquisitions, with look angles at the scene center of about 34° and 29° , respectively. The full resolution deformation time series and corresponding LOS mean velocity measurements of each PS have been computed by using the 1-arcsec Shuttle RADAR Topography Mission (SRTM) DEM of the study area, to remove the topographic phase component. The PSs were identified by selecting a temporal coherence threshold greater than 0.35. Table 2.1 summarizes the main parameters of the exploited datasets.

Table 2.1. Main parameters of ASC and DES CSK datasets (modified from [64]).

	ASC	DES
Average look angle	$\sim 34^\circ$	$\sim 29^\circ$
Time interval	[23/03/2011-11/03/2019]	[29/07/2011-13/03/2019]
Number of acquisitions	129	107
Wavelength	~ 3.1 cm	
Acquisition mode	Stripmap H-IMAGE	
Spatial extension	~ 40 km \times 40 km	
Spatial resolution of the interferometric data	~ 3 m \times 3 m	

The geocoded LOS mean velocity maps, achieved by independently processing the two ASC and DES CSK datasets at the full spatial resolution scale (about 3 m) and relevant to the overall metropolitan area of Roma (full frame analysis), are shown in Figure 2.11 and Figure 2.12, respectively. The two mean velocity maps show a very good PSs density, in particular in correspondence to the urbanized areas where almost all the structures and buildings are detected. Several subsidence patterns with a deformation rate greater than 1 cm/year can be distinguished in both velocity maps, with the most relevant ones in correspondence to the A90-A91 Roma-Fiumicino highway (Figure 2.13a, representing the zoom-in view of the full resolution SBAS-DInSAR results highlighted by the white box “A” in Figure 2.11.) and the Fiumicino airport runway (Figure 2.13b, representing the zoom-in views of the full resolution SBAS-DInSAR results highlighted by the white box “B” in Figure 2.12). For each selected PS, the corresponding deformation time series along the LOS direction are also provided, thus allowing to follow the temporal evolution of the deformation along the overall 2011-2019 observation interval.

These datasets have been used for the applications shown in the following §3.4, §4.1.2, §5.1.1.

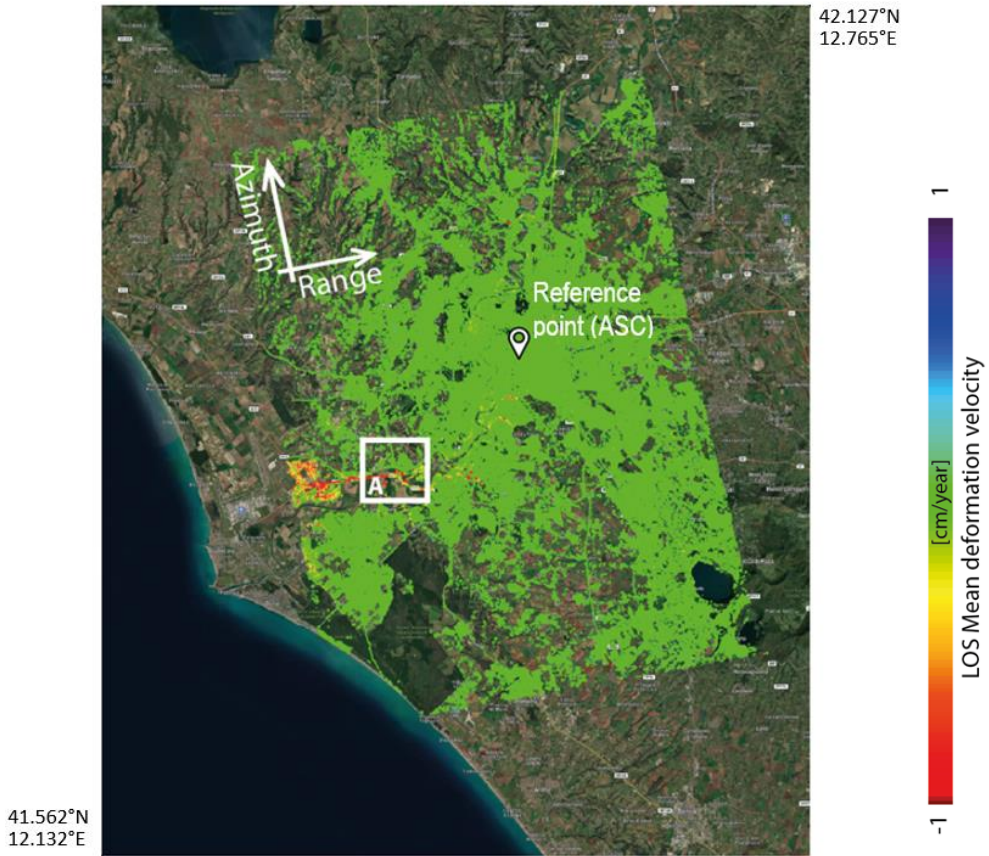


Figure 2.11. Full resolution SBAS-DInSAR results obtained from the CSK images collected along the 2011-2019 time in the urban area of Rome, relevant to ASC dataset (modified from [31]).

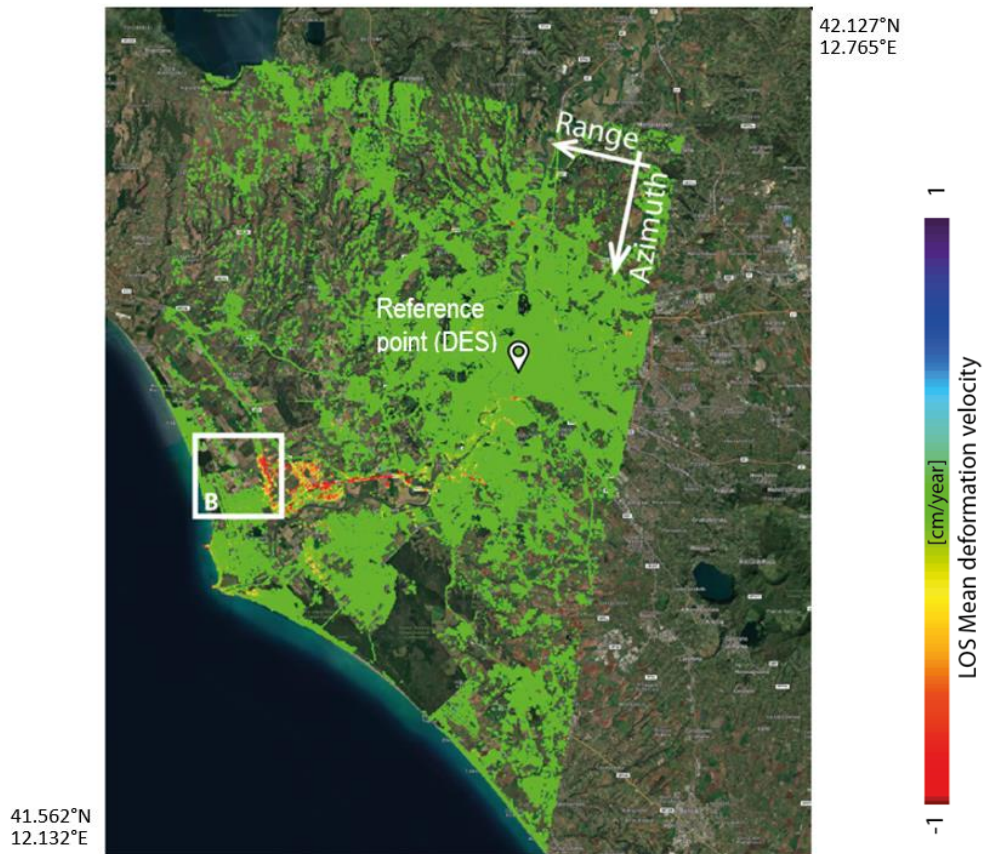


Figure 2.12. Full resolution SBAS-DInSAR results obtained from the CSK images collected along the 2011-2019 time in the urban area of Rome, relevant to DES dataset (modified from [31]).

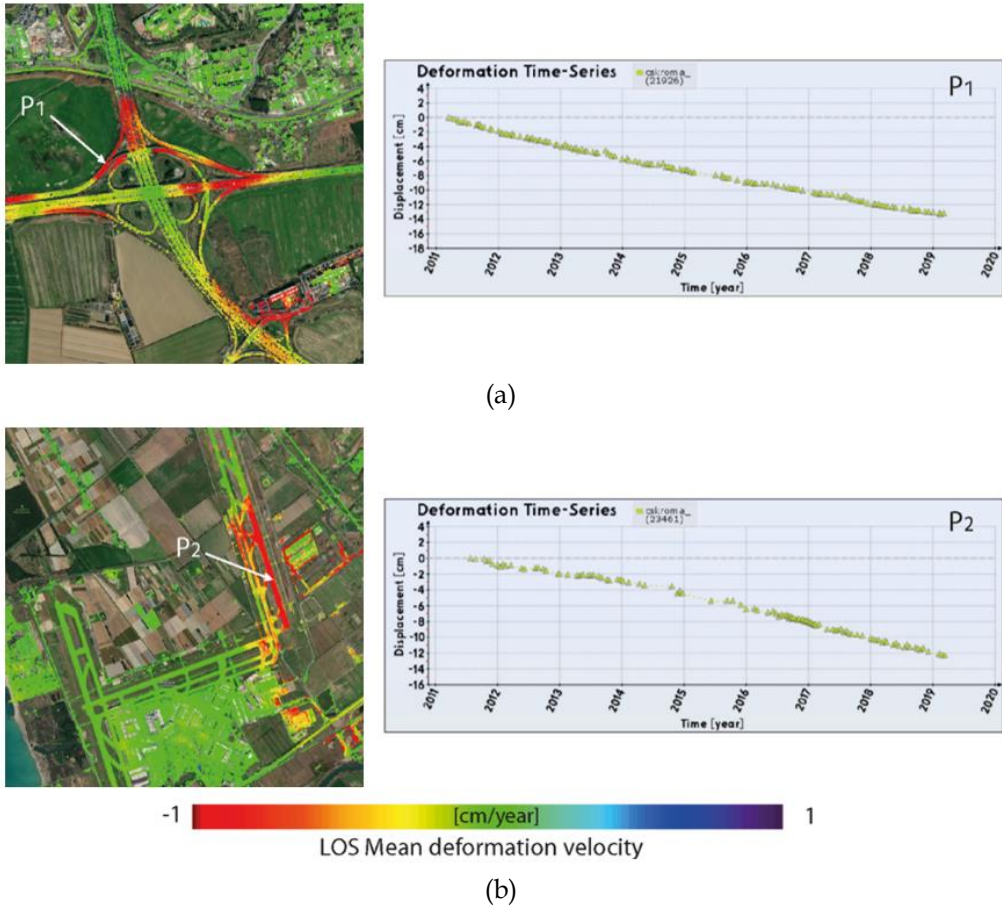


Figure 2.13. Zoom views of the full resolution SBAS-DInSAR results highlighted by the white boxes in Figure 2.12 and displacement time series of selected pixels: (a) mean velocity map of a portion of the A90-A91 Roma-Fiumicino highway (zone A); (b) mean velocity map of the Fiumicino airport runway (zone B) (modified from [31]).

2.3.2 CSK data processed through CPT technique (dataset of Moio della Civitella, Italy)

The second dataset of DInSAR products is subdivided into two time spans. They have been obtained through the processing of CSK SAR images collected from ASC and DES orbits in the intervals 2012-2016 and 2017-2019. The

information related to the two acquisition periods are synthetized in Table 2.2. In particular, 76 ASC and 66 DES images have been used for the first period, and 50 ASC and 47 DES have been used for the second one. The area of interest, in this case, is the whole urban settlement of *Moio della Civitella* municipality (covering about 3 km² [75]), in the *Campania* region (Southern Italy), affected by several slow-moving rainfall-triggered landslides. The processing is conducted by a PS-like approach technique, using Coherent Pixels Technique (CPT) algorithm [76], [77]. The latter has been implemented on SUBSOFT software, developed by the Remote Sensing Laboratory (RSLab) group from the Universitat Politècnica de Catalunya (UPC-Barcelona). CPT is able to extract the displacement evolution during long time spans from a stack of differential interferograms.

Table 2.2. CSK SAR data stacks processed through CPT technique for Moio della Civitella urban area.

Satellite	Orbit	1 st Period [57]	#Scenes	2 nd Period	#Scenes
Cosmo-SkyMed	Ascending	[Jan 2012 –	76	[Jan 2017 –	50
	Descending	Dec 2016]	66	Mar 2019]	47

The LOS mean velocity maps of targets identified within Moio della Civitella urban area by CSK data are shown in the first and second periods, along ASC (Figure 2.14a and Figure 2.15a) and DES (Figure 2.14b and Figure 2.15b) tracks. The reference point is indicated with a black star. Targets mainly correspond to man-made features, such as structures and roads. The use of CSK images allowed to obtain a good density of PS. The accuracy of interferometric products has been validated by comparing DInSAR results with conventional data recorded by instrumentations (inclinometers, topographic measure points, GPS network) installed during previous monitoring field campaigns [78], [79].

These datasets have been used for the application shown in the following §5.2.1.

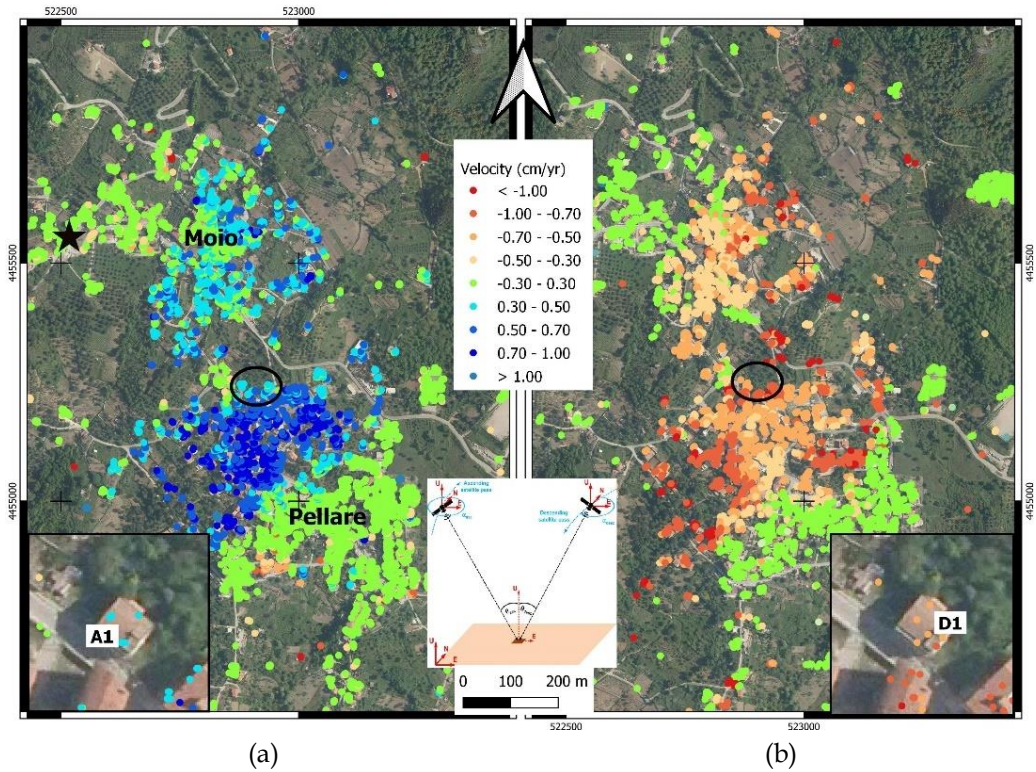


Figure 2.14. LOS mean velocity maps of targets identified within Moio della Civitella urban area by CSK data along (a) ASC and (b) DES tracks, for the period 2012-2016 [56].

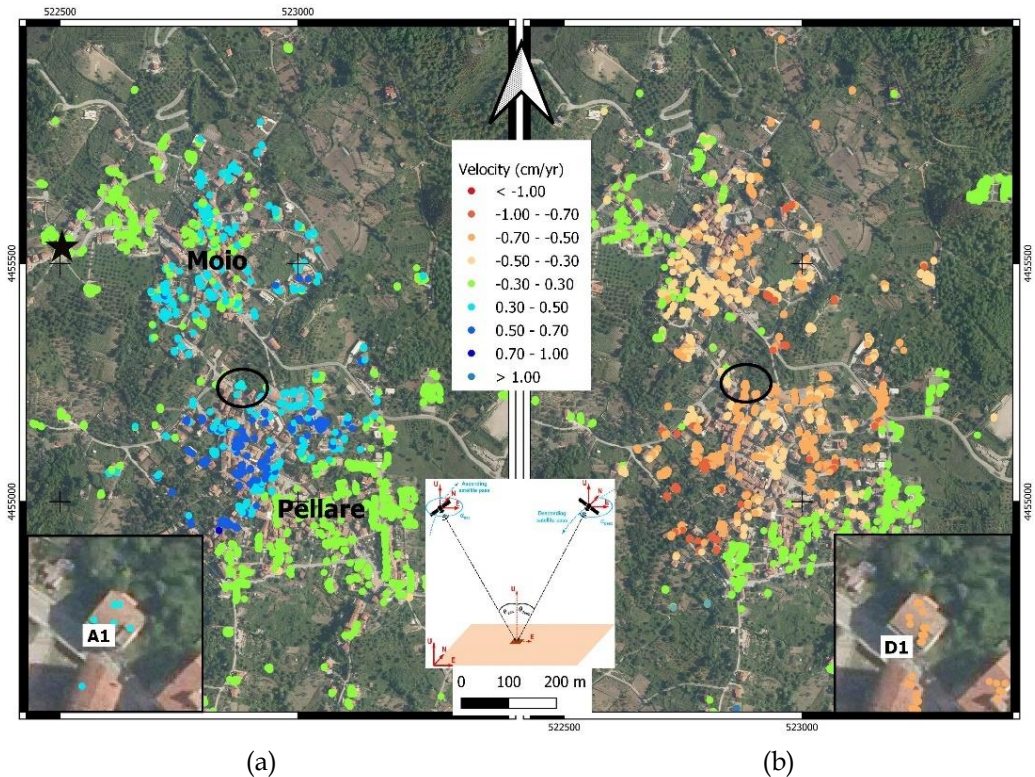


Figure 2.15. LOS mean velocity maps of targets identified within Moio della Civitella urban area by CSK data along (a) ASC and (b) DES tracks, for the period 2017-2019 [56].

2.3.3 EGMS data (dataset of Barcelona, Spain)

The third dataset is derived from the European Ground Motion Service (EGMS), the new service of the Copernicus Land Monitoring Service (CLSM [80]) approved in 2017 [18]–[20]. The purpose of the EGMS is to provide consistent, updated, standardized, harmonized information regarding ground deformation, all over Europe, to detect ground motion phenomena of any origin, natural or human-caused.

The EGMS furnishes products obtained through the multi-temporal interferometric processing of ASC and DES S-1A and S-1B RADAR images, using full resolution Advanced SAR Interferometry (A-DInSAR) [81], [82], all over the

European territory. The EGMS archive images start from 2015, at a revisiting time of six days (which has been degraded to twelve days starting from December 2021, due to a failure of the S-1B satellite) and will be updated on an annual basis.

The EGMS includes three levels of products. The first level is the *basic* one, constituted by geocoded LOS mean velocity maps, in ASC and DES orbits, where the measures are referred to a local reference point. The second level is the *calibrated* one, constituted by the product of the first level, mosaicked and integrated with Global Navigation Satellite Systems (GNSS) data. The second level measures are not referred to a local reference point. The third level is the *Ortho* one, constituted by deformation components along the Vertical and East-West (EW) directions, resampled to a grid with a cell size of 100 m. The 3D geolocation accuracy of the EGMS products is lower than 10 m.

The data can be downloaded by every interested user from the Explorer platform [82], since the EGMS products have a free and open data access policy. Each of the EGMS products has undergone an extensive quality control protocol in order to generate the best possible results. The key elements of the EGMS are stated in the White Paper [83].

Examples of calibrated and ortho products are respectively shown in Figure 2.16 and Figure 2.17 for the area of *Campi Flegrei*, in Naples (Italy), which caldera is well known for its ongoing deformation phenomenon, that has been the object of studies based on multi-temporal DInSAR technique in the last decade [65], [70], [84], [85].

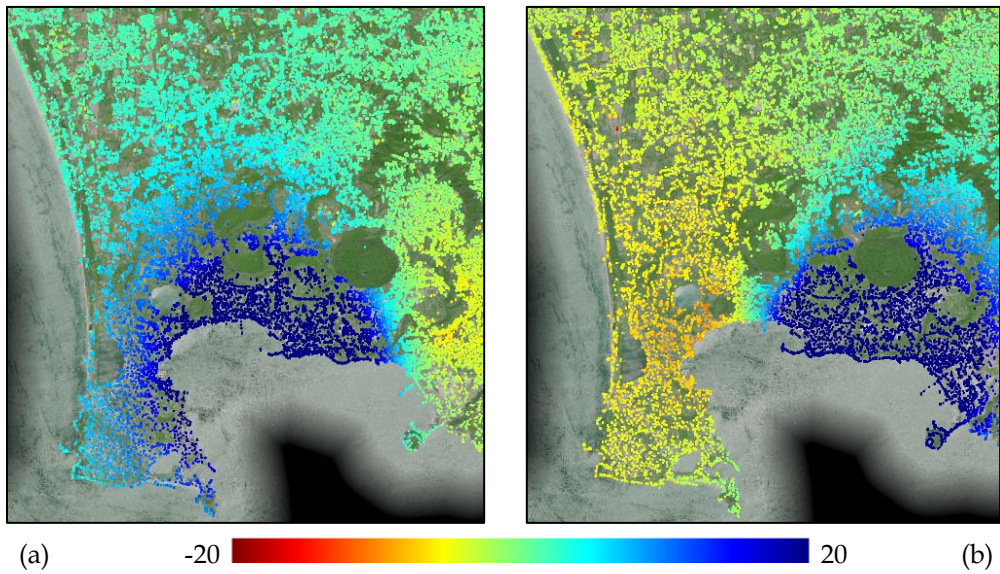


Figure 2.16. Example of calibrated product by EGMS: (a) ASC and (b) DES (Campi Flegrei, Naples, Italy). Velocities expressed in mm/year.

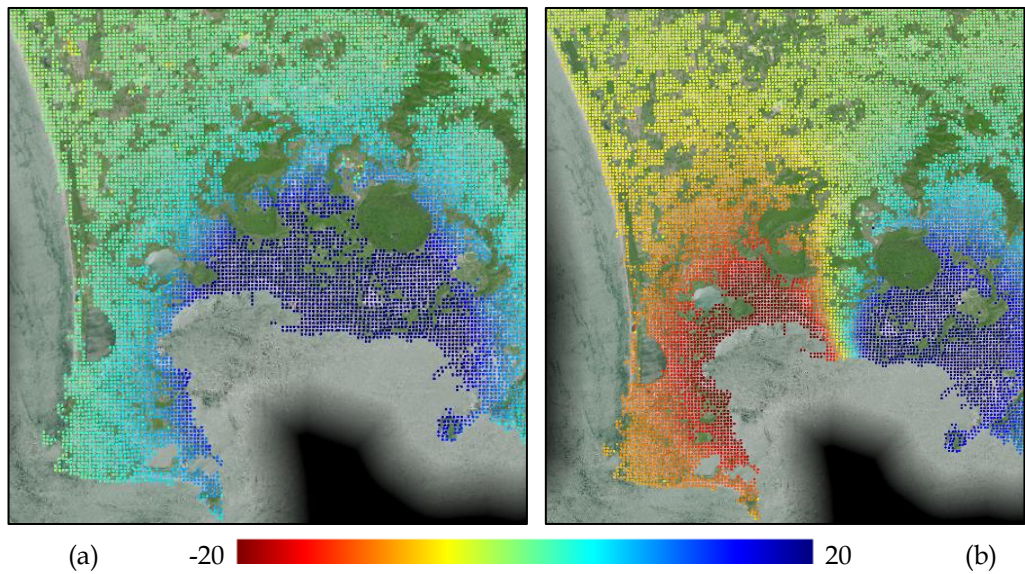


Figure 2.17. Example of ortho product by EGMS: (a) Vertical and (b) horizontal EW (Campi Flegrei, Naples, Italy). Velocities expressed in mm/year.

In Figure 2.18 and Figure 2.19, the calibrated products for the area of Barcelona (Spain) that will be used in the following applications (§4.2.2) are shown, respectively for ASC and DES orbits. The LOS velocities are expressed in mm/year using the classical false color scale shown in the legend.

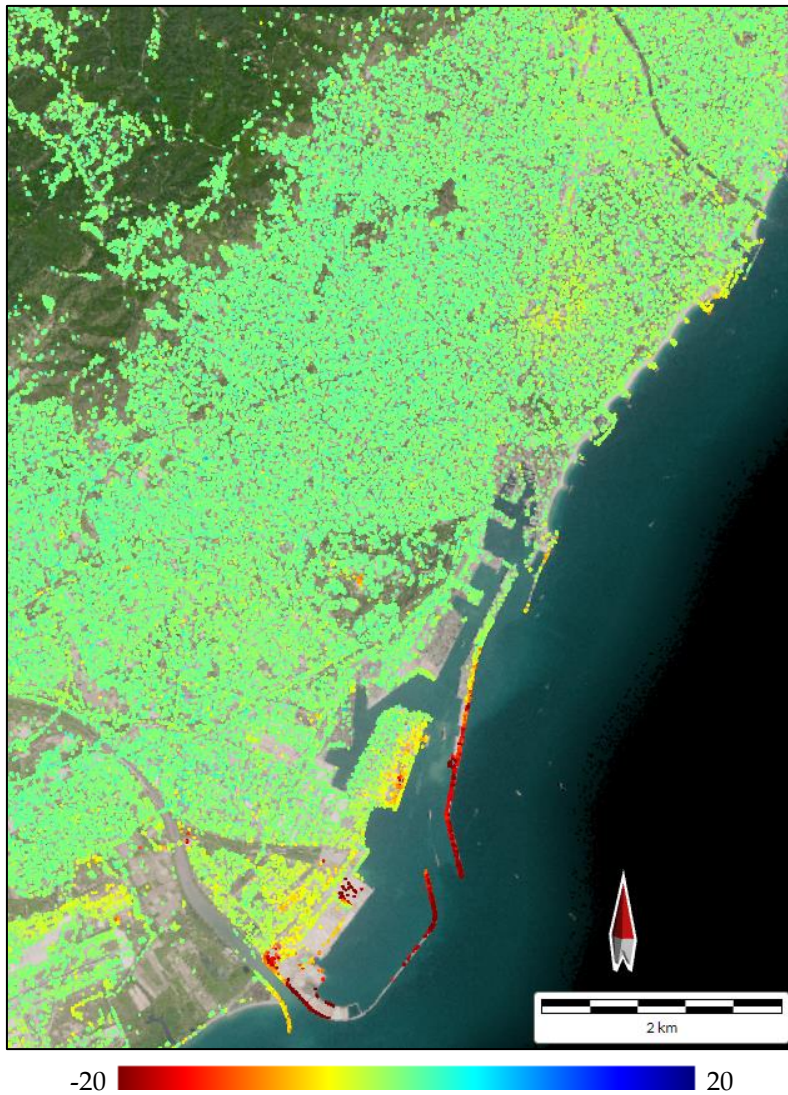


Figure 2.18. ASC calibrated products by EGMS, Barcelona (Spain). Velocities expressed in mm/year.

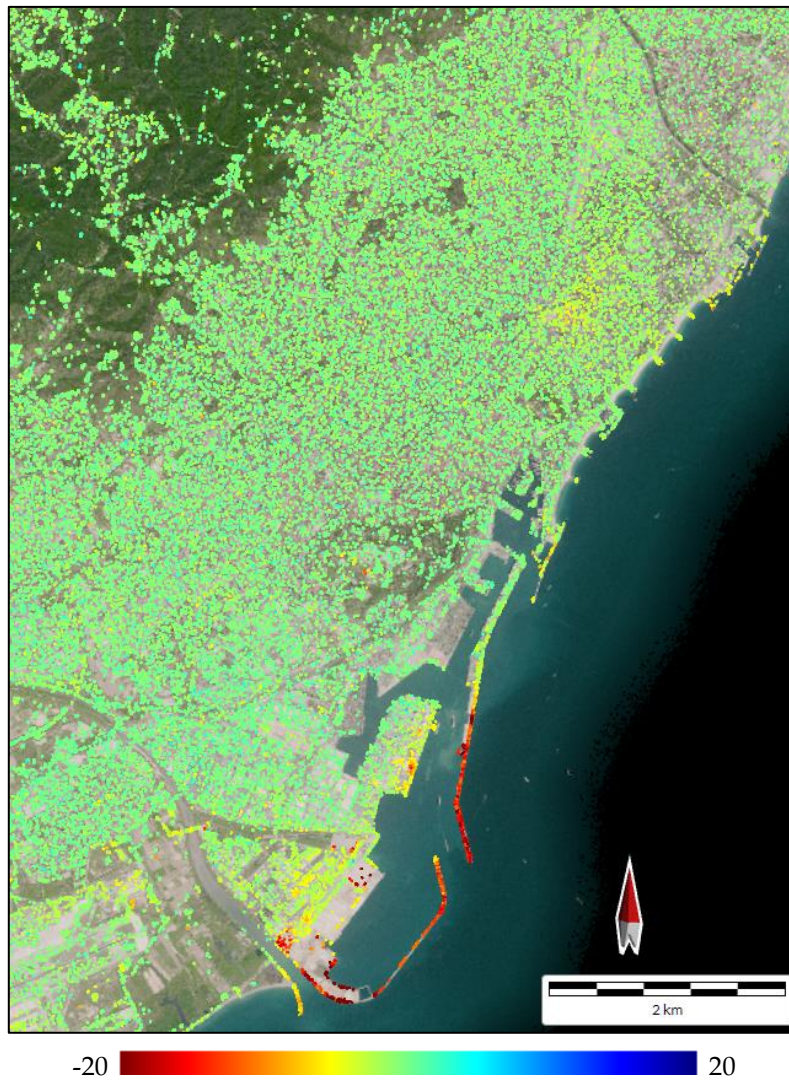


Figure 2.19. DESC calibrated products by EGMS, Barcelona (Spain). Velocities expressed in mm/year.

Chapter 3

3. Elaboration of the DInSAR satellite data for structural applications

This Chapter presents different strategies that can be employed to analyze the achieved DInSAR measurements, to provide a clear and direct representation of the ground deformation condition of an area or of a construction, useful for the monitoring and assessment of constructions.

Some analyses require to perform further additional elaborations on the DInSAR products, especially those carried out at the structural level. As described in §2.1, it is possible to obtain RADAR images of the same area from the two different perspectives: ASC and DES. However, also when only one of the two datasets is available, useful information can be retrieved. For many of the proposed approaches, both ASC and DES DInSAR datasets of the examined area are required, in order to obtain a better definition of the displacement and mean velocity vectors. The proper combination of ASC and DES SAR acquisitions in different time frames over the same geographical area allows retrieving, under some specific hypothesis, two of the three components of the real deformation pattern, i.e., the Vertical and the EW components of the displacement measurements.

An important aspect concerns the selection of PSs to be considered according to the analyses to be carried out (e.g., territorial scale or single construction scale), which must be evaluated on a case-by-case basis, depending on the degree of

spatial correlation of deformation phenomena at ground and construction level (thinking for example about the movements of the deck of a bridge, not necessarily related to those of the ground below). It is always convenient to use as many PSs as possible in order to minimize the uncertainties related to the single reading. For this reason, sometimes, spatial interpolation is preferred to the use of individual PSs. The conditions of applicability of the different techniques of spatial resampling and their limits must be clear to avoid incurring possible misinterpretations of a deformative phenomenon (§3.3).

In the following, the proposed analysis techniques are described, and some useful application examples are provided.

3.1 Use of a single dataset

The analysis of the results obtained from the processing of a single orbit dataset can provide preliminary information with respect to the deformation phenomena in progress. As previously explained, the deformation measure given by a single dataset is the component along the sensor LOS direction. The percentage of real deformation detectable from the satellite data depends on the difference between the direction of the real deformation vector and on the LOS direction, expressed through the incidence angle, defined by the *heading angle* Φ and the *look-angle* θ , as indicated in Figure 3.1. These angles slightly differ from one pixel to another of the observed area, even in the same satellite and acquisition mode.

For a PS, if the generic measure X_{LOS} - i.e., the displacement or the mean velocity measurement - along the LOS of the sensor is available, the following system can be written:

$$\begin{cases} X_{LOS,ASC} = X_{EW} \cdot n_{EW,ASC} + X_{NS} \cdot n_{NS,ASC} + X_V \cdot n_{V,ASC} \\ X_{LOS,DES} = X_{EW} \cdot n_{EW,DES} + X_{NS} \cdot n_{NS,DES} + X_V \cdot n_{V,DES} \end{cases} \quad (7)$$

where X_{ASC} and X_{DES} are expressed in terms of its EW (X_{EW}), North-South (NS, X_{NS}) and Vertical (X_V) components and of the LOS direction cosines $n_{EW,ASC/DES}$, $n_{NS,ASC/DES}$ and $n_{V,ASC/DES}$, i.e., the direction cosines of the angles $\alpha_{EW,ASC/DES}$,

$\alpha_{N,ASC/DES}$, $\alpha_{V,ASC/DES}$, defined between the EW, NS and vertical directions and $LOS_{ASC/DES}$ directions respectively, as indicated in Figure 3.1. They represent the components of the unit vectors of the ASC and DES LOS directions, respectively indicated as i_{ASC} and i_{DES} , and they can be expressed, as widely known, as functions of LOS direction:

$$\begin{cases} n_{EW,ASC/DES} = \cos \Phi_{ASC/DES} \cdot \sin \theta_{ASC/DES} \\ n_{NS,ASC/DES} = \sin \Phi_{ASC/DES} \cdot \sin \theta_{ASC/DES} \\ n_{V,ASC/DES} = \cos \theta_{ASC/DES} \end{cases} \quad (8)$$

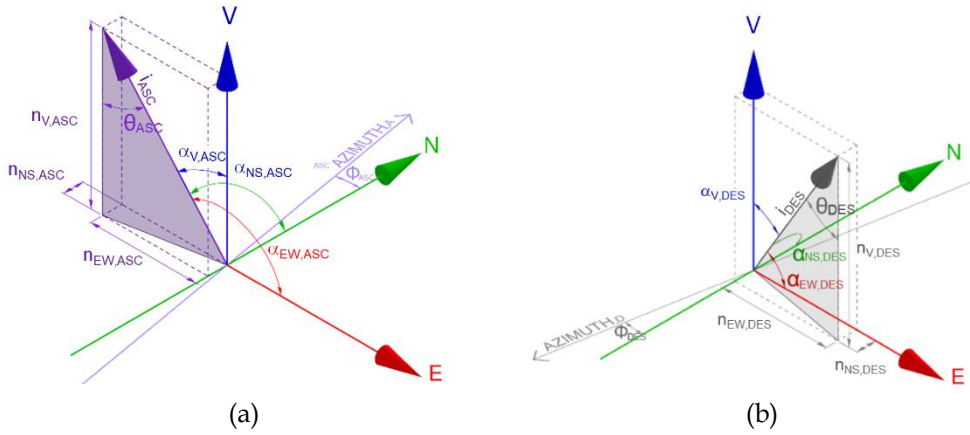


Figure 3.1. Satellite acquisition geometry for (a) ASC and (b) DES orbits [64].

It's clear, from Eq. (7), that the amount of deformation which can be detected and measured along the LOS direction depends on the values of the cosine terms. In Table 3.1, the percentage of deformation detectable by satellite (sensitivity analysis of the technique) referred to the NS, EW, and Vertical directions, for the principal satellites, are reported. It can be observed that the Vertical displacements are almost entirely detected in both acquisition geometries, for all the considered satellites and acquisition modes, the horizontal displacements in EW direction are detected only partially, while in NS direction a very small percentage can be detected in both LOSs, due to the quasi-polar nature of the satellite orbits. Then, the deformation component along the NS direction has very little influence

on the LOS deformation values due to the very low sensitivity when retrieving the NS deformation component.

Table 3.1. Sensibility evaluation of the instruments in the different directions.

Satellite	ERS1/2	ENVISAT-ASAR	RADARSAT-1/2	COSMO-SkyMed
ϕ [°]*	8.5	8.5	8.6	7.86
θ [°]**	23	15 – 45	20 – 50	20 – 60
n_{EW} [%]	38.6	25.6 – 69.9	33.8 – 75.7	33.9 – 85.8
n_{NS} [%]	5.8	3.8 – 10.5	5.11 – 11.4	4.7 – 11.8
n_V [%]	92.1	96.6 – 70.7	93.9 – 64.3	93.9 – 50

* Courtesy of official ESA EO portal [86]

**[87]

In summary, the more the direction of the real deformation vector deviates from the LOS direction, the smaller the component detected by the satellite. In Figure 3.2 it is represented an example, with reference to the case of mean velocity. From Figure 3.2a to Figure 3.2c, the mean velocity vector direction moves away from the satellite LOS direction, until the limit condition of the direction of the real deformation vector perpendicular to the LOS; in such a case, the component measured by the sensor is zero.

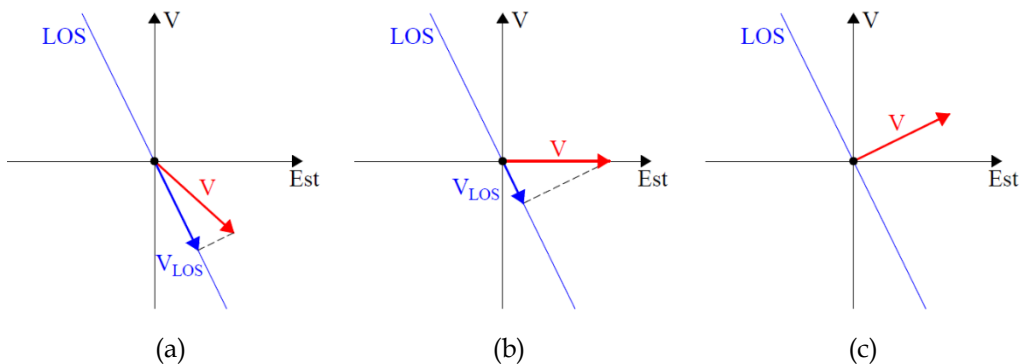


Figure 3.2. Variability of the measured LOS mean velocity component as a function of the real deformation direction: (a)-(b) real mean velocity vector with a component parallel to the LOS; (c) real mean velocity vector orthogonal to the LOS.

For this reason, it is important to note that a high LOS component deformation is certainly a sign of an ongoing deformation process, but a low LOS component deformation does not guarantee the absence of ongoing deformation.

The use of a single dataset can be associated with data deriving from existing studies or traditional on-site monitoring techniques, such as optical levelling or GNSS measurements. If the latter are available, it can be argued that the deformation phenomena is previously known (for example, a subsidence, or a landslide), so the prevailing direction of the ongoing deformation is known. In such a case, a DInSAR dataset could be used to derive the intensity of the deformation along that known direction. However, such assumptions are not generalizable and should be in any case adopted with great caution, evaluating each specific case.

It is worth to highlight that the distribution of the PSs is not spatially homogeneous. For this reason, in order to extend the information on the deformations even in areas without RADAR targets, it could be appropriate to apply a spatial resampling technique to deformation data related to the dataset, as will be explained in §3.3.

3.2 Use of both ASC and DES datasets

The DInSAR products are commonly provided as ASCII text files, typically subdivided into quadrants, different for ASC and DES datasets, each one representative of a geographical area and containing the portion of corresponding PSs for which the information is available.

An example of the spatial distribution of the PSs, obtained by processing ASC and DES datasets of CSK images via the full resolution SBAS-DInSAR approach, is shown in Figure 3.3. The ASC and DES PSs are represented with red and green markers, respectively.

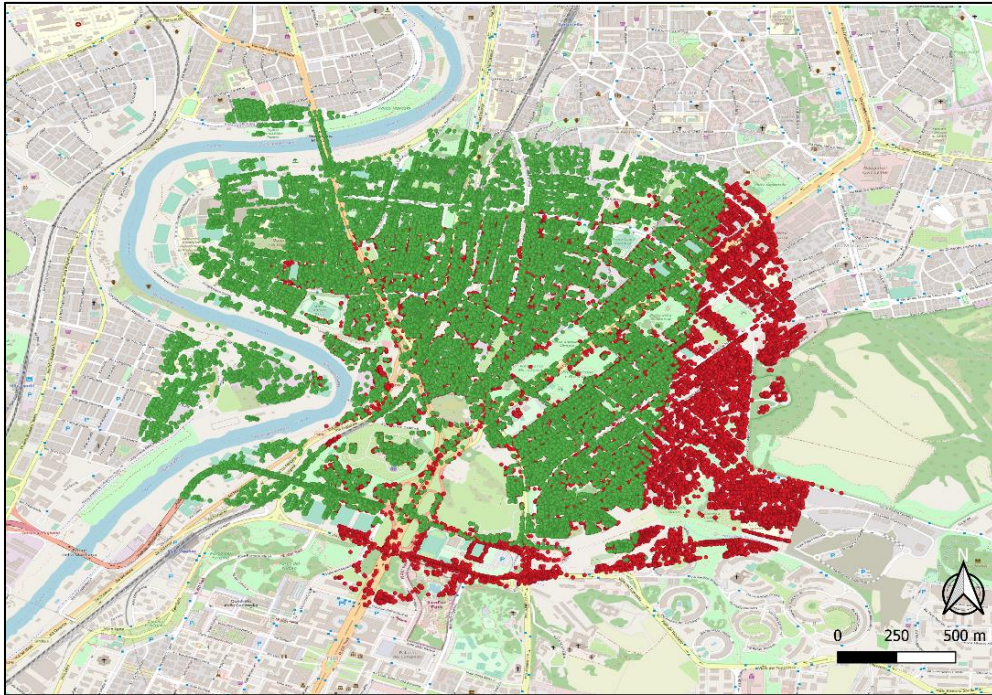


Figure 3.3. Example of PSs spatial distribution of ASC (red markers) and DES (green markers) orbits.

Generally, the pixel densities and spatial distributions differ, because of the different geometric and electromagnetic characteristics of the investigated area, as well as the temporal distribution of the datasets; for this reason, ASC and DES pixels are usually non-coinciding points.

It is also important to note that the reference points of the ASC and DES DInSAR datasets are located in the same area but at slightly different geographical positions, therefore it may occur that ASC and DES results are not straightforwardly comparable to each other. Accordingly, this problem is figured out by applying a topographic rigid translation to all the pixels of one or both datasets, thus allowing one to get the same topographic reference.

To understand how the measures along the two orbits referred to a PS “communicate”, four examples of ideal configurations of mean velocity can be observed in Figure 3.4. Negative V_{LOS} values indicate that the PS is moving away

from the satellite; on the contrary, positive V_{LOS} values indicate that the PS is moving toward the satellite. When mean velocities are purely Vertical or purely EW directed, being the angle of incidence substantially the same for both ASC and DES acquisition geometries, the moduli of the LOS mean velocity are equal for both datasets. In particular:

- Figure 3.4a and Figure 3.4b represent the case of a nearly Vertical mean velocity vector. In this case, $V_{LOS,ASC}$ and $V_{LOS,DES}$ are almost equal in value and have the same sign. For a downward mean velocity (Figure 3.4a), the PS is moving away from the satellite in both acquisition geometries, while for an upward mean velocity (Figure 3.4b) the PS is moving towards the satellite in both acquisition geometries;
- Figure 3.4c and Figure 3.4d depict the case of a purely horizontal EW mean velocity vector, towards East and West, respectively, for which $V_{LOS,ASC}$ and $V_{LOS,DES}$ are almost equal in value and have opposite signs. In fact, in such a case, for one acquisition geometry, the point moves toward the satellite, while for the other acquisition geometry, the point moves away from the satellite.

Accordingly, a first comparison of the mean LOS mean velocity values obtained from the two geometries allows to identify at a first glance whether the investigated phenomenon is mainly characterized by mean velocity components along the Vertical or horizontal EW directions.

Generally, the mean velocity vectors have both a Vertical and a horizontal component. The information of the ASC and DES SAR data measurements can be combined to trace back to the actual direction of the displacement vector of each PS of the whole investigated area if the ASC and the DES measurements are referred to the same target. As explained in §3.1, for a PS, if the generic measure X along the LOS of the sensor is available (as $V_{LOS,ASC}$ and $V_{LOS,DES}$ in Figure 3.5), Eq. (7) can be written.

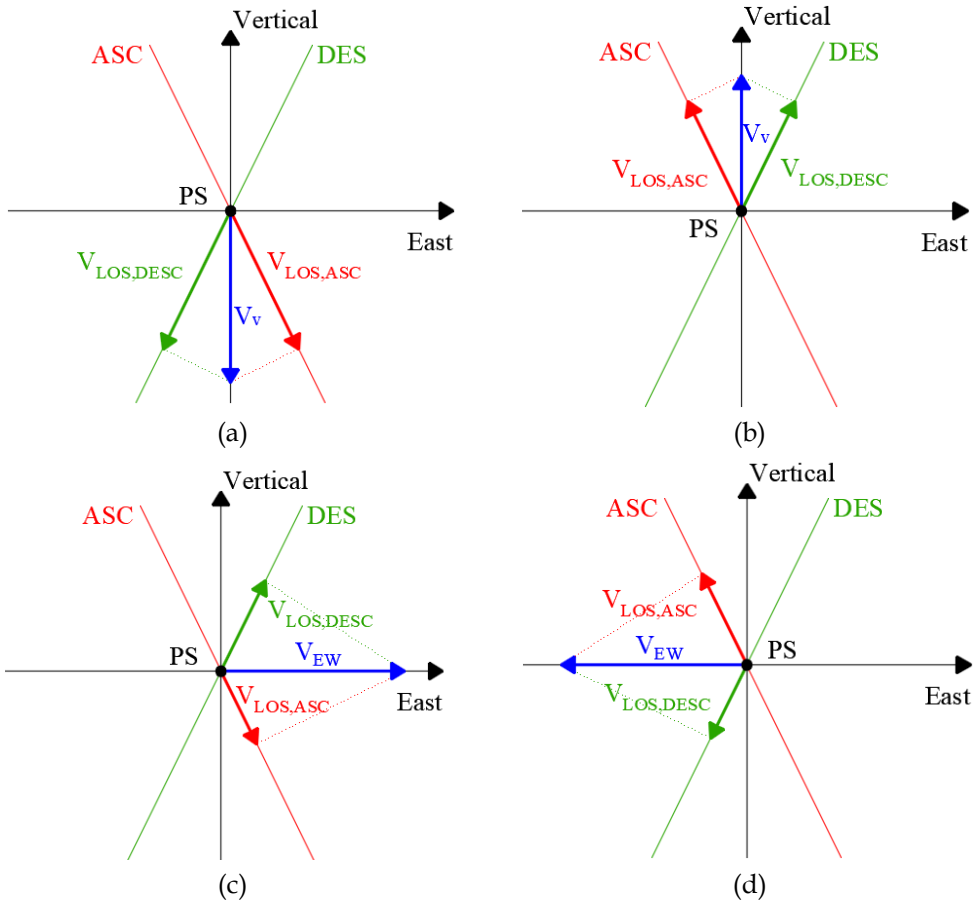


Figure 3.4. Decomposition of (a)-(b) vertical real mean velocity vector and (c)-(d) horizontal EW real mean velocity vector along the ASC and DES LOS directions.

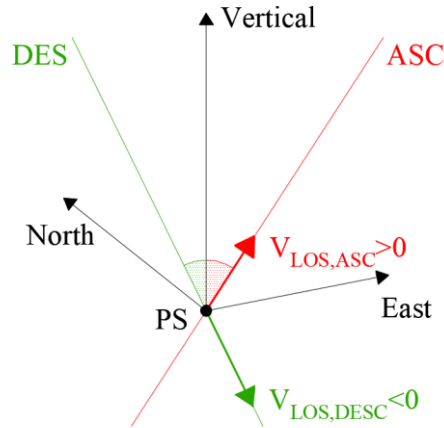


Figure 3.5. LOS directions and mean LOS velocities for ASC and DES orbit acquisitions represented in a three-dimensional Cartesian reference system.

Since the ASC and DES satellite orbits are quasi-polar, i.e., they are nearly perpendicular to the NS direction, as reported in Table 3, the cosine terms $n_{NS,ASC/DES}$ are almost negligible. Accordingly, this component can be neglected in Eq. (7) with a good approximation, allowing, however, a good estimation of deformation values for engineering purposes. Then, the system of equations (7) simplifies in Eq. (9), which allow the estimation of the unknown components X_{EW} and X_V :

$$\begin{cases} X_{LOS,ASC} = X_{EW} \cdot n_{EW,ASC} + X_V \cdot n_{V,ASC} \\ X_{LOS,DES} = X_{EW} \cdot n_{EW,DES} + X_V \cdot n_{V,DES} \end{cases} \quad (9)$$

When system (9) is used to estimate the mean velocity components, $V_{LOS,ASC}$ and $V_{LOS,DES}$ should be referred to comparable time intervals, in terms of the monitoring period length and its first and last acquisition time. If the difference between the first and/or the last data frames of the two series is remarkable, the related mean LOS velocities could not be effectively comparable. In such a case, in order to refine the results, the ASC and DES time series could be redefined before the calculation of the mean velocity components, by considering the overlapping time interval between the two datasets.

When, instead, system (9) is used to estimate the displacement components in a certain acquisition time, the LOS displacement components, $d_{LOS,ASC}$ and $d_{LOS,DES}$, can be appropriately combined only if those values are referred to the same acquisition time. Nevertheless, the satellite acquires SAR images along ASC and DES orbits in different times, so the retrieved DInSAR measurements relevant to the two orbits are never referred to the same acquisition times. For this reason, a temporal resampling of the ASC and DES PS time series is needed in order to estimate the displacement components along the Vertical and EW directions using Eq. (9).

It is worth remarking that the availability of LOS deformation measures related to both ASC and DES orbit for the same PS is a condition that seldom occurs in practical situations, due to the geometrical properties of the acquisition system and the different electromagnetic and geometrical properties of the scattering surfaces. A coincidence can occur when the observed PS corresponds to an artificial reflector, specifically installed for the purpose.

Commonly, especially for buildings, this is an almost unrealistic condition, since satellites investigate one or more fronts or portions of the building in their motion along the two different orbits, but never the same ones (and, in the case of the same front, from a point of view always different). In other words, it is rather unusual to find a biunivocal spatial correspondence between points of the two datasets, also because it is not possible to a priori define where the PSs concretely are located within a structure or a building. For this reason, in order to calculate the deformation components along the Vertical and EW directions over a building or in an area, it could be appropriate to apply a spatial resampling technique to deformation data related to the two acquisition geometries, as mentioned in §3.1. To this aim, the PSs can be spatially interpolated, providing two continuous LOS mean velocity maps, one from the ASC and one from the DES original dataset. Subsequently, these continuous LOS mean velocity maps can be projected on a defined grid, making it thus possible to compute the vectors of the mean interpolated LOS velocities $V_{LOS,ASC}$ and $V_{LOS,DES}$ in each vertex of the grid. In this way, the Vertical and EW components (V_V and V_{EW} , respectively), associated with each point of the abovementioned grid, can be evaluated with Eq. (9).

3.3 Spatial resampling

Spatial resampling techniques can be employed to obtain a set of georeferenced points. In particular, it is important to get information on LOS deformation for both ASC and DES orbit at the same point. The resampling and combination phases can be performed either in raster or vector (e.g., nearest neighbors approaches) space.

In raster space, for example, interpolation methods can be performed. These techniques require different rasterization steps (one for each ASC and DES geometry) that introduce the related uncertainties. Working with interpolation techniques has the advantage of providing continuous maps, although it is more difficult to account for the three-dimensional nature of the DInSAR data and it is more complex to combine the displacement histories. The spatial interpolation algorithms can be deterministic (e.g., Inverse Distance Weighted - IDW) or geostatistical (e.g., Kriging techniques). In deterministic methods, the value in a location is estimated by averaging the values of the nearest points, weighed by the distance from the point within a search circle. The geostatistical (or stochastic) methods are based on fitting spatial models to data. The application of data interpolation techniques allows to pass from a discrete PS map to a continuous map, more immediate and easier to read than the individual DInSAR data. An example is shown in Figure 3.6.

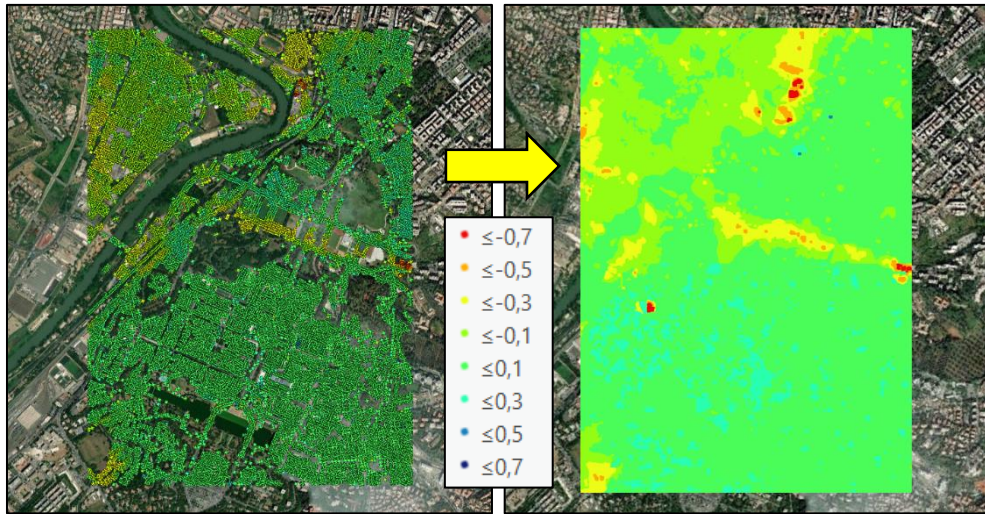


Figure 3.6. From the discrete mean velocity map to the interpolated map.

Regarding a building, the spatial interpolation of the points can be performed at different levels, for example, at the ground, and the roof levels. This is important because the comparison between a map referring to the ground and a map referring to the roof can be useful to recognize any differential displacement with the height. However, it is important to note that such spatial interpolation operations are performed in areas where the density and the distribution of the PSs are representatives of the area itself and the type of the analyzed deformation phenomenon is characterized by spatial correlation. Moreover, attention should be paid to areas characterized by high shadowing phenomena, namely, PSs are present in the immediate surrounding of a building only along sides exposed to the view of the satellite. Some examples will be reported in §3.4. The main spatial interpolation techniques can be performed using some of the many GIS software available (e.g., QGIS [88] ArcGIS [89]).

In vector space, for instance, working with nearest neighbors approaches, the ASC and DES datasets are combined without any rasterization process, to avoid the uncertainties associated with it. Working in vector space accounts easily for the actual 3D position of the points and easily permits the combination of displacement histories to compute the Vertical and horizontal EW components of

displacement. In some cases, it is suitable to adopt combination approaches that made use of the provided PSs, combining ASC and DES information of pair of neighbor PSs, belonging to the two datasets, which are close to each other. This approach requires the definition of a search distance value, to identify pair of PSs. Generally, it is assumed that ASC and DES PSs nearby, within the accuracies of the planimetric and altimetric positioning, can be representatives with a good approximation of the same reflective target. In such a hypothesis, Eq. (9) can be applied with acceptable reasonableness. Regarding the precision and accuracy of the PSs georeferencing on a planimetric scale, the height reconstruction of each PS is strictly dependent on the accuracy of the estimation of the residual topographic phase component with respect to the used DEM within the interferometric processing, which is on the order of 1-2 m. Consequently, by considering the full resolution CSK SBAS-DInSAR analysis, the precision of the PSs georeferencing is about 1-2 m, 2-3 m, and 1-2 m along the NS, the EW, and the Vertical directions, respectively, which corresponds to about one standard deviation. It is worth noting that an error in the georeferencing of the reference point can affect the position of all PSs of the examined area.

Finally, another technique has been proposed by TRE [62], named grid subsampling. In this case, the area of interest is subdivided into square resampling cells of an arbitrarily chosen size. A deformation equal to the average of the deformation values of the PSs falling within the cell is assigned in the center of the cell, which represents a synthetic PS.

3.4 Applications in Rome

In the following, applications regarding some elaboration of satellite SAR data referred to two case studies, that are part of a paper published in 2022 [38], are presented to demonstrate the procedures previously described. The applications regard the performing of a methodology for the structural analysis of existing buildings using SAR satellite data, historical graphical documents, and an accurate 3D modelling of the buildings. The accurate 3D model, created in this case via historical sources, provides a consistent positioning of the PSs in the GIS

environment. The correct positioning of the PSs allows for improvement in the study of the three interpretative approaches, described in the previous paragraphs yet, referring to them as Approach 1, Approach 2, and Approach 3 for simplicity, to study the active deformative processes of the examined buildings. As will be discussed in §4, the final aim is the performing of civil SHM. The two case studies represent applications of some elaboration methodologies mentioned in §3.2 but also highlight some peculiarities of the data themselves.

The case studies are relevant to a masonry building and two 20th century buildings in Rome (Italy): the residential buildings *Torri Stellari*, the *Collector sewer's point of disposal n. 7*, and the housing complex known as *Corviale*. The first two are located in the *Valco San Paolo* housing quarter [90], which is an area included in the larger area of the *Tiber River* bend and is characterized by significant ground movements affecting relevant constructions. The dataset used for these applications has been described in §2.3.1. In Figure 3.7a and Figure 3.7b (for ASC and DES orbits, respectively) the maps of the area of Rome in which the case study buildings fall, is shown. They are indicated by a white, a violet, and a black benchmark (for the *Torri Stellari*, the *Collector sewer's point of disposal n. 7*, and the *Corviale*, respectively), while the colors refers to the LOS mean velocity, expressed in mm/year.

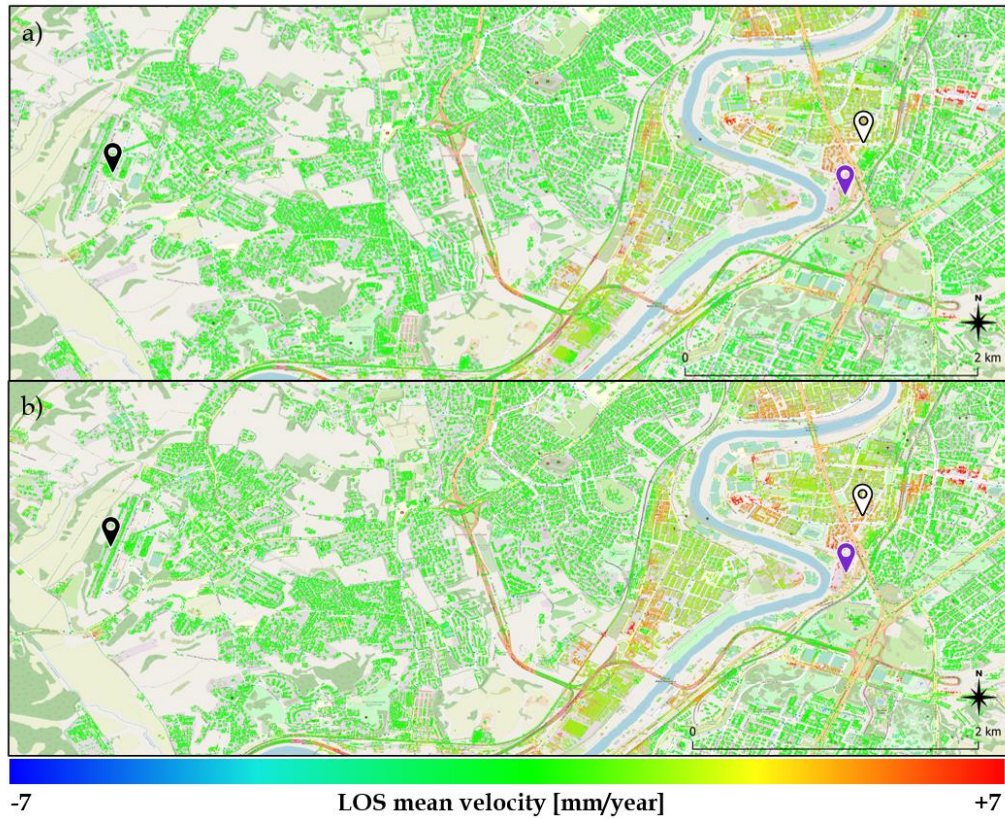


Figure 3.7. LOS mean velocity maps of the investigated area: (a) ASC and (b) DESC. White, violet, and black benchmarks indicate Torri Stellari, Collector sewer point of disposal n. 7, and Corviale, respectively (modified from [38]).

3.4.1 Application – Torri Stellari

The first application regards the Torri Stellari, included in the Valco San Paolo housing quarter [90] in Rome (Italy), which is representative of a significant displacement scenario. This housing district is characterized by four 8-floor buildings with a star-shaped plan, built in the years 1949-1952. The load-bearing structure of the four towers is a RC frame with brick walls and hollow block slabs.

The first approach requires a graphical representation, so the construction of the geometrical model of the building volumes for the graphical positioning of the PSs around the model in the space is needed. Approximated volumes can be extruded starting from the open-source Regional Technical Numerical Map (CTR, [91]) of Lazio region. Nevertheless, a deep 3D modelling process, based on the available original design drawings and documentation collected in the archive of the architect Mario De Renzi (1897-1967) (Figure 3.8) provides a more accurate geometry. The historical data allows the 3D surface modelling of the building volumes, limiting the on-site survey (e.g., on-site measuring and laser scanning) to specific building details.

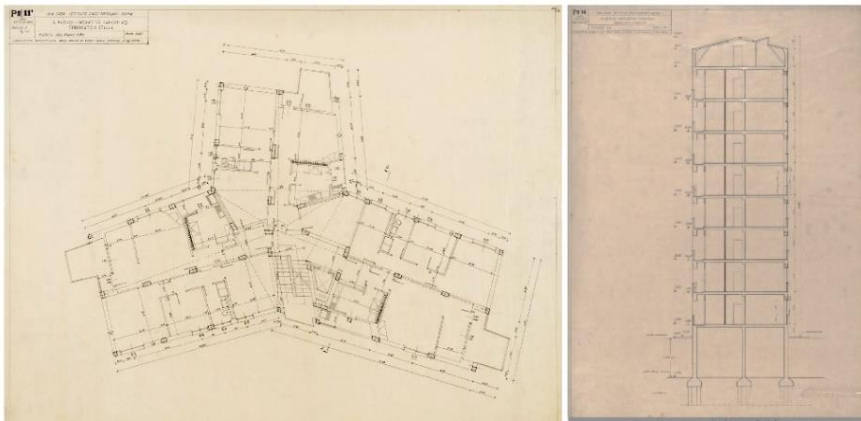


Figure 3.8. Original design drawings of Tower n. 1 (M. De Renzi): plan of the first floor and section AA, 27 June 1950 (courtesy of *Accademia Nazionale di San Luca*).

The 3D surface models are georeferenced. Exploiting interoperability with the GIS environment, through interchange file format, the 3D surface models are merged with the positioning of the PSs in ArcGIS Pro [89]. Figure 3.9 shows the comparison between the PSs positioning (representing ASC and DES PSs with red and green markers, respectively) on the accurate 3D model of Torri Stellari and the CTR-derived schematic volumes. It can be noted that only in the accurate 3D volume of the towers, the PSs are properly aligned along the external volumes of the buildings, considering the pitched roof, and the balconies.

The first procedure (Approach 1) is based on the nearest neighbour approach. It allows to accurately investigate the maximum displacement components, over the satellite data acquisition period. Supported by the 3D representation, it starts with the selection of couples of PSs belonging to ASC and DES datasets, sufficiently close to be assumed representative of the same reflecting target, unless the positioning error. A temporal window, common for ASC and DES datasets, is chosen. Then, a cutting of the initial part of the displacement history of the ASC dataset is done. A temporal resampling of the time series is performed, taking care to ensure the overlapping of the acquisition periods of the two datasets, cutting previous or subsequent acquisitions, compared to the common acquisition period. The displacement value measured at the first time is subtracted from the remaining time history, allowing a null measure in the first instant common to ASC and DES datasets. In this way, since the two time-series refer to the same time instants, a combination of the LOS displacements of the two orbits can be done through Eq. (9), to evaluate the Vertical and EW components, d_V and d_{EW} . Then, Approach 1 allows to evaluate the maximum values of these displacement components, with reference to points spatially uniquely determined, starting from the combination of the selected PSs couple. As an example, Figure 3.10 shows a couple of ASC and DES points (represented with triangular and circular symbols, respectively), selected in the proximity of the ground level of the South facade of Tower n. 1.

The selection of points can be performed in several ways and must comply with the following criteria: i) the distance between the PSs and the building must be lower than the planimetric positioning error; ii) the planimetric (EW and NS) and altimetric (Vertical) distances between points must be lower than the error of the SAR data positioning; ii) being the first and second conditions satisfied, among all identified couples of points, the selected couple is the one characterized by the highest coherence value.

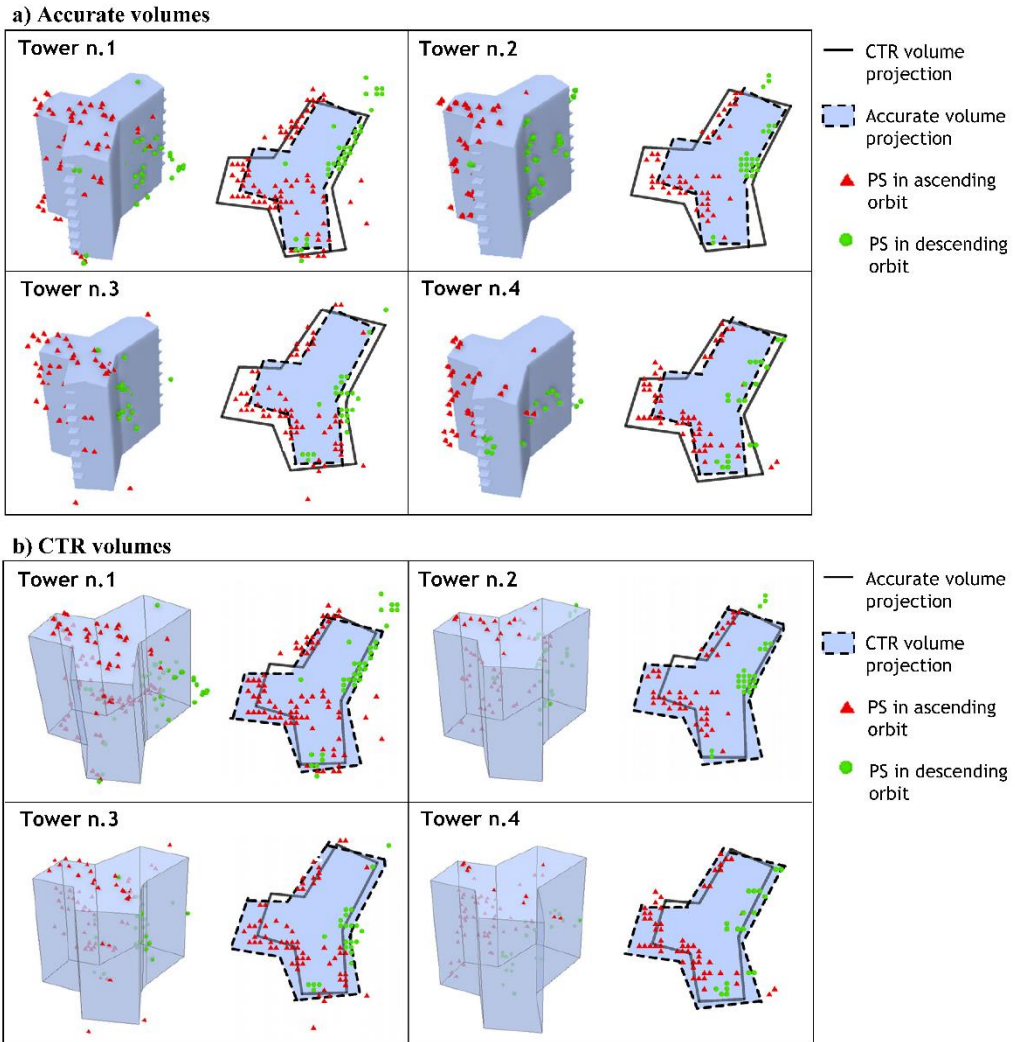


Figure 3.9. PSs localization on Torri Stellari (a) accurate volumes and (b) CTR volumes, in ASC (red triangles) and DESC (green circles) orbits [38].

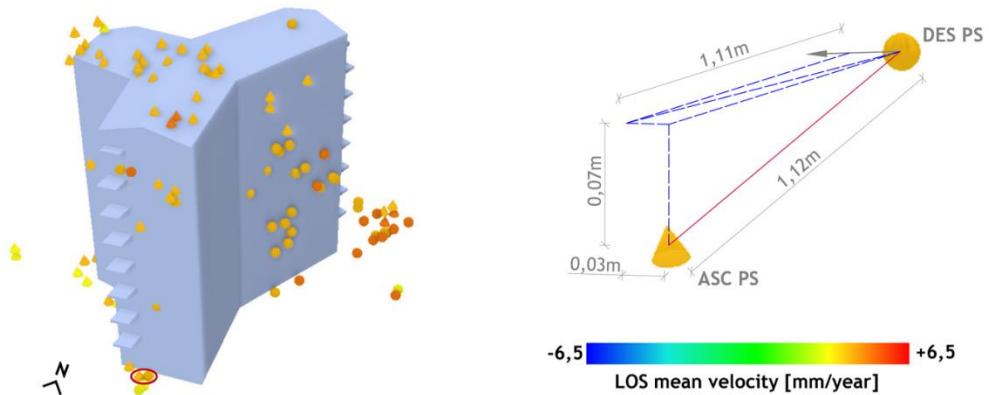


Figure 3.10. Selection of a pair of ASC (triangles) and DES (circles) PSs of Tower n. 1 [38].

Approach 1 represents a very suitable procedure for the evaluation of the maximum values of the displacement components but is computationally onerous. Alternative approaches that avoid temporal resampling can be adopted, exploiting the yearly LOS mean velocity values, for example, Approach 2. Also, this procedure is based on the nearest neighbour selection of couples of ASC and DES PSs. Then, the mean LOS velocities $V_{LOS,ASC}$ and $V_{LOS,DES}$ of the selected PSs are combined with Eq. (9), to evaluate the components of the mean velocity along the Vertical and EW directions, V_V and V_{EW} , respectively. An estimation of the maximum displacement components d_V and d_{EW} is obtained by multiplying the mean velocity components for the duration of the acquisition period.

Finally, the third procedure (Approach 3) reduces the computational effort required by the previous ones. Approach 3 is based on a spatial resampling (see §3.3) of the $V_{LOS,ASC}$ and $V_{LOS,DES}$ values of the selected PSs. The resampled continuous maps are appended on a grid with a fixed side (see §3.2), and the values of the mean velocities V_V and V_{EW} associated to each point of the auxiliary grid defined for the area of interest are estimated through Eq.(9). Then, d_V and d_{EW} are evaluated multiplying V_V and V_{EW} for the duration of the acquisition period. The interpolated LOS mean velocity maps obtained through Empirical Bayesian Kriging (EBK) technique, related to the *Torri Stellari* area at ground level, are

shown in Figure 3.11a and Figure 3.11b, with superimposed the PSs located at the ground level, belonging to ASC and DES orbits, respectively. The points have been selected considering the ground profile of the area and choosing a confidence band around the specific ground level of ± 2 m, equal to the altimetric error in positioning of the PSs. To analyze the area at the scale of the single building, the continuous mean velocity maps have been projected on a defined grid with a cell size set at 5 m (Figure 3.12), not exceeding the 3×3 m² resolution of the COSMO-SkyMed products and at the same time representing a value comparable with the distance between the columns of an RC building. Adopting a deterministic approach, no information can be derived for cells characterized by the absence of PSs belonging to both datasets. In this case, an improvement can be given by adopting probabilistic resampling techniques, especially if the overall area results to be characterized by many points, well-spaced, and belonging to both datasets. In Figure 3.11c and Figure 3.11d, respectively, the values of the mean velocity along the Vertical and EW directions are shown for the examined case study. This type of graphical representation immediately highlights the presence of zones affected by substantial values of the mean velocity and zones characterized on the contrary by a more stable behavior. In the adopted convention, negative values represent downward and West-directed displacements, while positive values represent upward and East-directed displacements. Areas covered by green points are characterized by a stable deformative behavior along the specific direction, presenting values of the Vertical and/or EW mean velocity, ranging around zero. By observing Figure 3.11c, it can be noted that there is evidence of a pretty Vertical deformational phenomenon ongoing, which can be connected to the subsidence of the area close to the Tiber River, already studied in the literature [9]. In particular, the four towers are in an orange zone of the Vertical mean velocity map (Figure 3.11c) with values ranging between -5 and -3 mm/y, while falling in a green zone of the EW map (Figure 3.11d), with values ranging between -3 and -1 mm/y.

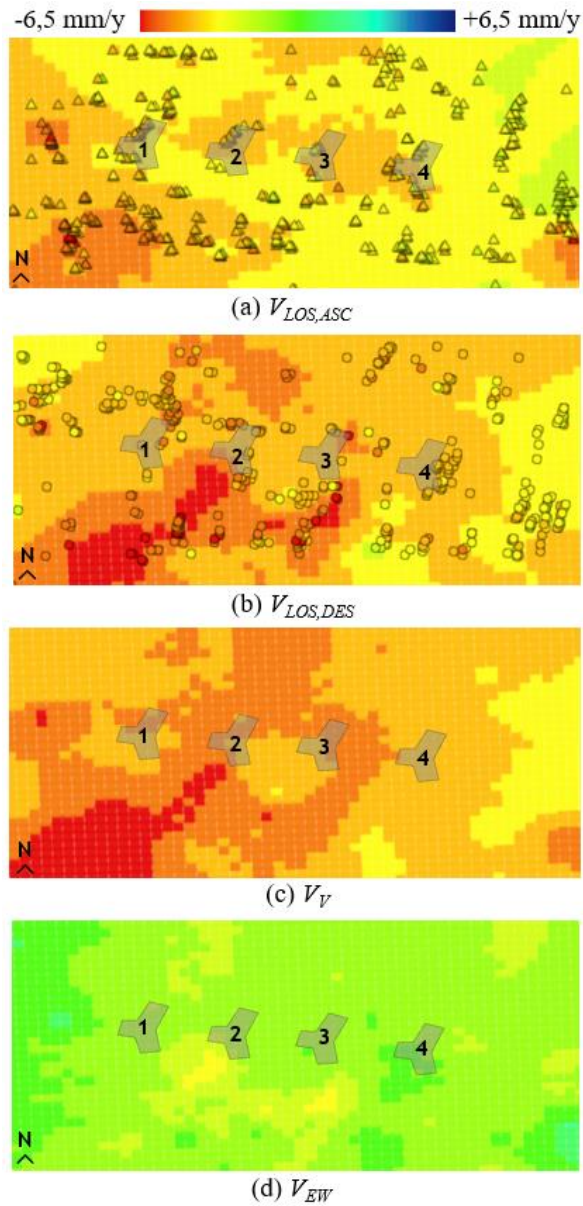


Figure 3.11. Mean velocity maps of the Torri Stellari area: (a) ASC and (b) DES data, through EBK interpolation; (c) Vertical and (d) EW components of the mean velocity (period 2011-2019) [38].

Considering the couple of points belonging to the ground level of Tower n. 1 selected in Figure 3.10, Figure 3.13 shows a comparison of the results of the application of the three approaches. In particular, the trend of the Vertical and EW components of the displacement of the selected couple of points over the acquisition period, e.g., Approach 1, is represented with cyan and red circles, respectively. For each displacement component, two series exist, because of the two temporal resampling (Figure 3.13 a and b, Figure 3.13 c and d). The higher values among the two series give the Vertical and EW components corresponding to Approach 1, indicated as $D_{max,Ap1}$. The slope of the continuous grey line and the violet dashed line represent the component of the mean velocity along the considered direction for Approaches 2 and 3, respectively. In general, the latter can differ from the regression line of the time series of the resampled displacements of Approach 1. Adopting Approach 2, the maximum displacement components of the selected couple of points ($D_{max,Ap2}$) have been evaluated by multiplying the mean velocity values for the duration of the acquisition period. The values of the mean velocity components relative to Approach 2 are also indicated in the figure as v_{Ap2} . Regarding Approach 3, the displacement values ($D_{max,Ap3}$) are evaluated considering the nearest point of the abovementioned auxiliary grid to the selected couple of points. Similarly to Approach 2, the mean velocity components obtained through the maps have been multiplied by the duration of the acquisition period. The values of the mean velocity components relative to Approach 3 are also reported in Figure 3.13a-d as v_{Ap3} .

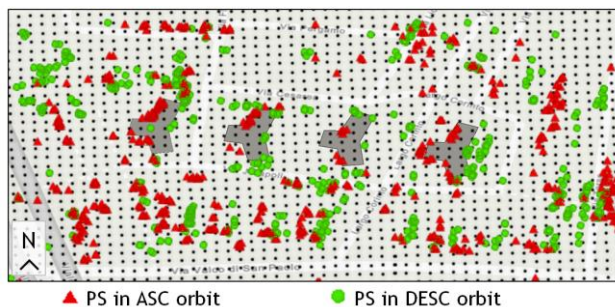


Figure 3.12. Adopted grid in the Torri Stellari area, with superimposed ASC (red) and DES (green) PSs [38].

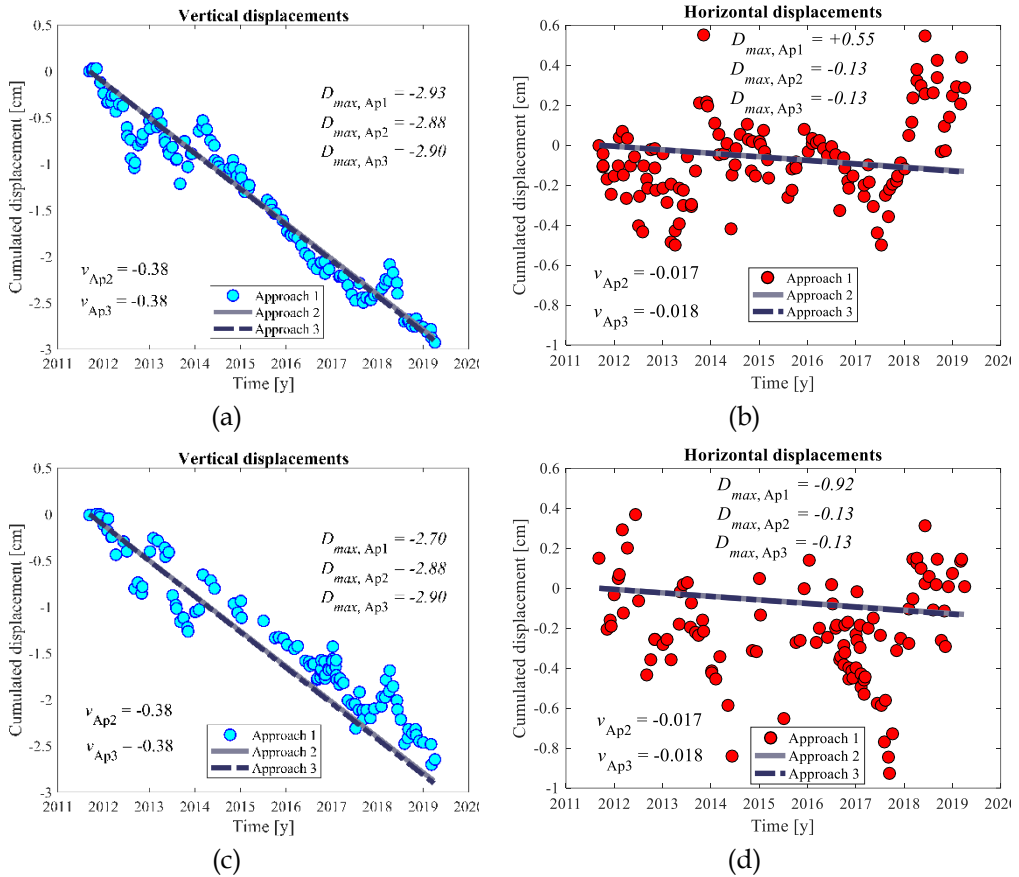


Figure 3.13. Comparison of the Vertical and EW displacement components for the three approaches: (a) and (b) DES data resampled on ASC ones; (c) and (d) ASC data resampled on DES ones [38].

Observing the results of the examined couple of points, it can be noted that a linear decreasing trend over the acquisition period is obtained for the Vertical displacement component, and similar values of Vertical D_{max} are provided by the three approaches. Vice versa, the horizontal displacement component presents a high oscillation around 0, the maximum displacements in this direction are comparable with the error for the single deformation measurement. For horizontal direction, from a statistical point of view, the applicability of Approaches 2 and 3 is lost, due to the low values of the gradient of the regression line and

determination coefficients. Under these assumptions, the most effective procedure is represented by Approach 1.

The existence of a well-defined trend of the displacement-time series is required to guarantee the applicability of Approach 2. In addition to this condition, Approach 3 provides good results if many points exist in the examined area, well-spaced, and belonging to both datasets, necessary for a proper evaluation of the mean velocity maps along the LOS, Vertical, and EW directions. Approach 3 is the simplest procedure to be implemented.

3.4.2 Application – Collector sewer’s point of disposal n. 7

The second application regards the Collector sewer point of disposal n. 7, that is a one-story building in tuff masonry positioned above an underground tunnel of an ovoid shape (5 m x 7 m, the Collector sewer), constructed in masonry. The building, built at the end of 1800, can be considered a hydraulic infrastructure since it represents the point of disposal n. 7 of the Collector sewer. Original design drawings are reported in Figure 3.14.

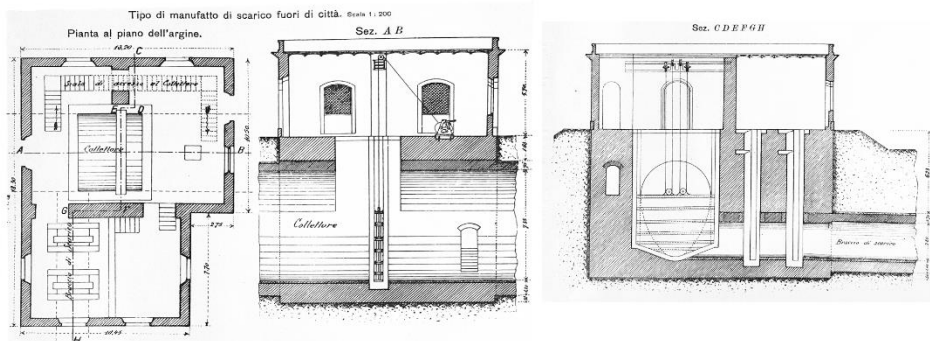


Figure 3.14. Collector sewer’s point of disposal n. 7: original design drawings (1882) (Courtesy of Rome State Archive, Ufficio Speciale per il Tevere e l’Agro Romano collection).

The Vertical and EW components of the mean velocity measured through the multi-temporal DInSAR analysis on the ground surface are estimated according to the procedure named “Approach 3” in the previous §3.4.1, which consists in

the application of Eq. (9), after a spatial resampling of both ASC and DES LOS mean velocity data, using an EBK interpolation method (see §3.3). Initially, the PSs located at the ground level, represented in Figure 3.15a from a top view (ASC and DES orbits, respectively represented with red triangles and green circles), have been considered. It is evident that the number of DES PSs is very low, and that their distribution around the manifold does not cover all the building sides. For this reason, to have a more consistent DES dataset, all the PSs around the manifold have been considered, without selecting them by height (Figure 3.15d, same symbol convention of Figure 3.15a). The mean velocity maps of V_V and V_{EW} have been derived starting from DInSAR measurements either using only ground PSs (Figure 3.15b,c) or all the PSs around the manifold (Figure 3.15e,f).

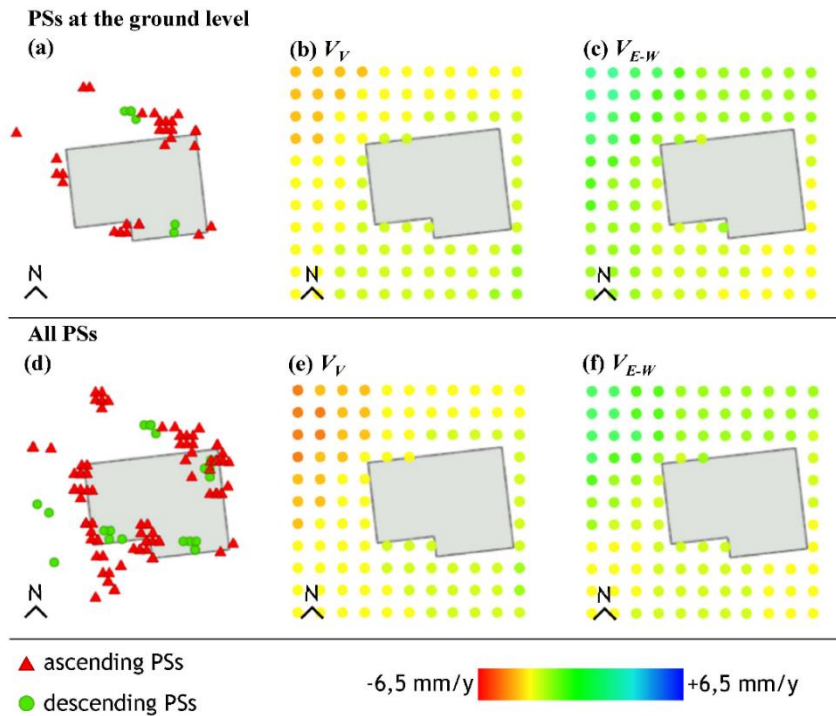


Figure 3.15. Collector sewer's point of disposal n. 7. Considering PSs at the ground level: (a) ASC and DES PSs; mean velocity maps along (b) Vertical and (c) EW direction. Considering all PSs: (d) ASC and DES PSs; global mean velocity maps along (e) Vertical and (f) EW direction [46].

Significant differences between the two maps are not observed, due to the low height of the construction. Then, the maps show the existence of downward Vertical settlements, and horizontal components comparable to the Vertical ones. In this case, the cell size of the auxiliary grid has been set equal to 3 m, aiming at maximizing the number of measure points useful to build the settlement profile along the manufact's sides.

3.4.3 Application - Corviale

The Corviale housing complex (constructed between 1975 and 1983 [92]) is composed of a main block 968 m long, 33 m wide, and 11 stories. The building is entirely in RC, combining cast on-site and industrialized elements. Every 36 m there is an expansion joint. The study of the Corviale is based on the execution design documentation conserved in the ATER (Public Housing Agency) historical archive in Rome, focusing on one building block (Figure 3.16).

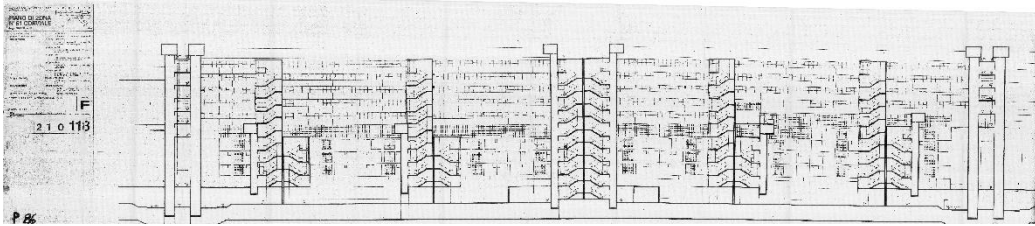


Figure 3.16. Original design drawings of Corviale complex, sector F (ATER Archive).

Also for the Corviale complex, the 3D representation is performed for the graphical positioning of the PSs around the model in the space. The approximated volume extruded starting from the CTR [91] and the 3D surface model created based on the available original design documentation are shown in Figure 3.17, with ASC and DES PSs represented with red and green markers, respectively. It can be noticed that, in the simplified CTR volume, the typical cross section of the building - featuring a larger top volume and a sloped basement - is not represented, with the consequent incorrect localization of the PSs into the building volume.

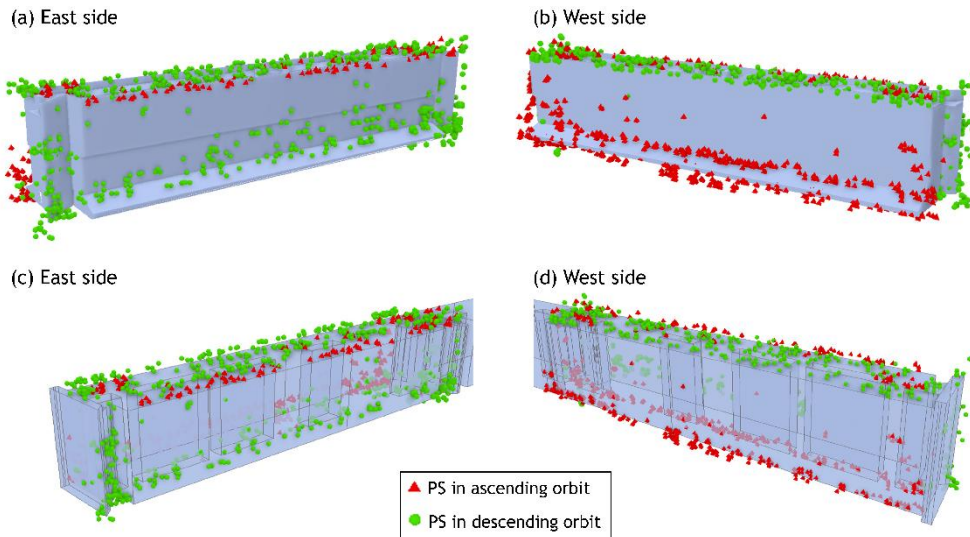


Figure 3.17. PSs localization in ASC (red triangles) and DESC (green circles) orbits, on the Corviale block B accurate volume: from (a) East and (b) West sides; on the Corviale block B CTR volume: from (c) East and (d) West sides [38].

Looking at the Corviale complex area, the LOS mean velocities reveal a general stability of the area, as can be seen in Figure 3.18. Then, for the Corviale complex, it is not significant to implement one of the approaches explained and shown with refers to the Torri Stellari for the displacement detection. On the contrary, this case is very useful to show some limits in the applicability of spatial interpolation. In fact, Figure 3.18 also shows the existence of wide zones characterized by a low number of PSs, or even by the lack of PSs. Moreover, the ASC and DES PSs at ground level, represented in Figure 3.19, are aligned respectively along the western and eastern sides of the building (see also Figure 3.17). In such a case, the results of a spatial interpolation for the definition of mean velocity maps must be used taking into account that results provided for areas without PSs are extrapolated values and could have low reliability.

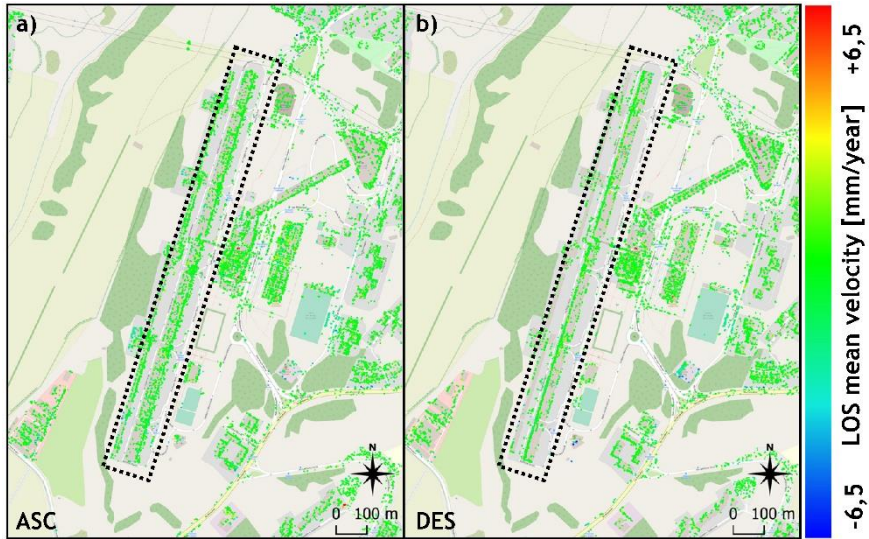


Figure 3.18. LOS mean velocity of all the PSs identified in the area of the Corviale complex: (a) ASC and (b) DESC [38].

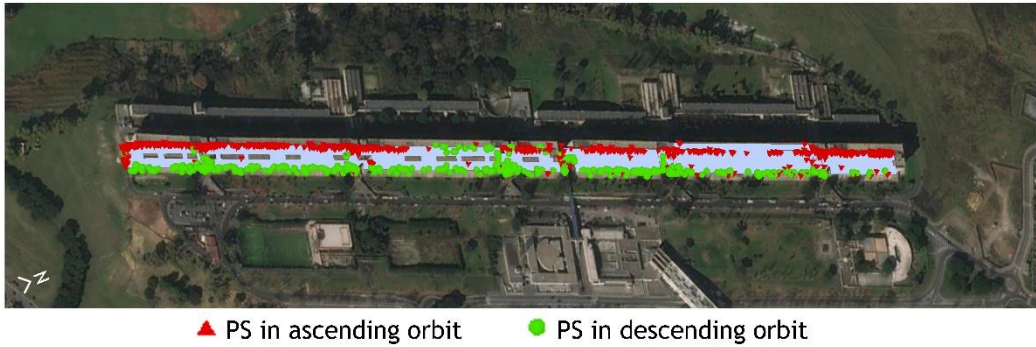


Figure 3.19. ASC (red) and DESC (green) PSs distribution for the Corviale complex in Rome [38].



Chapter 4

4. Potential use for SHM purposes at territorial scale

In this thesis, two methodologies for the management and elaboration of satellite data at a territorial scale are presented.

The first methodology, which will be described in §4.1, is based on machine learning (ML) algorithms. It consists of the extraction of cloud points (“clusters”, each one representing one building of the area) from datasets of satellite DInSAR PSs relative to a chosen area, by applying the artificial intelligence (AI) techniques referred to as clustering methods. The deformative condition of each cluster is studied, and deformation maps with all the retrieved clusters (buildings), are created. All the clusters are represented in the maps, also the stable ones, to have a framework of the total situation in the monitored built area. This methodology works well with satellite SAR data with high resolution and a sufficiently reliable topography location (e.g., CSK).

The second methodology, which will be described in §4.2, is based on the use of a tool specifically developed at the Research Unit of Geomatics of the CTTC for the management of DInSAR products. Its aim is the identification of the buildings affected by displacements above a given threshold (defined as “critical”), among all the buildings included in an investigated area. Only the critical buildings are represented in the final deformation maps. This methodology can

be used for wider areas (districts, municipalities, towns) and using data with a resolution not necessarily high, but with good spatial distribution (e.g., S-1).

The two methodologies provide real support for the management of urban areas, in particular about the identification of the most critical buildings to be investigated with a higher degree of information (e.g., on-site inspections and measurements). Some of the possible investigation strategies to carry out are only briefly cited in this work since they are out of its aims. For example, surveys to ascertain the conditions of these buildings could be done, and, if necessary, on-site monitoring could be provided. If satellite SAR data with high resolution are available, it is possible to integrate the procedure by analyzing the critical buildings at a single construction scale by adopting other approaches, as will be discussed in §5.

4.1 Preliminary identification and ranking of critical constructions based on DBSCAN technique

The proposed methodology is based on the clustering method known as *Density-based Spatial Clustering of Applications with Noise* (DBSCAN [93]). Clustering methods are AI techniques aimed to identify groups of similar instances in a multivariate dataset: the so-called clusters. Among the different approaches existing in literature, the density-based clustering methods perform cluster identification by exploiting the idea that a cluster is a contiguous region of high point density in a data space, whereas low-density regions represent noise.

In short, the DBSCAN algorithm works by considering three types of points: core points, density-reachable points, and outliers. A point in some space to be clustered can be identified as a core point if it is characterized by at least a minimum number of points (*minPoints*) within a selected distance (*eps*). These two hyper-parameters have to be opportunely set to have good results. As for density-reachable points, they are points reachable from a core point through a path such as p_1, p_2, \dots, p_n where p_1 is a core point and p_n is the density-reachable point. A point that is not reachable from any other point is classified as an outlier, i.e.,

it represents noise. DBSCAN starts by selecting a point B randomly. Then, it collects all the points within a space with center B and radius eps . This space is referred as to the neighborhood of point B. If the neighborhood of point B does not contain a number of points equal to $minPoints$, point B is marked as an outlier. Otherwise, the algorithm creates a first cluster containing B and all points density-reachable from it. In turn, the new points are marked as core points if their eps -neighborhood contains at least a number $minPoints$ of points, and the points density-reachable from them are added to the cluster. In brief, the cluster is built, incrementally, by adding all the points density-reachable from a core point already present in the cluster. The cluster is complete when there are no other points that can be added. This occurs when the newly added points are not core points. Once a cluster is completed, the DBSCAN algorithm selects a new random point out of the already completed clusters and repeats the process. It is worth noting that a point recognized as an outlier can be found in the neighborhood of a different point and can be introduced in the cluster of this point. Therefore, only at the end of the algorithm process, it is possible to mark a point as an outlier. Figure 4.1 reports an example to clarify the functioning of the DBSCAN algorithm.

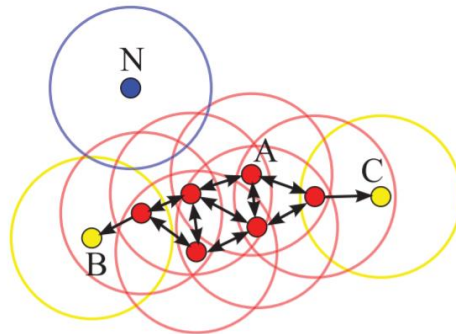


Figure 4.1. Example representing how DBSCAN works. In this figure, the $minPoints$ hyper-parameter is 4, and the eps radius is indicated by the circles. N is a noise point, A is a core point, and points B and C are density reachable from A [94].

DBSCAN algorithm has been successfully used in several domains such as

urban planning, traffic congestion management, and anomaly detection [95]. In the context of spatially extended data, DBSCAN has been already used for dealing with LiDAR data [96], [97], and Terrestrial Laser Scanning Data [98]. The main advantage of this clustering algorithm is the ability to discover clusters of arbitrary shapes in spaces of any dimension. For this reason, DBSCAN seems a suitable approach for achieving one of the goals of this methodology, which is the identification of buildings by exploiting data acquired through the SAR satellite derived data, without knowing a priori the number of buildings in the area, their shape, and the dimension of the initial dataset.

The proposed methodology is explained in detail in §4.1.1. It is applied to three case study macro-areas in Rome (Italy), including distinct typologies of buildings, in order to show the potential of the proposed methodology applied to different kinds of urbanized districts. The PSs used in the applications are derived by processing a set of CSK images through the SBAS-DInSAR technique, illustrated in §2.3.1. The applications will be shown in §4.1.2. The discussion on potential and limitations of the proposed methodology is reported in §4.1.3.

To implement the proposed approach, Python code language has been used, and the available libraries have been exploited to speed up the process and reduce possible errors.

4.1.1 Proposed methodology

This paragraph presents the proposed methodology for preliminary identification and ranking of the critical constructions in urban areas, based on the joint exploitation of satellite DInSAR measurements and DBSCAN-based techniques.

The flowchart of the methodology, shown in Figure 4.2, is composed of three elements:

- The first one (green box) regards the acquisition and the processing of the SAR images relevant to the analyzed area, in the period of interest (in this case, CSK images in the period 2011-2019). The images are processed through a multi-temporal DInSAR technique (in this case, through the full-resolution SBAS-DInSAR algorithm), in order to obtain spatially
-

- dense maps of coherent measurement points (referred to as PSs);
- The second one (red box) regards the clustering operation, performed by using the DBSCAN algorithm. The identified clusters represent the different buildings in the investigated area;
 - The third one (blue box) regards the analysis of the deformation evolution of each building in the observation period, by analyzing the mean velocity trends and statistics of the PSs belonging to the cluster-identified buildings. This allows, through the retrieval of synthetic deformation maps of the investigated area (with a focus on the buildings), to carry on a preliminary identification and ranking of critical buildings to be further investigated.

The main characteristics of the satellite input data relevant to the first step of the proposed methodology, i.e., the DInSAR products obtained through the full-resolution SBAS technique, have been already explained in detail in §2.3.1. The other two main blocks of the procedure are described in deep hereafter.

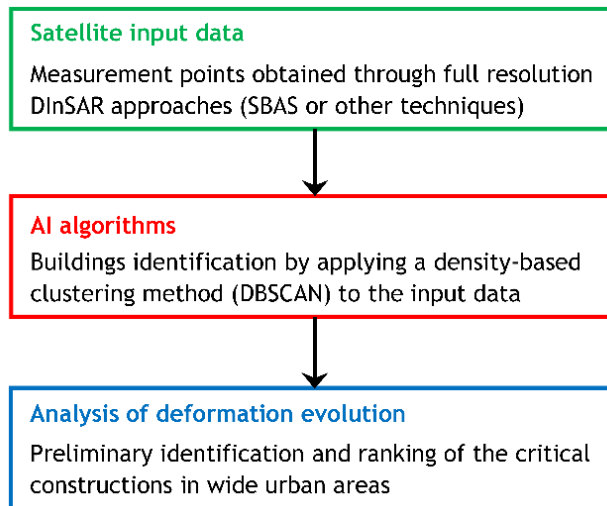


Figure 4.2. Flowchart of the proposed methodology [36].

The flowchart presented in Figure 4.3 describes the identification of the buildings employing an AI algorithm based on DBSCAN, starting from the ASC and

descending datasets of PSs (merged to maximize the PSs density), and improved through additional conditions derived by engineering considerations.

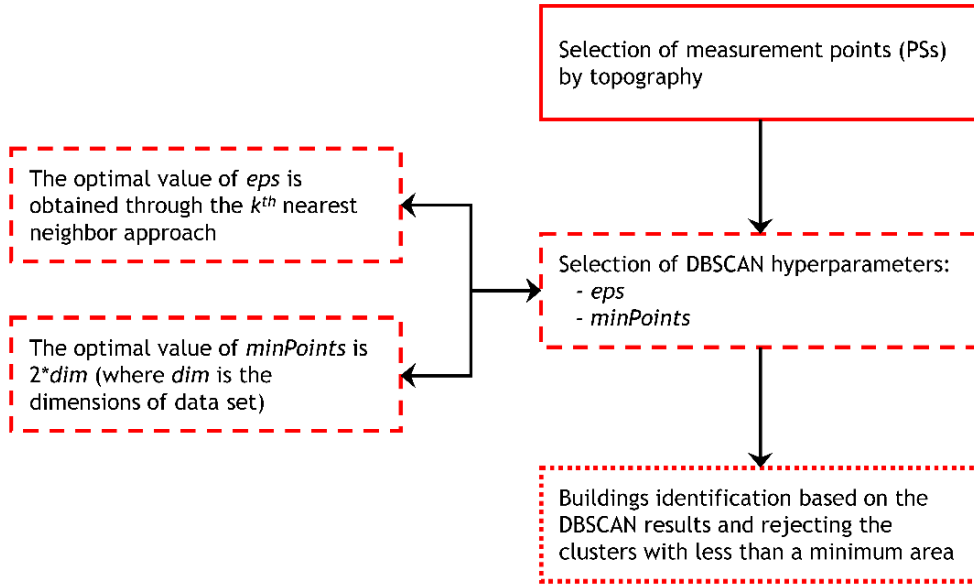


Figure 4.3. Flowchart of the identification of the buildings through the DBSCAN algorithm [36].

The first step of the procedure regards the selection of the PSs by topography (red continue box in Figure 4.3). In areas between buildings, the PSs are most likely relative to the ground, so, for the purposes of this study, they represent noise and must be neglected. All the PSs having a height δ lower than a value are considered to be on the ground. For the choice of this value, the distribution of the frequency of δ for the dataset of the examined area, is observed. In particular, attention is paid on the δ value that shows a first decrease in the frequency with respect to the previous one. The ground level is considered to have a topography given by the δ mean value of all the discarded PSs. An additional vertical error of ± 2 m is considered, corresponding to about one standard deviation, as specified in §2.3.1. The latter, summed to δ associated with the ground PSs, led to the definition of the value under which all the PSs are neglected for the

clustering. Moreover, since the one-floor points positioning can show an overlapping with the ground points (because of the mentioned possible errors of positioning), an additional δ can be considered, equal to the height of the one floor buildings (e.g., 3.00 – 3.50 m, based on the engineering judgment of the user).

Once this first noise cut is done, the clustering algorithm DBSCAN can be implemented (red dashed box of the flowchart in Figure 4.3). The optimal value for neighborhood radius eps is generally determined through an approach consisting in plotting the mean of the distances between each point and its k^{th} nearest neighbor, sorted in ascending order, where k is generally equal to $minPoints$ [99], [100]. Then, the optimal value for eps corresponds to the point of maximum curvature of the obtained graph. In this application, to have a better estimation based on the observation of the domain, eps has been evaluated for different values of k , ranging in the interval $[k_{inf}; k_{sup}]$, where the boundaries are related to the PSs density of the examined area, obtained by dividing the number of PSs for the corresponding area occupied by buildings. In particular, k_{inf} has been obtained by multiplying the number of PSs in a m^2 for the minimum unity surface. The parameter k_{sup} , instead, has been obtained by multiplying the number of PSs in a m^2 for the mean area of the buildings in the area. Then, for each value of k included in the interval $[k_{inf}; k_{sup}]$, a curve can be drawn, and the point of maximum curvature can be found. Finally, the mean of the ordinates of the retrieved points gives the optimal value for eps . Anyway, the value of eps shall be greater than the minimum distance between the buildings of the area (known or estimated). Concerning the $minPoints$, instead, according to Ester et al. (1996) [93], the DBSCAN default value is 4 for 2-dimensional data. For data with more than 2 dimensions, according to Sander et al. (1998) [101], $minPoints$ is computed as $2 * dim$, where dim is the dimensions of dataset.

At the end of the clustering operations, a plot of the cluster results with buildings identification is created (red dotted box of the flowchart in Figure 4.3). As an additional check to remove unexpected noise, the users can choose to reject the clusters with less than a minimum area (for example the minimum unity surface of the building according to cities or regions regulations). Each cluster is

framed by a rectangle, to delimit the boundary between one cluster and another.

The flowchart presented in Figure 4.4 describes the third part of the methodology, which is the procedure for the preliminary SHM and ranking of the critical constructions in a built environment.

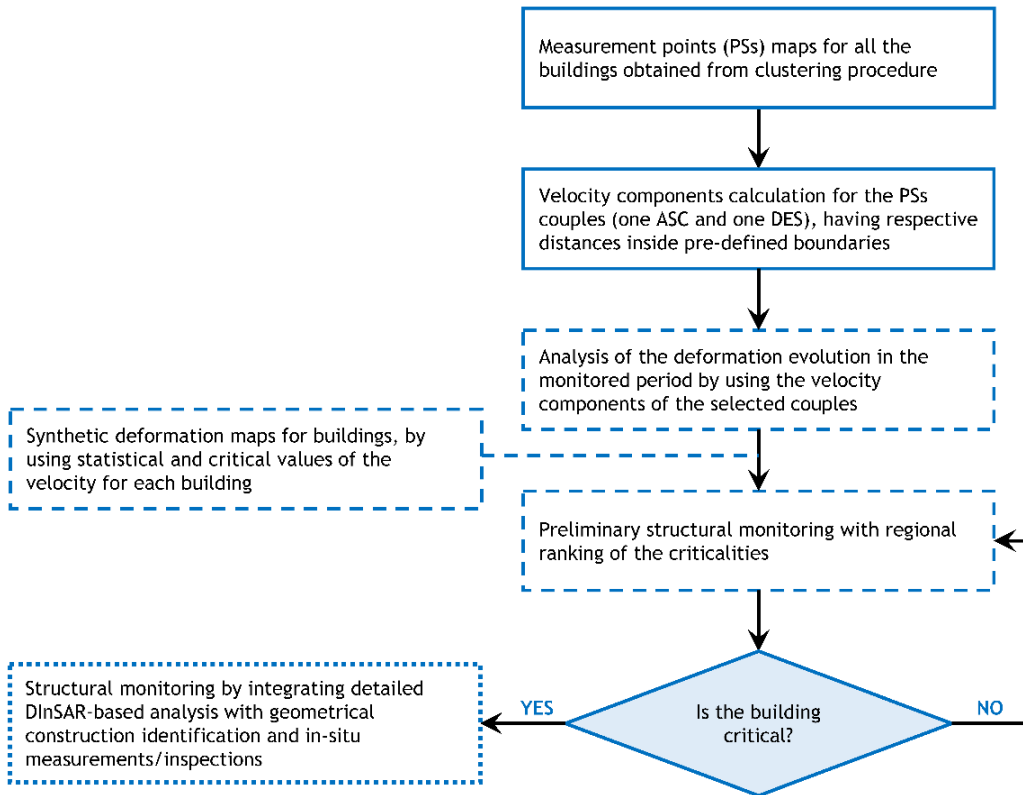


Figure 4.4. Flowchart of the operations for the preliminary identification and ranking of critical constructions [36].

The first part of the flowchart for the preliminary SHM is shown in the continued blue boxes in Figure 4.4. For each building, each cluster is subdivided into two sub-groups, according to the fundamental features (ASC and DES orbits). The relative distances between all the ASC and DES PSs of each cluster are analyzed. Only the couples of points constituted by one ASC and one DES PS,

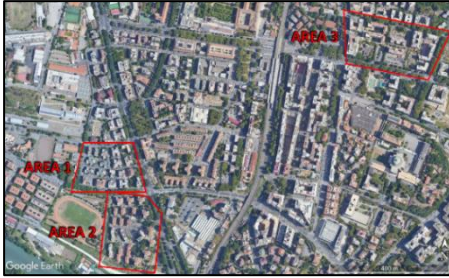
having planimetric and altimetric distances less than the values of error reported in §2.3.1, at once, are considered for the next steps. For the selected couples, the values of the mean velocity components V_V and V_{EW} are calculated according to §3.2 and plotted using a symbology with graduated colors. The values of V_V and V_{EW} are associated to a new point, spatially located in a mean position with respect to the original PSs forming the pair.

Then, the second step regards the analysis of the deformation evolution in the monitored period by using the mean velocity components of the selected couples with the goal of providing preliminary structural monitoring through the ranking of the criticalities (blue dashed box of the flowchart in Figure 4.4). In this phase, some statistical values of the mean velocity components are recognized in each cluster: the maximum ($V_{V,max}$ and $V_{EW,max}$), the minimum ($V_{V,min}$ and $V_{EW,min}$) and the mean velocity weighted on the values of the temporal coherence. Moreover, the maximum ($V_{V,max}$ and $V_{EW,max}$), and the minimum ($V_{V,min}$ and $V_{EW,min}$) values allow to understand if the building is interested by differential displacements and to estimate the differential mean velocity amount in the considered direction. The resulting components maps are a very useful tool to easily identify the buildings most affected by displacements, and to identify critical situations if existing. Generally, once the most exposed buildings are identified, the third phase can be activated for them (blue dotted box of the flowchart in Figure 4.4). In this phase, it is important to combine on-site information for the single critical building or the entire area (traditional measurements and geometrical and structural relief of the buildings) with more building-specific DInSAR measurements.

4.1.2 Applications in Rome

The three case study areas are part of the municipality of Rome (Italy), which is entirely interested in extensive multi-temporal interferometric processing [9], [31], [38], [42], [45], [47], [71]. The PSs used in the present applications, derived by the full resolution SBAS-DInSAR approach applied to two sets of SAR images collected from 2011 to 2019, from ASC and DES CSK orbits, have been described

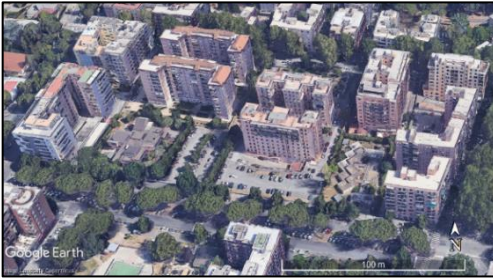
in §2.3.1. The areas differ each from the other for many characteristics: width (m²), number of buildings, planimetric shape, and number of floors of the buildings (Figure 4.5).



(a) Identification of Areas 1, 2 and 3



(b) Area 1 – 19 buildings



(c) Area 2 – 12 buildings



(d) Area 3 – 20 buildings

Figure 4.5. Areas chosen for the algorithm performance: (a) top view, (b) Area 1, (c) Area 2, (d) Area 3 (source: *Google Earth Pro*) [36].

The distributions of the frequency of all the PSs δ for the three areas are shown in Figure 4.6, Figure 4.7, and Figure 4.8. In this study, a reasonable value of 30% has been set as the limit of frequency variation. For Areas 1 and 3, a decreasing of frequency greater than 30% can be observed between 2 – 4 m and 4 – 6 m, while for Area 2 it happens between 4 – 6 m and 6 – 8 m. A resume of the topography values considered for each area is reported in Table 4.1. With δ limit it is indicated the value under which the PSs are neglected for the clustering, obtained by summing to the ground level measure δ the standard deviation ($\sigma = \pm 2$ m) and the supposed height of 1-floor buildings (3.50 m).

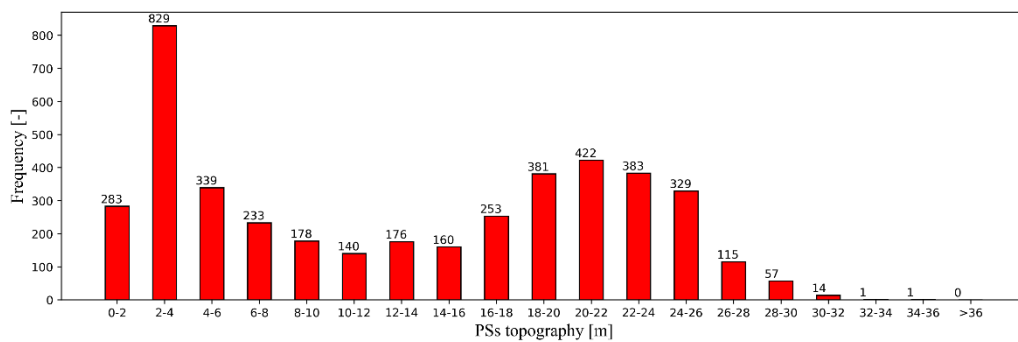


Figure 4.6. Frequency of PSs topography distribution, Area 1 [36].

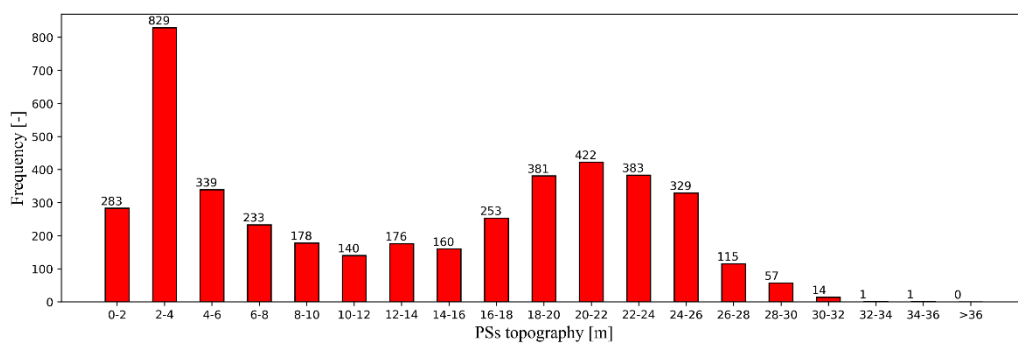


Figure 4.7. Frequency of PSs topography distribution, Area 2 [36].

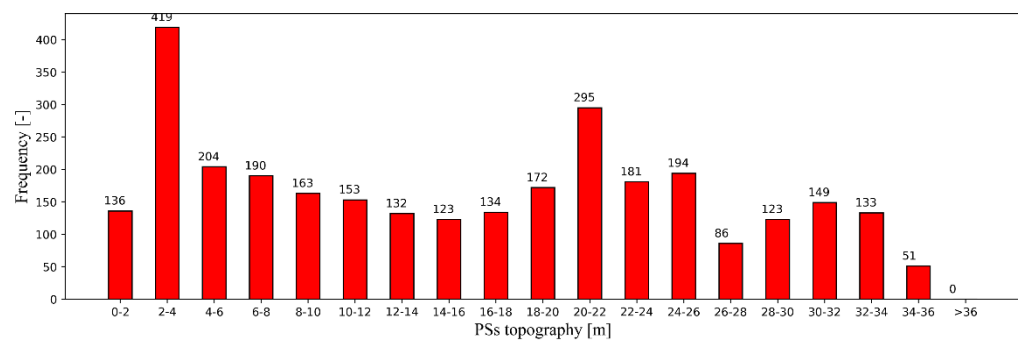


Figure 4.8. Frequency of PSs topography distribution, Area 3 [36].

Table 4.1. Topography ground level δ , and δ limit values.

Area number [-]	Ground level δ [m]	δ limit [m]
1	2.59	8.09
2	2.78	8.28
3	2.64	8.14

For all the areas, the minimum sample value *minPoints* has been set at 4, since the dataset used in this work has 2 dimensions. As regards *eps*, the approach mentioned in §4 has been implemented for the three areas. The results are shown in Figure 4.9, Figure 4.10, and Figure 4.11, both in terms of plots of the mean of the distances between each point and its k^{th} nearest neighbor, sorted in ascending order and reporting the information needed to find the *eps*: the numbers of ASC and DES PSs, and their sum (tot. PSs), the area, the PSs density (PSs/m²), the boundaries k_{inf} and k_{sup} , and, finally, the optimal value for neighborhood radius *eps*. The latter has been estimated as the mean of the ordinates of the maximum curvature points (represented with red circular markers) referred to each curve, given by a value of k included in the interval $[k_{inf}; k_{sup}]$. According to §4, the ends of this interval are estimated based on a PSs density obtained by dividing the number of PSs for the area occupied by buildings, approximately the 50% of the total area, for the case study areas. Then, k_{inf} has been obtained by multiplying the number of PSs in a m² for the minimum unity surface, set at 28 m² in this case, according to the Italian D.M. 05/07/1975 [102]. The value of k_{sup} , indeed, has been evaluated taking into count that the greater distribution is generally on the roof, and other PSs can be found on the facades, so herein a mean area of the buildings is estimated to be 250 m².

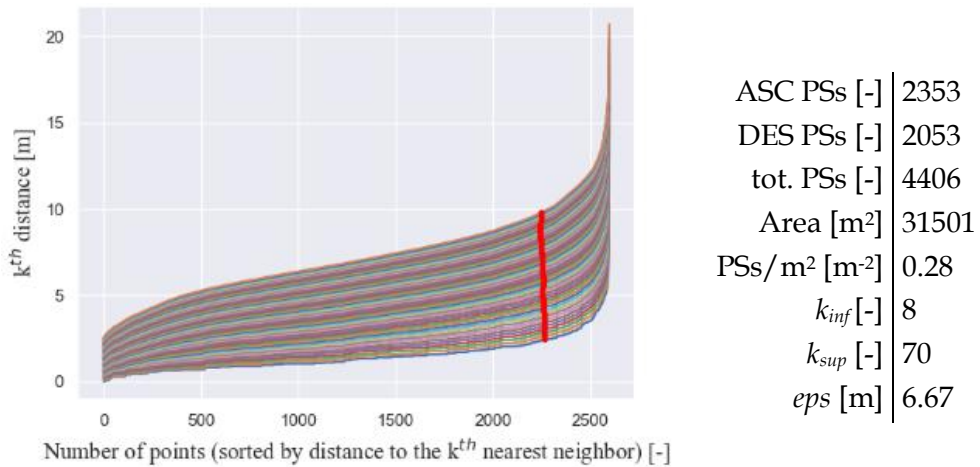


Figure 4.9. Points sorted by distance to the k^{th} nearest neighbor, Area 1 [36].

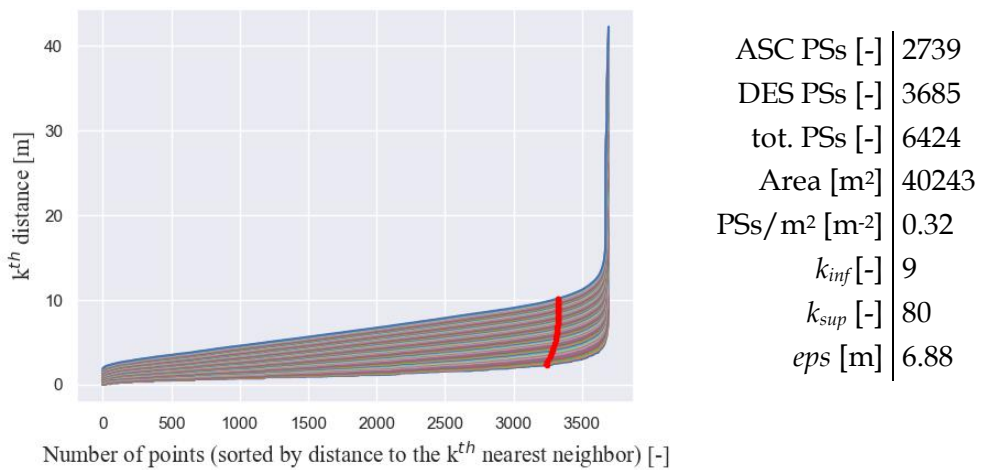


Figure 4.10. Points sorted by distance to the k^{th} nearest neighbor, Area 2 [36].

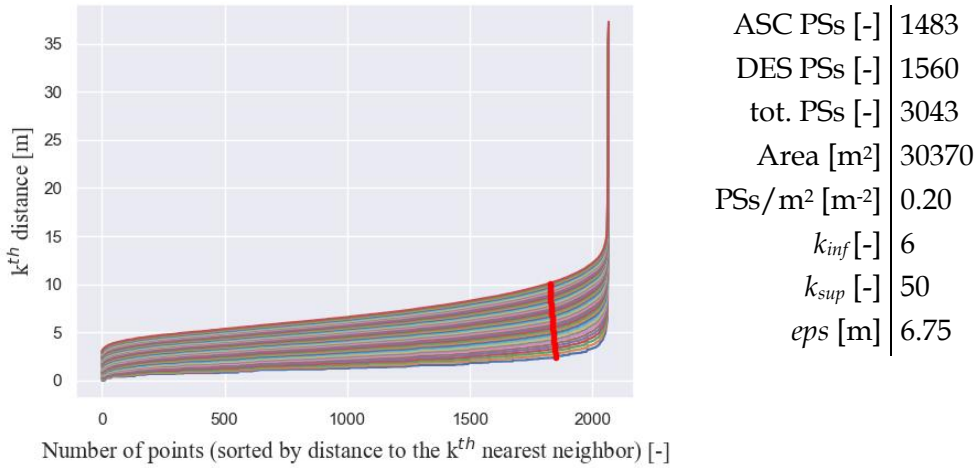


Figure 4.11. Points sorted by distance to the k^{th} nearest neighbor, Area 3 [36].

The optimal values obtained for eps are very similar for the three areas. These values are very close to the minimum distance between the buildings. Then, in absence of such analysis, for urban areas with similar features, an eps value between 6 and 7 m could be suggested.

In Figure 4.12, Figure 4.13, and Figure 4.14, the comparisons between the original PSs datasets distribution in the three areas and the clustering results, are proposed. In Figure 4.12a, Figure 4.13a, and Figure 4.14a, the buildings' footprints are marked with a black shape. There are 19 buildings in Area 1, 12 buildings in Area 2, and 20 buildings in Area 3. Moreover, the PSs, distributed all over the areas, marked with red circles for ascending PSs and green circles for descending PSs, are shown. In Figure 4.12b, Figure 4.13b, and Figure 4.14b, the results of the clustering are reported, where each cluster has been delimited by a rectangle. The clustering results have highlighted that the procedure is very performant. Each building having more than one floor is identified by a cluster. The only exception is represented by the one-floor manufact of Area 2, which is not included in the clustering results due to the additional δ considered for the height cut, aimed to avoid noise PSs (belonging to the ground), as previously exposed.

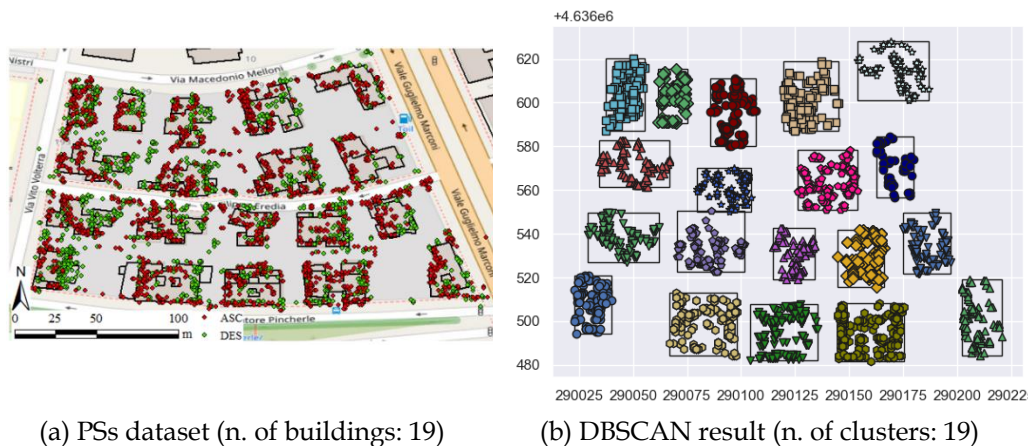


Figure 4.12. Area 1: (a) top view of ASC and DESC PSs, (b) clustering obtained through DBSCAN [36].

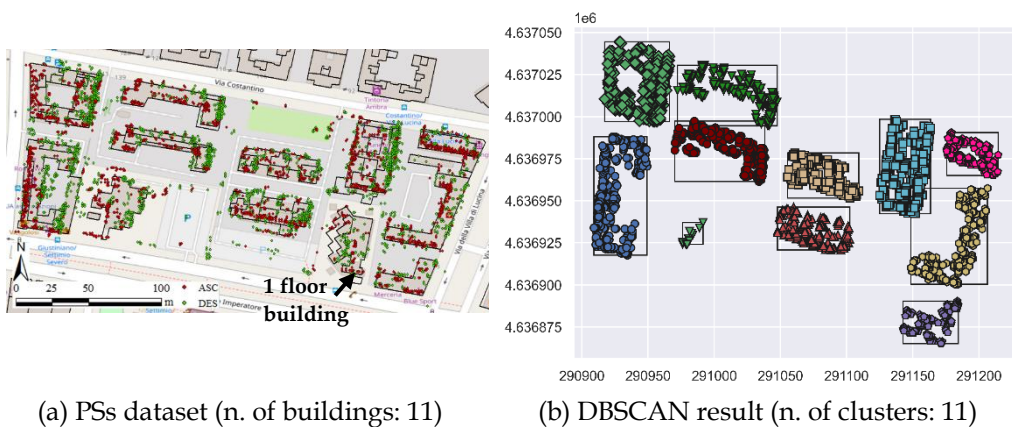
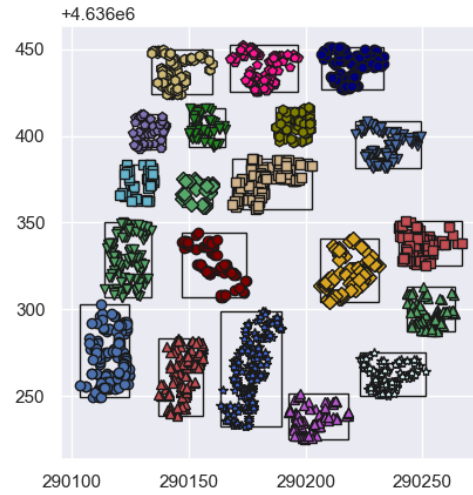


Figure 4.13. Area 2: (a) top view of ASC and DESC PSs, (b) clustering obtained through DBSCAN [36].



(a) PSs dataset (n. of buildings: 20)



(b) DBSCAN result (n. of clusters: 20)

Figure 4.14. Area 3: (a) top view of ASC and DESC PSs, (b) clustering obtained through DBSCAN [36].

In Figure 4.15, Figure 4.16, and Figure 4.17, the maps of V_V and V_{EW} are shown. The symbology has graduated colors ranging from dark red (downwards and West-directed displacements, respectively) to dark blue (upwards and East-directed displacements, respectively). The green points are representative of stable areas, not affected by displacements.

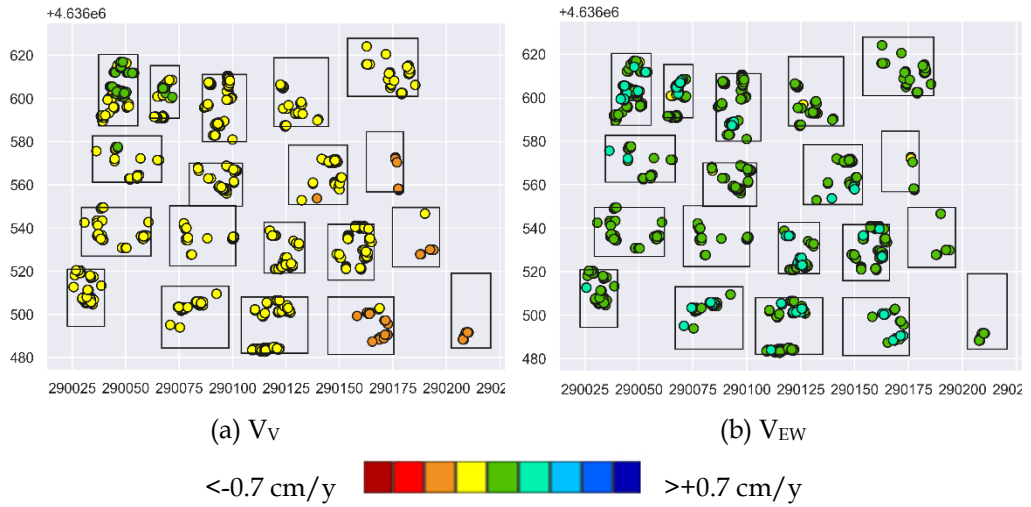


Figure 4.15. Area 1: (a) mean velocity Vertical component and (b) mean velocity East-West component for the combinable pairs of PSs [36].

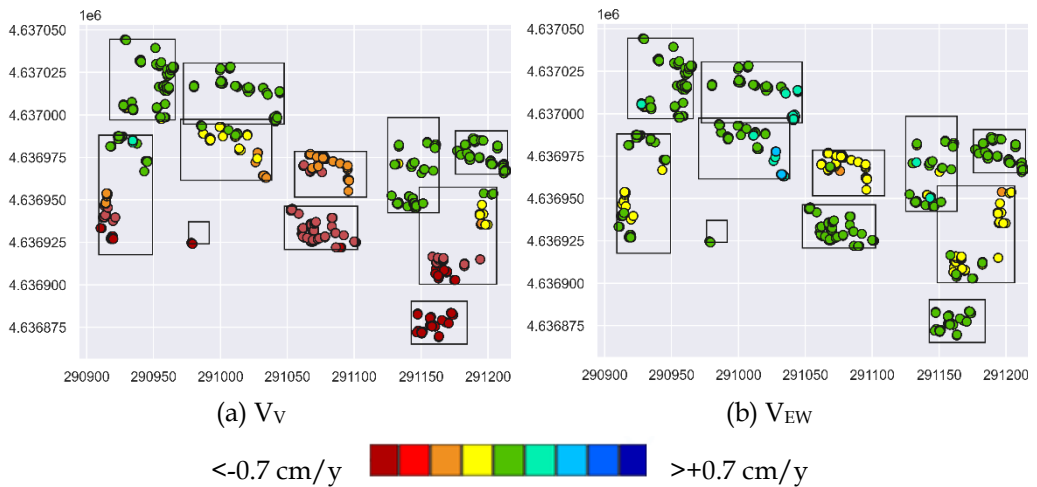


Figure 4.16. Area 2: (a) mean velocity Vertical component and (b) mean velocity East-West component for the combinable pairs of PSs [36].

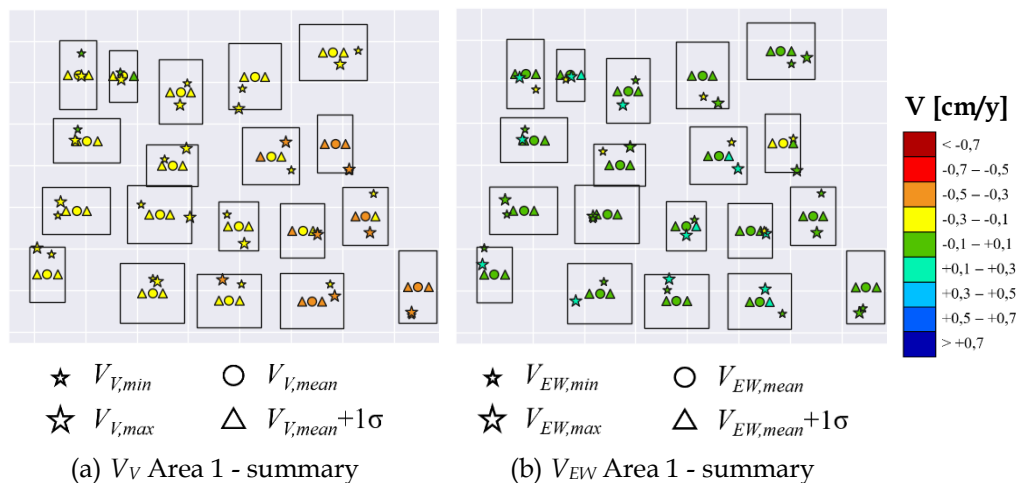


Figure 4.18. Summary maps for Area 1: graphical representation of the meaningful values of (a) mean velocity Vertical components and (b) mean velocity East-West components, for each cluster [36].

Also in Area 2, an even more clear ongoing deformation phenomenon can be observed (Figure 4.19). The vertical component is the prevailing one, with downward movements, but the EW component is not negligible in some buildings. The buildings most affected by the vertical deformation phenomenon are those of the Southern zone, that reaches values of V_V also lower than $-0,7$ cm/y. Significant displacements can also be observed on some buildings. For example, in the second building on the right, starting from the bottom, the vertical component increases from North to South, while, on the contrary, the EW component decreases from North to South. It is even more evident looking at the summary maps. The examined building, in fact, presents a $V_{V,min}$ in the green range ($[-0,1 - +0,1]$ cm/y) on the North-East side, and a $V_{V,max}$ in the dark red range ($[<-0,7]$ cm/y) on the South side. In the EW direction, it presents a $V_{EW,min}$ in the orange range ($[-0,5 - +0,3]$ cm/y) on the North-East side, and a $V_{EW,max}$ in the green range ($[-0,1 - +0,1]$ cm/y) on the South-West side.

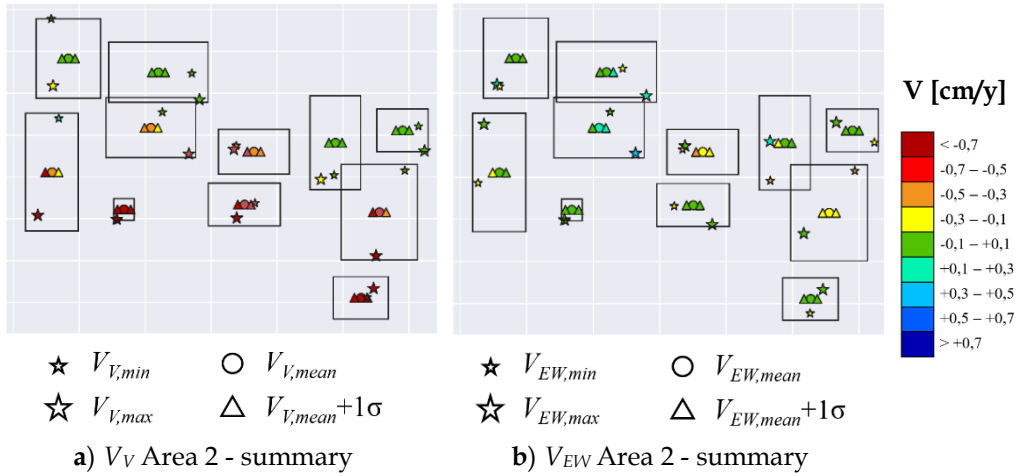


Figure 4.19. Summary maps for Area 2: graphical representation of the meaningful values of (a) mean velocity Vertical components and (b) mean velocity East-West components, for each cluster [36].

Finally, Area 3 presents the worst vertical ongoing deformation phenomenon among the three areas, while the EW component is quite negligible (Figure 4.20). Among each building, the mean velocity components are quite homogeneous, so they are not supposed to suffer from differential deformations.

The prevailing vertical mean velocity trend detected in the three areas is imputable, probably, to subsidence or consolidation phenomena [9].

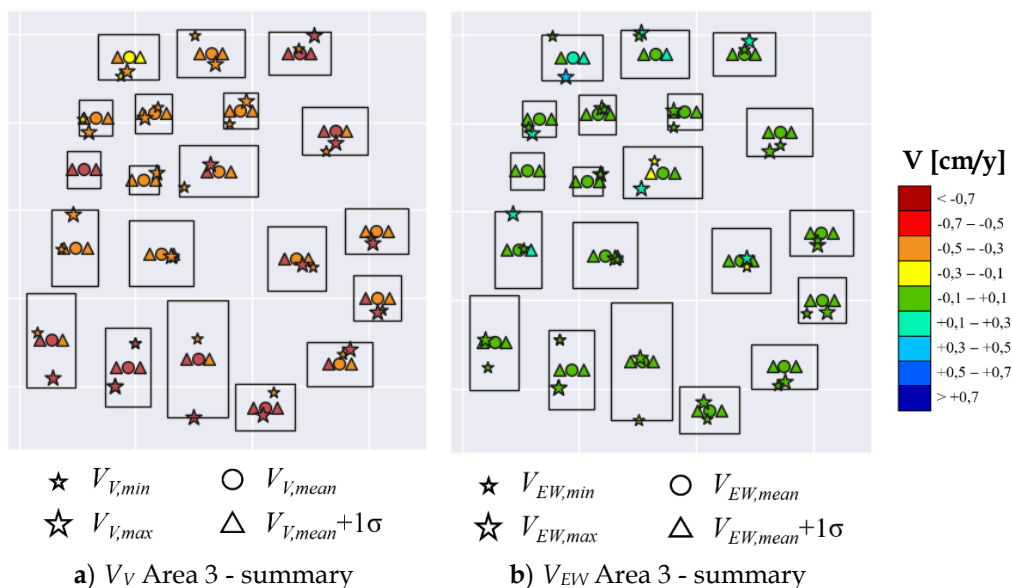


Figure 4.20. Summary maps for Area 3: graphical representation of the meaningful values of (a) mean velocity Vertical components and (b) mean velocity East-West components, for each cluster [36].

A validation of the results can be found in Mele et al. (2022) [36].

4.1.3 Discussion

The proposed methodology gives maps with all the buildings of the area, identified by a cluster, whatever its deformation condition is. It is possible to distinguish stable buildings from those affected by significant displacements (defined as “critical”) by observing the maps, through the color scale, but all the buildings are represented, to have a framework of the total situation in the monitored built area.

The conditions that make a building defined as critical can be related to several considerations correlated to many factors of an investigated zone (e.g., the geology of the area, ongoing deformation phenomena in the entire area, widespread structural typologies, average construction age of the buildings, etc.).

However, exploiting the complete pattern of the mean velocity trends of all the buildings in the monitored area, differential “attention” thresholds could be imposed regarding: i) a building showing mean velocity values greater than those of the buildings around; ii) a change in the mean velocity trends of many parts of a building over the observation period; iii) building sides affected by differential displacements.

Then, once the critical buildings are identified, further and more in-depth investigations should be performed at a detail scale, as will be discussed in §5.

One of the limits of the proposed methodology is its inability to sharply distinguish single building units when they are built in. Other than isolated buildings, in urbanized areas, it is very common to find two or more buildings, with a common wall or separated only by a seismic joint. It is worth noting that the proposed approach does not allow to distinguish single units, but, in the above-mentioned cases, the structural aggregate is considered as a single “building”. From a structural point of view, if two buildings have a common wall or common structural foundations, they constitute a single structure. In this case, no approximation subsists in the methodology. When two buildings are separated by a seismic joint, instead, they have completely different structural behaviors and do not interact with each other. In this case, it is not possible to distinguish buildings so close through the input satellite data, and an approximation is done. So, if the output clusters are very large it is suggested to focus on it to understand if it is a single building, an aggregate, or joined buildings, to make appropriate considerations for the specific case. Another limitation of the proposed methodology is the difficulty in identifying the clusters referred to one-floor buildings since they are classified as noise in order to avoid the creation of false clusters, as explained in §4. This assumption is necessary since it strengthens the correct identification of the two-to-n floors buildings, by eliminating any interaction with the ground points. Nevertheless, it eliminates the possibility to identify one-floor buildings and some very few points of the n-floors buildings’ facades. This limit could be exceeded by integrating the proposed clustering algorithm with an additional clustering, to execute by opportunely setting the cut on δ and the *eps*. For example, the clustering could be repeated excluding only the PSs supposed to be on

the ground. Then, the new clusters, not overlapping those obtained through the first clustering, should be added to the previous result. Maybe, in some cases, this second clustering could also help in finding a more refined shape of the two-floor buildings, since some points can be excluded in the initial cut, as a consequence of the topographic error. However, it is worth noting that it is very rare to find one-floor buildings in very urbanized areas (in fact, as it has been shown in this work, only one has been found in three areas). Then, neglecting them in a preliminary phase is not a very strong limitation.

Finally, it is worth specifying that the clustering result is quite sensitive to small hyper-parameters changes, so the latter should be set with attention.

4.2 ADAfinder tool for SHM of urban settlements

ADAfinder tool is one of the four modules, called *ADAtools* [27], [103], [104], aimed at the semi-automatic extraction and preliminary analysis of Active Deformation Areas (ADA) starting from PSI-derived deformation maps. In particular, the *ADAfinder* tool has the main objective of identifying the ADA in the area of interest, starting from a dataset of PSs. An application that highlights its potential can be found in Tomás et al. (2019) [105].

For the first time, we focused our study on the applicability of *ADAfinder* tool in urban areas, including other engineering parameters in the flowchart of the methodology, intending to identify the buildings affected by displacements above a given threshold, among all the buildings included in the investigated area. Such buildings are recognized, and their study could be deepened, for example, through surveys or the installation of on-site monitoring systems. The identification of a cluster of deforming buildings may also be due to a deformation phenomenon related to a larger portion of the area, which may be identified by such analysis.

The proposed methodology is explained in detail in §4.2.1. Two case study areas including distinct typologies of buildings (characterized by different materials, dimensions, and structural schemes) have been considered (§4.2.2), in order to show the potential of the proposed methodology applied to different kinds of

urban settlements. The first one is part of the *Eixample* neighborhood, while the second one is part of the industrial area near the harbor, known as *Zona Franca* (§4.2.2.1 and §4.2.2.2, respectively). The PSs used in the applications are derived from the EGMS, which principles are illustrated in §2.3.3.

This research work has merged into the work of Mele et al. 2022 [106].

4.2.1 Proposed methodology

A flowchart of the proposed methodology is shown in Figure 4.21.

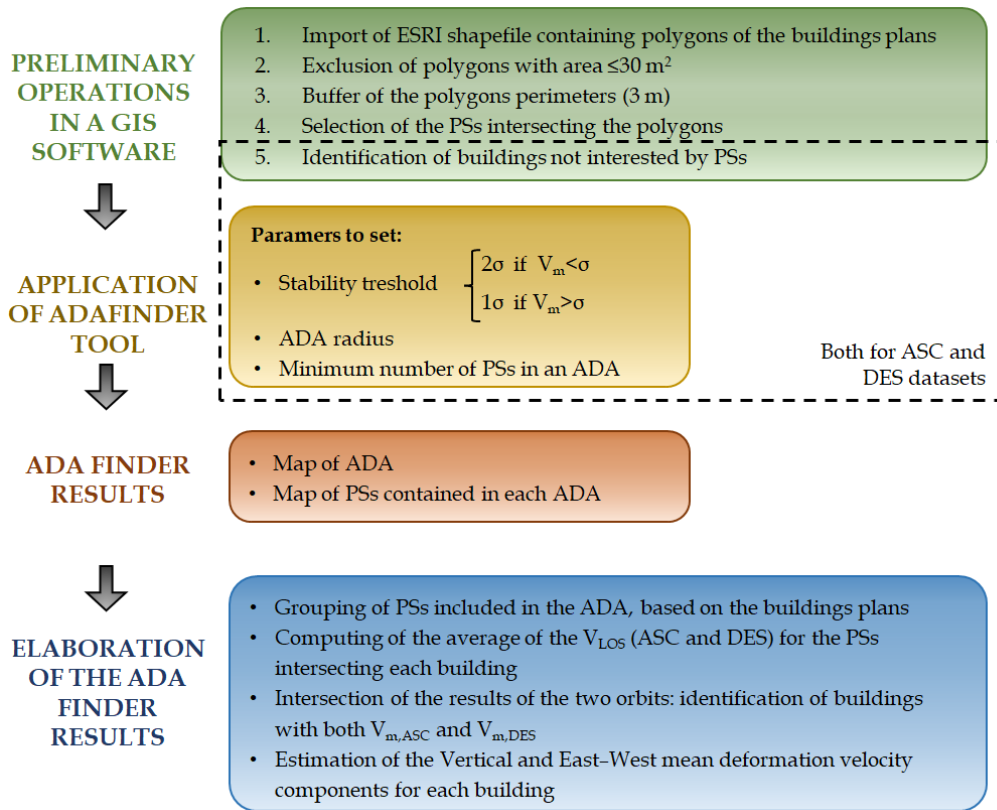


Figure 4.21. Flowchart of the proposed methodology (modified from [28]).

The necessary data to implement the procedure are i) an *ESRI shapefile* containing the polygons of the building plans and ii) the two datasets referred to ASC and DES orbits, containing information about the PSs of the monitored area. The information necessary for each PSs are coordinates, mean velocity (expressed in mm/year), and deformation time series in the period of interest.

Since the proposed methodology is dedicated to data processing for SHM, preliminary operations should be done (listed in the green box of the flowchart) to filter the PSs datasets to direct the procedure towards the analysis of ADAs only on the buildings. For this reason, a filter is made on the polygons: those having an area in the plan lower than 30 m² are excluded since they are not considered to be buildings. In fact, sometimes, other little elements can be included in the available shapefiles, for example, cabins, canopies, small buildings, silos, or containers in harbor areas. Then, a buffer of the perimeters of the polygons is done, to consider the inaccuracies that they might have. Since the presented methodology is focused on the buildings, all the PSs related to any other construction or reflective target must be discarded. For this reason, a selection of the PSs intersecting the polygons (including the buffer previously mentioned) is done, while the buildings not intersected by PSs are identified and pointed out. This operation is separately done using both the ASC and DES datasets.

The following step is the application of the ADAfinder tool (yellow box of the flowchart). The “stable” PSs, defined as points having a mean velocity lower than a fixed “stability threshold”, according to the standard deviation (σ) of the velocities of all the PSs of the dataset (V_{LOS}), are removed. A criterion to establish the value of the stability threshold is to compare the average value of the V_{LOS} of the dataset of PSs, V_m , with the relative σ . In particular, the stability threshold is set at 2σ if $V_m < \sigma$, while it is set at 1σ if $V_m > \sigma$. This comes from the consideration that a higher value of V_m can induce to consider more constructions in the monitoring phase and then a lower threshold value can be fixed. Moreover, the first case usually verifies in large areas with different deformation processes included, so a great dispersion of the V_{LOS} values can be detected and a cut at 2σ is more convenient to exclude the lower deformation values. In the second case, on the contrary, the values of V_{LOS} are greater, and a trend of deformations more or

less defined is present, so it is convenient to keep a larger number of PSs. Also, the PSs with no other PSs around included within a defined distance, named “isolated” are removed. Moreover, the ADA radius (in meters) should be set, and the minimum number of PSs in an ADA must be imposed. In the proposed methodology, it is recommended to set the minimum number of PSs equal to the minimum value accepted by the tool, that, in the current version (ADAtools 2.0.3), is 3. The operation described until this step must be carried out both for the ASC and the DES datasets.

Then, for both orbits, the results of the ADAfinder tool are obtained (orange box of the flowchart), consisting of two maps: one with the ADA (a polygonal *ESRI shapefile*), and one with the PSs contained in each ADA (a point *ESRI shapefile*). These products are spatially superimposed to the polygons of buildings, obviously, as they are obtained from the PSs previously selected based on them.

Finally, the ADAfinder results are managed and elaborated to obtain the definitive maps with information reclassified according to the buildings, following the steps listed in the blue box of the flowchart. First of all, each PS is associated with the ID of the building in which it falls. In this way, two groups of “unstable” PSs are recognized for each “unstable” building (one group for each orbit). Then, the average values of the V_{LOS} of the two groups (ASC and DES) of PSs belonging to each building are computed, separately for each building. In this way, finally, only two values of V_{LOS} are associated to each building, representing the average of the mean velocity along the LOS of the unstable PSs falling on the building itself: one along ASC ($V_{m,ASC}$) and one along DES ($V_{m,DES}$) orbits. At this step, an intersection of the results deriving from the ASC and DES datasets is performed, to identify the buildings overlapped by at least one ADA from the ASC and one ADA from the DES dataset. The buildings not having both ASC and DES information are excluded from the following steps of the procedure since the availability of both orbits is necessary for the estimation of the Vertical and EW mean velocity components (see §3.2). Then, the Vertical and EW components of the mean velocity for each building are estimated according to the formulas described in §3.2.

The steps of the illustrated methodology can be implemented by combining simple operations to execute in QGIS and algorithms written in a code language (e.g., Matlab).

It is important to underline that the lack of ADA could be related not only to the absence of active deformation but also to the absence of PSs [107]. The ESRI shapefile containing polygons of the building plans has been downloaded from *OpenStreetMap* [108].

4.2.2 Applications in Barcelona

Two applications of the proposed methodology explained in §4.2 are reported in §4.2.2.1 and in §4.2.2.2, about a portion of the Eixample city center and of the industrial area Zona Franca, respectively. The two case study areas are very different for the building typologies included. The PSs used in the applications are extracted from the maps of calibrated products downloaded by the EGMS, shown in §2.3.3 (Figure 2.18 and Figure 2.19 for ASC and DES orbits, respectively), in the area of Barcelona.

4.2.2.1 Application – Eixample

Eixample is a district that occupies the central part of the city of Barcelona (Spain), in an area of 7,45 km². It was built in the second half of the XIX century based on the design of Ildefons Cerdà. The area is conceived as a regular pattern formed by quadrangular blocks of 113,30 m per side (that occupy an area of about 12500 m² each), trunked on the vertices with a bevel of 15 m, and separated by a regular pattern of avenues. The blocks are constituted by adjoining buildings, mainly jointed, predominantly in masonry, with an average height of 30 m. For the following application, an area of 0,45 km² has been selected, where the blocks are also crossed by the *Avinguda Diagonal*.

The distribution of the PSs in the Eixample district is shown in Figure 4.22 a and b, for ASC and DES orbits, respectively. In Table 4.2 the statistics of the V_{LOS} of the PSs in the selected area are reported. It can be observed that the ASC PSs

are more than the DES ones (almost 50% more), and that for both the datasets the V_m is lower than the σ . The different number of PSs is probably due to the different viewing geometry of ASC and DES. The values of the V_{LOS} in this area are not significantly high, so the area can be considered stable. It is worth underlining, in fact, that this area has been chosen for the configuration of the included constructions, and not for the entity of their deformation.

As mentioned before, the Eixample is characterized by the presence of adjoining buildings with a small surface. In fact, about 90% of the total number of buildings have an area lower than 1000 m². In this case, over a total of 540 buildings, 524 are covered by at least 1 ASC PS and 532 are covered by at least one DES PS. However, all the buildings except two are covered by a number of PSs greater than 4. In Table 4.3 a summary of the number of monitorable buildings is reported. With respect to the total number of buildings, 4% of them are not covered by both ASC and DES PSs in this area of the Eixample.

Table 4.2. Statistics of the mean velocity of the selected area of Eixample [28].

	Count	Minimum V_{LOS}	Maximum V_{LOS}	V_m	σ
Ascending	6389	-7.30	6.60	0.11	0.82
Descending	4347	-6.20	7.30	0.15	0.94

Table 4.3. Summary of the number of buildings in Eixample area [28].

	Eixample
Total number of buildings	540
% of buildings with no ASC PSs	3%
% of buildings with no DESC PSs	1%
% of monitorable buildings	96%

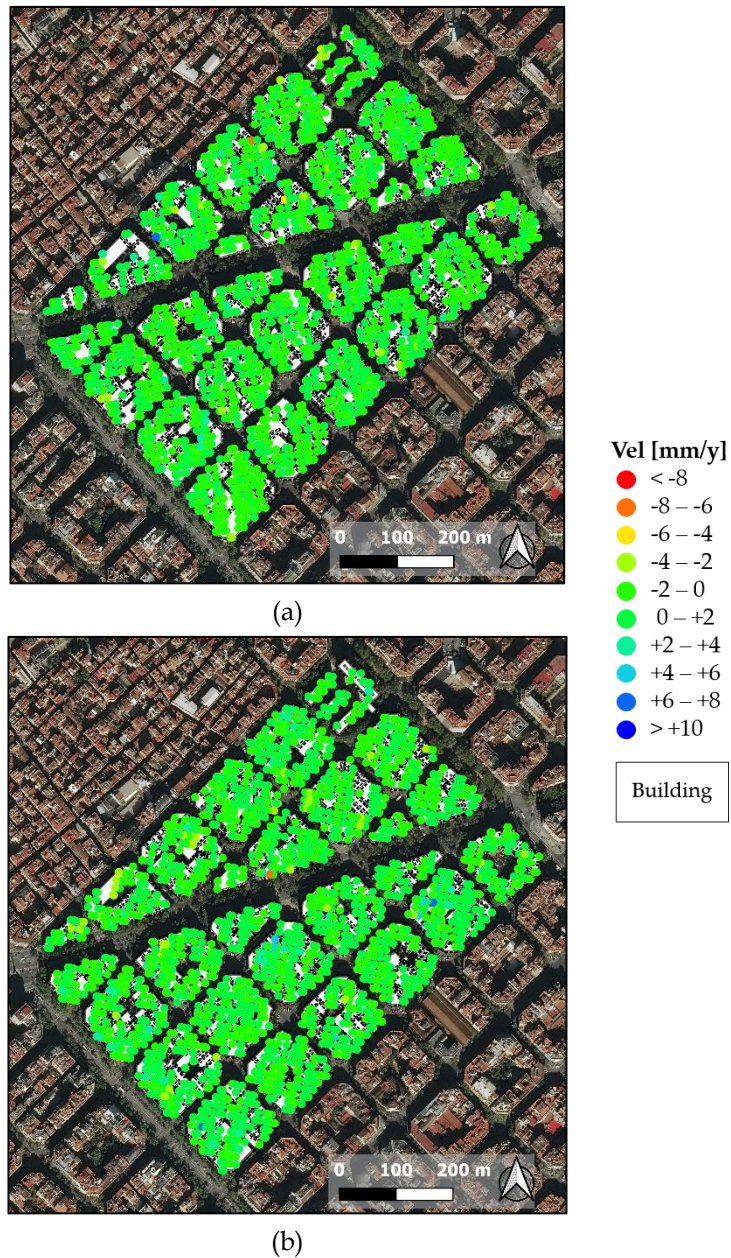


Figure 4.22. Distribution of the selected PSs on the buildings of the selected area of Eixample: (a) ASC and (b) DESC [28].

Figure 4.23 shows the extracted ADA for both orbits. The polygons and the “active” PSs are represented, where the definition of “active” depends on the stability threshold, which is area-dependent. In general, the stability threshold has been set at 2σ , in accordance with what is explained in §4.2.1. Moreover, the ADA radius has been set at 25 m and the minimum number of PSs to be included in an ADA has been fixed to 3. It can be observed that the number of PSs over the areas is greatly reduced with respect to the input datasets (in Figure 4.22). Only 75% of ASC and 37% of DES PSs are preserved. In Table 4.4 the statistics of the V_{LOS} of the active PSs are reported. The percentage of buildings included in an ADA is 54% for ASC and 53% for DES orbit.

Table 4.4. Statistics of the mean velocity of the active PSs in the selected area of Eixample [28].

	Count	Minimum V_{LOS}	Maximum V_{LOS}	V_m	σ
Ascending	4800	-7.30	6.90	0.12	1.06
Descending	1624	-6.20	7.30	0.15	1.28

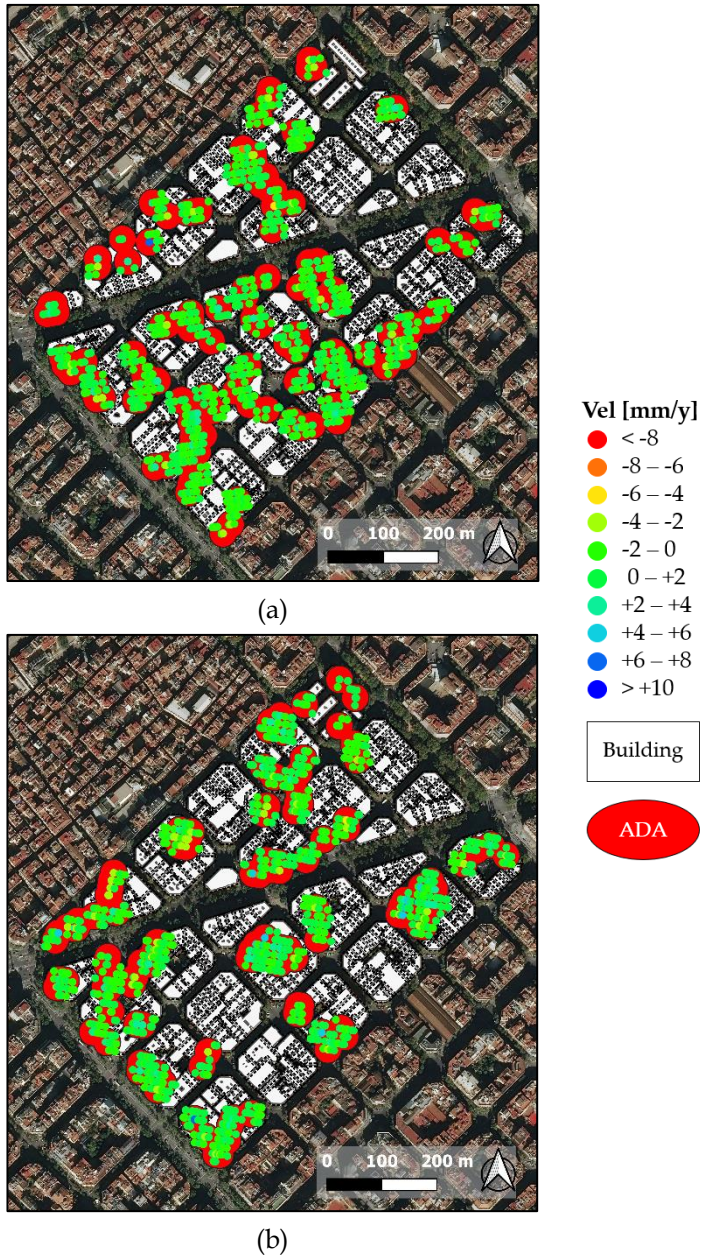


Figure 4.23. ADA extraction from the active PSs of the selected area of *Eixample* from (a) ASC and (b) DESC datasets [28].

The maps of $V_{m,ASC}$ and $V_{m,DES}$ estimated for each building are shown in Figure 4.24. The buildings characterized by a lack of PSs are covered by violet polygons. The number of PSs used to compute the average $V_{m,ASC}$ and $V_{m,DES}$ for each building is important because the more points there are, the more reliable the measurement can be. For Eixample, this number varies between 2 and 82 for ASC and between 1 and 37 for DES. The upper bound is a function of the dimension of the building surface.

The maps of the Vertical and EW components of the mean velocity are respectively shown in Figure 4.25. In these final maps, the union of the buildings characterized by a lack of PSs in the original datasets is marked with violet polygons. The final number of monitored buildings is 140. The mean velocity component maps remark that this portion of Eixample area is stable.

A focus on one of the quadrangular blocks of the Eixample is reported in Figure 4.26 a and b for ASC and DES PSs, respectively.

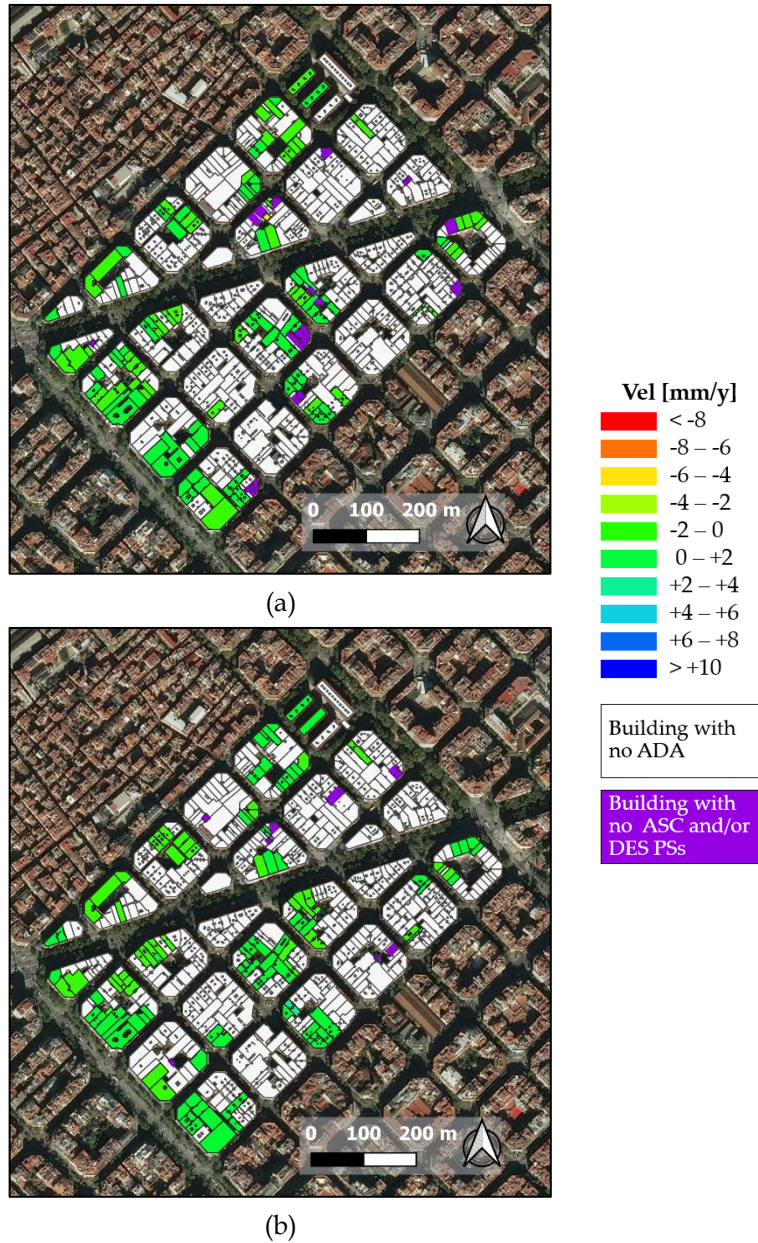


Figure 4.24. Maps of buildings in Eixample area having an average value of mean velocity along (a) ASC and (b) DESC orbit [28].

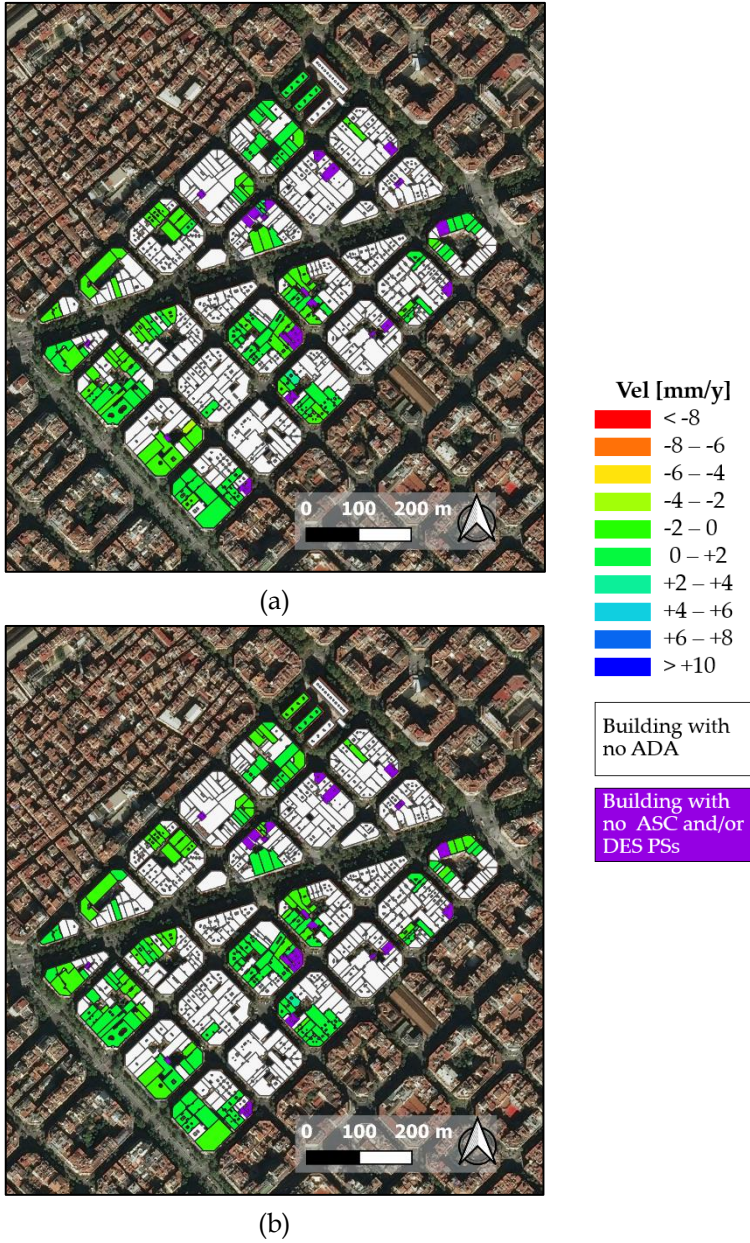


Figure 4.25. Maps of (a) V_{EW} and (b) V_V components for the “unstable” buildings in Eixample area [28].

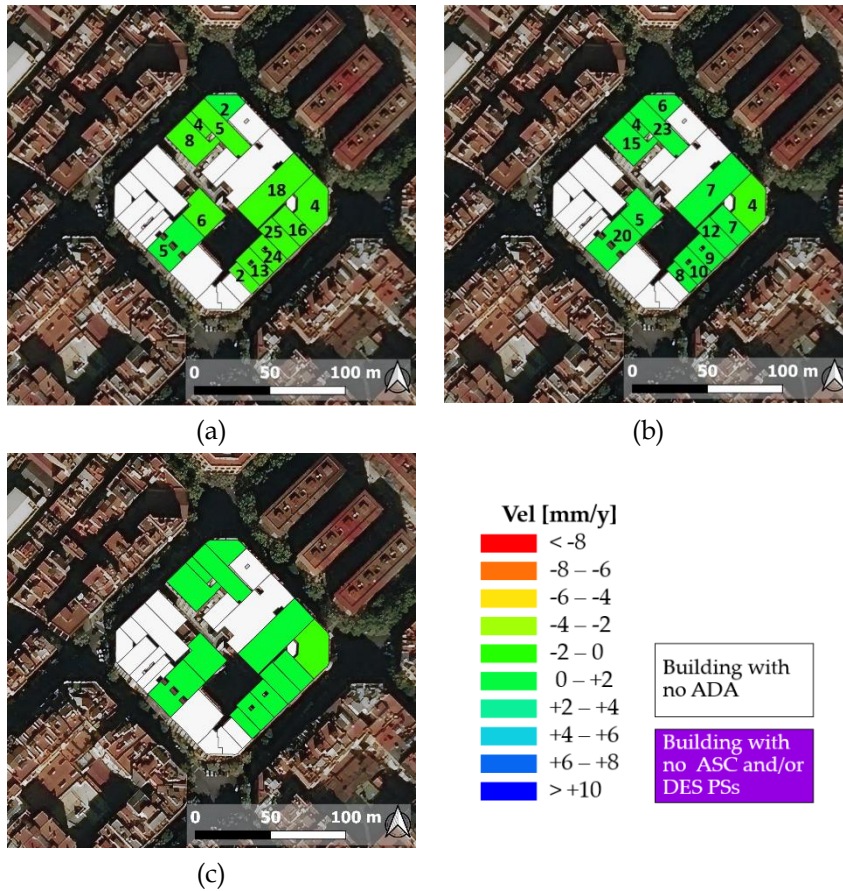


Figure 4.26. Maps of average values of mean velocity along (a) ASC and (b) DESC orbit for one of the quadrangular blocks of the Eixample and (c) map of $V_{EW/V}$ components for one of the quadrangular blocks of the Eixample. The labels indicate the number of PSs used to compute the average mean deformation velocities for each building [28].

4.2.2.2 Application – Zona Franca

Zona Franca is a very large logistics and industrial area located in the *Sants-Montjuïc* district of Barcelona, near the harbor and the airport. This area was used for the construction of several factories during the industrialization period of Catalonia, in the middle of 1900. It is completely different for the Eixample, since the constructions in this area are predominantly large sheds with plan roofs,

located without a planned scheme. An area of 17 km² of Zona Franca has been selected for the following application.

The distributions of the PSs in the area of the Zona Franca district are shown in Figure 4.27 a and b, for ASC and DES orbits, respectively. In Table 4.5 the statistics of the V_{LOS} of the PSs in the selected area are reported. Also in this case, it can be observed that the ASC PSs are many more of the DES ones (about 75% more), and that for both the datasets the V_m is lower than the σ . The values of the V_{LOS} in this area are greater, reaching, for example, -10.5 mm/y in moving away from the satellite along the ASC LOS. In particular, the greatest deformations can be observed in the southern part of the area, while the central and upper regions appear to be stable.

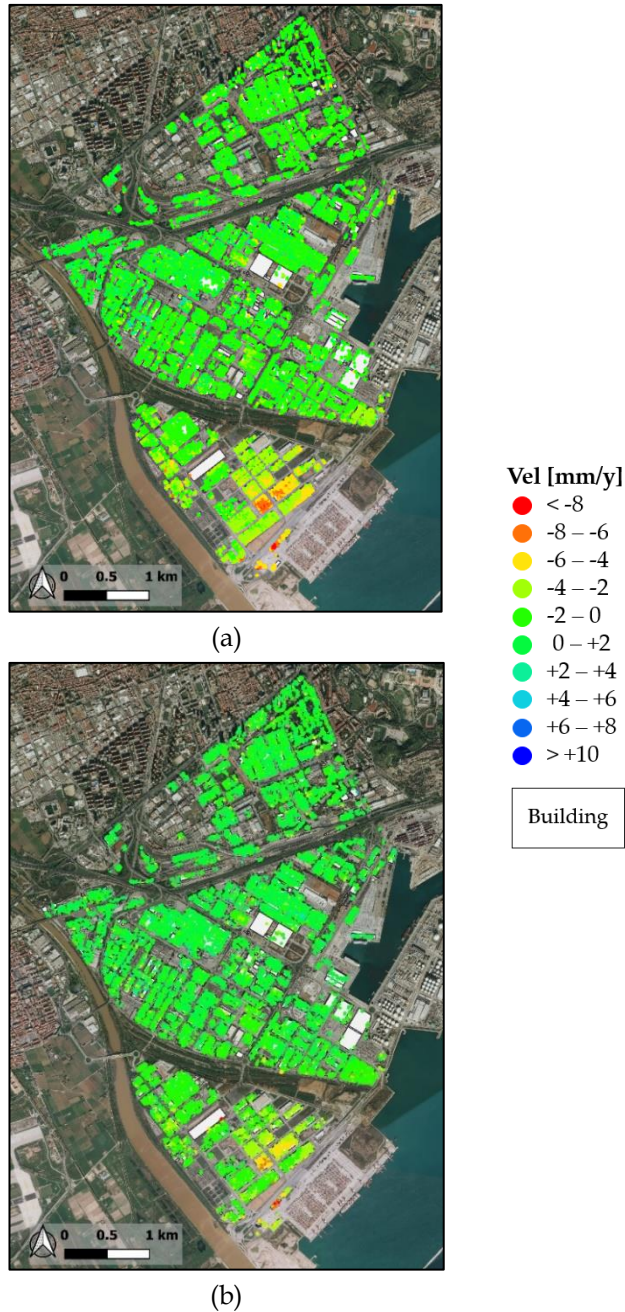


Figure 4.27. Distribution of the selected PSs on the buildings of the selected area of Zona Franca: (a) ASC and (b) DESC [28].

Table 4.5. Statistics of the mean velocity of the selected area of Zona Franca [28].

	Count	Minimum V_{LOS}	Maximum V_{LOS}	V_m	σ
Ascending	33965	-10.5	6.9	-0.90	1.54
Descending	19333	-8.6	7.7	-0.12	1.35

In the area of the Zona Franca district, almost half of the total number of buildings has an area greater than 1000 m². Despite the larger size, many buildings do not even have one PS. In fact, over a total of 1358 buildings, only 1198 are covered by at least one ASC PS and 1111 are covered by at least one DESC PS.

In Table 4.6 a summary of the number of monitorable buildings is reported. With respect to the total number of buildings, 23% of them are not covered by both ASC and DES PSs in Zona Franca. This effect could be related to the different viewing geometry of ASC and DES data and to the greater presence of reflecting elements in the area (e.g., antennas, parapets, balconies).

Table 4.6. Summary of the number of buildings in Zona Franca area [28].

	Zona Franca
Total number of buildings	1358
Number of buildings with no ASC PSs	12%
Number of buildings with no DESC PSs	18%
Number of monitorable buildings	77%

Figure 4.28 shows the extracted ADA for both orbits. The polygons and the “active” PSs are represented. Also in this case, the stability threshold has been set at 2σ , in accordance with what is explained in §4.2, the ADA radius has been set at 25 m and the minimum number of PSs to be included in an ADA has been fixed to 3. For the Zona Franca the cut of the number of PSs over the area is even more drastic compared to the Eixample, with a loss of more than 80% of PSs in both datasets. This largest cut is justified by the presence of different gradients of deformation in the considered portion of the Zona Franca, previously commented, with a greater variability of V_{LOS} values. In Table 4.7 the statistics of the

V_{LOS} of the active PSs are reported. The percentage of buildings included in an ADA is 13% for ASC and 10% for DES orbit.

The maps of $V_{m,ASC}$ and $V_{m,DES}$ estimated for each building are shown in Figure 4.29. The buildings characterized by lack of PSs are covered by violet polygons. For Zona Franca, the number of PSs used to compute the average $V_{m,ASC}$ and $V_{m,DES}$ vary between 1 and 476 for ASC and between 1 and 169 for DES. The upper bound is a function of the dimension of the building surface.

Table 4.7. Statistics of the mean velocity of the active PSs in the selected area of Zona Franca [28].

	Count	Minimum V_{LOS}	Maximum V_{LOS}	V_m	σ
Ascending	6333	-10.50	6.80	-2.82	2.15
Descending	2248	-8.60	7.70	-1.50	2.49

The maps of the Vertical and EW components of the mean velocity are respectively shown in Figure 4.30. In these final maps, the union of the buildings characterized by a lack of PSs in the original datasets is marked with violet polygons.

The final number of monitored buildings is 75. The mean velocity component maps remark that in the southern part of the Zona Franca there are buildings affected by vertical deformations. In particular, three buildings reach vertical downwards average velocities included between 8 and 10 mm/y, other three between 6 and 8 mm/y, but the most populated velocity range is between 4 and 6 mm/y, with twenty buildings affected by vertical velocities of this entity.

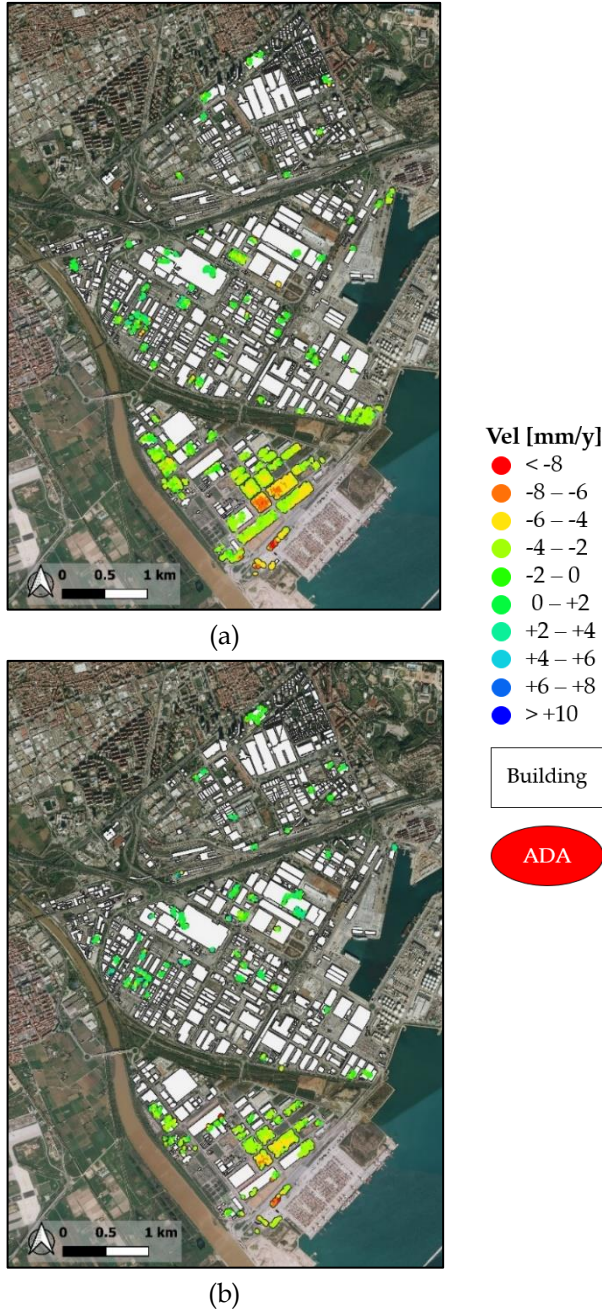


Figure 4.28. ADA extraction from the active PSs of the selected area of Zona Franca from (a) ASC and (b) DESC datasets [28].

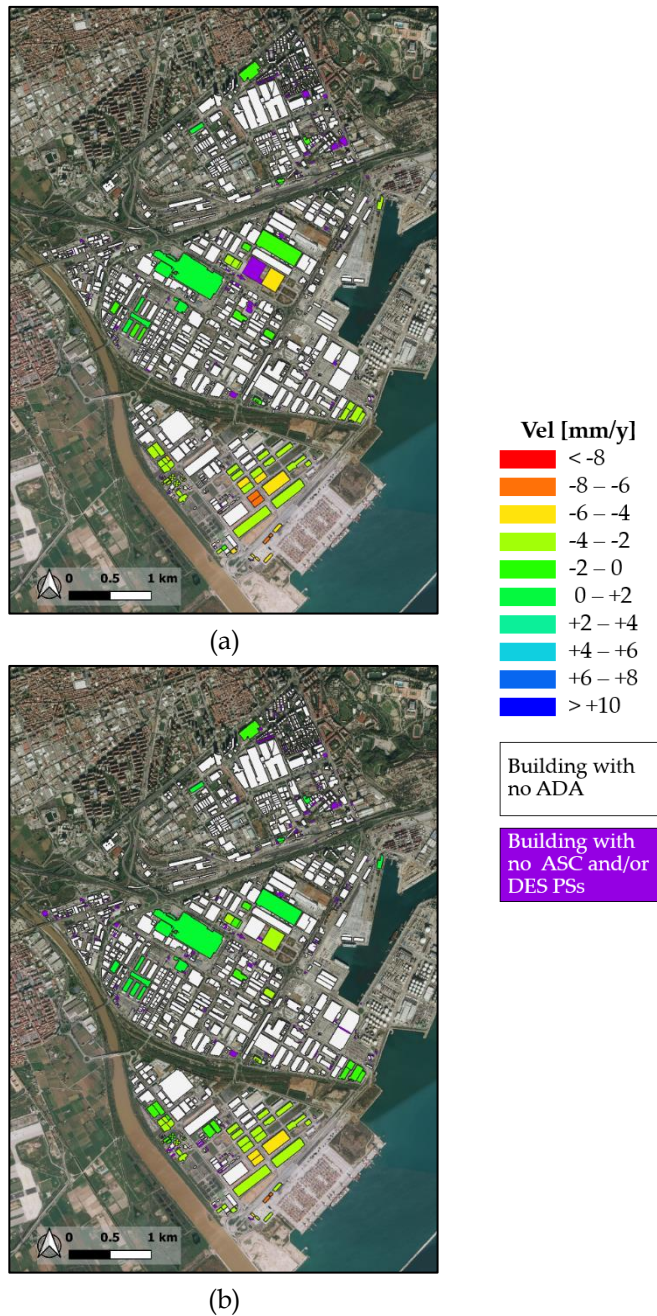


Figure 4.29. Maps of buildings in Zona Franca area having an average value of mean velocity along (a) ASC and (b) DESC orbit [28].

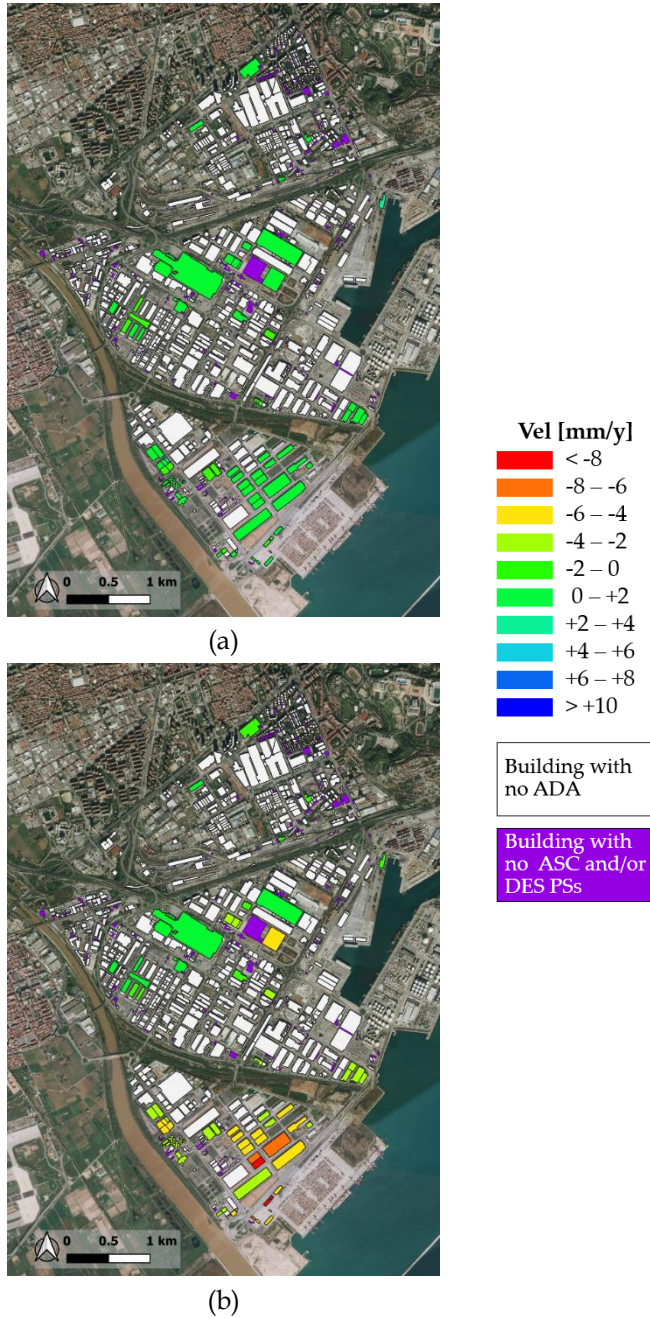


Figure 4.30. Maps of (a) V_{EW} and (b) V_V components for the “unstable” buildings in Zona Franca area [28].

4.2.3 Discussion

The ADAfinder tool has been applied to datasets of PSs subjected to pre-processing operations. This kind of application somewhat departs from the original use of the tool because the aim is different since it focuses only on the buildings. In fact, in the cited applications (e.g., Barra et al. (2017) [27]) the input PSs dataset is usually referred to an entire area, without any preselection. Then, the identified ADA refer to any part of the area under monitoring. In this work, instead, the structure of the desired results is opportunely channeled, to obtain information related to the buildings, and, in particular, to each building affected by deformations exceeding the imposed velocity threshold.

The final maps of the Vertical and EW mean velocity components contain one value for each “active building”. From one side, this could appear simplistic, giving limited information. On the other side, considering the great dimensions of the areas where the proposed methodology could be applied, that could be districts, municipalities, or towns, these final synthetic maps give precious preliminary information about the most critical buildings of the area. Moreover, it is worth to highlight that the resolution of the Sentinel-1 data is not sufficient to perform detailed analysis at the scale of single buildings. Then, the component mean velocity maps could be used as a preliminary tool to identify buildings that are affected by significant deformations and need to be further investigated.

The procedure can be repeated yearly, every time that the EGMS data are updated. This can guarantee not only monitoring of the absolute value of the velocity/displacements on the whole time but also differential comparisons between the mean velocity for each year, establishing additional thresholds of alert on the maximum acceptable values of variation.

The two case study areas have different urbanistic features, concerning the dimensions and distribution of the included buildings, which generate a different PSs covering. The applications show that not all the buildings in the chosen areas are monitorable. In fact, when no PS intersects the building plan, as well as if the building is intersected only by PSs along one single orbit, that building is automatically excluded. The absence of PS should not be interpreted as an

absence of movement. It could be related to the decorrelation effects [109] which could provide a lack of deformation measurement points. Another reason could be the presence of anomalies in the deformation signal, such as leading to very low values of the temporal coherence due to the estimation of PSs displacement time series characterized by a strong variability in time. However, if the unmonitored building is rounded by a significant number of other buildings with significant deformations, one idea could be to use an IDW approach, by achieving the velocity Vertical and horizontal components for the building from the linear interpolation of the other buildings.

An important parameter to consider is the number of PSs on each building. Theoretically, the methodology works when the number of ASC and DES PSs is almost 1 for each building, but the reliability of the results increases when the number of PSs increases.

The results on the area of *Eixample* highlight that a difficulty can be found in reading the final maps because the buildings are very close to each other and have very small plans (even if they develop in height). This reading difficulty could be seen as a limitation, but it is not relevant if thinking about the fact that it is expected that buildings so close will have the same deformation trends, at least if the cause concerns a deformation phenomenon of the underlying soil, which therefore affects the foundations.

Finally, regarding the *ESRI shapefile* containing the buildings plans, it is to note that *OpenStreetMap* constitutes a convenient service, free and open, for worldwide users. Nevertheless, the provided *shapefiles* are manually created by a community of contributing mappers, so may contain approximations or imprecisions. By improving the accuracy of the input *ESRI shapefile* containing the buildings plans, also the accuracy of the results could increase. If geometrical reliefs of the area are available, they can be included in the procedure.



Chapter 5

5. Potential use for SHM purposes at single construction scale

In this paragraph, procedures for the SHM and assessment at a single construction scale, based on direct and elaborated DInSAR results, are illustrated and critically discussed. The need to perform a SHM at single constructions using DInSAR measurements could emerge by looking at the deformation maps derived from the results of territorial scale monitoring through satellite SAR data, as illustrated in §4. In this case, the constructions that could need a detailed study are those identified as “critical”, which means, those affected by significant displacements, that are not stable. Although it would always be useful and interesting to frame a single building in its context, a single construction scale monitoring through satellite SAR data could also be performed independently from a territorial study, using high-resolution data.

Structural assessment of constructions subjected to differential settlements is performed by evaluating the type and amount of damage caused to the constructions. DInSAR measurements can be employed in structural assessment procedures in terms of both trend and cumulative displacements of the deformation time series. The trend provides qualitative information regarding the motion of the structure, which can help in the interpretation of the structural deformation evolution. If the displacement time series are periodically recomputed by using a growing set of SAR acquisitions, updated with the latest available RADAR

images, a variation of the trend can be monitored, that could indicate the onset of a phenomenon which can cause construction deformation. The cumulative displacements could be used to compute differential settlements, which can be modeled as distortions of part of the foundation structures, to analyze the structural response and so estimating damages of structural and non-structural elements.

Two levels of structural assessment can be performed based on the deformations monitored through a multi-temporal DInSAR technique. The first level is a preliminary structural assessment and monitoring performed by combining the information about the construction, obtained from available documentation, with the DInSAR measurements. The aim is a qualitative damage assessment, performed by using limit threshold values of foundation distortions. The preliminary structural assessment procedures are described in §5.1 and applied to three cases study (§5.1.1). The second level consists of a deeper structural assessment and monitoring, based on effective measures of differential settlements derived from total cumulative displacement and an advanced description of the analyzed structures, aimed at obtaining an accurate estimation of structural response and quantification of damages. In §5.2, the more accurate structural assessment procedures are described and illustrated through an application (§5.2.1).

These procedures are performed by possibly combining DInSAR measurements with information derived from documentation, surveys, and on-site data. When possible, information about the geology of the area can be very useful to make a correlation between the soil condition and the long-term satellite DInSAR deformation time series relevant to the building [71],[8],[46], [47]. The knowledge of soil stratigraphy is important to understand if the causes of the deformation are induced by ground settlements or if there are other phenomena in progress.

5.1 Preliminary structural assessment and monitoring

Different interpretations of both direct and elaborated satellite SAR data can be performed to formulate a preliminary structural assessment and monitoring of the existing constructions.

An engineer who wants to perform a qualitative correlation between settlements and expected damage is supposed to have the Vertical and EW components of the displacement for the structure of interest or, at least, their LOS components. The best situation is the possibility to exploit settlement profiles along the sides of the structures. The settlement profiles can be obtained from the results of the elaboration of the DInSAR satellite data from both ASC and DES orbits. In particular, a nearest neighbors approach is not recommended, and often is not implementable and has the highest computational burden to rebuild the settlement profiles. The main obstacle consists in finding couples of ASC and DES PSs, close enough to be considered representative of the same reflecting target, along every building façade, or at least at each end. This is very difficult, because of the lateral and inclined sensor acquisition system, as explained in §3.2. When applicable, spatial interpolation is the easier procedure to create the displacement profiles, having continuous mean velocity maps along the Vertical and EW directions. Taking the mean velocity values in the desired direction, along the examined alignment, they can be multiplied by the number of years in which that mean velocity trend can be extended, and the settlement profiles are obtained.

Using these data, a correlation between the detected displacements and the expected damage can be done based on the classical literature [48]–[54]. Burland and Wroth (1975) [52] proposed definitions and symbols for the foundations' movements which do not make assumptions about the mode of deformation of the superstructure. The main definitions regard the settlement ρ , the relative settlement $\delta\rho$, the rotation θ and the angular strain α , summarized in Figure 5.1a. Moreover, Figure 5.1b defines the relative deflection Δ and the deflection ratio Δ/L and Figure 5.1c identifies the tilt ω and the angular distortion β .

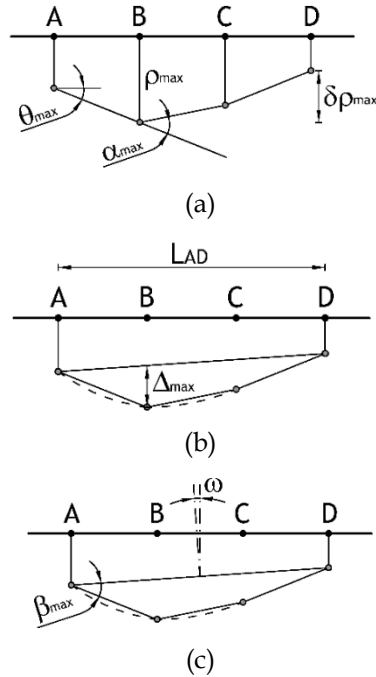


Figure 5.1. (a) Definitions of settlement ρ , relative settlement $\delta\rho_{max}$, rotation θ and angular strain α ; (b) definitions of relative deflection Δ and deflection ratio Δ/L ; (c) definitions of tilt ω and relative rotation (angular distortion) β .

A state-of-the-art report proposed by Poulos et al. (2002) [110] is shown in Table 5.1, where the different limitations as a function of the type of structure and the type of damage/concern are summarized. The main adopted criteria for the identification of the limiting values related to structural damage are related to β .

These simple limiting criteria are mainly based on indirect evidence, and not exhaustive to define the comprehensive damage state of the structure.

A preliminary structural assessment can be developed also based on the integration of data derived using advanced multi-temporal DInSAR techniques and the outcomes of on-site damage reliefs. The knowledge of the damage pattern at the beginning of the monitoring period, e.g., through on-site surveys, is very useful. Moreover, a relief of the condition of the structure at the end of the monitored

period can be valuable to validate the displacement-induced forecasts, in terms of damage condition.

Table 5.1. Summary of criteria for settlement and differential settlement of structures by literature source (L=length between panels, H=height).

Type of structure	Type of damage/concern	Criterion	Limiting value(s)
Framed buildings and reinforced load bearing walls	Structural damage	Angular distortion	1/150 - 1/250
	Cracking in walls and partitions	Angular distortion	1/500 (1/1000-1/1400) for end bays
	Visual appearance	Tilt	1/300
	Connection to services	Total settlement	50 - 75 mm (sands) 75 - 135 mm (clays)
Tall buildings	Operation of lifts & elevators	Tilt after lift installation	1/1200-1/2000
Structures with unreinforced load bearing walls	Cracking by sagging	Deflection ratio	1/2500 (L/H=1) 1/1250 (L/H=5)
	Cracking by hogging	Deflection ratio	1/5000 (L/H=1) 1/2500 (L/H=5)
Bridges - general	Ride quality	Total settlement	100 mm
	Structural distress	Total settlement	63 mm
	Function	Horizontal movement	38 mm
Bridges - multiple span	Structural damage	Angular distortion	1/250
Bridges - single span	Structural damage	Angular distortion	1/200

Three applications showing examples of preliminary assessment and monitoring are reported in §5.1.1.1, §5.1.1.2, and §5.1.1.3.

5.1.1 Applications in Rome

The following applications regard the use of elaborated DInSAR satellite data for the preliminary assessment and monitoring of existing buildings of different types. For all of them, the CSK satellite data illustrated in §2.3.1 are exploited for the preliminary assessment and monitoring. The first application regards the Torri Stellari (§5.1.1.1) for which the satellite data elaborations have been shown in §3.4.1. The second one is about the Collector sewer's point of disposal n. 7 (§5.1.1.2), which deformative condition has been previously analyzed in §3.4.2. For both of them, the methodology proposed for the structural monitoring is based on the GIS integration of DInSAR measurements, geological investigation, historical surveys, and 3D modelling. The abovementioned applications are part of a journal paper published in 2022 [46]. The third one is the Vittorino da Feltre school building, a masonry structure that will be described and analyzed in §5.1.1.3. This case study is included in a journal paper [111].

5.1.1.1 *Application – Torri Stellari*

The detailed description and the creation of the 3D surface model of the external volumes of the Torri Stellari can be found in §3.4.2. The preliminary SHM of the towers is carried out by the integration of the 3D models of the structures under monitoring, the 3D model of the soil stratigraphy of the area and the DInSAR measurements. To integrate the building volumes in the geological 3D model, foundations and underground constructions have been implemented in the architectural model (Figure 5.2).

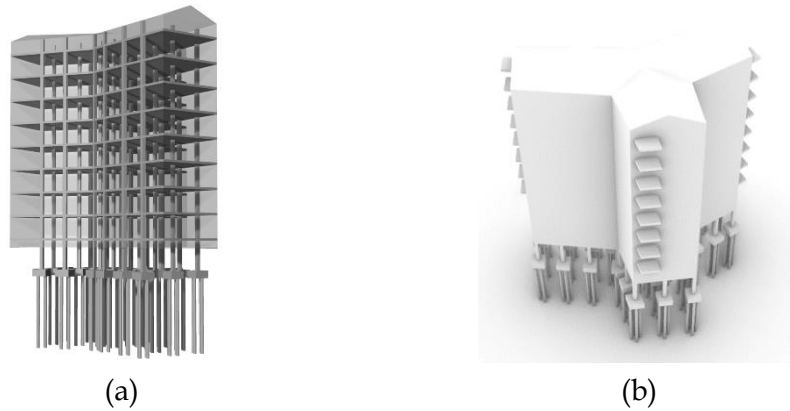


Figure 5.2. 3D model of the structure of Tower n. 1: (a) section and (b) lateral view [46].

The integrated model constituted by the buildings' volumes and the geological model, embedding the PSs, is represented in Figure 5.3. The union of the models is carried in ArcGIS Pro [89] environment exploiting a unique georeferenced system (using the World Geodetic System 1984 coordinate system, WGS 84) together with the positioning of the PSs. An empirical check of the relative PSs positioning to the buildings' volumes is done.

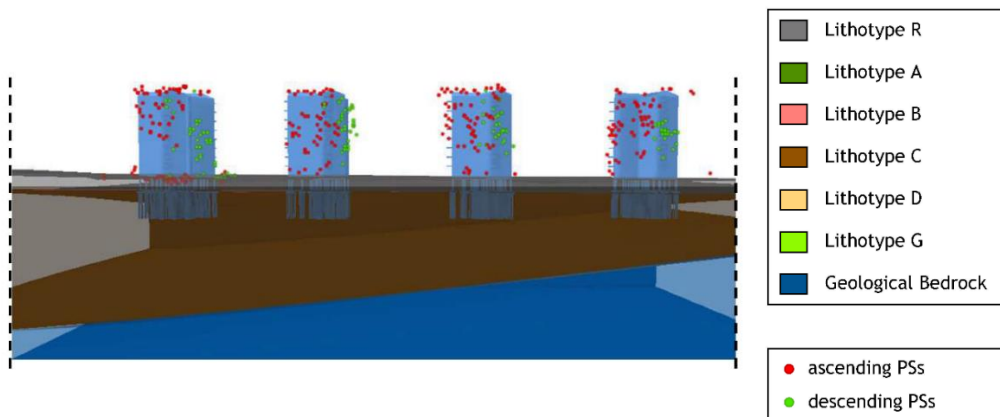


Figure 5.3. 3D integrated model of Torri Stellari (modified from [46]).

The presented application is extracted from the work of Miano et al. (2022) [46], in which all the details of the geological 3D model of Valco San Paolo subsoil

used for the presented application are described in detail. The following lithotypes (from the top to the bottom in the legend of Figure 5.3) of the recent alluvial body of the Tiber River have been distinguished:

- Lithotype R: anthropic fill material characterized by abundant, variously sized brick fragments and blocks of tuff embedded in a brown-green Silty-sandy matrix;
- Lithotype A: mainly silty and secondly sandy deposits with traces of organic matter;
- Lithotype B: brown to yellow (more rarely grey) colored, sandy and silty-sand deposits;
- Lithotype C: grey clay and silty clay with variable organic content. Occasional up to 100 mm thick peat levels and rare sandy silt layers with gravel is also present;
- Lithotype D: alternating silty-sandy, sandy-silty, clayey-silty, and clayey levels. Viewed together, this unit is grey;
- Lithotype G: predominantly limestone gravel in a grey, sandy-silty matrix;
- Geological Bedrock: all the other pre-Holocene deposits that form the bottom and the flanks of the Tiber erosive paleo valley. It is assumed that these over-consolidated sediments do not contribute to the settlement transmitted to the topographic surface and buildings.

As it has been observed in §1, the area of Torri Stellari is characterized by predominantly vertical settlements (Figure 3.11c), with negligible horizontal displacements (Figure 3.11d). It is worth noting that Torri Stellari foundations pass through the man-made fill and rest directly in Lithotype C alluvium (Figure 5.3). Effectively, a subsidence phenomenon has been active for many years in the area [9], [112].

Starting from the mean velocity values along the Vertical and EW directions of the maps shown in Figure 3.11c (V_V) and Figure 3.11d (V_{EW}) along the alignment of interest, the base settlement profiles on the sides of the Torri Stellari have been outlined. They have been estimated by multiplying the velocities for the

number of years in which that mean velocity trend has occurred. In the specific, for framed buildings, the mean velocity values have been taken in correspondence of the columns. An example is given, for the Torri Stellari building number 2. The settlement profiles in the Vertical and horizontal EW directions for the South side of Tower n. 2 are represented in Figure 5.4b. The displacement values obtained considering a time interval of 8 years, are marked in correspondence of the three columns (1, 2, and 3) highlighted in Figure 5.4a, assuming that the structural scheme is the same for the four towers. This side of Tower n. 2 is representative because of the existence of an evident differential displacement phenomenon between the two ends of the considered facade, for both settlement directions.

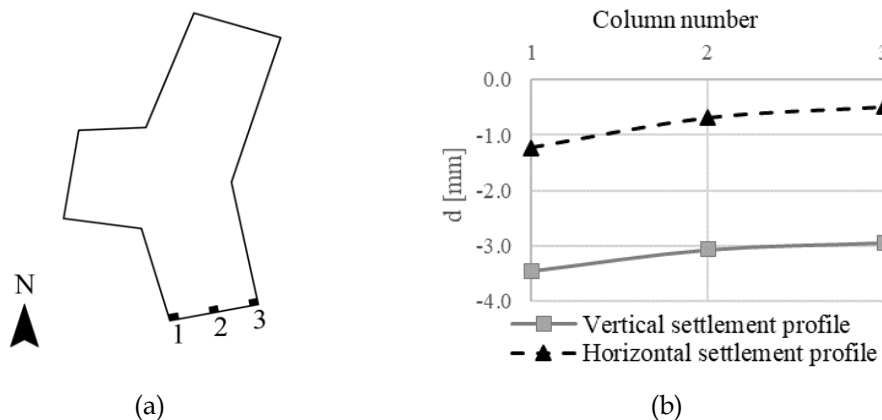


Figure 5.4. (a) Scheme of Tower n. 2 with the position of the three considered columns; (b) example of settlement profiles of the southern side of Tower n. 2 along Vertical and horizontal East-West direction (modified from [38]).

5.1.1.2 Application – Collector sewer’s point of disposal n. 7

A detailed description of the Collector sewer’s point of disposal n.7 can be found in §3.4.2. As for Torri Stellari, also for this application a 3D model of the building volumes for the graphical positioning of the PSs around the model in the space is created, based on the historical documentation collected in the Genio Civile of Rome Archive, shown in Figure 3.14a. For the building of the Collector

sewer's point of disposal n. 7, the georeferenced 3D modelling focuses on both the reconstruction of the building's external volume and the Collector sewer underground tunnel (Figure 5.5).

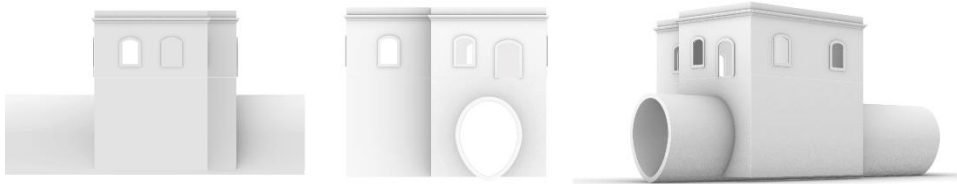


Figure 5.5. Lateral views of the 3D model of the building of the Collector sewer's point of disposal n. 7 with the Collector sewer underground tunnel [46].

Analogously to the previous application, the PSs are located on the 3D model in ArcGIS Pro [89]. The integrated model (described in Miano et al. (2022) [46]), embedding the PSs, is represented in Figure 5.6. For the description of the lithotypes, refers to §5.1.1.1.

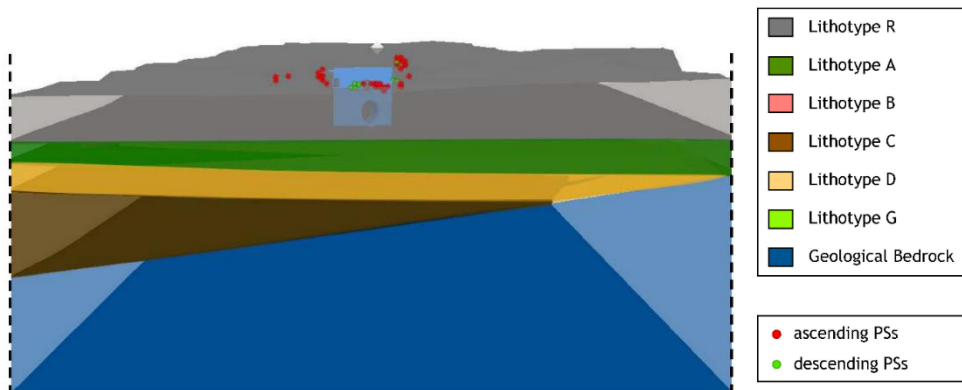


Figure 5.6. A 3D integrated model of the Collector sewer's point of disposal n. 7 (red circles: ASC PSs, green circles: DES PSs) (modified from [46]).

A detailed evaluation of the ground deformation has been conducted for the Collector's sewer point of disposal n. 7, as damage compatible with settlements at the foundation depth has been observed on its facades. In fact, as it can be seen

in Figure 5.6, the manufact is located above Lithotype R placed on top of lateral heteropy between Lithotype A and Lithotype B, on top of about 8 m thickness of Lithotype D lens. The displacement maps (Figure 3.15e and Figure 3.15f) have been exploited to derive base settlement profiles along the building's sides, by fixing a temporal span. For the masonry walls of the Collector sewer's point of disposal n.7, the mean velocity values in the grid vertexes have been considered. The Vertical and horizontal EW displacement profiles relative to each facade of the manufact (see Figure 5.7a) are represented in Figure 5.7b.

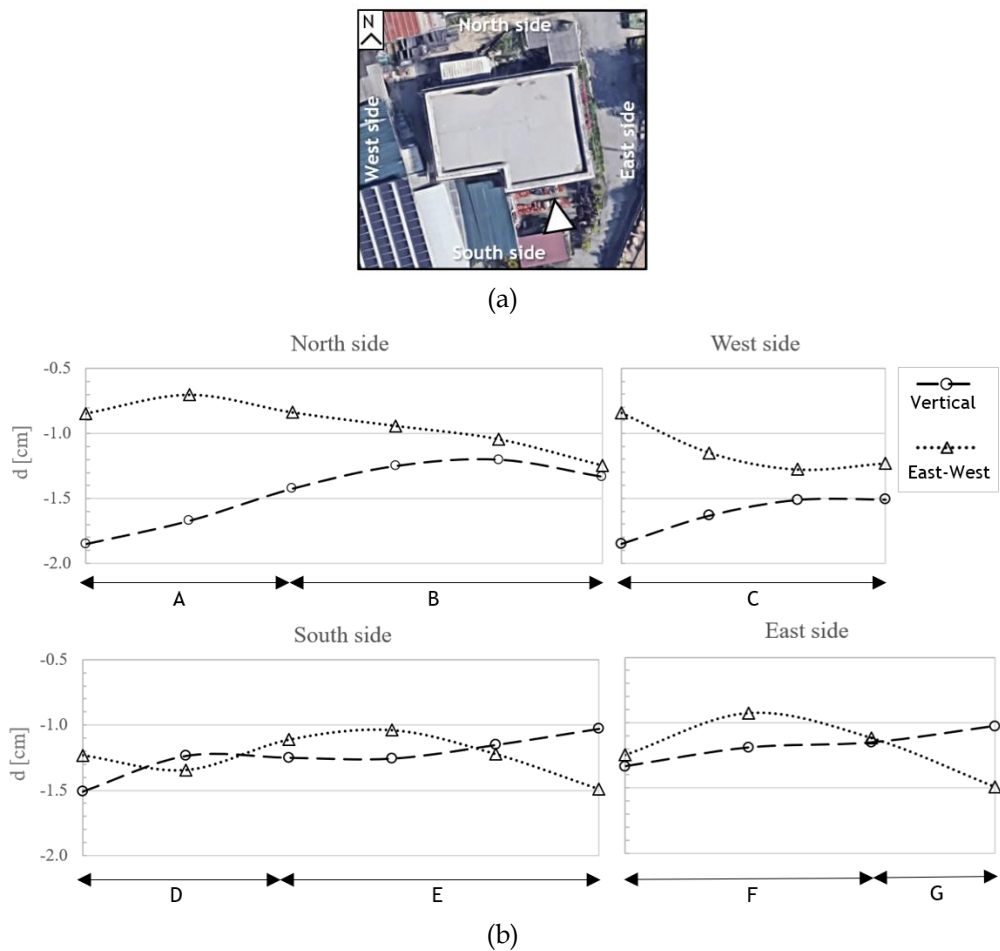


Figure 5.7. Collector sewer's point of disposal n. 7: (a) plan view; (b) settlement profiles along the four building sides (modified from [46]).

This approach for the damage assessment is reported with an application to the Southern external wall of the Collector sewer's point of disposal n. 7, whose condition in December 2020 is reported in Figure 5.8.



Figure 5.8. Collector sewer's point of disposal n. 7: picture of the Southern side (survey in November 2021).

According to Boscardin and Cording (1989) [54], the on-site survey led to classifying the wall condition as slight damage because of the presence of cracks easily filled. Figure 5.8 represents the real condition of the case study building wall, for which no previous information is available at the starting time of the monitoring. In this case, the information about the damage at the end of the monitoring time (e.g., slight damage) is depicted in Figure 5.9 with a yellow-colored area. The blue arrows, instead, indicate the calculated horizontal strain/angular distortion couples of the selected wall, based on the displacement profiles shown in Figure 5.7. These arrows are shown in multiple positions because the precedent deformation history is not known. However, it can be argued that the ending point should be inside the yellow area.

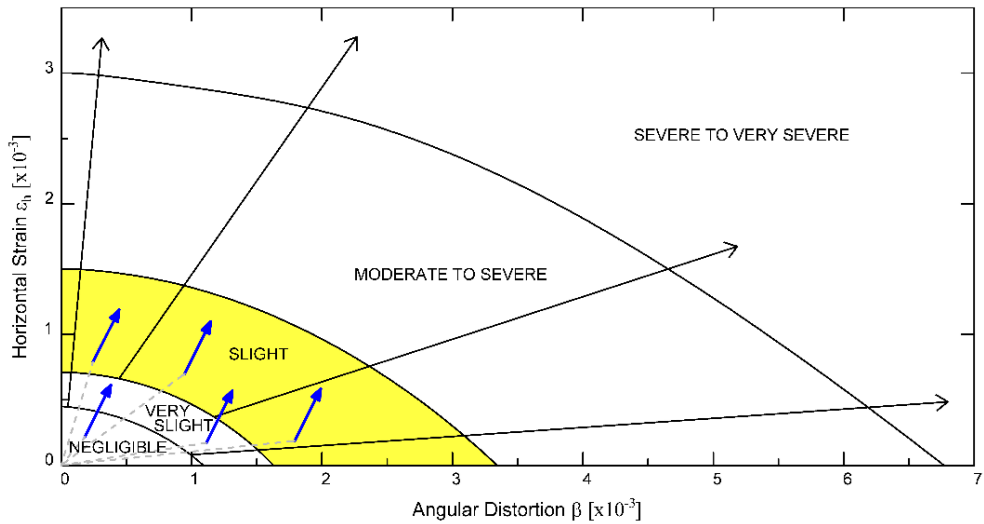


Figure 5.9. Damage assessment for the considered wall, based on Boscardin and Cording scheme, in function of the angular distortion β and horizontal strain ε_h [46].

Figure 5.10, instead, represents a conceptual application of the case in which information at time zero is supposed to be available. The intensity of the arrow is the same as the precedent case. In this case, an initial damage status can be assigned to the building wall/side. Then, by summing up the calculated horizontal strain/angular distortion couple for the selected wall (herein proposed with different colored arrows based on the starting damage status), based on the displacement profiles, a new border surface can be identified at the end of the monitoring period (grey dashed curves). In some cases, the previous deformation can be considered negligible, while in other cases, an initial damage status should be assigned. It could be argued that it is not conservative to set the lower boundary curve of the identified damage status, as presented in the example of Figure 5.10. In fact, the authors suggest a criterion to solve this issue, based on the AeDES format sheets [113], accounting for the extension of the damage concerning the structural element. The lower boundary curve of the damage status could be considered if its extension is between 0% and 33%, the median boundary curve (drawn with the same shape as the lower and upper boundary curves) if the extension is between 34% and 66%, and, finally, a curve just under

the upper boundary curve if the extension is between 67% and 100%. In case of negligible damage, the starting point could be coincident with the origin of the axes of Figure 5.10, due to the low distance up to the achievement of the very slight damage, or the lower boundary curve of the very slight damage status could be conservatively considered.

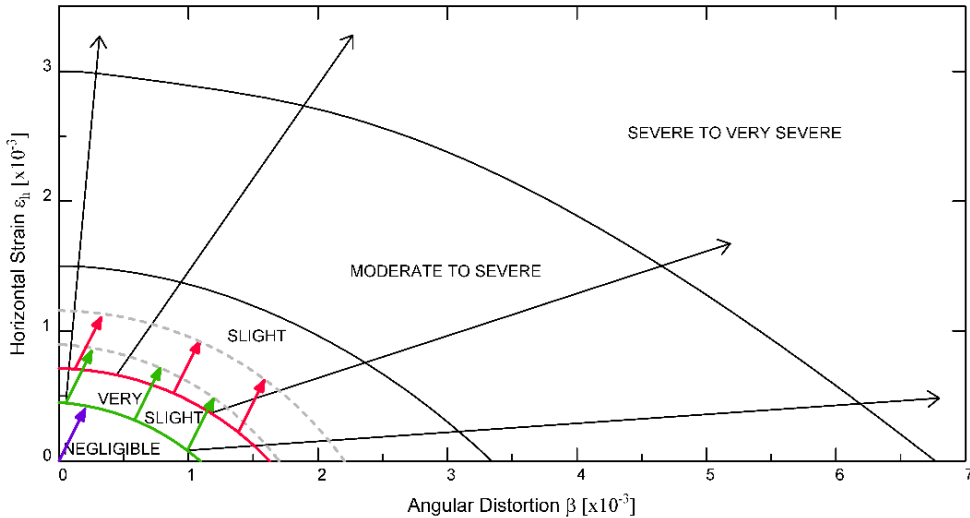


Figure 5.10. Damage assessment for the considered wall, based on Boscardin and Cording’s (1989) [54] scheme, in function of the angular distortion β and horizontal strain ϵ_h , by conceptually supposed to know the damage state at the beginning of the monitoring period [46].

In Figure 5.7 the settlement profiles along the four sides of the building of the Collector sewer point of disposal n. 7 are represented, distinguishing the sagging and hogging portions with letters from A to G. Regarding the EW-oriented external walls, the values of the maximum angular distortion (β_{max}) and of the horizontal strain (ϵ_h) are reported in Table 5.2, for the different segments A, B, D, and E, in accordance with the sagging and hogging portions of the settlement profiles (Figure 5.7).

Table 5.2. Maximum angular distortion β_{\max} and horizontal strain ε_h of the East-West directed walls.

Settlement profile segment	β_{\max} [-]	ε_h [-]
A	0.6E-03	0.1E-04
B	0.8E-04	0.4E-03
D	0.3E-03	0.2E-03
E	0.2E-03	0.4E-03

For the NS-oriented walls, both Polshin and Tokar's [50] and Meyerhof's [49] criteria, which are specific for masonry walls structures, can be adopted.

5.1.1.3 Application – Vittorino da Feltre

The Vittorino da Feltre school building was constructed at the end of 1880, in the city centre of Rome. Figure 5.11a and Figure 5.11b show a top view of the building and an external view of the building (identified using a red hatch). The school features one underground level, three floors above ground, and two internal. The point of view of Figure 5.11b is located in Largo Gaetana Agnesi (Figure 5.12).

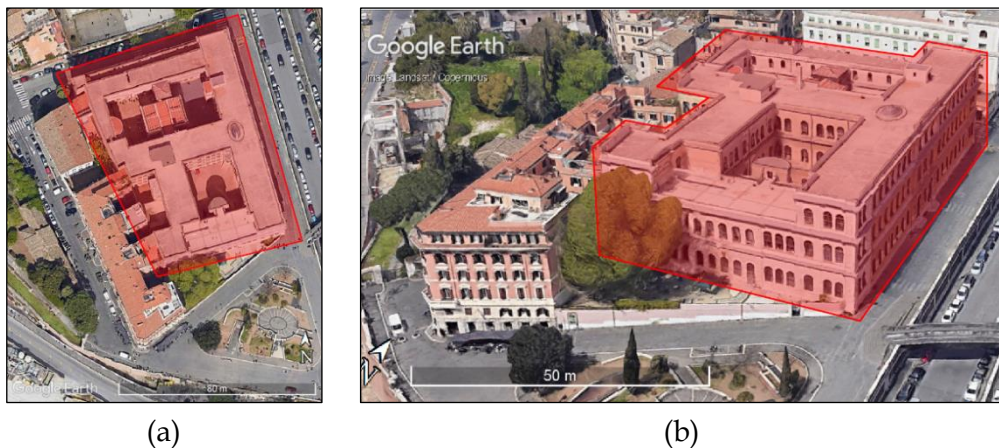


Figure 5.11. (a) Top view and (b) external lateral view of the Vittorino da Feltre school building (source: *Google Earth*) [111].

The masonry walls are made either with tuff stones and bricks or brick only. Figure 5.12 shows the plan of the first floor of the building. Regarding the horizontal structures, all spaces belonging to the basement level are characterized by lowered barrel vaults with lunettes, while in the upper three floors above ground, the classrooms and hallways feature flat floors with steel profiles perpendicular to the perimeter walls and barrel vaults, respectively. The foundation system, having a mean depth of 4 m, is characterized by two overlapping masonry layers, realized in dry stone and tuff stone.

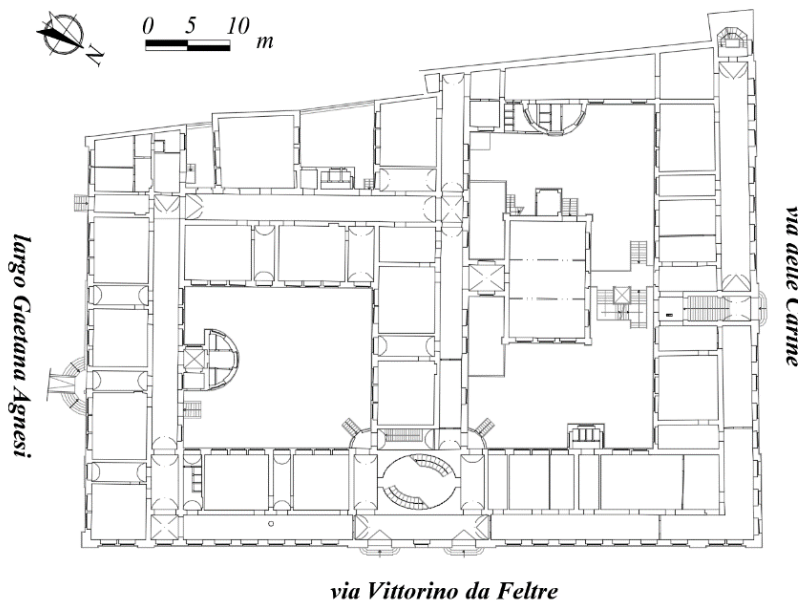


Figure 5.12. Plan of the first floor.

The building has explored various damage conditions throughout its life. The first crack along the barrel vault of the hallway of the ground floor was born in 1889. Further damages were encountered in the years between 1901 and 1904 in the south-west corner of the schoolyard, requiring the execution of a retrofit intervention in the area with steel ties joining the perimeter walls. Subsequently, foundation settlements affected the side of the building towards Largo Agnese, in the years between 1941 and 1942, during the construction of Line B of the

Rome Metro. Therefore, a retrofit intervention of the foundation system and of the cracks developed in the masonry walls was made. An increase of the damage pattern was found later, during the renovation program of the abovementioned Line B: further cracks were observed in the basement level in the south-west corner of the schoolyard, and a crack parallel to the side of the building towards Via Vittorino da Feltre was found in the barrel vault between the ground and first floors. A retrofit intervention of the foundation system of the south side of the building towards Largo Agnese was executed in 2001, including cement injections and 230 micro piles under the main bearing masonry walls, as well as the retrofitting of some floor systems with steel profiles and barrel vaults with the realization of RC slabs at the extrados. In 2012, restoration and strengthening interventions of unsafe cornices of the façade towards Largo Agnese were performed. The school building is currently object of an overall retrofit project, concerning the vertical masonry walls and the horizontal structures (both barrel vaults and flat floors) by means of RC slabs, properly connected to the existing beams.

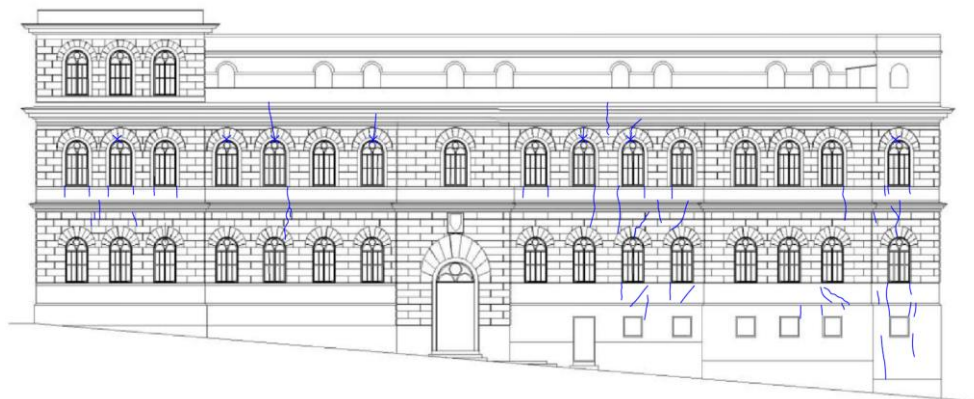
Various reliefs of the damage pattern of the building have been carried out over years: in 1989 by Eng. Morelli; in 2008 by the Metro C company for the execution of excavation works in the area; in 2010 by the Municipality of Rome; in 2012 by the school building Department; in 2021 by me and other colleagues. The damage surveys allowed to highlight the existence of a slowly evolving in-time cracking phenomenon in the building, which could be due to different causes, e.g., the presence of a thick fill soil layer ranging between 8 m and 10 m, the small depth of the foundation of the inner masonry walls, equal to about 1.5 m, the execution of excavation works for the construction of either the Metro Line B or the Colosseo Station of the Metro Line C.

A comparison of the results of the different reliefs is performed in the following, when possible, for the main facades.

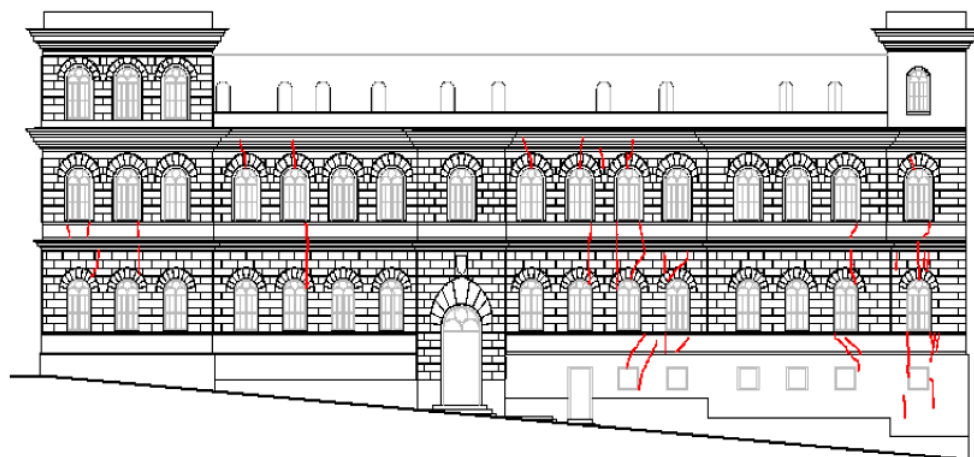
The cracking pattern of the North façade in November 2021 can be observed in Figure 5.13a. In this façade, the cracks are mostly concentrated around the windows. Nevertheless, in addition to the sub-vertical cracks starting from the arch keystone and reaching the frame above, vertical cracks are also found,

starting from the two bottom sides of the window and continuing downward, often crossing the frame of the lower order. Moreover, in this façade the presence of marked vertical cracks in the basement of the right part of the façade (North-East corner) can be observed. As a comparison, Figure 5.13b shows the cracking pattern in 2010. The overall damage condition of the masonry wall is substantially similar in the investigated period. Sub-vertical cracks starting from the arch keystone and reaching the frame above can be observed, as well as vertical cracks starting from the two bottom sides of the window and continuing downward. Finally, the cracks occurring in the basement of the right part of the façade are almost identical to the ones detected in November 2021.

The result of the relief performed in November 2021 on the South façade is shown in Figure 5.14a. No noticeable cracks were found, except for two small vertical cracks located at the left side of the base of the wall, between the two windows of the ground floor. It is worth highlighting that the South façade has been renewed in 2012 with recovery and consolidation works, so the damage pattern in 2021 results to be very different from the one detected in 2010 and shown in Figure 5.14b, characterized by the presence of many cracks, mostly located in the left side of the façade, along a sub-vertical direction. These cracks generally interest the arch key, and, in many cases, reach the frame above. Because of the renovation interventions that have affected the South façade, a direct comparison between the two reliefs performed in 2010 and 2021 cannot be done. However, the two small vertical cracks found in the left side of the basement in 2021 were not present in 2010.

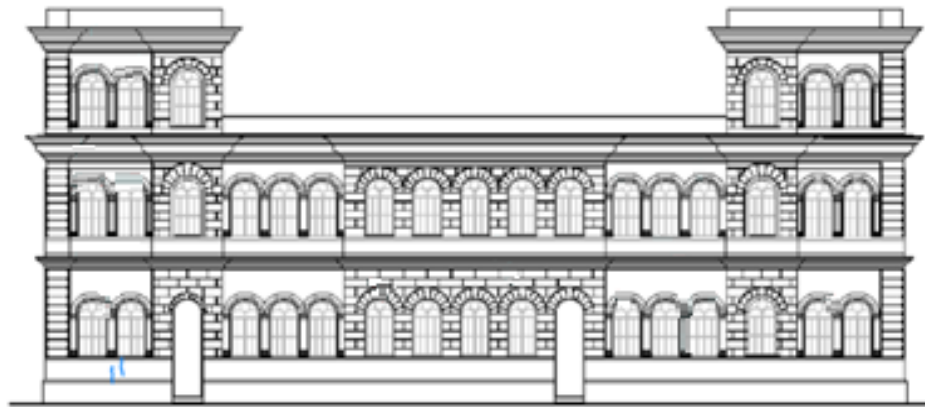


(a)

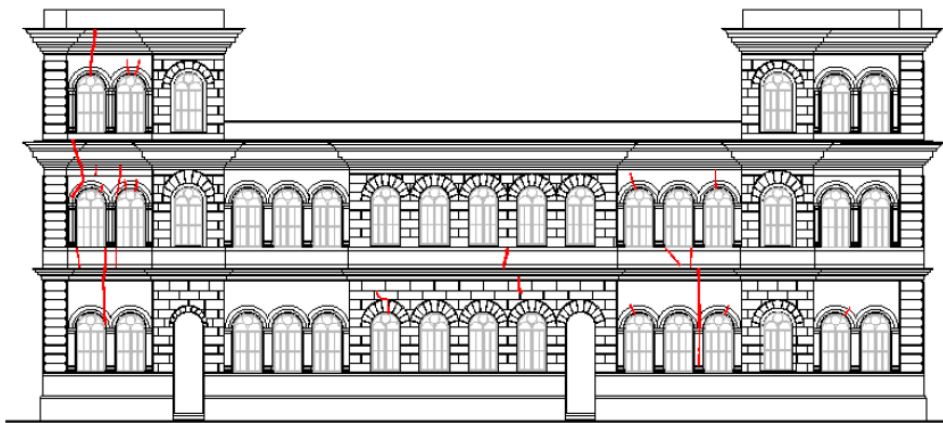


(b)

Figure 5.13. North façade. Cracking pattern detected in (a) 2021 (blue lines) and (b) 2010 (red lines) [111].



(a)



(b)

Figure 5.14. South façade. Cracking pattern detected in (a) 2021 (blue lines) and (b) 2010 (red lines) [111].

Regarding the East façade, the left vertical end band that includes the first two verticals of windows has been recently affected by renovation interventions, as suggested by the different colors and finishes compared to the remaining part of the façade. Figure 5.15a shows the cracking pattern detected in 2021, characterized by cracks mainly located on the top of the windows, in particular starting from the arch keystone and in many cases reaching the frame above, along a sub-vertical direction. The third floor is the most damaged one. No cracks have been

found in the basement. For this façade, the picture of the cracking pattern in 2010 was not available. A picture of the crack pattern in 1989 (Figure 5.15b) has been retrieved. The comparison of the two damage patterns detected in 1989 and 2021 shows a similar crack distribution and cracking pattern.

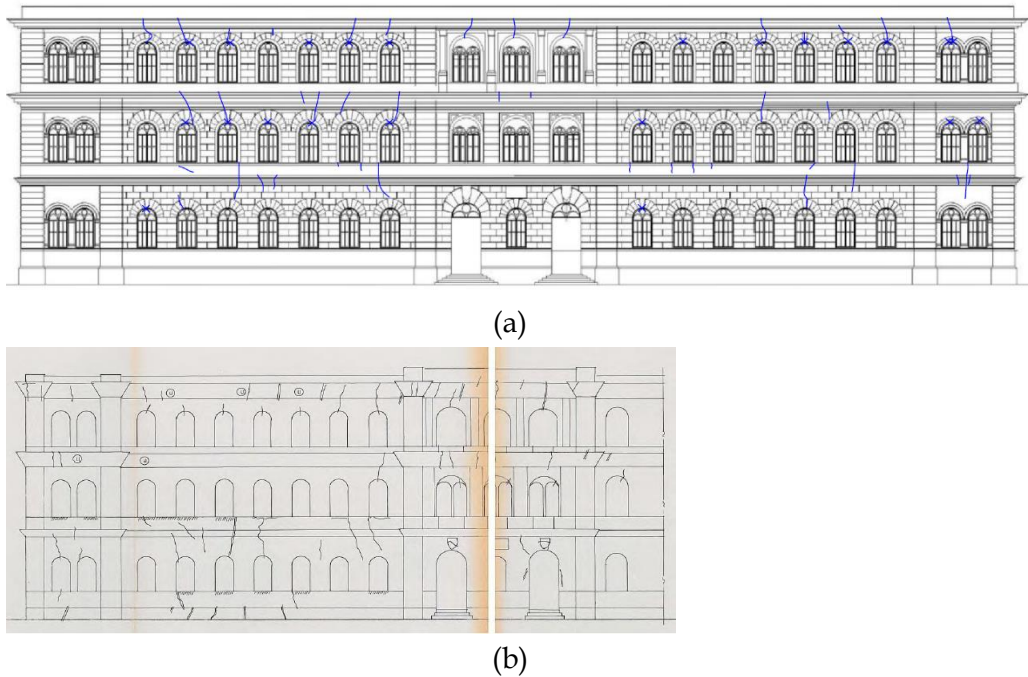


Figure 5.15. East façade. Cracking pattern detected in (a) 2021 (blue lines) and (b) 1989 (black lines) [111].

Inside the building, slight widespread damage has been detected. On the first floor, the following significant damage in localized parts has been observed: a long-standing vertical crack located at the intersection between the North and West external walls (Figure 5.16a), a crack in the barrel vault, orthogonal to the vault director line (Figure 5.16b), and double cracks in the barrel vault parallel to the vault director line (Figure 5.16c) in the hallway parallel to the North façade. Moreover, there is a diagonal crack in the wall orthogonal to the vault director line, passing across the masonry (Figure 5.16d) in the hallway parallel to the East façade.



(a)



(b)



(c)



(d)

Figure 5.16. Damage at the 1st floor: (a) vertical crack, North-West corner; (b) crack orthogonal to the vault director line in the barrel vault of the hallway parallel to the North façade; (c) double cracks parallel to the vault director line in the barrel vault of the hallway parallel to the North façade; (d) passing diagonal crack in the wall orthogonal to the vault director line in the hallway parallel to the East façade.

On the second floor, among other minor cracks, the continuation of the vertical crack located at the intersection between the North and West external walls on the first floor (shown in Figure 5.16a), has been found. Moreover, in the hallway parallel to the East façade, a crack in the floor, parallel to the external wall

is found. The crack is a sort of separation line, which creates a slope inward of the flooring. In the same hallway, many cracks orthogonal to the vault director line have been observed.

An integration between the satellite SAR data and the outcomes of the damage relief is performed to properly assess the damage pattern of the analyzed school building induced by one or more of the external actions.

The satellite SAR data used for this application are those illustrated in §2.3.1. The monitoring time interval is 2011–2019. The distribution of ASC and DES PSs around the school building, considered to be on the ground, is shown in Figure 5.17. In this case, in order to improve the spatial interpolation results, also the ASC and DES PSs relative to the adjacent building have been included.

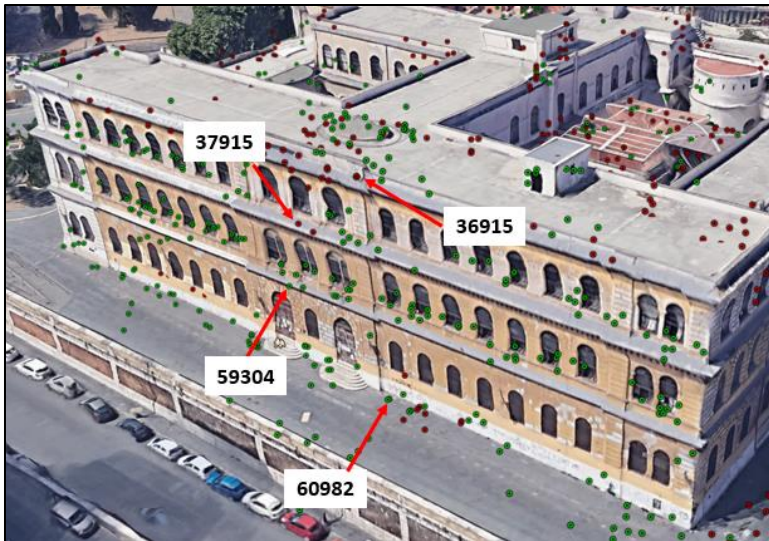


Figure 5.17. Distribution of ASC (red) and DESC (green) PSs relative to the school building and the adjacent building, considered to be referred to the ground [111].

The deformation time series of four PSs having the highest values of the LOS mean velocity, referred to one façade of the building and the surrounding area, are reported in Figure 5.18 with red and green markers, respectively for ASC and DES PS.



(a)

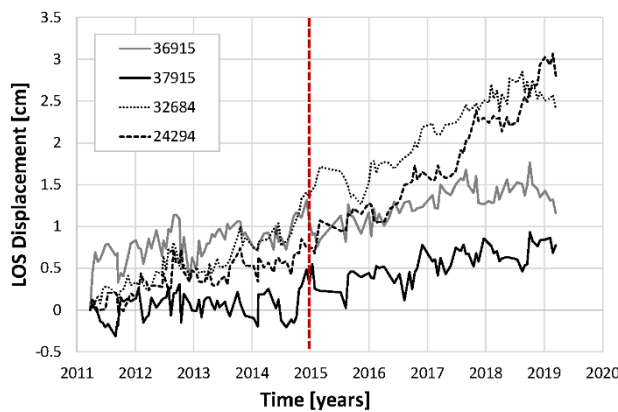


(b)

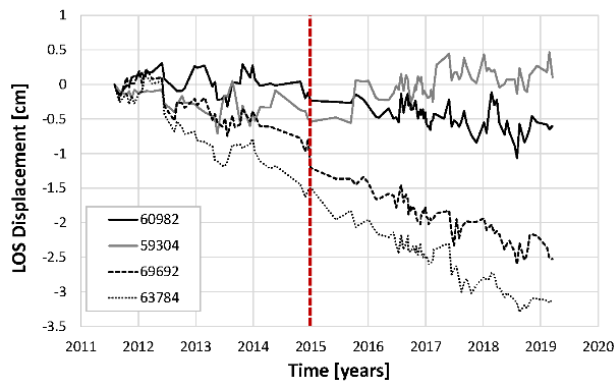
Figure 5.18. Location of the selected PSs: (a) top view with ASC and DESC PSs; (b) 3D view of the building with the selected ASC and DESC PSs on the structure [111].

The LOS displacement time series of the selected PSs are shown in Figure 5.19a and Figure 5.19b for the ASC and DES geometries, respectively. The continuous black and grey curves refer to the points belonging to the school

building, while the dashed and dotted black ones to those selected within the surrounding area. As can be noticed, a change in the trend of the LOS displacements, characterized by a higher derivative, occurs approximately around the year 2015 in all examined PSs recently (the year of excavation works in the area). The difference in the trend of the LOS displacement before and after 2015 is also more marked for the PSs located in the area surrounding the school building, very likely due to a wider deformation process. Furthermore, the curves of the examined PSs do not appear to have attained a condition of stability at the end of the investigated period (i.e., the year 2019), a sign of an ongoing phenomenon.



(a)



(b)

Figure 5.19. LOS displacement time series of the selected (a) ascending and (b) descending PSs [111].

In order to take into account the change in the trend of the LOS displacements observed at single PSs scale around the year 2015, the deformation information of the ASC and DES databases have been subdivided into two time sub-intervals. In particular, the first sub-interval ranges between the start of the observation period and September 2014, while the second one is between September 2014 and the end of the acquisition period. Continuous maps of the mean LOS displacement velocities have been computed by adopting the EBK interpolation technique according to §3.2. The maps of the Vertical and EW components are shown in Figure 5.20a and b and Figure 5.20c and d, respectively.

For the North façade it is possible to use the literature scale of damage in the plane. The reconstruction of the profiles of the displacement component under the considered façade, along the Vertical and EW direction, respectively, are shown in Figure 5.21a and Figure 5.21b (where L is the length of the wall and d is the displacement). They are referred to the periods 2011-2015 (grey dotted line with triangular markers) and 2015-2019 (black dotted line with circular markers). As it can be noted, an in-progress cracking phenomenon seems to exist. Concerning the EW direction, a change in the trend of displacement occurs between the two analyzed periods. In the second time interval, a variable displacement profile is found, increasing towards the corner with via del Colosseo, and having a negative sign, compatible with the occurrence of a settlement towards the area surrounding the school building, object of excavation works in the analyzed period.

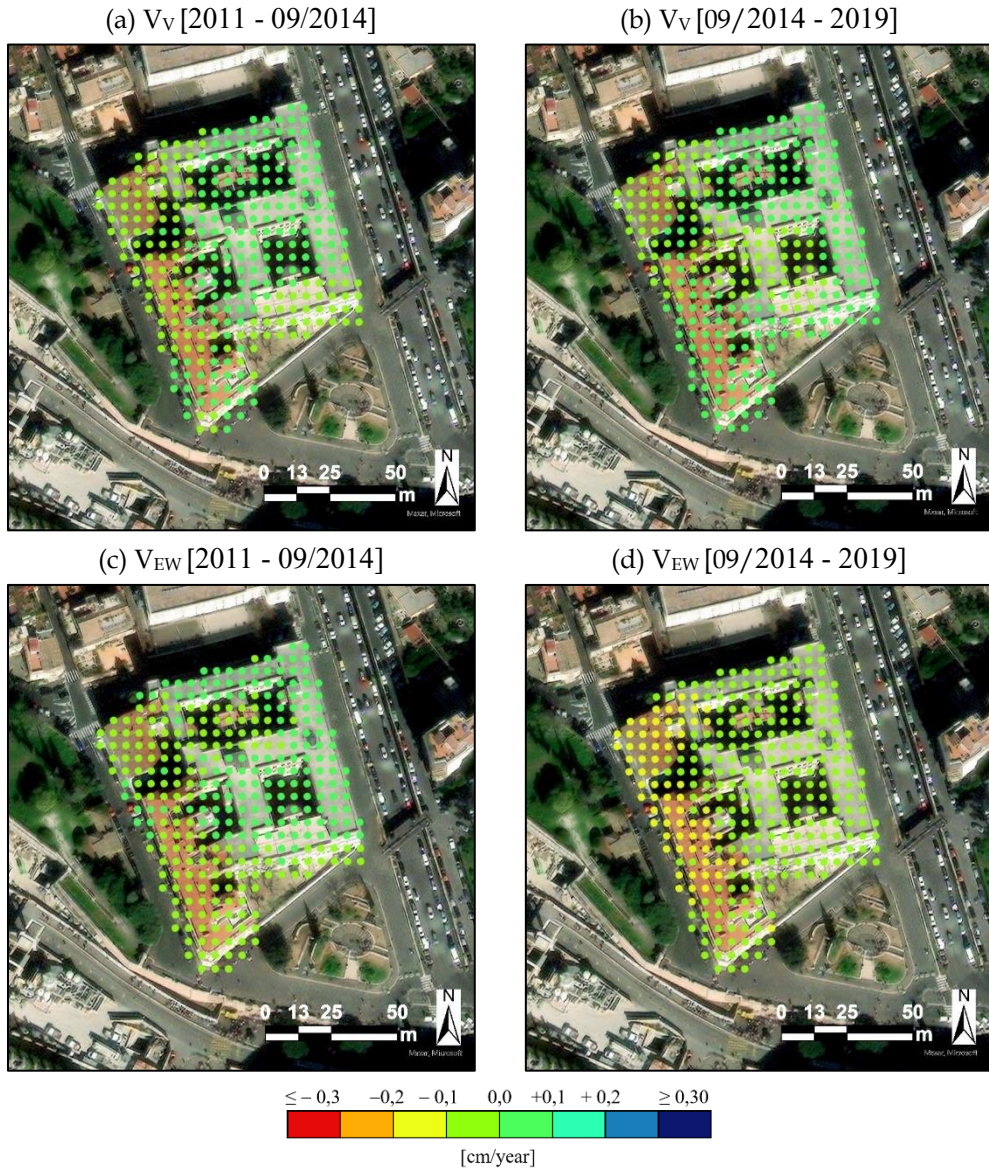


Figure 5.20. Maps of the mean velocity components related to the school buildings considering only the PSs located at the ground level along (a)-(b) Vertical and (c)-(d) East-West directions, for the two considered time sub-intervals (modified from [111]).

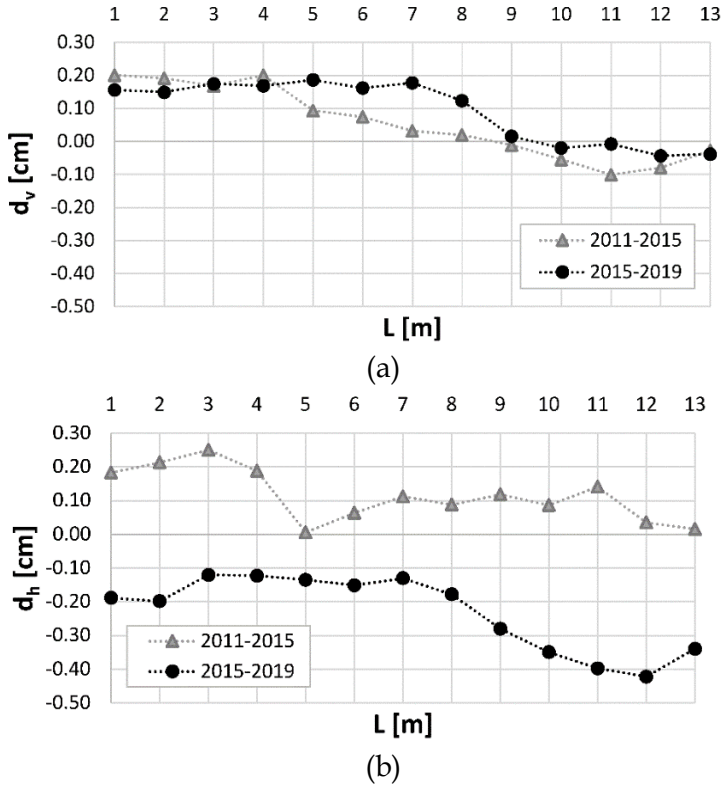


Figure 5.21. Displacement profiles of North façade along (a) Vertical and (b) horizontal East-West component [111].

Regarding the damage assessment, according to Boscardin and Cording (1989) [54], the on-site survey performed in November 2021 led to classify the condition of the overall walls as “slight damage”, because of the presence of cracks easily filled, several slight fractures inside the building and exterior cracks visible, with an approximate width lower than 5 mm. In Figure 5.22 a graph derived from Boscardin and Cording (1989) [54] represents a set of curves for brick bearing-wall structures characterized by different degrees of cracking damage, expressed as a function of ε_h and β . The superimposed arrows indicate the calculated couples of values of ε_h or β of the selected wall, based on the displacement profiles shown in Figure 5.21a and Figure 5.21b. In particular, the direction and magnitude of the grey and black arrows represent the damage condition

attained in the period 2011-2015 and 2015-2019, respectively. The values of the β_{max} and of ϵ_h evaluated in the two considered periods are reported in Table 5.3.

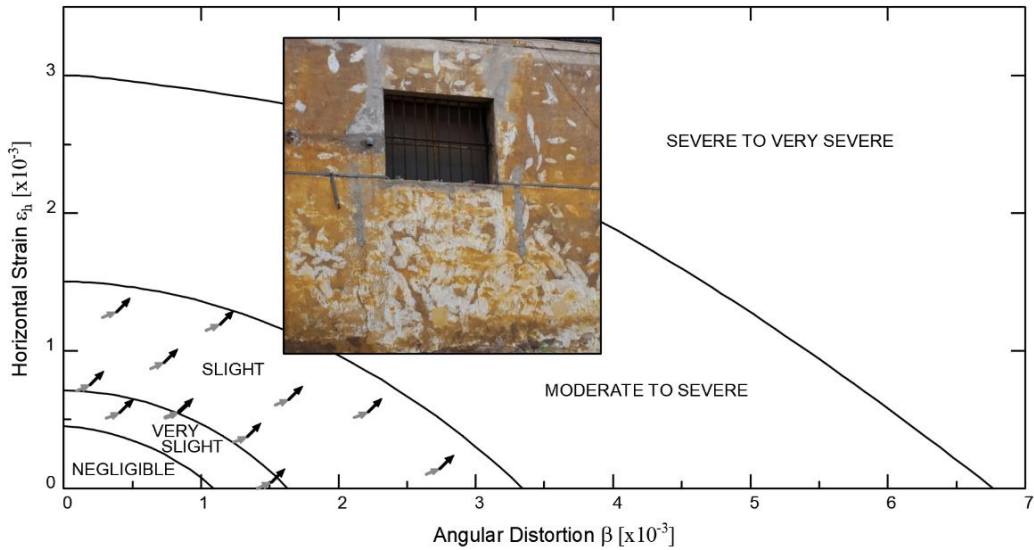


Figure 5.22. Relationship of damage to angular distortion and horizontal extension strain (modified from Boscardin and Cording [54]) [111].

Table 5.3. North façade, maximum angular distortion β_{max} and horizontal strain ϵ_h [111].

	β_{max}	ϵ_h
2011-2015	3,2 E-04	1, 4 E-04
2015-2019	3,5 E-04	-5, 9 E-04

It is worth of interest to highlight that, in this case, an initial damage state can be qualitatively assigned to the building wall, as the damage condition in 2010 (Figure 5.13b). Nevertheless, both the pre-existing deformation history and the damage path that led the wall to its current condition are unknown. For this reason, the potential damage evolution across the monitoring period 2011-2019 is represented by a set of arrows in Figure 5.22, starting from one of the possible points of the area representing the “very slight” or “slight” damage condition, but shown in different positions of the graph. In accordance with the detected

damage condition in November 2021, although there are 2 years of distance between the end of the monitoring and the relief, in which something else could have happened, the final damage condition falls in the “slight” area of the graph. A detail of the portion of the side of the North façade, which the β_{max} and the ε_h are referred, is superimposed on the graph in Figure 5.22.

For the South façade, the reconstruction of the relative displacement profiles along the Vertical and EW direction, respectively, are shown in Figure 5.23a and Figure 5.23b (where L is the length of the wall and d is the displacement). They are referred to the periods 2011-2015 (grey dotted line with triangular markers) and 2015-2019 (black dotted line with circular markers). The displacement profiles show a condition of more stability compared to the North façade. It is to note that this is the façade that has been affected by retrofit interventions through the years, in particular, the use of micro piles in the foundations. The condition at time zero of the South façade is considered to be the end of renovation activities and is represented in Figure 5.14a. The two small vertical cracks detected in the basement level in 2021 are in accordance with the displacement profiles referred to this façade.

The displacements profiles under the East façade, shown in Figure 5.24a and Figure 5.24b (where L is the length of the wall and d is the displacement) show that similarly to the case of the North façade, a change in the trend of the displacement along the EW direction exists between the two analyzed periods. In the second time interval, a negative sign is again found, compatible with the occurrence of a settlement towards the area surrounding the school building. The East façade is oriented approximatively along the NS direction. For this reason, no considerations can be made about in-plane displacements, because of the limitation of the SAR system on the evaluation of the NS displacement component. The use of literature scale accounting for only the vertical displacement could be not accurate enough, since the presence of an out-of-plane displacement would increase the damage. However, the final damage condition observed in 2021 can be classified as “slight” damage, although no information regarding the damage state at the time zero of the monitoring period has been collected.

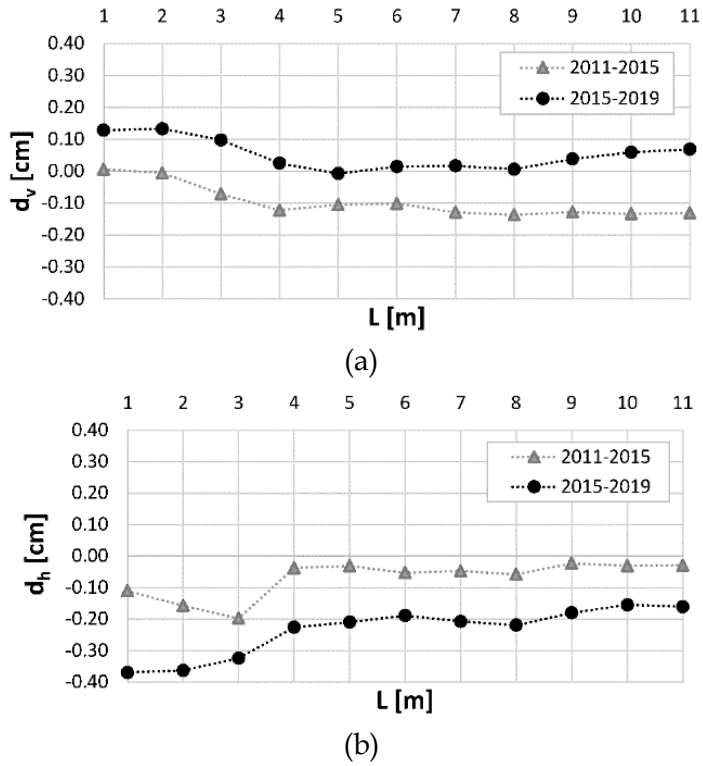


Figure 5.23. Displacement profiles of South façade along (a) Vertical and (b) horizontal East-West component [111].

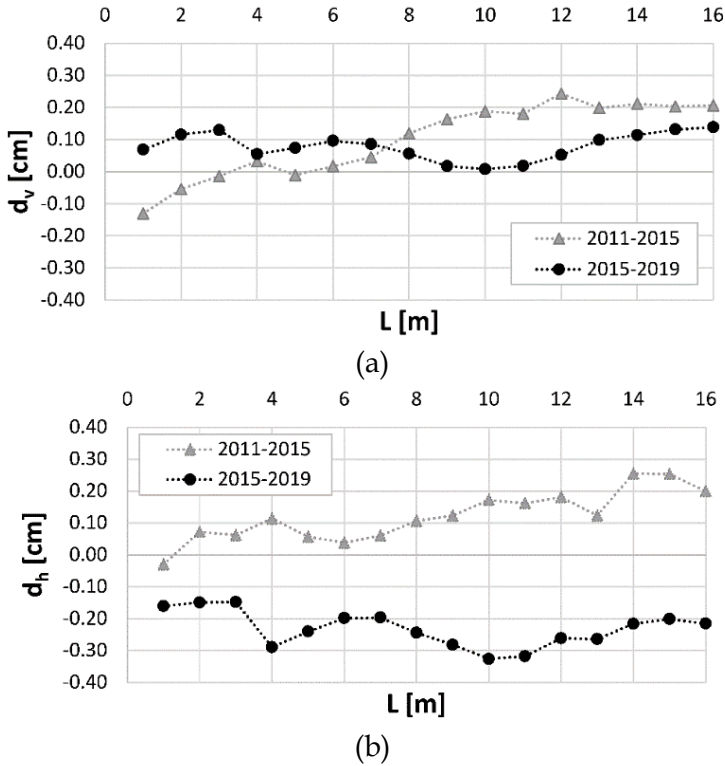


Figure 5.24. Displacement profiles of East façade along (a) Vertical and (b) horizontal East-West component [111].

5.1.2 Discussion

A discussion about the potential and limitations of the preliminary structural assessment and monitoring performed through Satellite SAR data is herein reported.

The possibility to create a volume of the construction is important when the monitoring regards a single building. In this case, when satellite data with great accuracy, such as those derived from COSMO-SkyMed constellation, are available, it is possible to verify the position of the PSs on the actual building volumes, to distinguish those relative to the roof from those relative to the facades or to the ground. Then, in the geological 3D model, the stratigraphic logs of the soil-

structure interaction can be visually checked. First of all, this information is important to understand if the final settlement profiles are those expected in relation to the soil typologies, to validate the reliability of the displacement results. Moreover, in the integrated model, it can be evaluated in which layer the structural foundations of the building are attested. This is very important for the final correlation of the estimated settlements under the monitored buildings with the geological characterization of the subsoil.

The error sources of the integrated model, constituted by the construction's volume and geological model, compared to the plano-altimetric error in the positioning of the PSs, are also limited. In general, it can be stated that

The accuracy level in the integrated model, constituted by the construction's volume and geological model, is derived mainly from the PSs coordinates accuracy. It is considered to be acceptable for preliminary structural assessment and monitoring, to maximize the information from the highest number of PSs and by using the deformations values with a step in the order of meters.

At the end of the monitoring period, the investigated structure could show visible damage related to the deformation processes induced by one or more of the external actions. The expected damage estimated for the monitored period, based on the settlement profiles constructed using satellite SAR data, can be confirmed with field surveys. The damage assessment is influenced by the knowledge of the condition of the monitored structure at the time zero of the overall monitoring period. In general, two different cases can be distinguished:

1. lack of information on the damage status of the building at the beginning of the monitoring time;
2. available on-site survey at time zero (e.g., pictures or output data of a previous monitoring campaign).

Within the second case, two sub-conditions can be identified:

- i) if the walls do not show visible damage at time zero, the current damage can be evaluated neglecting the previous one, and can be correlated to the cumulated displacements measured through the DInSAR observation time interval. This assumption should be carefully evaluated, because an ongoing tensional-deformational state, that has not induced visible damage in the structural
-

elements, could be active;

ii) if a damage pattern is deductible at time zero, the actual damage represents its evolution.

Another issue is relative to the applicability of the different damage classifications available in the literature, when dealing with the DInSAR data monitoring, taking into account the orientation of the monitored structural element. In fact, in the case of EW (or with a small angle with respect to this direction) oriented elements, the classification proposed by Boscardin and Cording (1989) [54] is applicable, such as all classifications accounting for the horizontal strain. Vice versa, because of the lack of information about the NS direction typical of the SAR acquisition systems, for NS-oriented elements, the use of literature classifications neglecting the horizontal strain is recommended.

Retrospective analysis and/or future previsions - limited to a few years - could be performed by extending the results if the data trend is well established in time. The extension could be done for the time series of the displacement components. For instance, regarding the Collector sewer point of disposal n. 7, different trends were observed through the 8 years of monitoring. Therefore, an extension of the global trend for past analysis and/or future previsions cannot be accurate and may induce error.

A correlation between the interpretation of displacement profiles derived by the elaboration of satellite SAR data and the damage relief can be considered a preliminary structural assessment. In fact, as shown for the Vittorino da Feltre school building, for EW-directed walls, the damage condition can be qualitatively extrapolated by the displacement profiles.

5.2 Structural assessment and monitoring

The structural assessment and monitoring can be performed if information about the monitored building are enough to create a reliable analytical structural model (the main are geometrical dimensions, number, shape, and position of structural elements, mechanical properties of the materials, typology of foundations). The aim is the prediction of the structural response and damage level

under a settlement distribution, in this case, DInSAR-derived. Two main categories of information are necessary: a) traditional measurements deriving from on-site surveys or monitoring; b) structural properties (e.g., geometrical properties and mechanical material properties). The traditional monitoring techniques that can provide, at this stage, useful information in terms of displacements or deformations, are related mainly to topographic levelling tools, crack meter instrumentation, strain gauges, and multi-sensor nodes. Moreover, dynamic monitoring can help in the identification of the dynamic properties of the structure, such as periods, modal shapes, and damping factors. This monitoring typology, when repeated in time, also allows for highlighting the presence of possible damages, based on the variation of the measured properties. Instead, a survey should bring evidence in the following fields: the construction age, the geometry of the structural elements, the mechanical materials properties, and the typology and position of the non-structural elements.

The reliability of the structural model, and, consequently, of the results of the analysis, depends on the amount and quality of available information. The structural model can be empirical, semi-empirical, or analytical, increasing refinement from the first to the third one. Also, the output of the preliminary assessment can be used as an initial framework.

In synthesis, by fixing an instant time t_i of interest along the monitored displacement time histories, these data can be used to implement a structural assessment of the selected construction. The overall procedure to perform the structural assessment and monitoring is described in the flowchart presented in Figure 5.25. First, the structural model needs to be defined, selecting a suitable modelling strategy (step 1). Then, the DInSAR deformation measurements, obtained from the processing of ASC and DES images, for the period of interest, integrated with the on-site information, can be used to detect surface ground movements. These displacement profiles can be applied at the ground level of the selected construction (step 2). Then, structural analysis can be conducted to predict the resulting behavior and to evaluate the damage level in the single members at a local level and in the overall building at a global level (step 3), according to the selected code requirements.

When a periodic evaluation of deformation measures through multi-temporal DInSAR considering the SAR images that become available over time is performed (see black line in Figure 5.25 with the progression in time of the structural monitoring from the beginning time t_0), it is possible to re-analyze the structural model with the updated displacement profiles at a newly selected time t_j . This could be a useful procedure to monitor effectively the structural behavior.

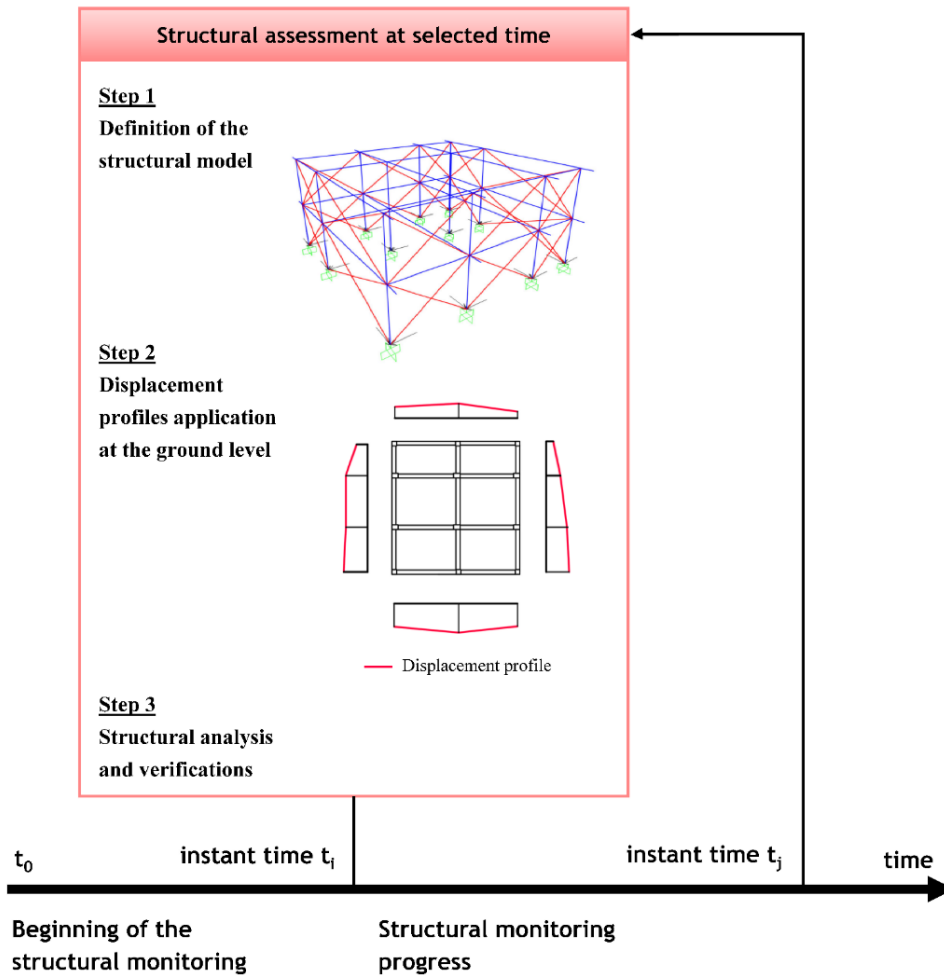


Figure 5.25. Structural assessment and monitoring procedure [31].

An application regarding an existing RC building affected by slow-moving landslides-induced settlements through the multi-temporal DInSAR technique, is presented in §5.2.1. The case study has been the object of a long research work, so over the time the knowledge of its geometry and materials has been enriched with new information. The research results have been published in two journal papers. In the first one (Miano et al., (2021) [57]), the SHM process for the building, considering the landslide action (LAN), to investigate the evolution of damage over infills over the years, is presented. The 3D structure, including the explicit infills consideration, has been modeled based on the information available from a visual survey, obtaining the missing parameters from a simulated design process and literature. Moreover, a global infills damage assessment of the case study building is proposed. Finally, assuming a constant increase of displacements in future years, a prediction of the future expected damage is shown. In the second one (Mele et al., (2022) [56]), other than the landslide, it is supposed the occurrence of an earthquake, considering a multi-hazard scenario, taking into account the stress-strain state induced by the landslide phenomena. A non-linear static analysis procedure is implemented for the code-based seismic safety assessment of the case study building, in two different scenarios: i) a condition of structure deformed only for gravity loads, and ii) in a state of the known landslide-induced deformed configuration. A comparison is proposed between the building seismic safety assessment performed in both cases, with or without the consideration of the landslide-induced displacements, showing the importance of a multi-hazard evaluation.

The steps of the methodology applied in the application are merged in the flowchart in Figure 5.26. The EW and Vertical displacement profiles under the building's sides are calculated. The 3D structural model is created, including structural elements (RC columns and beams) as well as "non-structural" elements (infills) which contribute to the structural behavior. If an active SAR-monitored landslide in the building area is present, the structural analysis begins with the application of the displacement profiles in the structural model, year by year, at the base of the frames representing the columns. Pushover analysis by applying landslide-induced displacements and code lateral forces distribution

on the building's deformed configuration, as a result of gravity loads and landslide-induced displacements, is performed.

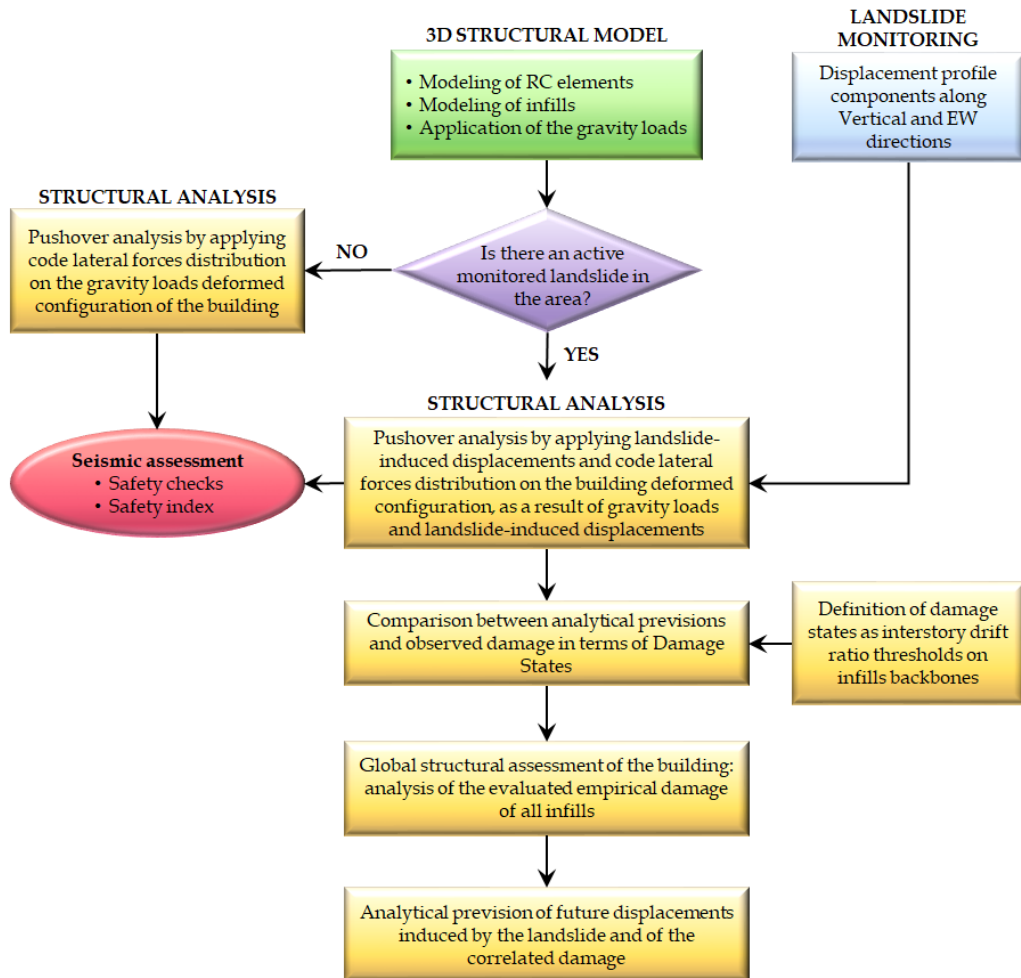


Figure 5.26. Flowchart of the proposed methodology (modified from [56]).

Then, the infills damage condition is assessed: the correspondence between the results of the analysis, in terms of prediction of the damage, are checked with the empirical damage hierarchies, having defined the significant damage states (DSs). The DSs identification is used also to provide a global damage assessment

of the case study building. Finally, a future prediction of the damage is done, repeating the presented methodology using the expected future displacement profiles obtained by extrapolation. If no active SAR-monitored landslide in the building area is present, a pushover analysis by applying code lateral forces distribution on the gravity loads deformed configuration of the building can be performed. After the structural analysis, a seismic assessment can be performed, through safety checks and the safety index evaluation.

A discussion about the proposed structural assessment and monitoring methodology is reported in §5.2.2.

5.2.1 Application in Moio della Civitella

The case study building is located in Moio della Civitella, a city in Campania Region (Italy), whose territory is widely affected by several slow-moving and intermittent rainfall-induced landslides [78]. The building is an independent RC structure, with a rectangular plan of 11,90 m by 11,95 m, built on three levels (Figure 5.27a,b). A visual survey conducted in December 2020 (Figure 5.27c-e) led to the recognition of an RC load-bearing structure with four plane parallel frames, a conventional construction type for a non-seismic structure, as well as the identification of three different types of infills in the perimeter walls. The South-West (SW) side presents regular tuff infills (Figure 5.28a) with a thickness of 25 cm on the ground floor and on one field of the second floor. The other field of the second floor is realized in solid clay bricks (Figure 5.28b) of 12+12 cm. The remaining infills are constituted by double-leaf vertical hollow clay bricks (Figure 5.28c) with a thickness of 8+12 cm.

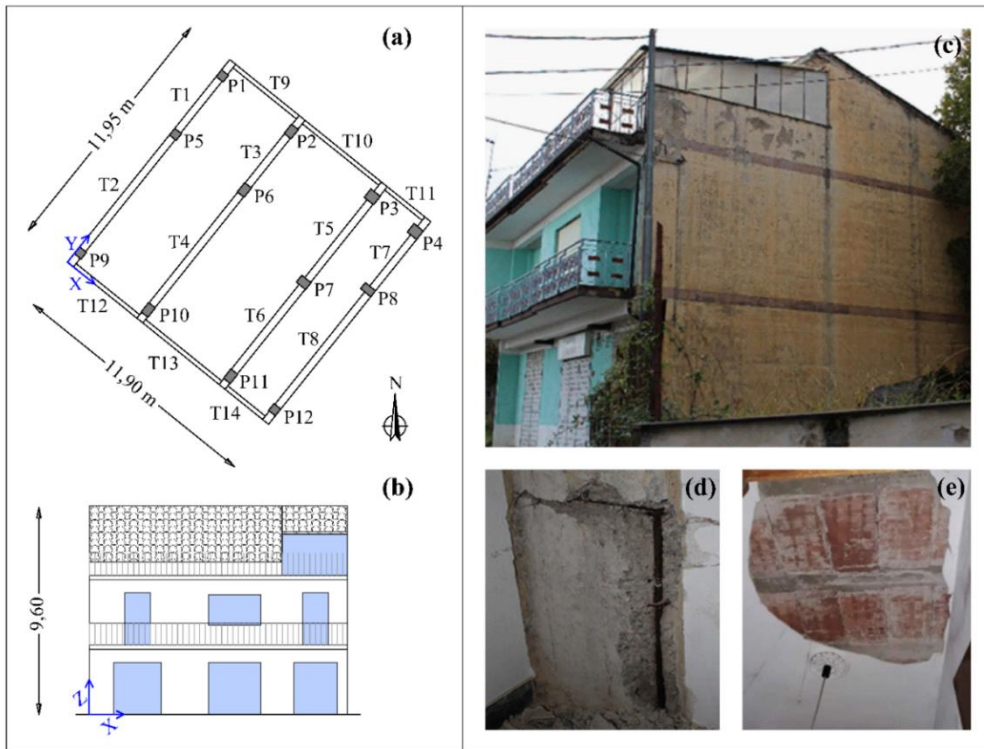


Figure 5.27. (a) Geometrical plan; (b) front view of the SW façade; (c) external picture; (d) smooth bars at the base of the column; (e) RC with hollow tiles mixed floor, focus on the RC joists and hollow bricks (on-site survey, December 2020) [56].

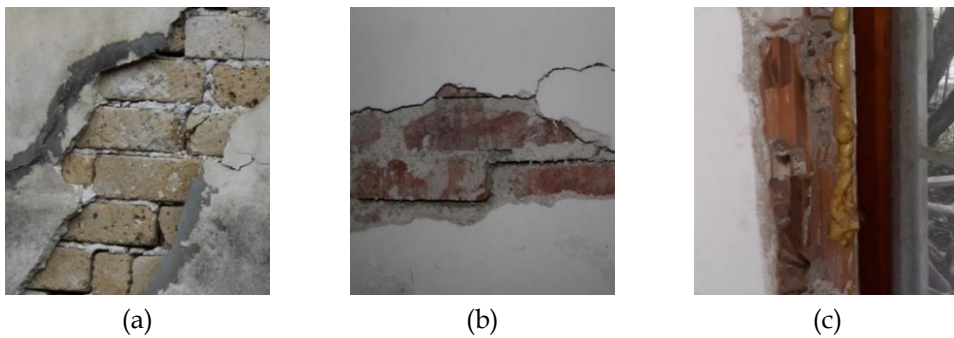


Figure 5.28. Infills details: (a) tuff, (b) solid clay bricks, and (c) hollow clay bricks [56].

In Figure 5.29, the labeling of the building fields is represented (AB, BC, A'B')

and $B'C'$ are the fields including infills without openings, while CD , DE , EF , $C'D'$, $D'E'$ and $E'F'$ are the fields including also infills with openings). The infills are differentiated as follows: i) for color, in hollow clay bricks (blue lines), solid clay bricks (orange lines), and tuff bricks (green lines); ii) for typology of line, in: without openings (continuous lines), and with openings (dashed line).

The building is affected by significant foundation settlements because of the intermittent landslide phenomenon with slow kinematics, as presented in [114].

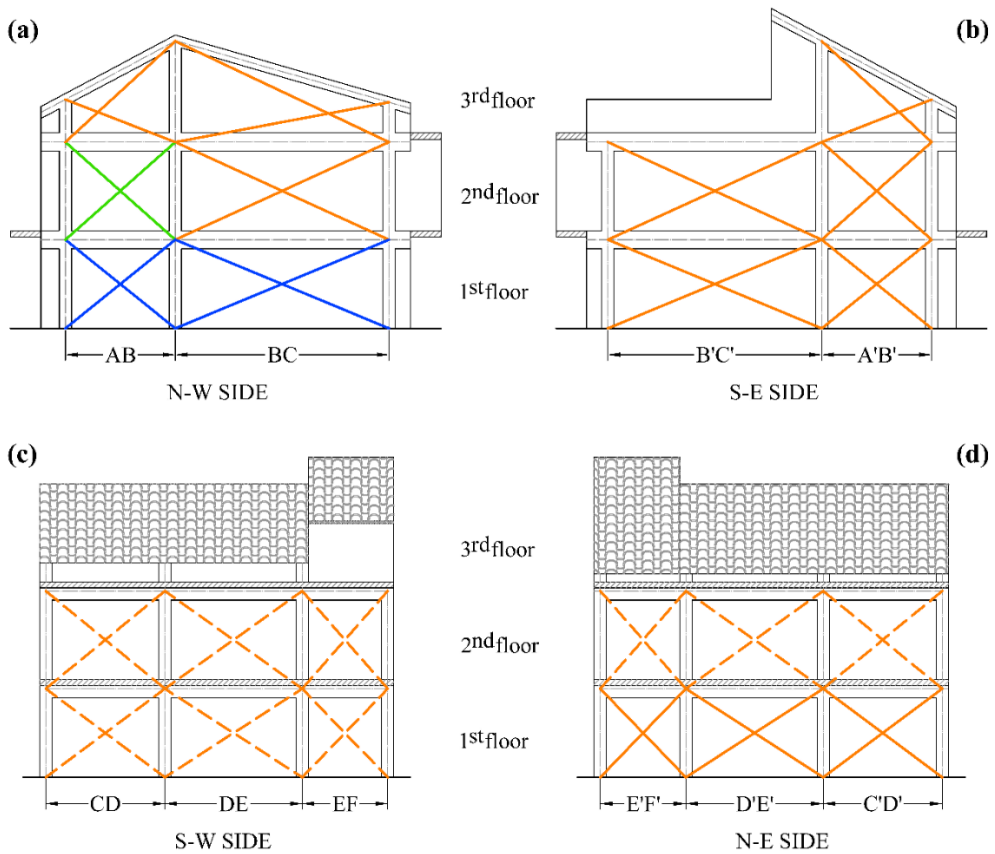


Figure 5.29. Building prospects with identification of the different infills types, differentiated: i) for color, in hollow clay bricks (blue lines), solid clay bricks (orange lines), and tuff bricks (green lines); ii) for typology of line, in: without openings (continuous lines, (a-b)) and with openings (dashed line, (c-d)) (modified from [56]).

5.2.2.1 Infill damage under landslide settlements

The first part of the application (Miano et al., (2021) [57]), was carried out before the on-site survey of December 2020. A structural scheme with frames in both directions was supposed. From the exterior, the presence of only two different types of masonry infills on the ground floor was found, consisting of a single wall facing in regular tuff bricks for three façades, and double-leaf horizontal hollow clay bricks infill walls for the fourth one. The typology found on the ground floor was extended to the whole façade. The mechanical material properties were estimated based on the Code references, and literature indications. No information about the reinforcement of the structural elements were available, then a simulated design was implemented to fill the lack of knowledge. Once defined all the characteristics of the main elements, a structural model has been created using the finite element software SAP2000 [115]. Beams and columns have been modeled as frame elements, while for the infills an equivalent strut model has been used; foundations have been schematized with fixed restrain joints at the base of the baseline columns. The pitched roof has been schematized with a fictitious level placed at a height such as to have an equivalence between the areas of the infills between the second and third-order beams. The mechanical behavior of the RC elements has been modeled through a concentrated plasticity model, considering the non-linear flexural behavior at the ends of structural elements. A simplified three-linear moment-rotation backbone curve has been assigned to beams and columns (considering critical the first two branches of the backbone). The typical responses constituted by the first cracking point ($M_{cr}; \theta_{cr}$), the yielding point ($M_y; \theta_y$), and the conventional ultimate capacity point ($M_u; \theta_u$) shown in Figure 5.30 (for beam T1 and column P1, see Figure 5.27), have been assigned at the end cross sections of each beam and column. The cracking moment M_{cr} and the corresponding chord-rotation θ_{cr} have been calculated based on the elastic theory. The yielding moment M_y has been calculated using a section analysis based on a fiber section method, while the yielding chord-rotation θ_y has been evaluated following the formulation based on the

Commentary to NTC 2018 [116] and Eurocode 8 part 3 [117]. The conventional ultimate capacity moment M_u is assumed to be equal to M_y , thus describing a plastic constant portion of the plastic hinges backbone, until the chord-rotation of conventional ultimate capacity, θ_u , is reached. The latter has been evaluated using the empirical formulation reported in the Commentary to NTC 2018 [116] and Eurocode 8 part 3 [117].

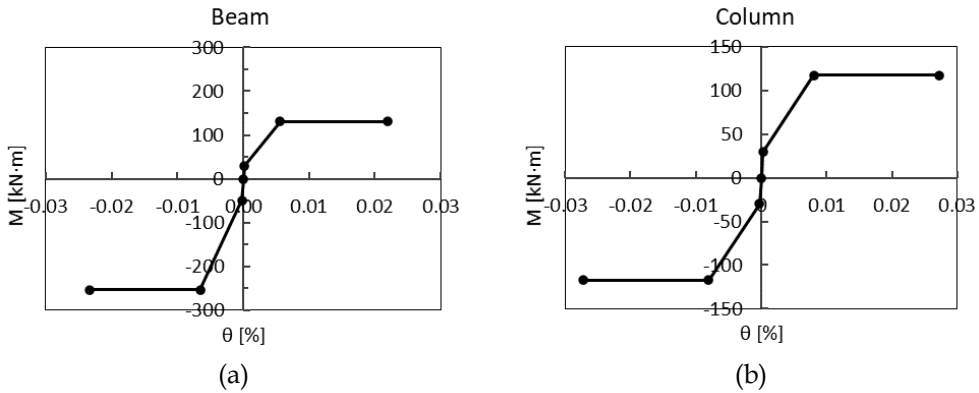


Figure 5.30. Example of plastic hinges backbones of RC (a) beam T1 and (b) column P1 on the 1st floor (with reference to Figure 5.27) [57].

The lateral force-displacement response of the infills has been modeled according to the equivalent single-strut model proposed by Panagiotakos and Fardis (1996) [118]. Then, according to Al-Chaar (2002) [119] and Fardis (2009) [120], the infill panel is represented by an equivalent diagonal strut resistant to compression, with the following geometric characteristics (Figure 5.31): equivalent width a , length D and net thickness of the masonry t_w . The three-linear lateral force-displacement bond has been assigned at the middle cross-section of each diagonal strut as axial hinges.

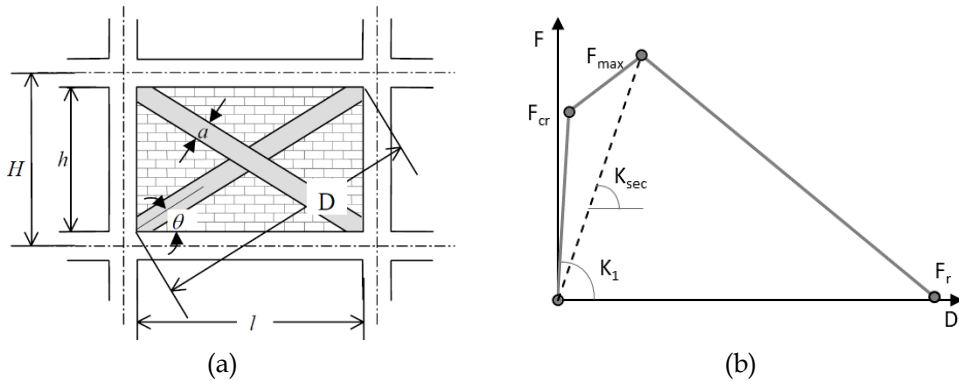


Figure 5.31. (a) Strut geometry (Al-Chaar, 2002 [119]); (b) Force-displacement envelope for infills by Panagiotakos and Fardis (1996) [118] [57].

In Figure 5.32 the 3D fine element model of the building is shown. For the model validation, modal and pushover analysis have been performed, both without and with the infill's presence. All the details about the modeling and the validation are not reported herein because are out of the aims of this thesis but can be found in Miano et al. (2021) [57].

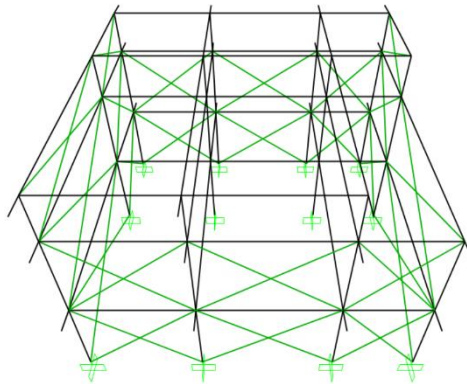


Figure 5.32. 3D structural model of the building [57].

Landslide-induced displacements have been assessed using the DInSAR-derived data, obtained from the processing of ASC and DES CSK images for the period 2012-2016 (see §2.3.2 for details). The overlapping of maps in Figure 2.14a and Figure 2.14b (where the case study building is indicated with a black oval)

with a 2-m buffer around the building scheme provides mean velocity (Figure 5.33) and time-series of identified scatterers.

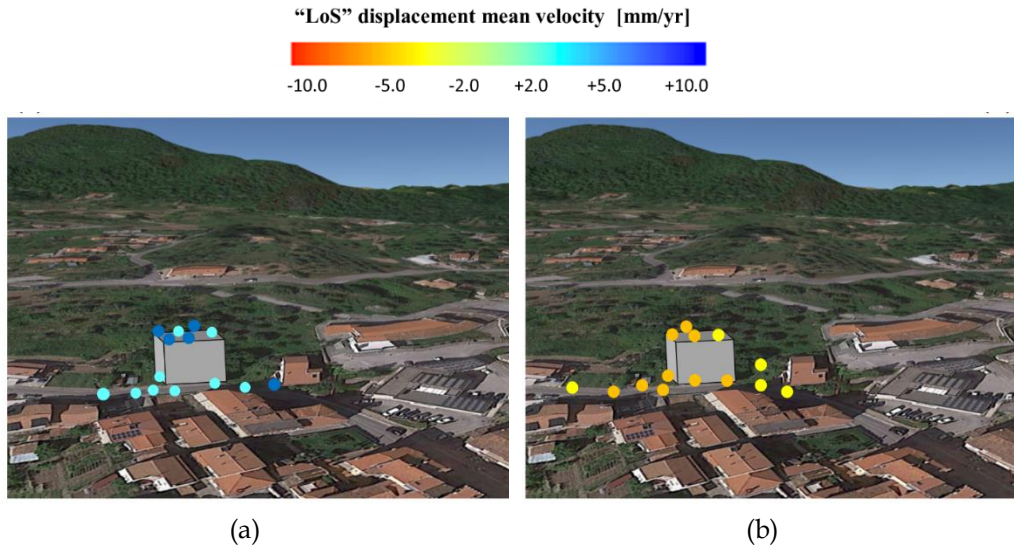


Figure 5.33. LOS mean velocity map of targets identified on the analyzed building using COSMO-SkyMed data: along (a) ascending and (b) descending tracks (modified from [57])

For a more detailed assessment of building structural performance affected by ground instability phenomena, the cumulated displacement of identified targets has been considered instead of their mean velocity. ASC and DES discretized points have been interpolated through the IDW method, thus providing continuous LOS displacement maps at the end of each year. The cell size of the IDW interpolation has been set at 3 m, according to the 3×3 m resolution of CSK products. Subsequently, the combination of maps obtained along the two tracks has allowed the detecting of cumulated Vertical and EW components of movement [121], [122] with millimeter accuracy at the end of each year in the period 2012–2016 thus providing profiles of cumulated Vertical and horizontal EW displacements occurred to building foundations, as shown in Figure 5.34.

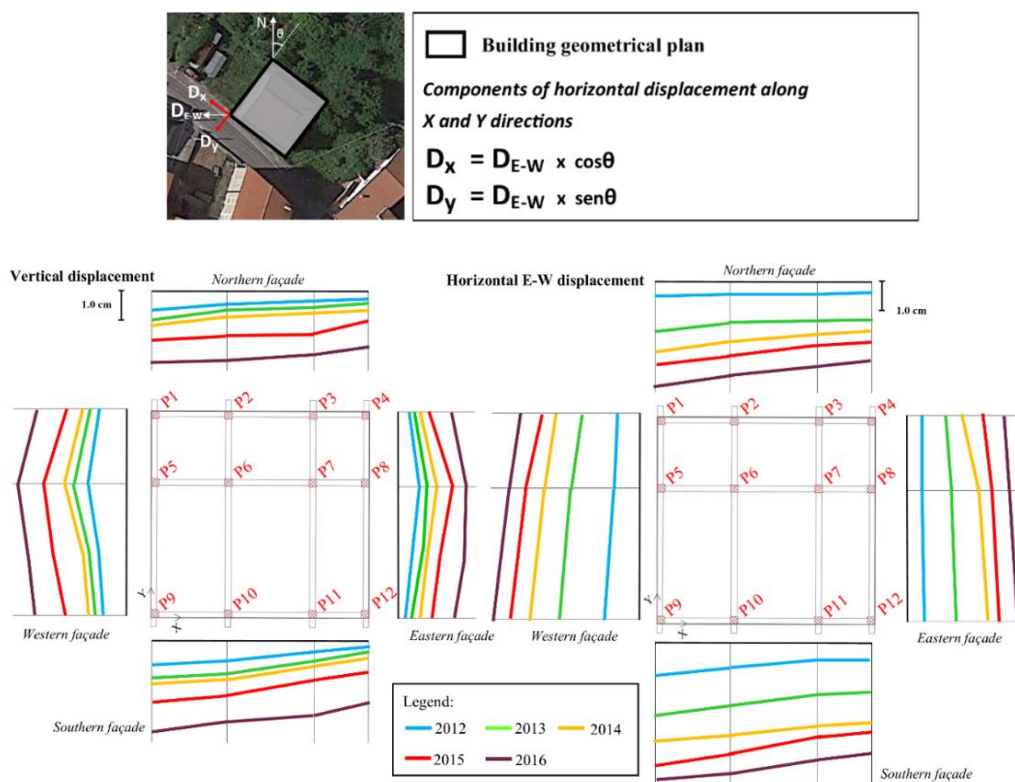


Figure 5.34. Displacement profiles affecting building foundations at the end of each year in the period 2012–2016 (modified from [57]).

In addition, the trigonometric decomposition of horizontal EW movement in the two components along each building façade direction allowed to get real components of movements along x , y , and z directions, applied to foundations elements. During the period 2012–2016, multi-temporal DInSAR analysis showed cumulated displacements at ground level in the surrounding areas up to 2.5 cm and 4.1 cm, along vertical (z) and horizontal (x , y) directions respectively, thus highlighting a movement characterized by a horizontal component higher than the vertical one.

For the NW and SE façades, a quantitative one-to-one comparison for the in-fills between the observed damage and the analytical previsions is reported. The

Same is not possible for SW and NE facades because of the presence of openings (that can partially alter the flow of diagonal tensions) and the difficulties of investigation during the survey, respectively.

Two photographs taken during an investigation in 2015 show how the damage has evolved up to that year (Figure 5.35a for the NW side and Figure 5.35b for the SE side). The lesions have been highlighted on the pictures with different colors, corresponding to different amplitudes: green indicates lesions of less than 1 mm of amplitude, yellow refers to lesions of the order of 1-5 mm, while in red are lesions with a width greater than 5 mm.

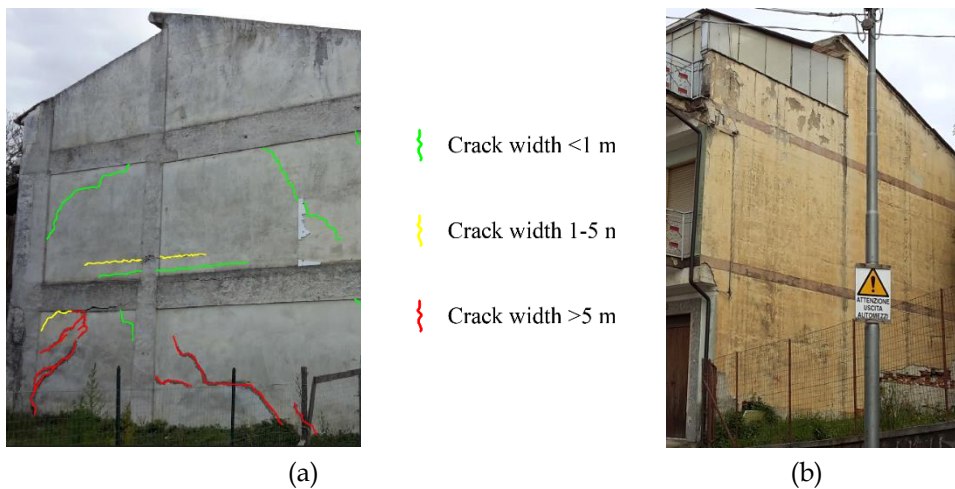


Figure 5.35. Identification of crack pattern on infills in 2015 of (a) NW side and (b) SE side (modified from [57]).

The DSs identification has been conducted for the infills, based on specific Interstory Drift Ratio (IDR) target thresholds, defined on the infills backbone curves: a first one for tuff bricks infills, according to Cardone and Perrone (2015) [123], and a second one for hollow clay bricks infills, based on the proposal formulated by De Risi et al. (2018) [102]. In Cardone and Perrone (2015) [123], the four considered DSs are described as follows (Figure 5.36):

- DS1 (Light cracking): detachment of the panel from the RC frame (top beam and mid-height columns), light diagonal cracking of the infill

(width <1 mm) in both directions;

- DS2 (Extensive cracking): extensive diagonal cracking (1 mm < width < 2 mm) in both directions (25-35% of the panel area). Possible failure of some brick units, located on the upper corners and top edge of the infill;
- DS3 (Corner crushing): detachment of large plaster area and significant sliding in the mortar joints, crushing and spalling of brick units (30% of the panel area);
- DS4 (Collapse): in-plane or out-of-plane global collapse of the wall;
- DS1 is assumed to occur for an IDR equal to 2/3 of the IDR associated with DS2, DS2 occurs for an IDR corresponding to the peak force strength, DS3 and DS4 are deemed to occur at the IDRs at which a strength loss in the skeleton curve is of the order of 20% and 50%, respectively.

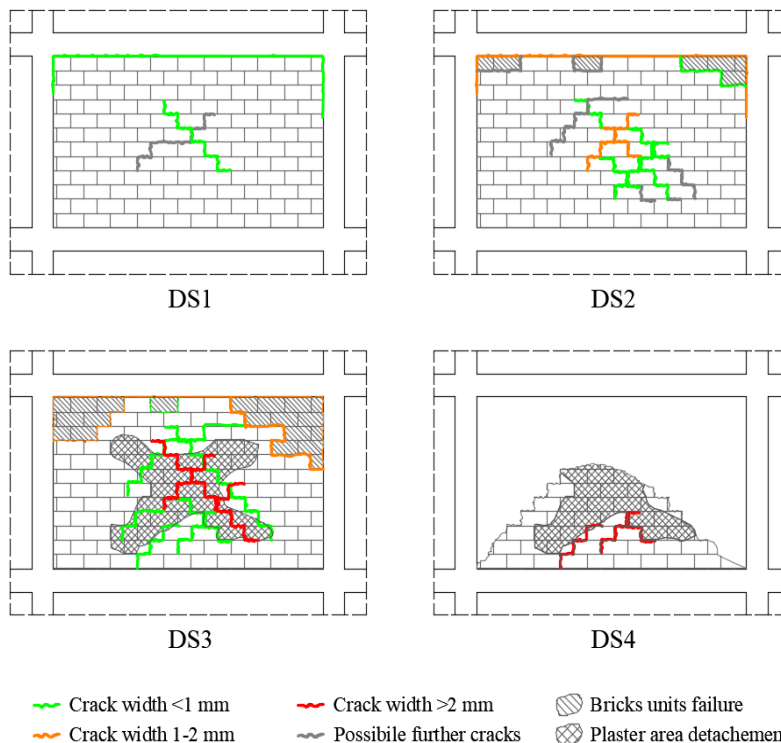


Figure 5.36. Damage states (DSs) of masonry infills without openings [57].

In De Risi et al. (2018) [102], the IDR value corresponding to the achievement of the i^{th} DS has been directly associated with the IDR value related to the peak load of the infill experimental response (IDR_{peak}), obtaining the definition of the following functional relation:

$$IDR_i = \alpha_i \cdot IDR_{peak} \quad (10)$$

where α_i is 0.30 for DS1, 1.00 for DS2, 2.50 for DS3 and 4.50 for DS4.

The amplitude of the cracks has been considered as the difference between the amplitude in 2015 minus the amplitude in 2011).

The NW side first-floor (AB and BC) shows mainly the typical infill damage called “diagonal tension” (Figure 5.35a) with diagonal cracks in both directions of width varying from less than 1 mm to more than 5 mm, affecting at least 25-35% of the panel area. The NW side second-floor infills (AB and BC) present horizontal cracks at the base and diagonal cracks in both directions (Figure 5.35a), of width up to 5 mm, affecting at least 25% of the panel area. It can be argued that the NW side infills are in a DS2 condition. Regarding the SE side (A'B' and B'C'), it can be observed that in the 2015 survey, a starting “sliding shear” mechanism was found on the first floor for the infill A'B' (Figure 5.35b), already existing in 2011 in a similar condition. This mechanism affects about 30% of the panel and can be associated with a DS3.

Regarding the infills analytical response, Figure 5.37 shows the compression backbones of each studied infill member. The points corresponding to the four considered DSs previously described are marked on each envelope. The status of the axial plastic hinge representing the infill is also indicated with a triangle, concerning the year for which the highest damage level is reached in the infill. This classification refers only to the compression side of the backbone, while it is not meaningful to report the condition of the tensile infills on these envelopes. A tensile infill is a panel in which both diagonal struts are in traction. The potential damage is however expected and coherent with the analytical previsions (e.g., diagonal cracks parallel to the less tensile diagonal). Concerning the NW façade, analytical previsions evidence that the most severe damage condition for the infills field AB occurs in 2012, where at both the first and second floor DS2 is

reached (Figure 5.37a and b). Regarding the infills field BC in 2012, when the maximum damage is expected coherently with the other infills field of the NW façade, both the struts are in tension at the first floor. Nevertheless, it is not possible to report the DS on the backbone, it can be argued that extensive damage parallel to the less tensile strut may have occurred. This condition is reported with the letter T in Table 3 and can be compatible with a DS2 condition. Moreover, the analysis shows that the infill reaches a DS2 also in compression in 2016 (Figure 5.37c). For the infills field BC on the second floor, there is a DS0 condition, while it is confirmed that the higher displacements level is reached in 2012. Finally, regarding the S-E side ($A'B'$ and $B'C'$), it can be observed that in 2015, the state of damage is DS0 (Figure 5.37e, f, g, and h), but quite close to the onset of DS1 for the $A'B'$ infills, coherently with the observed small detachments from the upper beam.

The quantitative one-to-one comparison between analytical results and observed damage in 2015 (the year of the on-site survey) is proposed in Table 5.4 for the NW and SE façades.

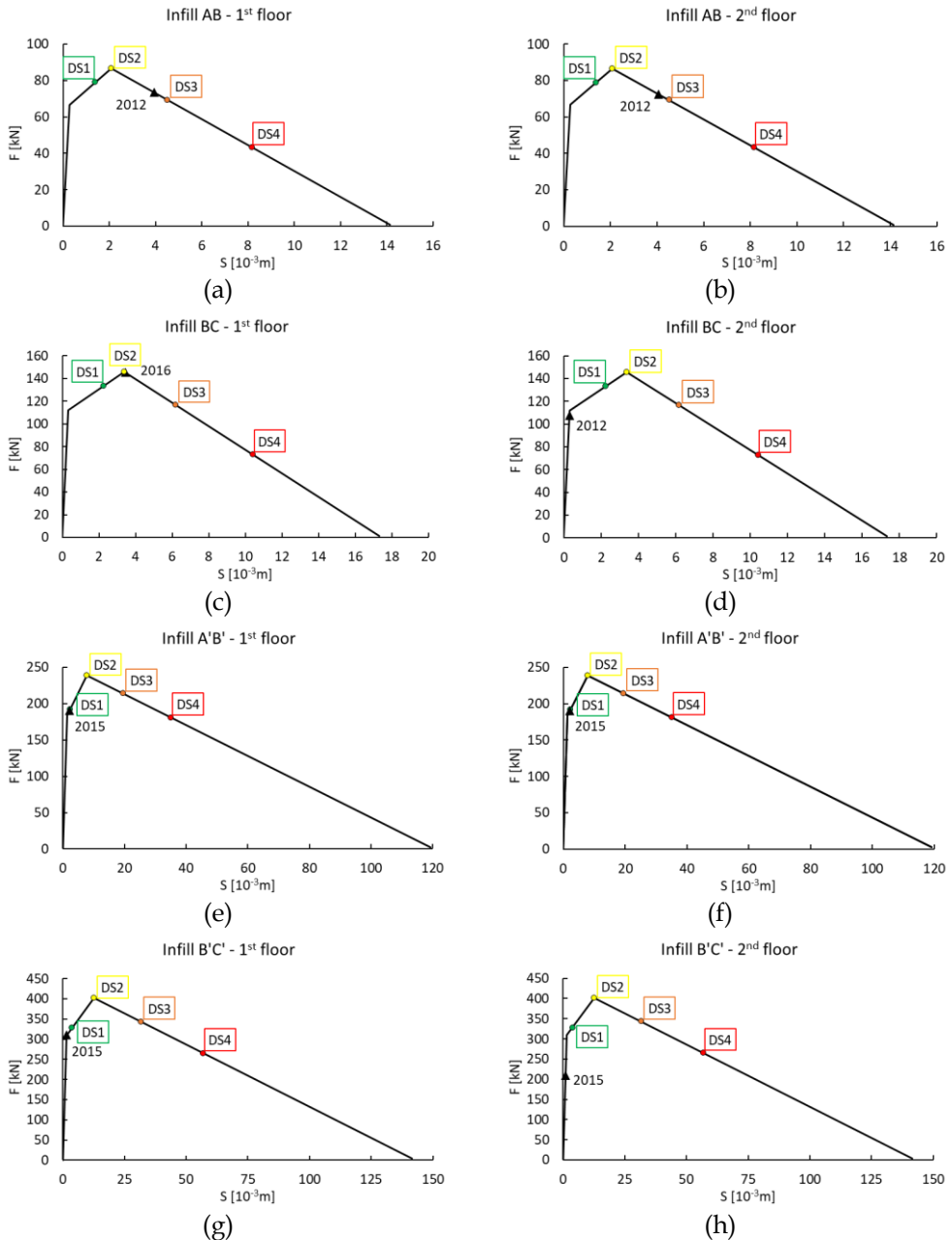


Figure 5.37. Identification of DSs on infills' backbone according to: (a)-(d) Cardone and Perrone (2015) [123] and (e)-(h) De Risi et al. (2018) [102], [57].

Table 5.4. Comparison between the DSs classification based on empirical observation and the classification obtained by analytical previsions (DS0=no damage, DS1=light cracking, DS2=extensive cracking, DS3=corner crushing, DS4=collapse, T=both tense struts, compatible with extensive damage) (modified from [57]).

OBSERVED DAMAGE			ANALYTICAL PREVISIONS		
NW façade					
Observed DS	Infill field		Expected DS	Infill field	
	AB	BC		AB	BC
1 st floor	DS2	DS2	1 st floor	DS2	T
2 nd floor	DS2	DS2	2 nd floor	DS2	DS0
(a)			(b)		
SE façade					
Observed DS	Infill field		Expected DS	Infill field	
	A'B'	B'C'		A'B'	B'C'
1 st floor	DS3	DS0	1 st floor	DS0	DS0
2 nd floor	DS0	DS0	2 nd floor	DS0	DS0
(c)			(d)		

As demonstrated in Table 5.4, there is a reliable agreement between the empirical and the analytical infills' DSs definitions. Apart from the difference found on the first floor A'B' infill and related to the fact that the existing damage mechanism of sliding shear is not assessed by the adopted equivalent diagonal single strut model and it is already present in 2011, the only remarkable difference can be found in the infill field BC, where however the highest damage level is expected in 2012. This difference can have multiple reasons, e.g., the adoption of a seismic model in a different field (there are cases where both the diagonals are tense and then not quantitatively judicable) or the uncertainties in the geometrical and mechanical on-site survey of the structure. Finally, this result leads to affirm that a long displacement time series, acquired through the multi-temporal DInSAR technique, can be used to provide a good assessment of the infills of the building and to formulate predictions about the structural future damage. This may be possible if displacements increase showing a more or less constant trend over the years, as in the case of landslides-induced ones.

A damage assessment through the years of all the building infills on the first two floors is shown in Figure 5.38. The structural assessment results are reported in form of histograms, distinguished by floor and by year, from 2012 to 2016. Each column represents the number of infills on that floor, which in that year reached a particular DS. An additional DS has been considered, DS0, in which not only compressed infills that present no damage are included, but also tense infills for which it is not possible to analytically quantify the DS. In each graph, the total number of infills is 10, considering that there are 4 infills without openings on the SE side (AB, BC, A'B' and C'D') and 6 infills with openings on the NW side (CD, DE, EF, C'D', D'E', E'F'). It can be observed that no infill reaches DS3 or DS4, while damage is limited to extensive cracking (DS2). However, at the end of the assessment, in 2016, a significant number of elements is extensively damaged, with 4 and 2 infills in DS2 on the first and the second floor, respectively. Finally, it is to note that among the three modelled infills of the third floor, only one (AB) reaches a DS2 through the monitored years, while the other two don't show any damage. This global result was expected, as the landslide caused ever-increasing displacements of the foundation soil over the years.

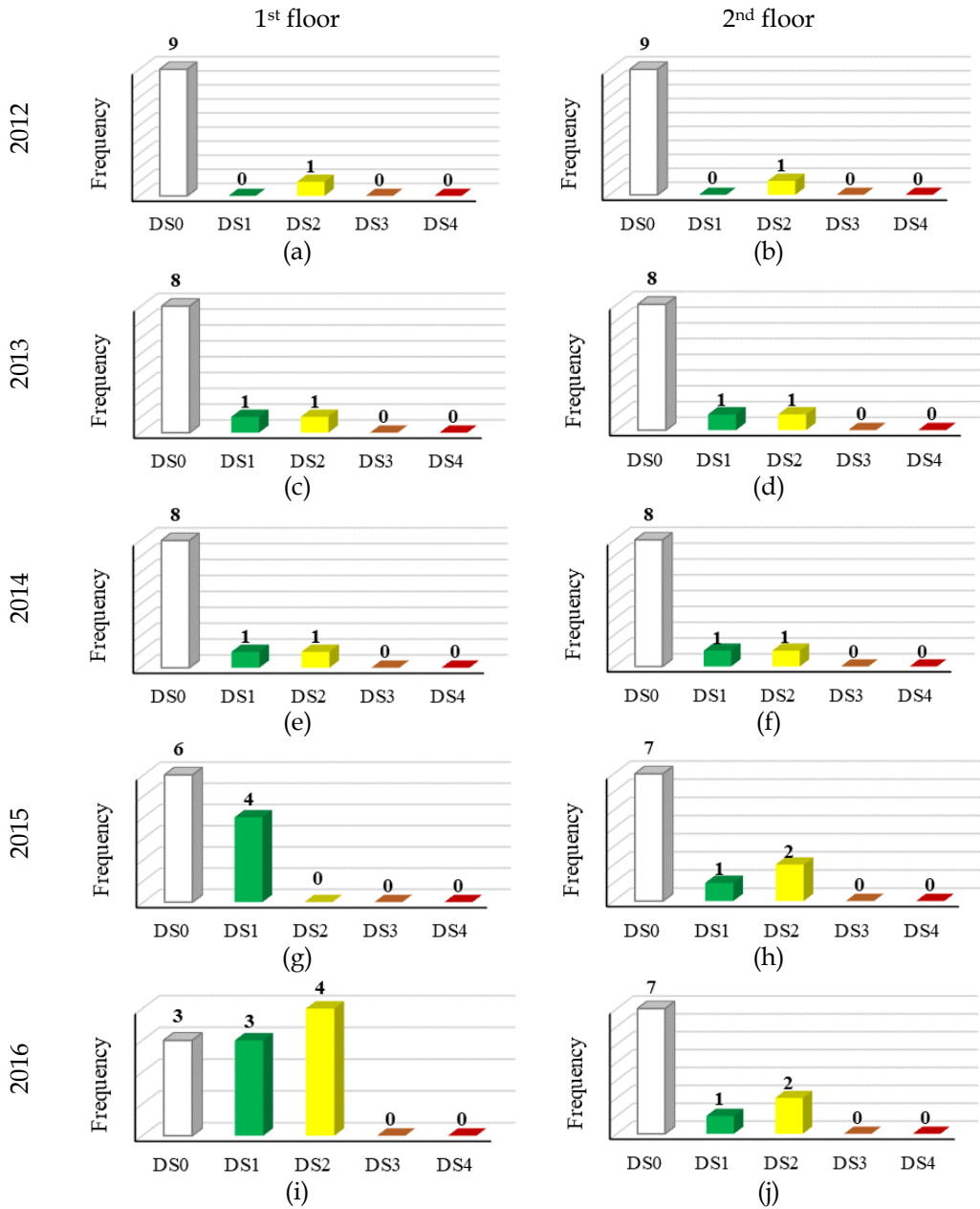


Figure 5.38. Infills that have reached the i -th DS, divided by floor and year of evaluation: (a) and (b) 2012; (c) and (d) 2013; (e) and (f) 2014; (g) and (h) 2015; (i) and (j) 2016 (modified from [57]).

Ground displacements at the base of the columns in the vertical (S_z) and in the two horizontal directions parallel to the building (S_x and S_y) have grown almost linearly in the period 2012-2016. A prediction of future displacements has been carried out assuming that the trend remains constant also in the following years, up to 2025. The displacements related to two significant columns located at opposite vertices of the building plan (Figure 5.39a) are shown. Cumulated displacements over the years are represented, for P1 (Figure 5.39b) and P12 (Figure 5.39c). X and Y directions are parallel to the building walls (Figure 5.39a), while the Z direction is vertical. Circles indicate the experimental data used for the linear regressions, while the predicted values in the year 2025 are represented by rectangular indicators. For the two horizontal displacement components, S_x and S_y , the negative values are referred to as displacements toward the East. The color associated to S_x is green, and the associated regression line is the dotted one. Displacements S_y are indicated in orange, with a continuous regression line. Finally, vertical displacements S_z are represented in blue, and the associated regression line is the long dotted one. In this case, the minus sign indicates downward displacements.

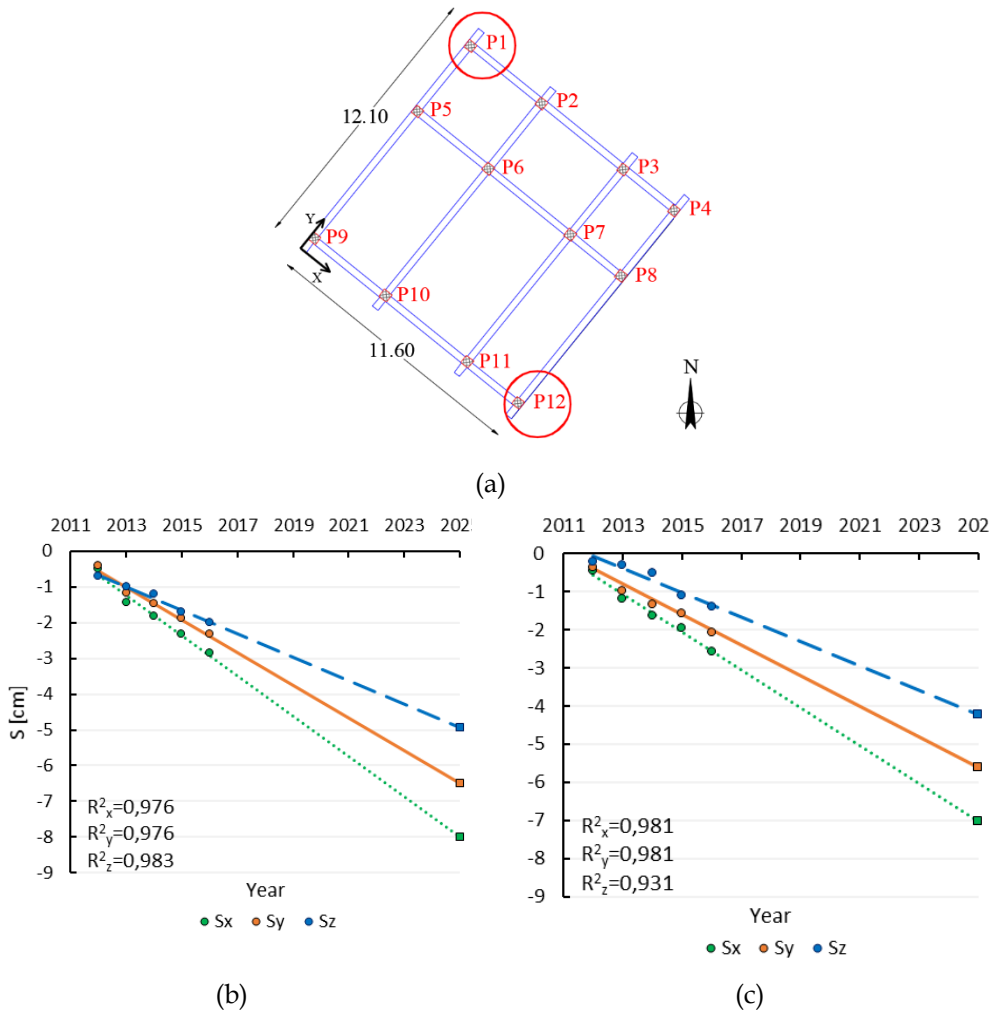


Figure 5.39. (a) Identification in plane of RC examined columns; linear regression of displacements along X, Y and Z direction at the base of (b) column 1 and (c) column 12 (modified from [57]).

A prediction of the expected damage in the year 2025 has been carried out by applying the displacements, forecast as just described, at the base of the columns of the ground level. The results are presented in Figure 5.40, where two histograms (one for each floor) report the number of infills on that floor which in that year reached a particular DS. It can be observed that on the first floor, the

situation does not change in terms of the reached DSs, compared to 2016, nevertheless, the damage is progressing. For the second floor, instead, an infill that was in DS0 reaches DS1. However, the maximum damage remains at the level of extensive cracking (DS2).

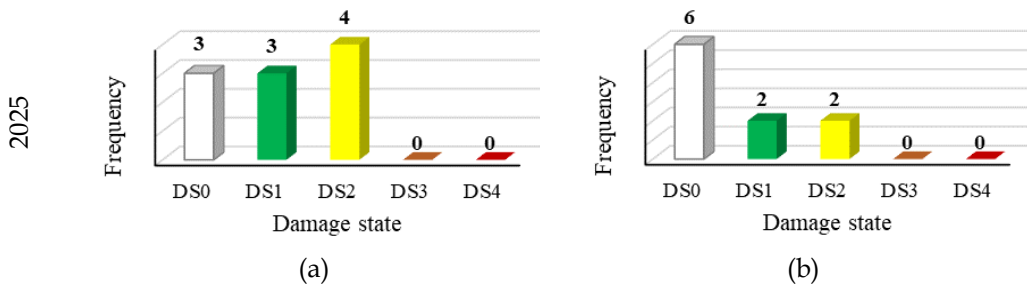


Figure 5.40. Prevision of the number of infills that will reach the i^{th} DS in 2025, on (a) first floor and (b) second floor [57].

5.2.2.2 Seismic safety assessment under landslide-induced damage

The second part of the application (Mele et al., (2022) [56]) was carried out after the on-site survey conducted ad December 2020. The visual inspections led to the recognition of the number and position of smooth longitudinal bars and transversal stirrups in RC elements (Figure 5.27d). The missing parameters, related to the mechanical material properties, have been taken from literature studies and codes. Once defined all the characteristics of the main elements, a structural model has been created using the finite element software SAP2000 [115], using all the modeling hypotheses mentioned in §5.2.2.2 (frame elements for beams, columns, and infills; fixed restrains joints for foundations; equivalent height for the pitched roof). The inelastic cyclic response of RC members has been reproduced by applying a modeling approach specifically elaborated for RC members with plain bars [124]. The non-linear flexural behavior, represented in Figure 5.41, has been concentrated at the ends of RC elements. Characteristic points/conditions of the base moment (M) - chord rotation (θ) multilinear relationship have been defined as the yielding point ($M_y; \theta_y$), the peak load point

$(M_{max}; \theta_{max})$, the “ultimate” condition point with the attainment of $(0.8 M_{max}; \theta_{ult})$, and the zero-resistance point, corresponding to the complete loss of lateral load capacity of the element. The infills have been modeled according as illustrated in §5.2.2.2.

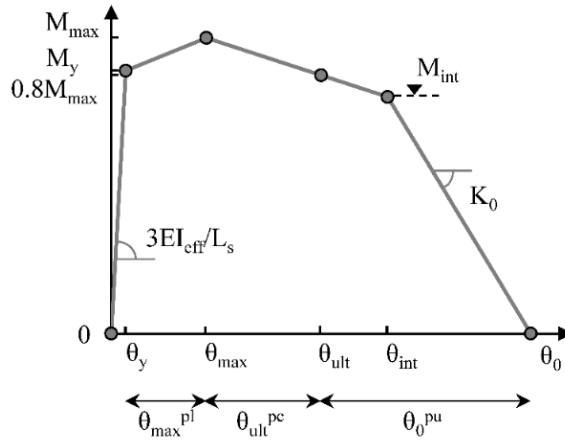


Figure 5.41. Characteristic points and assumed parameters of the base moment (M) - chord rotation (θ) response envelope [56].

In Figure 5.42 the 3D finite element model of the building is shown. Also, in this case, model validation has been performed through modal and pushover analysis, both without and with the infill’s presence. All the details about the modeling and the validation are not reported herein because are out of the aims of this thesis but can be found in Mele et al. (2022) [56]. The action of the earthquake (EQ) is applied to the slow-moving landslide-induced deformed configuration of the building (landslide plus earthquake [LAN+EQ] scenario).

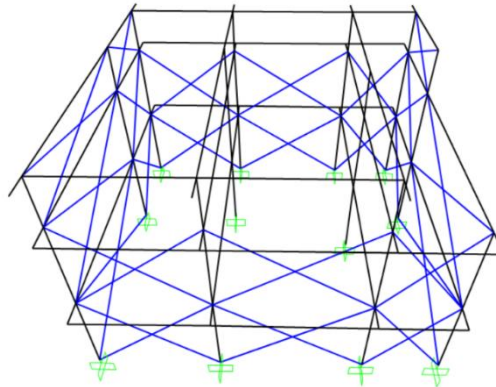


Figure 5.42. 3D structural model of the building [56].

In this second part of the application, the landslide-induced displacements are referred to the two investigated periods, respectively 2012-2016 and 2017-2019 (see §2.3.2 for details). As an example, the time series of displacements of two PSs are reported (Figure 5.43), respectively in ASC (A1) and DES (D1) orbits. The two time series of displacement assume opposite signs, meaning that the real displacement has a prevalent horizontal component.

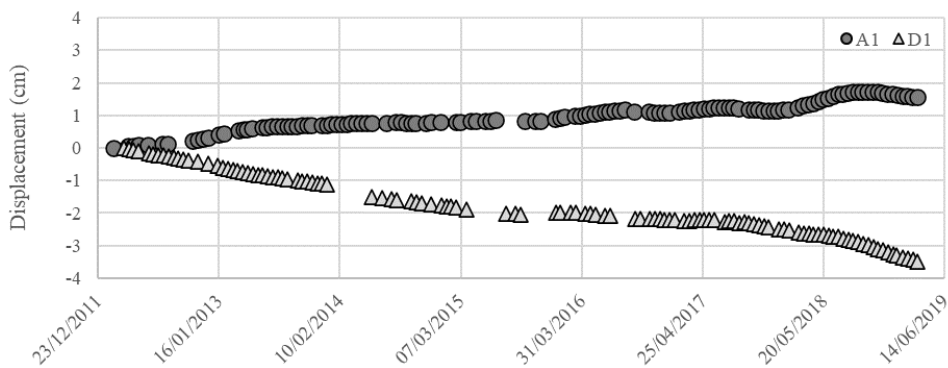


Figure 5.43. Time series of displacements of an ascending (A1) and a descending (D1) PS, located on the investigated building [56].

Subsequently, the combination of the maps obtained along the two tracks has allowed detecting of the cumulated Vertical and EW components of movement, with millimeter accuracy, at the end of each year of the period 2012-2018, and for

the first three months of 2019, providing profiles of cumulated Vertical and EW displacements occurred to building foundations (shown in Figure 5.44). The cumulated components of movement at the end of 2019 and 2020 have been obtained by extending the linear regression of the data calculated between 01/2012 and 03/2019 to the end of the mentioned years, for each column.

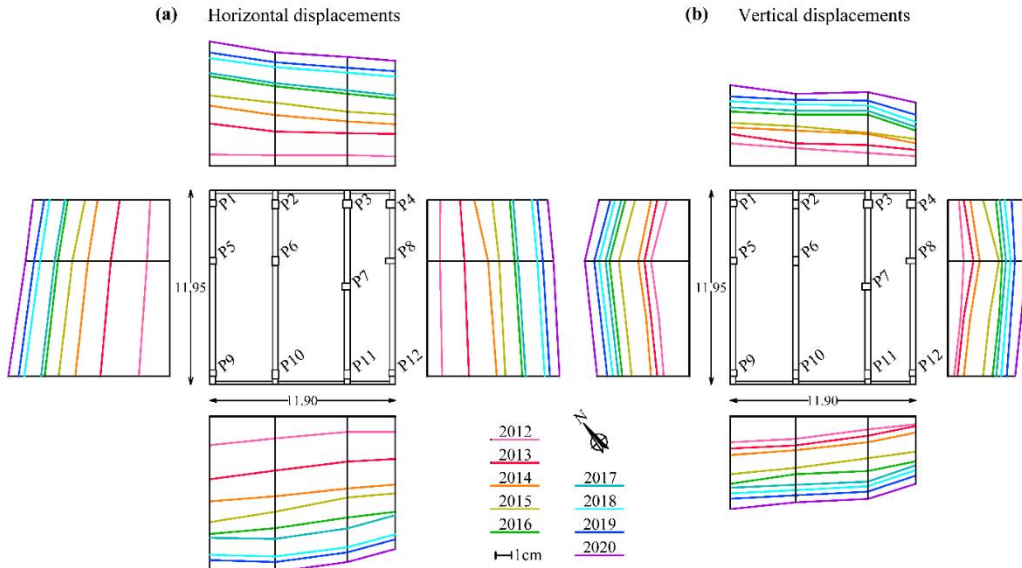


Figure 5.44. Displacement profiles extracted for the building foundations at the end of each year in the period 2012–2020: (a) horizontal, (b) Vertical (modified from [56])

The first part of the seismic assessment procedure consists of the seismic verifications for the capacity of the RC elements at the Life Safety limit state (LS-ls), and for the deformability at the Damage Limitation limit state (DL-ls). The seismic assessment procedure is widely explained in Mele et al. (2022) [56]. In synthesis, a non-linear static analysis procedure, also known as “pushover”, has been implemented. As recommended in NTC (2018) [125], two monotonically increasing patterns of lateral forces are applied to the structure in the control point, represented by the center of the roof floor masses. In the pushover curves of the Multi-Degree Of Freedom (MDOF) systems, the base shear, V_b , is expressed as a function of the roof displacement, Δ_{top} . The structural checks at LS-

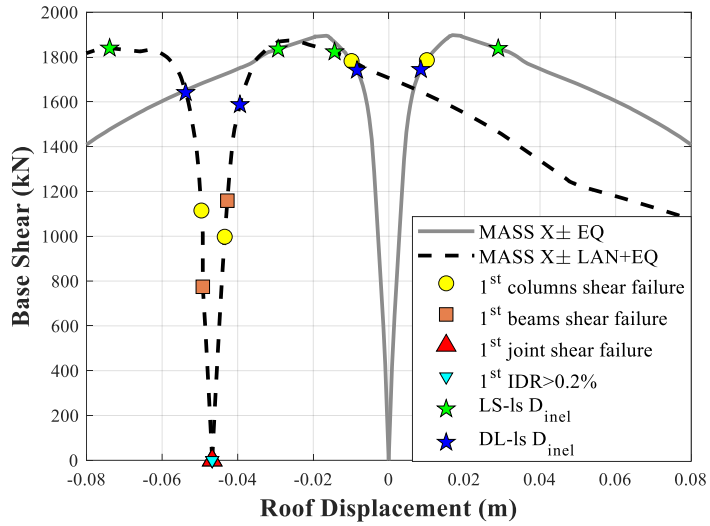
ls are performed with regard to ductile mechanisms and brittle mechanisms. The structural capacity of beams and columns in ductile terms is evaluated according to the capacity model suggested by the Commentary to NTC (2018) [116] (the same model adopted in EC8-3 [101]), in terms of chord rotation capacity. The brittle failures for beams, columns, and beam-column joints are checked according to the capacity models suggested by the codes [116], [117]. The structural checks at DL-ls are performed in terms of stiffness, with regard to the displacements. In this case, for CU II, and having explicitly considered the infills in the model, the condition can be considered satisfied when the limit provided by the NTC (2018) [125] for masonry structures is respected (interstory drift between two following floors lower than 0.2%).

The seismic action on the building has been evaluated based on a reference period, V_R , obtained by multiplying the nominal life of the structure, V_N (50 years for constructions with ordinary performance levels) by the coefficient of use, C_U (equal to 1 for ordinary residential buildings). The horizontal components of the seismic action have been considered through the elastic response spectra in acceleration, appropriately scaled according to the characteristics of the ground. In the LAN+EQ scenario, in the first step, the pattern of cumulative horizontal and vertical displacement components evaluated in the period 2012-2020, have been applied to the structural model. The landslide action causes the onset of a stress/strain state in the structural elements, which become the starting point for the successive application of the seismic action. Then, the seismic assessment procedure has been implemented on the structural deformed condition due not only to gravity loads but also to the differential displacements induced by the slow-moving landslide affecting the case study building.

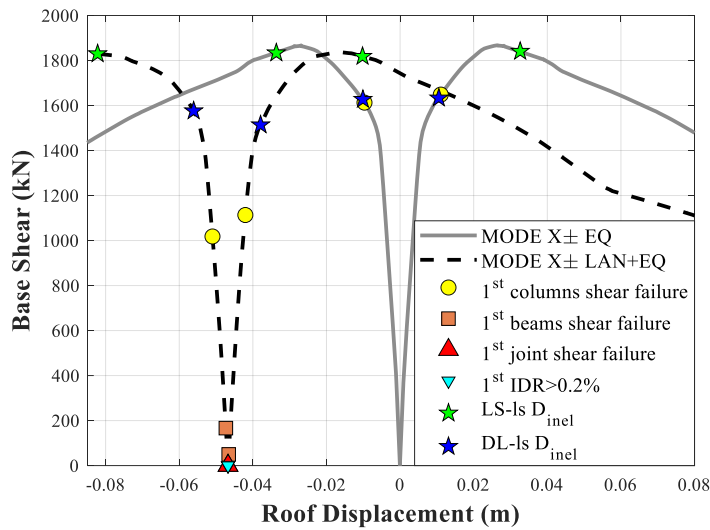
As mentioned in §5.2, nonlinear static analyses have been carried out through a step-by-step procedure, by subjecting the structure to two monotonically increasing patterns of lateral forces, applied at the centers of floor mass in the model, one proportional to the fundamental mode of vibration (Mode X and Mode Y), one proportional to the mass distribution (Mass X and Mass Y), where X and Y directions are assumed accordingly to Figure 5.27a. The seismic assessment is also implemented in a condition of integer structure, deformed only for

gravity loads, to verify the seismic safety level of the RC structure ([EQ] scenario). The pushover curves are represented in Figure 5.45 (for Mass X and Mode X cases) and Figure 5.46 (for Mass Y and Mode Y cases), with grey continuous lines for the EQ scenario and black dashed lines for the LAN+EQ scenario. The evolutions of the failure sequences found at the two ls for both scenarios are compared. The step of the analysis at which the first structural element experiences a failure mechanism has been found and remarked on the related pushover curve. In particular, for LS-ls, the tensile-shear failures in beam-columns unconfined joints are represented with red triangles, while brittle shear failures, in beams and columns, are indicated with orange squares and yellow circles, respectively. For DL-ls, the limit step is marked with a cyan inverted triangle.

The evidence of the structural checks, up to the inelastic demand point D_{inel} at LS-ls, for the EQ scenario (indicated with a green pentagram in Figure 5.45 and Figure 5.46), have shown that ductile failures are never attained, while tensile-shear failure in beam-columns unconfined joints and shear failure mechanisms in beams and columns are expected. Then, the ductile failures are never achieved at LS-ls. The numerical analyses have also shown that the first failure mechanism attained in the structure is the tensile-shear failure in beam-columns unconfined joints.

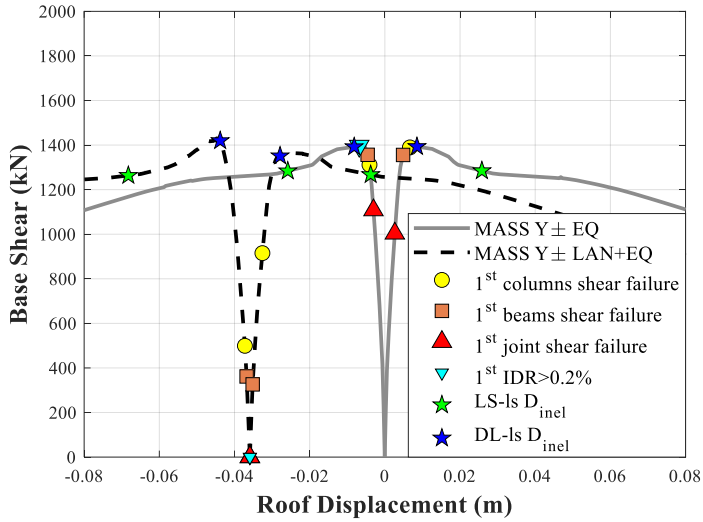


(a)

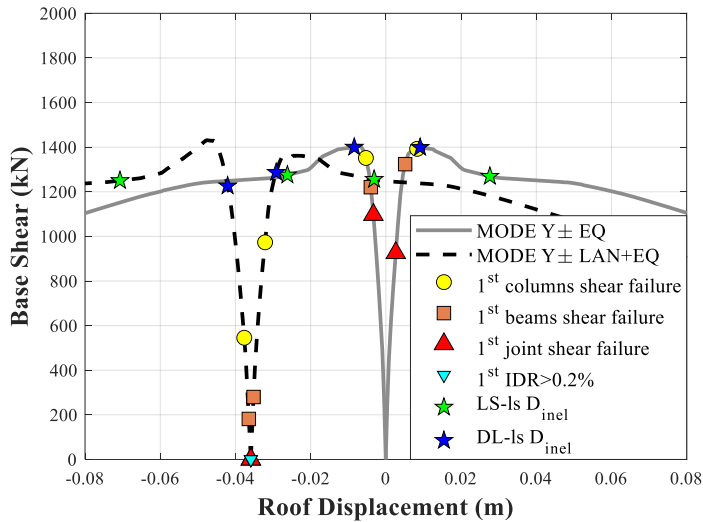


(b)

Figure 5.45. Comparison of the pushover curves and relative failure mechanism progress of structural elements, until the demand point, in the EQ and LAN+EQ for scenarios (a) Mass X and (b) Mode X (modified from [56]).



(a)



(b)

Figure 5.46. Comparison of the pushover curves and relative failure mechanism progress of structural elements, until the demand point, in the EQ and LAN+EQ for scenarios (a) Mass Y and (b) Mode Y (modified from [56]).

The seismic verifications for LS-ls, repeated for the LAN+EQ scenario, have highlighted that the differential displacements applied at the base of the

structural model cause an aggravation of the stress state in the structural elements, that experience failures for lower steps compared to those attained in the EQ scenario. Moreover, the number of elements in crisis at the LS-Is increases. The results of the non-linear static analysis, performed in the LAN+EQ scenario, have shown that the first elements in crisis are still the joints, for the tensile-shear mechanism, at step zero of the pushover. It means that the action of the landslide causes the failures before the application of the seismic action. The following failure mechanisms attained in the whole structure are beams and columns shear failures. The effect of the landslide does not cause ductile crises in the structure. Then, in the LAN+EQ scenario, such as in the previous EQ scenario, at LS-Is, only brittle failures in the structural elements are expected.

As regards the DL-Is, the corresponding D_{inel} is indicated with a blue pentagram in Figure 5.45 and Figure 5.46. The first failure at the DL-Is is related to the first-floor infills in every case. For the LAN+EQ scenario, it can be observed that the infill located in the AB first floor field (see Figure 5.29) in each case attains the DL-Is threshold at step zero of the pushover. Then, the DL-Is is exceeded due to the landslide action. This result is in line with the in-situ observation made by the authors during the experienced visual surveys. In fact, the mentioned infill is currently damaged, as can be seen in Figure 5.47b. The step at which the first failure is attained (performance point) characterizes the capacity of the whole structural system for the considered Is.

An overview of the number of failures at LS-Is and DL-Is thresholds, in the corresponding demand points, is reported in Figure 5.47. In particular, for LS-Is, the number of columns and beams experiencing shear failures, as well as the number of joints showing tensile-shear failures are reported. For DL-Is, the number of infills for which the maximum IDR exceeds the Is threshold is presented. The summary also constitutes a comparison between the seismic assessment performed in the two scenarios. It can be observed that from the EQ scenario to the LAN+EQ scenario, the number of elements experiencing brittle failures at LS-Is passes from 11 to 19 for joints, from 7 to 17 for columns, and from 2 to 8 for beams. Moreover, the number of infills attaining DL-Is passes from 4 to 10. This increase of the number of elements exceeding the Is can be attributed to the action

of the landslide, which is acting independently from the earthquake.

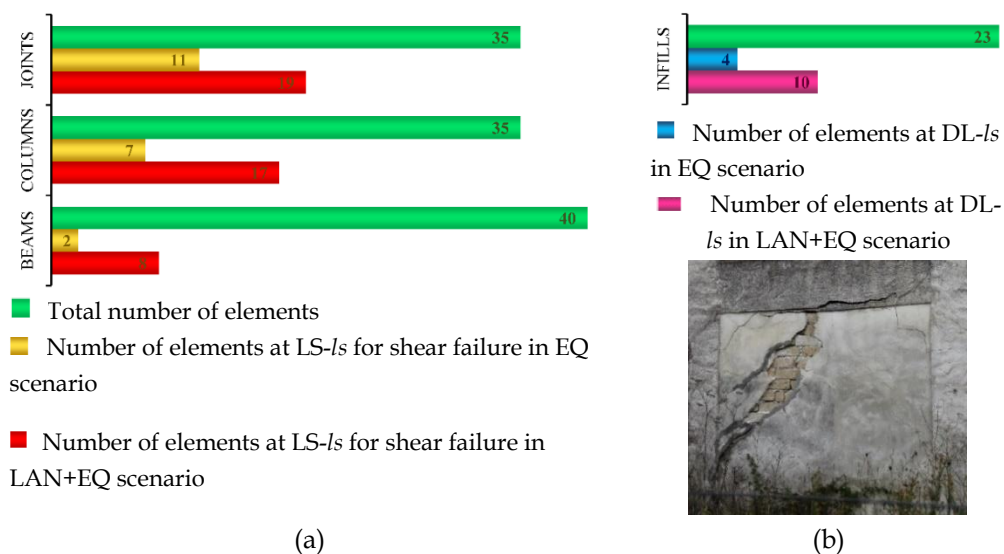


Figure 5.47. Number of elements in crisis at LS-ls and at DL-ls, versus number of total elements, in EQ and LAN+EQ scenarios, with a focus on the most damaged infill in the 2020 survey.

The second phase of the seismic assessment procedure regards the calculation of the safety index, ζ_E [126], defined as the ratio between the demand peak ground acceleration (PGA), based on the seismic actions prescribed from the code for the considered limit state, and the capacity PGA of the building. An overall comparison of the global structural condition between the two scenarios has been carried out in terms of safety index, by using the performance point to calculate the minimum anchoring PGA determining building failure mechanism and the safety index ζ_E . The results are reported in Figure 5.48.

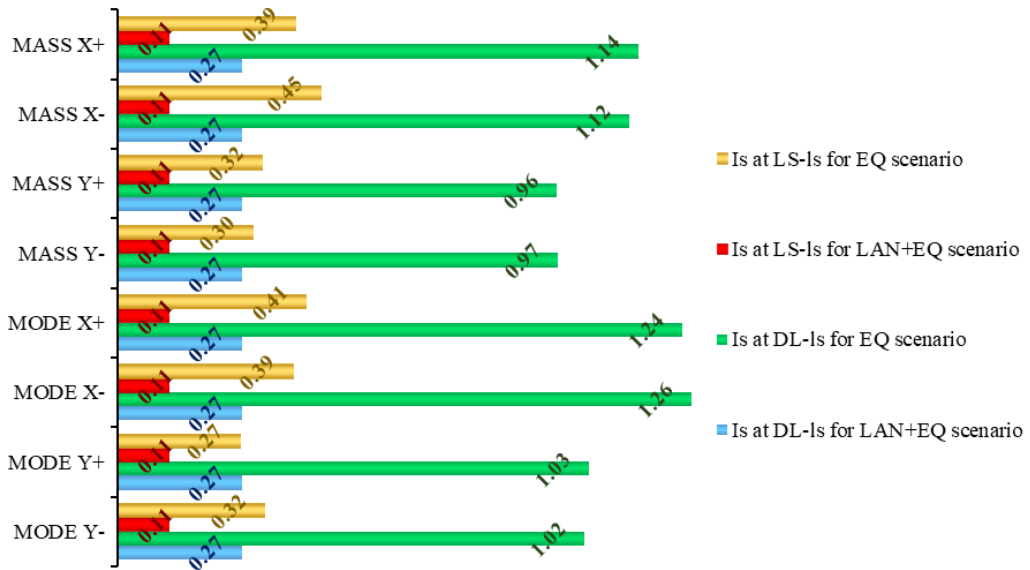


Figure 5.48. Comparison of the structural safety index in the EQ and LAN+EQ scenarios, at LS-ls and at DL-ls, for the eight performed analyses.

It can be observed that the safety index at LS-ls, $\zeta_{E,LS-ls}$ always assumes values less than unity. In particular, the minimum $\zeta_{E,LS-ls}$ corresponds to the EQ scenario (equal to 0.27). In the LAN+EQ scenario, $\zeta_{E,LS-ls}$ is equal to 0.11. This means that the structure is not able to withstand the seismic action from which, according to the code, could be invested, but only 27%, in the EQ scenario, and 11%, in the LAN+EQ scenario. At DL-ls, $\zeta_{E,DL-ls}$ assumes values very close to unity in the EQ scenario, while in the LAN+EQ scenario, the occurrence of the landslide drastically lowers the $\zeta_{E,DL-ls}$. In this case, the first failures at DL-ls occur at step zero, so $\zeta_{E,DL-ls}$ assumes a unique value of 0.27, corresponding to a spectrum with a return period equal to 10 years.

The illustrated comparison remarks that by neglecting the effects of the existing differential displacements landslide-induced, the safety index obtained for the structure can be overestimated. The differences in terms of ζ_E between the two scenarios have a significant influence on seismic upgrading/retrofit strategies and relative costs, according to the indications of NTC (2018) [116].

5.2.2 Discussion

The potential use of the satellite SAR data to perform a structural assessment and monitoring has been shown, analyzing different aspects with refers to an infilled RC building. An accurate structural model is necessary to perform a structural assessment and monitoring.

A good agreement has been found between the analytical previsions and the existing damage pattern on the infills, according to literature damage scales. The methodology presented in §5.2.2.1 can be quickly repeated for large sets of RC buildings, in particular for small urban centers that present a repetitiveness of the constructive systems of RC buildings. Moreover, assuming linearity in the progress of the slow-moving landslides as for the case study, useful indications can be provided to enrich the civil protection prevention plans for a predefined number of future years. The prediction of the future displacements following the past trend is reasonable in the presented case since the landslide-induced ground displacements at the base of the columns have grown almost linearly in the monitored period.

In the second part of the application, the seismic safety assessment of the building has been carried out twice: in a traditional scenario and a multi-hazard scenario, explicitly considering the effect of the slow landslide-induced movements affecting the structure. The landslide phenomenon, which analytically results in differential displacements applied at the base of the building columns in the model, causes a heterogeneous stress-strain path in the structural elements, that becomes the starting condition for the application of the following seismic action. The seismic safety checks at LS-Is have highlighted, both for EQ and for LAN+EQ scenarios, that only brittle failures in the structural elements are expected (tensile-shear failure in beam-columns unconfined joints, shear failure mechanisms in beams and columns). At the DL-Is, indeed, the first failure is always related to the first-floor infills. An overall comparison of the global structural condition between the two scenarios has been provided in terms of safety index.

It is evident that the differential displacements cause an aggravation of the

stress-strain state in the structural elements. Then, in the building seismic assessment, the neglect of a pre-existing stress-strain condition leads to an overestimation of the actual residual seismic capacity, represented in a value by the safety index, and consequently to a potential underestimation in the definition of the interventions needed to increase the seismic safety.

The proposed assessment procedure in a multi-hazard analysis can be easily repeated elsewhere to quantify the effect of the active landslide on the seismic assessment of the RC buildings.

The methodology presented in this work could furnish useful indications from a forecasting perspective, i.e., in support of the civil protection prevention plans. For phenomena linearly evolving in time, such as slow-moving landslides, a prevision of the future displacements for a small number of years could be done, if the trend of the displacements at the structure's base is known. These displacements could be used to carry out an application analogous to that presented in §5.2.2.2, to evaluate the seismic safety margin of the structure, affected by the landslide, in a certain number of years.

6. Conclusions

In this thesis, the most important aspects of the use of satellite SAR data for the monitoring and structural assessment of the built environment, in particular through DInSAR techniques, have been analyzed in detail. The advantages of such new remote sensing monitoring technology are various and very attractive for structural engineering applications. First of all, the covered areas are really large, and the data sampling has a relatively high frequency. The satellite image acquisition covers large periods of investigation (from 1992) and does not strictly need ground instrumentation. Then, the environmental impact is almost zero, and the monitoring costs are very limited if compared to the extent of the analyzed areas or the observation period, compared to traditional on-site methods. The technology also has some limitations, for example, the absence of measurements in areas without reflecting objects (e.g., vegetated areas) and the impossibility to establish the number of PSs and their distribution a priori. Moreover, it should be noted that the technique is suitable to monitor slow phenomena over time, but is not appropriate for rapid kinematic deformations.

Proper elaborations make DInSAR-derived data useful for SHM purposes of the built environment (which means constructions and surroundings). First of all, the study of mean velocity maps at the territorial scale allows to understand if the area of interest is stable or affected by displacements, and to assess the direction along which potential displacements are ongoing. In fact, the main outputs of the elaborations are Vertical and EW components mean velocity maps,

which condense the most significant information for the SHM of constructions, from an engineering point of view. Thanks to the deformation maps, it is possible to circumscribe the most unstable zones in which exposed constructions are located.

Two methodologies for the elaboration of satellite data at territorial scale, with SHM purposes, have been illustrated and applied to three case studies (§4.1.2 and §4.2.2). The first methodology highlights the importance of the use of ML algorithms for the management and elaboration of DInSAR-derived data for SHM purposes. The DBSCAN clustering algorithm is applied to ASC and DES datasets of PSs in a built-up zone, with no information about the number, the shape, and the distribution of the buildings in the area, for their automatic identification in the form of PSs clusters. Then, for each cluster, the deformation condition in the investigated period is obtained and a preliminary ranking of critical buildings to be further investigated is carried out. The second methodology is based on the use of ADAfinder tool, aimed to identify the buildings affected by displacements above a given threshold, among all the buildings included in the investigated area, neglecting the other ones. The presented methodologies are very promising; nevertheless, they could be improved by the introduction of a classification of the buildings, for instance, based on structural features (e.g., material, number of floors, construction period), and giving velocity thresholds specific for each class, to distinguish the “stable” from the “unstable” condition. The products of the two proposed methodologies at the territorial scale are very clear, simple, and useful to provide real support for the monitoring of urban areas.

The identification of the most critical buildings to be investigated at a detailed scale, with a higher degree of information (e.g., on-site inspections and measurements), is very important since settlements could induce damage to structures and create dangerous situations. In this regard, a focus on the potential use of DInSAR satellite data for SHM purposes at a single construction scale has been made. The two levels of analysis (territorial and single scale) should be considered as parts of a unified approach for the structural assessment and monitoring of the built environment.

The structural assessment at a single construction scale, based on DInSAR-derived data, can be performed at two levels, with increasing accuracy of the results. The evaluation of the maximum displacement components, as well as the calculation of the maximum differential settlement related to a building facade, represent a crucial issue in the identification of possible criticalities for the monitored building. The trend of displacement time series of single PSs is also important to track the deformation evolution, focusing in particular on the detection of possible slope changes.

A preliminary structural assessment and monitoring, based on the combination of DInSAR data with information concerning the construction geometry (e.g., retrieved from historical documentation), 3D modelling, and consistent positioning of the PSs in a GIS environment, can be implemented (§5.1.1.1 and §5.1.1.2). The qualitative comparison between the DInSAR-derived mean velocity maps and the 3D engineering-geological model can highlight possible correlations between ground settlements and litho-stratigraphic setting. Moreover, when the damage condition of the construction at time zero of the DInSAR time series is known, the displacements cumulated during the monitoring interval can be used to draw considerations on the structural damage evolution, and to qualitatively estimate the damage, according to literature damage scales (§5.1.1.2). On the contrary, in the absence of information on the damage condition at time zero, it is possible to compare the cumulated differential displacement with limit thresholds associated with classes of damage conditions, but it is almost impossible to reconstruct the damage evolution. A damage classification of constructions can help establish a list of priorities of the more vulnerable ones, for better planning of more in-depth evaluations. A preliminary structural assessment can also be developed based on the integration of DInSAR-derived data and the outcomes of on-site damage reliefs, as shown in the presented application (§5.1.1.3).

A more depth structural assessment and monitoring consist of the estimation of the structural response of a reliable analytical model of the construction, under differential settlements DInSAR-derived, with higher accuracy in the results with respect to the previous approach. The analytical damage previsions can be compared to the existing damage pattern (§5.2.2.1) to validate the structural model. Then, the influence of displacements induced by an ongoing

phenomenon (detected from satellite) on the seismic safety assessment of a construction can be investigated (§5.2.2.2). This could furnish useful indications in a forecasting perspective, i.e., in support of the civil protection prevention plans. In fact, for linearly evolving in time phenomena (e.g., the case of slow-moving landslides), expected future settlements could be estimated, starting from the DInSAR-derived time-series, and exploited to evaluate the seismic safety margin of the structure, in a certain number of years. However, particular attention should be paid to future forecasts (or retrospective) analyses: it is always desirable to integrate satellite data with on-site information.

It is worth to highlight that the cumulative displacements retrieved through the DInSAR technique represent the amount relative only to the time series interval. Therefore, if the construction under monitoring has been built before the beginning of the time series, information on earlier deformation phenomena affecting the building needs to be gathered in order to use the DInSAR cumulative displacement for structural assessment.

The applications shown in this thesis have been performed using satellite SAR data derived by the processing of SAR images acquired from different satellites (CSK and S-1), using different processing techniques (SB and PS). It has also been highlighted that the choice of the dataset features should be a function of the application to be performed because the resolution of the data is not the same for every satellite constellation and processing approach. For a single construction SHM, for example, it is suggested to use at least CSK-derived data. It is also worth to highlight that several national and international space agencies are planning to launch new missions to put into orbit constellations of SAR satellites characterized by even more frequent revisit time, extension of the ground coverage, and higher spatial resolutions capable of providing an increasing amount and quality of data.

The performed analysis allows to highlight that the main open issues concerning the use of DInSAR measurements for structural applications, on which the future research lines should be focused, are the following:

- the correct altimetric and planimetric PSs positioning, together with the possibility to further improve and automatize the precision and accuracy of
-

the PSs georeferencing by means of GNSS measurements;

- the reduced effectiveness of the multi-temporal DInSAR techniques in some structural typologies, for example, due to the impossibility to evaluate the displacement component of the PSs along the NS direction or to the existence of areas characterized by the lack of points, caused by the presence of unexpected effects that may lead to anomalies in the associated deformation signal, with the need to develop specific algorithms;
- the importance to account for the spatial correlation among PSs when performing interpolation operations to study a specific construction;
- the importance to choose a “stable” *reference point* (§2.2), to not affected the measurements of all the dataset by a wrong under/over-estimation.

As a future prospect, the DInSAR data could be applied for the definition of alerts and threshold levels for the SHM of a construction, once DInSAR measurements are validated through the structural model.

Bibliography

- [1] R. Tomás and Z. Li, "Earth Observations for Geohazards: Present and Future Challenges," *Remote Sens*, vol. 9, no. 3, 2017, doi: 10.3390/rs9030194.
- [2] A. K. Gabriel, R. M. Goldstein, and H. A. Zebker, "Mapping small elevation changes over large areas: Differential radar interferometry," *J Geophys Res Solid Earth*, vol. 94, no. B7, pp. 9183–9191, 1989.
- [3] D. Massonnet and K. L. Feigl, "Radar interferometry and its application to changes in the Earth's surface," *Rev Geophys*, vol. 36, no. 4, pp. 441–500, 1998.
- [4] P. A. Rosen, S. Hensley, I. R. Joughin *et al.*, "Synthetic aperture radar interferometry," *IEEE T Geosci Remote S*, 88, 333–382, 2000.
- [5] F. Raspini, S. Bianchini, A. Ciampalini *et al.*, "Continuous, semi-automatic monitoring of ground deformation using Sentinel-1 satellites," *Sci Rep*, vol. 8, no. 1, Dec. 2018, doi: 10.1038/s41598-018-25369-w.
- [6] P. Confuorto, D. Di Martire, D. Infante *et al.*, "Monitoring of remedial works performance on landslide-affected areas through ground- and satellite-based techniques," *Catena*, vol. 178, pp. 77–89, 2019, doi: <https://doi.org/10.1016/j.catena.2019.03.005>.
- [7] A. Ferretti, C. Prati, F. Rocca *et al.*, "Satellite interferometry for monitoring ground deformations in the urban environment," in *Proc of the 10th IAEG Congress*, 2006, pp. 100–110.
- [8] M. Manunta, M. Marsella, G. Zeni *et al.*, "Two-scale surface deformation analysis using the SBAS-DInSAR technique: A case study of the city of Rome, Italy," *Int J Remote Sens*, vol. 29, no. 6, pp. 1665–1684, Mar. 2008, doi: <https://doi.org/10.1080/01431160701395278>.
- [9] S. Stramondo, F. Bozzano, F. Marra *et al.*, "Subsidence induced by urbanisation in the city of Rome detected by advanced InSAR technique and geotechnical investigations," *Remote Sens Environ*, vol. 112, no. 6, pp. 3160–

- 3172, 2008, doi: <https://doi.org/10.1016/j.rse.2008.03.008>.
- [10] D. Infante, P. Confuorto, D. Di Martire *et al.*, "Use of DInSAR Data for Multi-level Vulnerability Assessment of Urban Settings Affected by Slow-moving and Intermittent Landslides," *Procedia Eng*, vol. 158, pp. 470–475, 2016, doi: <https://doi.org/10.1016/j.proeng.2016.08.474>.
- [11] D. Peduto, G. Nicodemo, J. Maccabiani *et al.*, "Multi-scale analysis of settlement-induced building damage using damage surveys and DInSAR data: A case study in The Netherlands," *Eng Geol*, vol. 218, pp. 117–133, 2017, doi: <https://doi.org/10.1016/j.enggeo.2016.12.018>.
- [12] V. Macchiarulo, P. Milillo, M. J. DeJong *et al.*, "Integrated InSAR monitoring and structural assessment of tunnelling-induced building deformations," *Struct Control Health Monit*, vol. 28, no. 9, p. e2781, 2021.
- [13] M. Costantini, A. Ferretti, F. Minati *et al.*, "Analysis of surface deformations over the whole Italian territory by interferometric processing of ERS, Envisat and COSMO-SkyMed radar data," *Remote Sens Environ*, vol. 202, pp. 250–275, 2017, doi: <https://doi.org/10.1016/j.rse.2017.07.017>.
- [14] J. F. Dehls, Y. Larsen, P. Marinkovic *et al.*, "INSAR.No: A National InSAR Deformation Mapping/Monitoring Service In Norway - From Concept To Operations," in *IGARSS 2019 - 2019 IEEE Int Geosci Remote Sens Symp*, 2019, pp. 5461–5464. doi: 10.1109/IGARSS.2019.8898614.
- [15] A. C. Kalia, M. Frei, and T. Lege, "A Copernicus downstream-service for the nationwide monitoring of surface displacements in Germany," *Remote Sens Environ*, vol. 202, pp. 234–249, 2017, doi: <https://doi.org/10.1016/j.rse.2017.05.015>.
- [16] M. Del Soldato, L. Solari, F. Raspini *et al.*, "Monitoring ground instabilities using SAR satellite data: A practical approach," *ISPRS Int J Geoinf*, vol. 8, no. 7, p. 307, 2019.
- [17] L. Solari, M. del Soldato, R. Montalti *et al.*, "A Sentinel-1 based hot-spot analysis: landslide mapping in north-western Italy," *Int J Remote Sens*, vol.

- 40, no. 20, pp. 7898–7921, 2019, doi: 10.1080/01431161.2019.1607612.
- [18] M. Crosetto, L. Solari, J. Balasis-Levinsen *et al.*, “Ground deformation monitoring at continental scale: The European Ground Motion Service,” in *ISPRS Archives*, Aug. 2020, vol. 43, no. B3, pp. 293–298. doi: 10.5194/isprs-archives-XLIII-B3-2020-293-2020.
- [19] M. Crosetto, L. Solari, J. Balasis-Levinsen *et al.*, “Deformation monitoring at European scale: The Copernicus ground motion service,” in *Int arch photogramm remote sens spat inf sci*, Jun. 2021, vol. 43, no. B3-2021, pp. 141–146. doi: 10.5194/isprs-archives-XLIII-B3-2021-141-2021.
- [20] M. Costantini, F. Minati, F. Trillo *et al.*, “European Ground Motion Service (EGMS),” in *IEEE Int Geosci Remote Sens Symp (IGARSS)*, 2021, pp. 3293–3296.
- [21] M. del Soldato, A. Riquelme, S. Bianchini *et al.*, “Multisource data integration to investigate one century of evolution for the Agnone landslide (Molise, southern Italy),” *Landslides*, vol. 15, no. 11, pp. 2113–2128, 2018.
- [22] D. Di Martire, S. Tessitore, D. Brancato *et al.*, “Landslide detection integrated system (LaDIS) based on in-situ and satellite SAR interferometry measurements,” *Catena*, vol. 137, pp. 406–421, 2016.
- [23] F. Bozzano, C. Esposito, P. Mazzanti *et al.*, “Imaging multi-age construction settlement behaviour by advanced SAR interferometry,” *Remote Sens*, vol. 10, no. 7, p. 1137, 2018.
- [24] L. Cascini, S. Ferlisi, G. Fornaro *et al.*, “Subsidence monitoring in Sarno urban area via multi-temporal DInSAR technique,” *Int J Remote Sens*, vol. 27, no. 8, pp. 1709–1716, 2006.
- [25] R. Tomás, R. Romero, J. Mulas *et al.*, “Radar interferometry techniques for the study of ground subsidence phenomena: a review of practical issues through cases in Spain,” *Environ Earth Sci*, vol. 71, no. 1, pp. 163–181, 2014.
- [26] G. Zeni, M. Bonano, F. Casu *et al.*, “Long-term deformation analysis of

- historical buildings through the advanced SBAS-DInSAR technique: The case study of the city of Rome, Italy," *J Geophys Eng*, vol. 8, no. 3, pp. S1-S12, 2011.
- [27] A. Barra, L. Solari, M. Béjar-Pizarro *et al.*, "A methodology to detect and update active deformation areas based on Sentinel-1 SAR images," *Remote Sens*, vol. 9, no. 10, Oct. 2017, doi: 10.3390/rs9101002.
- [28] A. Mele, M. Crosetto, A. Miano *et al.*, "ADAFinder Tool Applied to EGMS Data for the Structural Health Monitoring of Urban Settlements," *Remote Sens*, vol. 15, no. 2, p. 324, Jan. 2023, doi: 10.3390/rs15020324.
- [29] M. Zhu, X. Wan, B. Fei *et al.*, "Detection of building and infrastructure instabilities by automatic spatiotemporal analysis of satellite SAR interferometry measurements," *Remote Sens*, vol. 10, no. 11, p. 1816, 2018.
- [30] M. Del Soldato, L. Solari, F. Poggi *et al.*, "Landslide-induced damage probability estimation coupling InSAR and field survey data by fragility curves," *Remote Sens*, vol. 11, no. 12, p. 1486, 2019.
- [31] D. A. Talledo, A. Miano, M. Bonano *et al.*, "Satellite radar interferometry: Potential and limitations for structural assessment and monitoring," *J Build Eng*, vol. 46, Apr. 2022, doi: 10.1016/j.jobbe.2021.103756.
- [32] K. Zhang, J. Yan, and S.-C. Chen, "Automatic Construction of Building Footprints From Airborne LIDAR Data," *IEEE Trans Geosci Remote Sens*, vol. 44, no. 9, pp. 2523-2533, 2006, doi: 10.1109/TGRS.2006.874137.
- [33] H. Aljumaily, D. F. Laefer, and D. Cuadra, "Urban point cloud mining based on density clustering and MapReduce," 2017.
- [34] L. Zhang and L. Zhang, "Deep Learning-Based Classification and Reconstruction of Residential Scenes From Large-Scale Point Clouds," *IEEE Trans Geosci Remote Sens*, vol. 56, no. 4, pp. 1887-1897, 2018, doi: 10.1109/TGRS.2017.2769120.
- [35] Z. Guo, H. Liu, L. Pang *et al.*, "DBSCAN-based point cloud extraction for

- Tomographic synthetic aperture radar (TomoSAR) three-dimensional (3D) building reconstruction," *Int J Remote Sens*, vol. 42, no. 6, pp. 2327–2349, 2021, doi: 10.1080/01431161.2020.1851062.
- [36] A. Mele, A. Vitiello, M. Bonano *et al.*, "On the Joint Exploitation of Satellite DInSAR Measurements and DBSCAN-Based Techniques for Preliminary Identification and Ranking of Critical Constructions in a Built Environment," *Remote Sens*, vol. 14, no. 8, Apr. 2022, doi: 10.3390/rs14081872.
- [37] M. Rahimzad, S. Homayouni, A. Alizadeh Naeini *et al.*, "An Efficient Multi-Sensor Remote Sensing Image Clustering in Urban Areas via Boosted Convolutional Autoencoder (BCAE)," *Remote Sens*, vol. 13, no. 13, 2021, doi: 10.3390/rs13132501.
- [38] F. Di Carlo, A. Miano, I. Giannetti *et al.*, "On the integration of multi-temporal synthetic aperture radar interferometry products and historical surveys data for buildings structural monitoring," *J Civ Struct Health Monit*, vol. 11, no. 5, pp. 1429–1447, Nov. 2021, doi: 10.1007/s13349-021-00518-4.
- [39] S. Arangio, F. Calò, M. Di Mauro *et al.*, "An application of the SBAS-DInSAR technique for the assessment of structural damage in the city of Rome," *Struct Infrastruct Eng*, vol. 10, no. 11, pp. 1469–1483, Nov. 2014, doi: 10.1080/15732479.2013.833949.
- [40] F. Chen, W. Zhou, C. Chen *et al.*, "Extended D-TomoSAR Displacement Monitoring for Nanjing (China) City Built Structure Using High-Resolution TerraSAR/TanDEM-X and Cosmo SkyMed SAR Data," *Remote Sens*, vol. 11, no. 22, 2019, doi: 10.3390/rs11222623.
- [41] N. Cavalagli, A. Kita, S. Falco *et al.*, "Satellite radar interferometry and in-situ measurements for static monitoring of historical monuments: The case of Gubbio, Italy," *Remote Sens Environ*, vol. 235, p. 111453, 2019, doi: <https://doi.org/10.1016/j.rse.2019.111453>.
- [42] L. Berto, A. Doria, A. Saetta *et al.*, "Assessment of the Applicability of DInSAR Techniques for Structural Monitoring of Cultural Heritage and

- Archaeological Sites," in *Civ Struct Health Monit: Proc of CSHM-8 Workshop 8*, 2021, pp. 691–697.
- [43] A. Drougkas, E. Verstrynge, K. Van Balen *et al.*, "Country-scale InSAR monitoring for settlement and uplift damage calculation in architectural heritage structures," *Struct Health Monit*, vol. 20, no. 5, pp. 2317–2336, 2021, doi: 10.1177/1475921720942120.
- [44] D. Cusson, C. Rossi, and I. F. Ozkan, "Early warning system for the detection of unexpected bridge displacements from radar satellite data," *J Civ Struct Health Monit*, vol. 11, no. 1, pp. 189–204, 2021.
- [45] F. C. Ponzio, C. Iacovino, R. Ditommaso *et al.*, "Transport Infrastructure SHM Using Integrated SAR Data and On-Site Vibrational Acquisitions: 'Ponte Della Musica-Armando Trovajoli' Case Study," *Appl Sci*, vol. 11, no. 14, p. 6504, 2021.
- [46] A. Miano, F. Di Carlo, A. Mele *et al.*, "GIS Integration of DInSAR Measurements, Geological Investigation and Historical Surveys for the Structural Monitoring of Buildings and Infrastructures: An Application to the Valco San Paolo Urban Area of Rome," *Infrastructures*, vol. 7, no. 7, Jul. 2022, doi: 10.3390/infrastructures7070089.
- [47] S. Scifoni, M. Bonano, M. Marsella *et al.*, "On the joint exploitation of long-term DInSAR time series and geological information for the investigation of ground settlements in the town of Roma (Italy)," *Remote Sens Environ*, vol. 182, pp. 113–127, 2016.
- [48] A. W. Skempton and D. H. MacDonald, "The allowable settlements of buildings.," *Proc of the Inst Civ Eng*, vol. 5, no. 6, pp. 727–768, 1956.
- [49] G. G. Meyerhof, "Discussion on paper by AW Skempton and DH MacDonald. The allow-able settlement of buildings," in *Proc of the Inst Civ Eng* 5(6), 1956, pp. 774–775.
- [50] D. E. Polshin and R. A. Tokar, "Maximum allowable non-uniform settlement of structures," in *Proceedings of the 4th Int Conf on Soil Mech Found*

- Eng*, 1957, vol. 1, pp. 402–405.
- [51] L. Bjerrum, “Allowable settlement of structures,” in *Proc of the 3rd European Conf on Soil Mech Found Eng*, Wiesbaden, Germany, 1963, vol. 2, pp. 135–137.
- [52] J. B. Burland and C. P. Wroth, “Settlement of buildings and associated damage,” No, CP 33/75, 1975.
- [53] J. B. Burland, “Behaviour of foundations and structures on soft ground,” *Proc of the 9th Int Conf on Soil Mech Found Eng*, vol. 2, pp. 495–546, 1977.
- [54] M. D. Boscardin and E. J. Cording, “Building response to excavation-induced settlement,” *J Geotech Eng*, vol. 115, no. 1, pp. 1–21, 1989.
- [55] D. Infante, D. Di Martire, P. Confuorto *et al.*, “Assessment of building behavior in slow-moving landslide-affected areas through DInSAR data and structural analysis,” *Eng Struct*, vol. 199, p. 109638, 2019, doi: <https://doi.org/10.1016/j.engstruct.2019.109638>.
- [56] A. Mele, A. Miano, D. Di Martire *et al.*, “Potential of remote sensing data to support the seismic safety assessment of reinforced concrete buildings affected by slow-moving landslides,” *Arch Civ Mech Eng*, vol. 22, no. 2, May 2022, doi: 10.1007/s43452-022-00407-7.
- [57] A. Miano, A. Mele, D. Calcaterra *et al.*, “The use of satellite data to support the structural health monitoring in areas affected by slow-moving landslides: a potential application to reinforced concrete buildings,” *Struct Health Monit*, vol. 20, no. 6, pp. 3265–3287, 2021, doi: 10.1177/1475921720983232.
- [58] N. Nappo, D. Peduto, M. Polcari *et al.*, “Subsidence in Como historic centre (northern Italy): Assessment of building vulnerability combining hydrogeological and stratigraphic features, Cosmo-SkyMed InSAR and damage data,” *Int J Disaster Risk Reduct*, vol. 56, p. 102115, 2021.
- [59] R. J. Finno, F. T. Voss Jr, E. Rossow *et al.*, “Evaluating damage potential in

- buildings affected by excavations," *J Geotech Geoenviron*, vol. 131, no. 10, pp. 1199–1210, 2005.
- [60] C. Elachi, "Spaceborne radar remote sensing: applications and techniques," *New York*, 1988.
- [61] G. Franceschetti and R. Lanari, *Synthetic aperture radar processing*, CRC press, 1999.
- [62] Tele-Rilevamento Europa (T.R.E. s.r.l.), <https://site.tre-altamira.com/in-sar/> (accessed on April 2020).
- [63] A. Bouaraba, A. Belhadj-Aissa, and D. Closson, "Drastic improvement of change detection results with multilook complex SAR images approach," *Prog Electromagn Res*, vol. 82, pp. 55–66, 2018.
- [64] Reluis WP6 – Monitoraggio e dati satellitari, "Linee Guida per l'Utilizzo dei dati Interferometrici Satellitari ai fini dell'Interpretazione del Comportamento Strutturale delle Costruzioni", draft August 2021, (in italian).
- [65] M. Bonano, M. Manunta, A. Pepe *et al.*, "From previous C-band to new X-band SAR systems: Assessment of the DInSAR mapping improvement for deformation time-series retrieval in urban areas," *IEEE Trans Geosci Remote Sens*, vol. 51, no. 4, pp. 1973–1984, 2013, doi: 10.1109/TGRS.2012.2232933.
- [66] R. Lanari, O. Mora, M. Manunta *et al.*, "A small-baseline approach for investigating deformations on full-resolution differential SAR interferograms," *IEEE Trans Geosci Remote Sens*, vol. 42, no. 7, pp. 1377–1386, Jul. 2004, doi: 10.1109/TGRS.2004.828196.
- [67] A. Hooper, D. Bekaert, K. Spaans *et al.*, "Recent advances in SAR interferometry time series analysis for measuring crustal deformation," *Tectonophysics*, vol. 514–517, pp. 1–13, 2012, doi: <https://doi.org/10.1016/j.tecto.2011.10.013>.
- [68] Tele-Rilevamento Europa (T.R.E. s.r.l.), "PSInSAR™ - Manuale d'uso,"

July 2008 (in italian).

- [69] A. Pepe and R. Lanari, "On the Extension of the Minimum Cost Flow Algorithm for Phase Unwrapping of Multitemporal Differential SAR Interferograms," *IEEE Trans Geosci Remote Sens*, vol. 44, no. 9, pp. 2374–2383, 2006, doi: 10.1109/TGRS.2006.873207.
- [70] M. Bonano, M. Manunta, M. Marsella *et al.*, "Long-term ERS/ENVISAT deformation time-series generation at full spatial resolution via the extended SBAS technique," *Int J Remote Sens*, vol. 33, no. 15, pp. 4756–4783, 2012, doi: 10.1080/01431161.2011.638340.
- [71] F. Bozzano, P. Ciampi, M. Del Monte *et al.*, "Satellite A-DInSAR monitoring of the Vittoriano monument (Rome, Italy): implications for heritage preservation," *Ital J Eng Geol Environ*, no. 2, pp. 5–17, 2020.
- [72] R. Lanari, D. Reale, M. Bonano *et al.*, "Comment on 'Pre-collapse space geodetic observations of critical infrastructure: the Morandi bridge, Genoa, Italy' by Milillo *et al.* (2019)," *Remote Sens*, vol. 12, no. 24, p. 4011, 2020.
- [73] F. Casu, M. Manzo, and R. Lanari, "A quantitative assessment of the SBAS algorithm performance for surface deformation retrieval from DInSAR data," *Remote Sens Environ*, vol. 102, no. 3–4, pp. 195–210, Jun. 2006, doi: 10.1016/j.rse.2006.01.023.
- [74] M. Manunta, C. De Luca, I. Zinno *et al.*, "The Parallel SBAS Approach for Sentinel-1 Interferometric Wide Swath Deformation Time-Series Generation: Algorithm Description and Products Quality Assessment," *IEEE Trans Geosci Remote Sens*, vol. 57, no. 9, pp. 6259–6281, 2019, doi: 10.1109/TGRS.2019.2904912.
- [75] D. Infante, S. Tessitore, P. Confuorto *et al.*, "Monitoring of strategic buildings in civil protection activities via remote sensing data," *IEEE Aerosp Electron Syst Mag*, vol. 34, no. 10, pp. 6–16, 2019.
- [76] O. Mora, J. J. Mallorqui, and A. Broquetas, "Linear and nonlinear terrain

- deformation maps from a reduced set of interferometric SAR images," *IEEE Trans Geosci Remote Sens*, vol. 41, no. 10, pp. 2243–2253, 2003.
- [77] R. Iglesias, J. J. Mallorqui, D. Monells *et al.*, "PSI deformation map retrieval by means of temporal sublook coherence on reduced sets of SAR images," *Remote Sens*, vol. 7, no. 1, pp. 530–563, 2015.
- [78] D. Di Martire, M. Ramondini, and D. Calcaterra, "Integrated monitoring network for the hazard assessment of slow-moving landslides at Moio della Civitella (Italy)," *Rendiconti Online Soc Geol Ital*, vol. 35, pp. 109–112, 2015.
- [79] D. Infante, "Integrated analysis of building vulnerability in urban areas affected by slow-moving, intermittent landslides using SAR Interferometry," PhD thesis, 2018.
- [80] Copernicus Land Monitoring Service, <https://www.copernicus.eu/en/copernicus-services/land> (accessed on April 2020).
- [81] A. Ferretti, E. Passera, and R. Capes, "Algorithm Theoretical Basis Document. EGMS documentation", <https://land.copernicus.eu/user-corner/technical-library/egms-algorithm-theoretical-basis-document.>, 2021 (accessed on February 2022).
- [82] Copernicus Land Monitoring Service, European Ground Motion Service Explorer, <https://egms.land.copernicus.eu/> (accessed on February 2022).
- [83] Copernicus Land Monitoring Service, "White paper of European Ground Motion Service", Sept. 21, 2017, <https://land.copernicus.eu/user-corner/technical-library/egms-white-paper> (accessed on February 2022).
- [84] E. Sansosti, P. Berardino, M. Bonano *et al.*, "How second generation SAR systems are impacting the analysis of ground deformation," *Int J Appl Earth Obs Geoinf*, vol. 28, pp. 1–11, 2014, doi: <https://doi.org/10.1016/j.jag.2013.10.007>.
- [85] M. Polcari, S. Borgstrom, C. Del Gaudio *et al.*, "Thirty years of volcano

- geodesy from space at Campi Flegrei caldera (Italy)," *Sci Data*, vol. 9, no. 1, pp. 1-13, 2022.
- [86] European Spatial Agency Earth Observation portal, <https://directory.eoportal.org/web/eoportal/satellite-missions/> (accessed on February 2022).
- [87] E. Sansosti, P. Berardino, M. Bonano *et al.*, "How second generation SAR systems are impacting the analysis of ground deformation," *Int J Appl Earth Obs Geoinf*, vol. 28, no. 1, pp. 1-11, 2014, doi: 10.1016/j.jag.2013.10.007.
- [88] QGIS Geographic Information System. Open Source Geospatial Foundation Project, 2020, <https://qgis.org/it/site/> (accessed on October 2020).
- [89] ArcGIS, 2020, www.esri.com (accessed on October 2020).
- [90] P. Capolino, A. Bonavita, A. Greco *et al.*, "Quartiere Valco San Paolo. Torri stellari," in *Il moderno attraverso Roma. Guida a 200 architetture e alle loro opere d'arte*, Rome: Palombi, 2000.
- [91] Carta Tecnica Regionale Numerica scala 1:500 Provincia di Roma, 2020, <http://dati.lazio.it/catalog/it/dataset/carta-tecnica-regionale-2002-2003-5k-roma.it> (accessed on April 2021) (in italian).
- [92] I. Giannetti, "Project and prototype: industrialized and prefabricated construction in Italy (1945-1980)," *TEMA*, vol. 1, no. 1, pp. 25-30, 2015.
- [93] M. Ester, H.-P. Kriegel, J. Sander *et al.*, "A density-based algorithm for discovering clusters in large spatial databases with noise," in *kdd*, 1996, vol. 96, no. 34, pp. 226-231.
- [94] F. Huang, Q. Zhu, J. Zhou *et al.*, "Research on the parallelization of the DBSCAN clustering algorithm for spatial data mining based on the spark platform," *Remote Sens*, vol. 9, no. 12, p. 1301, 2017.
- [95] E. Schubert, J. Sander, M. Ester *et al.*, "DBSCAN Revisited, Revisited: Why and How You Should (Still) Use DBSCAN," *ACM Trans Database Syst*, vol.

- 42, no. 3, Jul. 2017, doi: 10.1145/3068335.
- [96] C. Xie, P. Chen, D. Pan *et al.*, "Improved Filtering of ICESat-2 Lidar Data for Nearshore Bathymetry Estimation Using Sentinel-2 Imagery," *Remote Sens*, vol. 13, no. 21, p. 4303, 2021.
- [97] S. Roshandel, W. Liu, C. Wang *et al.*, "3D Ocean Water Wave Surface Analysis on Airborne LiDAR Bathymetric Point Clouds," *Remote Sens*, vol. 13, no. 19, p. 3918, 2021.
- [98] Q. Xu, L. Cao, L. Xue *et al.*, "Extraction of leaf biophysical attributes based on a computer graphic-based algorithm using terrestrial laser scanning data," *Remote Sens*, vol. 11, no. 1, p. 15, 2018.
- [99] A. Starczewski and A. Cader, "Determining the EPS parameter of the DBSCAN algorithm," in *Int Conf on Artif Intell Soft Comput*, 2019, pp. 420–430.
- [100] N. Rahmah and I. S. Sitanggang, "Determination of optimal epsilon (eps) value on DBSCAN algorithm to clustering data on peatland hotspots in sumatra," in *IOP Conf Ser: Earth Environ Sci*, 2016, vol. 31, no. 1, p. 12012.
- [101] J. Sander, M. Ester, H.-P. Kriegel *et al.*, "Density-based clustering in spatial databases: The algorithm gdbscan and its applications," *Data Min Knowl Discov*, vol. 2, no. 2, pp. 169–194, 1998.
- [102] Ministry of Health, "Decreto Ministeriale Sanità 5 luglio 1975 - Modificazioni alle istruzioni ministeriali 20 giugno 1896, relativamente all'altezza minima ed ai requisiti igienico-sanitari principali dei locali di abitazione." *Gazzetta ufficiale* n.190 del 18/07/1975 (in italian).
- [103] Centre Tecnològic de Telecomunicacions de Catalunya, "ADAtools. Release notes."
- [104] J. A. Navarro, R. Tomás, A. Barra *et al.*, "ADAtools: Automatic detection and classification of active deformation areas from PSI displacement maps," *ISPRS Int J Geoinf*, vol. 9, no. 10, Oct. 2020, doi: 10.3390/ijgi9100584.

- [105] R. Tomás, J. I. Pagán, J. A. Navarro *et al.*, “Semi-automatic identification and pre-screening of geological–geotechnical deformational processes using persistent scatterer interferometry datasets,” *Remote Sens*, vol. 11, no. 14, p. 1675, 2019.
- [106] A. Mele, M. Crosetto, A. Miano *et al.*, “ADAFinder tool applied to EGMS data for the Structural Health Monitoring of urban settlements,” *Remote Sens*, vol. 15, no. 324, 2023, doi: <https://doi.org/10.3390/rs15020324>.
- [107] A. Ferretti, A. Monti-Guarnieri, C. Prati *et al.*, “InSAR Principles: Guidelines for SAR Interferometry Processing and Interpretation, ESA TM-19.” ESA Publications Division, Noordwijk, The Netherlands, 2007.
- [108] OpenStreetMap, <https://www.openstreetmap.org/> (accessed on March 2022).
- [109] H. A. Zebker and J. Villasenor, “Decorrelation in interferometric radar echoes,” *IEEE Trans Geosci Remote Sens*, vol. 30, no. 5, pp. 950–959, 1992, doi: 10.1109/36.175330.
- [110] H. G. Poulos, J. P. Carter, and J. C. Small, “Foundations and retaining structures—research and practice,” in *Proc of the Int Conf on Soil Mech Geot Eng*, 2002, vol. 4, pp. 2527–2606.
- [111] A. Miano, F. Di Carlo, A. Mele *et al.*, “Damage assessment through the use of SBAS-DInSAR data: an application to the ‘Vittorino da Feltre’ masonry school building in Rome (under review),” 2023.
- [112] F. Bozzano, A. Caserta, A. Govoni *et al.*, “Static and dynamic characterization of alluvial deposits in the Tiber River Valley: New data for assessing potential ground motion in the City of Rome,” *J Geophys Res Solid Earth*, vol. 113, no. B1, 2008.
- [113] C. Baggio, A. Bernardini, R. Colozza, *et al.*, “Field manual for post-earthquake damage and safety assessment and short term countermeasures (AeDES),” *European Commission – Joint Research Centre – Institute for the Protection and Security of the Citizen, EUR*, vol. 22868, 2007.

- [114] D. Infante, P. Confuorto, D. Di Martire *et al.*, "L'utilizzo di dati DInSAR per la valutazione delle conseguenze indotte sugli edifici da frane intermittenti a cinematica lenta," *XXVI Convegno Nazionale Di Geotecnica. Rome, Italy*, pp. 20–22, 2017.
- [115] Inc. Computers and Structures, SAP2000 v21.0.2, 2019.
- [116] Ministry of Infrastructure and Transport, Circolare n. 7 C.S.LL.PP., "Instructions for the application of the 'Update of the Technical standards for construction' referred to in the ministerial decree of 17 January 2018.," 21 January 2019 (in Italian).
- [117] UNI EN 1998-3:2005, "Eurocode 8: Design of structures for earthquake resistance - Part 3: Assessment and retrofitting of buildings." 2005.
- [118] T. B. Panagiotakos and M. N. Fardis, "Seismic response of infilled RC frames structures," in *11th world conference on earthquake engineering*, 1996, vol. 23, p. 28.
- [119] G. K. Al-Chaar, "Evaluating strength and stiffness of unreinforced masonry infill structures," 2002.
- [120] M. N. Fardis, *Seismic design, assessment and retrofitting of concrete buildings: based on EN-Eurocode 8*, vol. 8. Springer, 2009.
- [121] D. Di Martire, A. Novellino, S. Tessitore *et al.*, "Application of DInSAR techniques to engineering geology studies in southern Italy," *Rendiconti Online Soc Geol Ital*, vol. 24, pp. 95–97, 2013.
- [122] J. Hu, Z. W. Li, X. L. Ding *et al.*, "Resolving three-dimensional surface displacements from InSAR measurements: A review," *Earth Sci Rev*, vol. 133, pp. 1–17, 2014, doi: <https://doi.org/10.1016/j.earscirev.2014.02.005>.
- [123] D. Cardone and G. Perrone, "Developing fragility curves and loss functions for masonry infill walls," *Earthq Struct*, vol. 9, no. 1, pp. 257–279, 2015.
- [124] M. Di Domenico, P. Ricci, and G. M. Verderame, "Empirical calibration of

hysteretic parameters for modelling the seismic response of reinforced concrete columns with plain bars," *Eng Struct*, vol. 237, p. 112120, 2021, doi: <https://doi.org/10.1016/j.engstruct.2021.112120>.

- [125] Ministry of Infrastructure and Transport, D.M. 17/01/18, "Technical standards for construction", 17 January 2018 (in Italian).
- [126] E. Cosenza, C. Del Vecchio, M. Di Ludovico *et al.*, "The Italian guidelines for seismic risk classification of constructions: technical principles and validation," *Bull Earthq Eng*, vol. 16, no. 12, pp. 5905–5935, 2018.

Author's publications

Publications on International Scientific Journals

1. A. Miano, A. Mele, D. Calcaterra *et al.*, "The use of satellite data to support the structural health monitoring in areas affected by slow-moving landslides: a potential application to reinforced concrete buildings," *Struct Health Monit*, vol. 20, no. 6, pp. 3265–3287, 2021, doi: 10.1177/1475921720983232.
2. F. Di Carlo, A. Miano, I. Giannetti *et al.*, "On the integration of multi-temporal synthetic aperture radar interferometry products and historical surveys data for buildings structural monitoring," *J Civ Struct Health Monit*, vol. 11, no. 5, pp. 1429–1447, Nov. 2021, doi: 10.1007/s13349-021-00518-4.
3. A. Miano, A. Mele, and A. Prota, A., "Fragility curves for different classes of existing RC buildings under ground differential settlements," *Eng Struct*, vol. 257, 114077, 2022, doi: <https://doi.org/10.1016/j.engstruct.2022.114077>.
4. D. A. Talledo, A. Miano, M. Bonano *et al.*, "Satellite radar interferometry: Potential and limitations for structural assessment and monitoring," *J Build Eng*, vol. 46, Apr. 2022, doi: 10.1016/j.jobe.2021.103756.
5. A. Mele, A. Miano, D. Di Martire *et al.*, "Potential of remote sensing data to support the seismic safety assessment of reinforced concrete buildings affected by slow-moving landslides," *Arch Civ Mech Eng*, vol. 22, no. 2, May 2022, doi: 10.1007/s43452-022-00407-7.
6. A. Mele, A. Vitiello, M. Bonano *et al.*, "On the Joint Exploitation of Satellite DInSAR Measurements and DBSCAN-Based Techniques for Preliminary Identification and Ranking of Critical Constructions in a Built Environment," *Remote Sens (Basel)*, vol. 14, no. 8, Apr. 2022, doi: 10.3390/rs14081872.
7. A. Miano, F. Di Carlo, A. Mele *et al.*, "GIS Integration of DInSAR Measurements, Geological Investigation and Historical Surveys for the Structural Monitoring of Buildings and Infrastructures: An Application to the Valco San Paolo Urban Area of Rome," *Infrastructures (Basel)*, vol. 7, no. 7, Jul. 2022, doi: 10.3390/infrastructures7070089.

8. A. Mele, M. Crosetto, A. Miano *et al.*, "ADAFinder tool applied to EGMS data for the Structural Health Monitoring of urban settlements," vol. 15, no. 324, 2023, doi: <https://doi.org/10.3390/rs15020324>.
9. A. Miano, Miano, F. Di Carlo, A. Mele *et al.*, "Damage assessment through the use of SBAS-DInSAR data: an application to the 'Vittorino da Feltre' masonry school building in Rome (under review)," 2023.

Other publications

1. A. Miano, A. Mele, D. Di Martire *et al.*, "Remote sensing data to support the structural monitoring of RC buildings affected by ground instability phenomena," *Rivista Italiana di Geotecnica*, anno LV n.4, ottobre-dicembre 2021.
2. A. Mele, A. Miano, D. Di Martire *et al.*, "Seismic assessment of an existing RC building affected by slow-moving landslides induced displacements monitored by remote sensing technique," *Proceedings of 8th ECCOMAS Thematic Conference on Computational Methods in Structural Dynamics and Earthquake Engineering (COMPADYN)*, Athens, 28-30 June 2021.
3. A. Mele, I. Giannetti, F. Di Carlo *et al.*, "From historical surveys to innovative MT-InSAR techniques: structural monitoring of 20th century heritage buildings in Rome", *Proceedings of International Conference on Metrology for Archaeology and Cultural Heritage*, Milan, 20-22 October 2021.
4. A. Mele, A. Miano, M. Bonano *et al.*, "GIS to support the built-up environment structural health monitoring using remote sensing data. An application in Rome", *Gis Day 2021, Il GIS per il governo e la gestione del territorio*, a cura di B Cardone e F. Di Martino, pp. 69-79, 2021, ISBN 979-12-218-0223-8.
5. A. Miano, A. Mele, and A. Prota. "Fragility analysis for parallel plane frames RC structures subjected to ground settlements". *Proceedings of 2nd fib Italy YMG Symposium on Concrete and Concrete Structures*, Rome, 18-19 November 2021.

6. A. Mele, I. Giannetti, M. Rompato *et al.*, "Structural monitoring of a masonry hydraulic infrastructure in Rome: GIS integration of SAR data, geological investigation and historical surveys," In *European Workshop on Structural Health Monitoring: EWSHM 2022-Volume 3*, pp. 563-571, Cham: Springer International Publishing.
7. A. Miano, A. Mele, M. Bonano *et al.*, "The use of MT-DInSAR data for the safety assessment and monitoring of structures and infrastructures: the case study of 'Torri Stellari' in Rome," In *European Workshop on Structural Health Monitoring: EWSHM 2022-Volume 2*, pp. 387-396, Cham: Springer International Publishing.
8. F. Di Carlo, A. Mele, A. Miano *et al.*, "An application of the DInSAR technique for the structural monitoring of the 'Vittorino da Feltre' school building in Rome," In *European Workshop on Structural Health Monitoring: EWSHM 2022-Volume 3*, pp. 582-592, Cham: Springer International Publishing.
9. D. Talledo, A. Stella, M. Bonano *et al.*, "Techniques for structural assessment based on MT-DInSAR data, applied to the San Michele complex in Rome." In *European Workshop on Structural Health Monitoring: EWSHM 2022-Volume 3*, pp. 593-603, Cham: Springer International Publishing.
10. A. Mele, A. Vitiello, M. Bonano *et al.*, "Criticality maps of built areas based on Artificial Intelligence applied to Satellite data," *14th fib PhD Symposium*, Rome, 05-07 September 2022.

